Simulation of non-Gaussian/non-stationary stochastic processes: beyond second-order orthogonality

by

Hwanpyo Kim

A dissertation submitted to The Johns Hopkins University in conformity with the requirements for the degree of Doctor of Philosophy

Baltimore, Maryland

May, 2018

Abstract

The theory of stochastic processes and their generations are indispensable to characterize wind fluctuations, ocean waves, and earthquake excitations among other quantities in engineering. To computationally analyze and simulate these stochastic systems, practical realization of samples of stochastic processes is essential. The object of this thesis is to introduce new state-of-the-art methodologies for the generation of stochastic processes with non-Gaussianity/non-stationarity possessing higher-order properties than the second-order orthogonality.

A new type of Iterative Translation Approximation Method (ITAM) using the Karhunen-Loève expansion was developed for simulating non-Gaussian and non-stationary processes utilizing translation process theory. The proposed methodology enhances the accuracy of simulated processes in matching a prescribed autocorrelation, maintains the computational efficiency, and resolves limitations caused by utilizing evolutionary power spectra for non-stationary processes.

A new generalized stochastic expansion, the bispectral representation method (BSRM), expanded from the traditional spectral representation method is introduced

to simulate skewed nonlinear stochastic processes. With new orthogonal increments to satisfy the conditions of the Cramér spectral representation up to third order orthogonality, the BSRM generates samples that match both the power spectrum and bispectrum of the process by modeling complex nonlinear wave interactions.

A model of phase angle distributions to characterize phase coupling in higher-order stochastic processes is presented. Relationships between the trigonometric moments of circular distributions of phase differences and higher-order cumulant spectra are derived. The prescribed properties are shown to accurately model quadratic and cubic phase couplings in simple stochastic processes and can easily be extended to general n-wave couplings.

Lastly, as applications of the prescribed methods, wind pressure and turbulent wind velocity time histories are generated with SRM, ITAM, and BSRM and applied to two different nonlinear dynamic structural systems. For structures having material and geometrical nonlinearities, performance of an elastic perfectly-plastic structure and the buffeting response of a long-span bridge with coupled aerodynamic forces are examined. The structures are investigated to observe the effect of higher-order properties of the excitations on the response when compared to conventional second-order Gaussian and non-Gaussian excitations.

Primary Reader: Michael D. Shields

Secondary Reader: Lori Graham-Brady, James K. Guest

Acknowledgments

I am thankful to my wife, Jeougeun, who has believed in and supported me for five years to finish this thesis and I would not make it without your endless love and generous consideration. Whenever I was in a slump, you always give your heartening hands to hold me. Also, I could not have made it without the love and encouragement of my parents, Jae Gyu and Suk Young. I am happy to finish this thesis with my seventeen-months old son, Hojune, who always smiles at me and runs to me whenever I enter my home.

I thank my advisor, professor Michael D. Shields for guiding me to achieve this goal in my academic life. Even though I was hard to adapt myself to the new changing environment in the US, he understood me and guided me in the right direction. I also thank my thesis committee members, Professor Lori Graham-Brady and Professor James K. Guest, who gave me great opportunities for my research. Also, in the department of Civil Engineering at Johns Hopkins University, I would like to thank Professors Somnath Gosh and Robert Dalrymple for teaching me interesting materials which became strong foundations in my research. I also am grateful to Professor

ACKNOWLEDGMENTS

James C. Spall in the Department of Applied Mathematics and Statistics and professor Yun Chen in the Department of Mechanical Engineering who broadened my view of research. I also need to thank my previous advisor, Professor Sung Soon Yhim, at the University of Seoul, who cared about me and supported me continuously. I also appreciate Lisa Wetzelberger for her continued support for what I need and request.

I am thankful to Dr. Youngsuk Kim in Risk Management Solutions who became my mentor with countless advice. I also am grateful to Dr. DongHun Yeo and Dr. Liang Shi of the National Institute of Standards and Technology for their willingness to share wind velocity data from their Large Eddy Simulation models. Finally, I am so appreciative of my colleagues in my department, Gary, Nicolas, Abdullah, Aakash, Jiaxin, Sirui, Lohit, Mohit, Wei, Anindya, Hamid, Zhaohao, Fardad, Preetish, Hak Young, May Thu, Mikhail, Sriram, Jinlei, Noah, Dr. Giovanis, and Dr. Wei. Especially, thanks to my true friend, Dr. V. S. Sundar in the University of California, San Diego who just have a beautiful son, Imai. I am happy to work with all of you and share our experiences together.

Thanks for all your encouragement.

Dedication

This thesis is dedicated to my parent, Jae Gyu Kim and Suk Young Yoon, and my love, Jeoungeun Lee.

Contents

List of Tables

List of Figures

Chapter 1

Introduction

The theory of random processes has broad applications in engineering from characterizing and simulating heterogeneous materials to time histories of ocean waves, wind fluctuations, and seismic excitations. Computational examination of these stochastic frameworks requires the realistic generation of sample functions of stochastic processes. For Monte Carlo(MC) simulation, a large number of samples of the stochastic processes are simulated and the results are statistically examined. Therefore, the generation of realistic stochastic processes/fields which include desired properties to an acceptable degree are important.

Even though there have been several methodologies for sample function realization introduced during the last 40 years, most are limited to stationary and Gaussian processes. The general form of the stochastic expansion we employ for simulation is

given by:

$$A(x,\omega) \approx \hat{A}(x,\omega) = \sum_{i=1}^{n} C_i(\omega)\theta_i(x); x \in D, \omega \in \Omega \tag{1.1}$$

where $\{C_i(\omega)\}$ are a set of random variables on a probability space (Ω, F, P) and $\{\theta_i(x)\}$ are basis deterministic functions. Most stochastic expansions have been derived form Eq. (1.1) only including second-order properties of the processes (by matching the covariance function, $C(x_1, x_2)$). The most common and popular expansions with Gaussian properties are the spectral representation method [1, 2, 3] and the Karhunen-Loève expansion [4, 5] with their random variables $\{C_i(\omega)\}$ derived such that:

$$C(x_1, x_2) = E[A(x_1)A(x_2)] \approx E[\hat{A}(x_1)\hat{A}(x_2)] \tag{1.2}$$

The spectral representation utilizes harmonic functions as $\{\theta_i(x)\}$ and its $\{C_i(\omega)\}$ are derived form the power spectral density function (Fourier transform of $C(x_1, x_2)$). Analogously, for the Karhunen-Loève expansion, the eigenfunctions and eigenvalues of $C(x_1, x_2)$ are $\{C_i(\omega)\}$ and $\{\theta_i(x)\}$ are uncorrelated zero mean, unit variance random variables.

The fundamental limitation of the prescribed methodologies is their second-order character, only satisfying the covariance of the process. There is no way to represent many real stochastic processes with strong non-Gaussian properties which come from nonlinear systems including turbulent fluctuations given by the Navier-Stokes equations, seismic excitation in nonlinear soil, and the systems approximated with n-th

order Volterra series [6, 7]. Processes with complex nonlinear dependencies and wave interactions that result from nonlinear systems are referred to as nonlinear processes.

One of the attempts to represent the nonlinear processes is nonlinear transformations (also referred to as translation processes [8]). For a translation process, a Gaussian process is mapped to a non-Gaussian process which is often depicted by its marginal non-Gaussian distribution. Another approach is to generate the process with prescribed higher-order spectra and correlations.

The objective of this thesis is to introduce new methodologies for simulation of non-Gaussian/non-stationary stochastic processes including higher-order properties beyond the second-order. Based on translation processes, the expanded Iterative Translation Approximation Method (ITAM) with Karhunen-Loève expansion is introduced for the enhanced performance to achieve desired non-stationary properties [9]. Secondly, a generalized spectral representation method, called as the Bispectral representation method, is developed to include the bispectrum in its expansion [10]. Thirdly, a new approach to model phase distributions is developed to possess higher-order phase coupling in the generation of stochastic processes. Finally, materially or geometrically nonlinear structural dynamics are analyzed to validate the effect of the higher-order properties in their simulation.

1.1 Spectral representation method

The spectral representation method to represent stochastic processes is introduced in this section. Cramér [11] represented a zero mean and stationary stochastic processes following the Fourier-Stiltjes integral as

$$f(t) = \int_{-\infty}^{\infty} e^{i\omega t} dz(\omega) \tag{1.3}$$

where a spectral process, $z(\omega)$, satisfies the following orthogonality conditions as [12, 13, 14]

$$\begin{aligned}
&E[dz(\omega)] = c[dz(\omega)] = 0 \\
&E[dz(\omega_1)dz^\star(\omega_2)] = c[dz(\omega_1)dz^\star(\omega_2)] = \delta(\omega_1 - \omega_2)S_{ff}(\omega_1)d\omega_1 \\
&E[dz(\omega_1)dz(\omega_2)dz^\star(\omega_3)] = c[dz(\omega_1)dz(\omega_2)dz^\star(\omega_3)] \\
&= \delta(\omega_1 + \omega_2 - \omega_3)B_{ff}(\omega_1, \omega_2)d\omega_1 d\omega_2 \\
&c[dz(\omega_1)dz(\omega_2)dz(\omega_3)dz^\star(\omega_4)] = \delta(\omega_1 + \omega_2 + \omega_3 - \omega_4)T_{ff}(\omega_1, \omega_2, \omega_3)d\omega_1 d\omega_2 d\omega_3 \\
&\qquad\qquad \vdots \\
&c[dz(\omega_1)dz(\omega_2)d\cdots dz^\star(\omega_k)] \\
&= \delta(\omega_1 + \omega_2 + \cdots - \omega_k)C_{ff}(\omega_1, \omega_2, \cdots, \omega_{k-1})d\omega_1 d\omega_2 \cdots d\omega_{k-1}
\end{aligned} \tag{1.4}$$

where $E[\cdot]$ denotes expectation, $c[\cdot]$ represents cumulant. $\delta(\cdot)$ and $S_{ff}(\omega)$ are delta function and the power spectrum, respectively. $B_{ff}(\omega_1, \omega_2)$ is the bispectrum, $T_{ff}(\omega_1, \omega_2, \omega_3)$

is the trispectrum, and $C_{ff}(\omega_1, \omega_2, \cdots, \omega_{k-1})$ is the kth-order polyspectrum. The definition and properties of cumulants and their spectra of various order will be discussed in Section 1.3.2.

The spectral representation of real processes in Eq. (1.3) can be derived as:

$$f_R(t) = \int^{\infty} [\cos(\omega t) du(\omega) + \sin(\omega t) dv(\omega)] \tag{1.5}$$

with two orthogonal increments $du(\omega) = 2\Re[dz(\omega)]$ and $dv(\omega) = -2\Im[dz(\omega)]$ and the prescribed orthogonality conditions [12, 14, 15] in Eq. (1.4) given as

$$\begin{aligned}
&E[du(\omega)] = E[dv(\omega)] = 0 \\
&E[du^2(\omega)] = E[du^2(\omega)] = 2S(\omega)d\omega \\
&E[du(\omega_1)du(\omega_2)] = E[dv(\omega_1)dv(\omega_2)] = 0 \text{ for } \omega_1, \omega_2 \geq 0; \omega_1 \neq \omega_2 \\
&E[du(\omega_1)dv(\omega_2)] = 0 \text{ for } \omega_1, \omega_2 \geq 0
\end{aligned} \tag{1.6}$$

The third-order conditions are expressed as

$$\begin{aligned}
&E[du(\omega_1)du(\omega_2)du(\omega_3)] \\
&= 2\Re[dB(\omega_1,\omega_2)\delta(\omega_1+\omega_2-\omega_3) + dB(\omega_1,\omega_3)\delta(\omega_1-\omega_2+\omega_3) \\
&+ dB(\omega_2,\omega_3)\delta(-\omega_1+\omega_2-\omega_3) + dB(\omega_1,\omega_2)\delta(\omega_1+\omega_2+\omega_3)] \\
&E[dv(\omega_1)dv(\omega_2)dv(\omega_3)] \\
&= -2\Im[dB(\omega_1,\omega_2)\delta(\omega_1+\omega_2-\omega_3) + dB(\omega_1,\omega_3)\delta(\omega_1-\omega_2+\omega_3) \\
&+ dB(\omega_2,\omega_3)\delta(-\omega_1+\omega_2-\omega_3) - dB(\omega_1,\omega_2)\delta(\omega_1+\omega_2+\omega_3)]
\end{aligned} \tag{1.7}$$

and

$$\begin{aligned}
&E[du(\omega_1)du(\omega_2)dv(\omega_3)] \\
&= 2\Im[dB(\omega_1,\omega_2)\delta(\omega_1+\omega_2-\omega_3) - dB(\omega_1,\omega_3)\delta(\omega_1-\omega_2+\omega_3) \\
&- dB(\omega_2,\omega_3)\delta(-\omega_1+\omega_2-\omega_3) - dB(\omega_1,\omega_2)\delta(\omega_1+\omega_2+\omega_3)] \\
&E[du(\omega_1)dv(\omega_2)dv(\omega_3)] \\
&= 2\Re[dB(\omega_1,\omega_2)\delta(\omega_1+\omega_2-\omega_3) + dB(\omega_1,\omega_3)\delta(\omega_1-\omega_2+\omega_3) \\
&- dB(\omega_2,\omega_3)\delta(-\omega_1+\omega_2-\omega_3) - dB(\omega_1,\omega_2)\delta(\omega_1+\omega_2+\omega_3)]
\end{aligned} \tag{1.8}$$

where $dB(\omega_1,\omega_2) = B(\omega_1,\omega_2)d\omega_1 d\omega_2$.

At first, the digital simulation of Gaussian stochastic processes was proposed by Rice [16] by satisfying the form in Eq. (1.5). Secondly, Shinozuka introduced the simulation of Gaussian multi-variate and multi-dimensional stationary processes

[1] and Shinozuka and Jan [2] included the non-stationary processes. Furthermore, Shinozuka and Deodatis [3, 17, 18] reviewed the properties of SRM deeply including Gaussianity, ergodicity of sample functions and so on.

Let us introduce the prescribed spectral methods to simulate a Gaussian process, $f_G(t)$ which is a zero-mean, stationary Gaussian stochastic process with a autocorrelation function $R_{f_G f_G}(\tau)$ and two-sided power spectrum $S_{f_G,f_G}(\omega)$ related through the Wiener-Khintchine theorem [19, 20] as

$$S_{f_G f_G}(\omega) = \frac{1}{2\pi} \int_{-\infty}^{\infty} R_{f_G f_G}(\tau) e^{-i\omega\tau} d\tau \tag{1.9}$$

$$R_{f_G f_G}(\omega) = \int_{-\infty}^{\infty} S_{f_G f_G}(\omega) e^{i\omega\tau} d\omega \tag{1.10}$$

For a real and Gaussian process, the former expression of Eq. (1.5) can be discretized as

$$f_G(t) = \sum_{k=0}^{N} [\cos(\omega_k t) du(\omega_k) + \sin(\omega_k t) dv(\omega_k)] \tag{1.11}$$

where $\omega_k = k\Delta\omega$. The process can be shown to have the corresponding first and

second-order orthogonal conditions from Eq. (1.6) [12] given as

$$\begin{aligned} &E[du(\omega)] = E[dv(\omega)] = 0 \\ &E[du(\omega)^2] = E[dv(\omega)^2] = 2S_{f_G f_G}(\omega)d\omega \\ &E[du(\omega_1)du(\omega_2] = E[dv(\omega_1)dv(\omega_2)] = 0; \omega_1 \neq \omega_2 \\ &E[du(\omega)dv(\omega)] = 0 \end{aligned} \tag{1.12}$$

The two forms of the spectral representation have been proposed by utilizing different orthogonal increments [21]. The first form of orthogonal increments [16] is following:

$$\begin{aligned} du(\omega_k) &= X_k \\ dv(\omega_k) &= Y_k \end{aligned} \tag{1.13}$$

where X_k and Y_k are independent and identically distributed Gaussian random variables following $N(0, \sqrt{2S(\omega_k)\Delta\omega})$. Eq. (1.11) is simplified as

$$f(t) = \sum_{k=0}^{N} A_k \sqrt{Q_k} \cos(\omega_k t - \theta_k) \tag{1.14}$$

where $A_k = \sqrt{2S(\omega_k)\Delta\omega_k}$ and $\theta_k = \tan^{-1}\left(\frac{Y_k}{X_k}\right) \sim U[-\pi, \pi)$ are independent random phase angles and

$$Q_k = \left(\frac{X_k}{A_k}\right)^2 + \left(\frac{Y_k}{A_k}\right)^2 \sim \chi_2^2 \tag{1.15}$$

The second form of the SRM was proposed by Shinozuka [2] having different

orthogonal increments as

$$\begin{aligned} du(\omega_k) &= \sqrt{2}A_k \cos(\theta_k) \\ dv(\omega_k) &= \sqrt{2}A_k \sin(\theta_k) \end{aligned} \tag{1.16}$$

where $\phi_k \sim u[-\pi, \pi)$ is uniformly independent random phase angles yielding an expansion of the form

$$f(t) = \sqrt{2} \sum_{k=0}^{N} A_k \cos(\omega_k t - \theta_k) \tag{1.17}$$

Both distinct expressions of the SRM, Eqs. (1.14) and (1.17), satisfy the mentioned orthogonal conditions up to second-order in Eq. (1.12). However, they have different properties in view of Gaussianity and ergodicity. The first representation, Eq. (1.14), is always Gaussian, but non-ergodic [3]. However, the second one, Eq. (1.17) has asymptotically Gaussian as $N \to \infty$, and is strongly ergodic [3]. Furthermore, the cosine series formula can be computed efficiently using the Fast Fourier Transform [3, 17, 22].

In this thesis, the second form of the SRM, Eq (1.17) is mainly utilized and researched. Eq. (1.17) has one independent uniformly distributed random phase angle per cosine term. However, in non-Gaussian processes, the random phase angles are not independent and this fact will be exploited for simulation purposes.

1.2 Karhunen-Loève expansion

Let assume $A(x,\theta)$ be a stochastic process defined on the probability space (Ω,σ,P) over the domain D with mean $\bar{A}(x)$ and finite variance $E[(A(x,\theta)-\bar{A}(x))^2]$. The process can be proposed as [4]

$$A(x,\theta)=\bar{A}(x)+\sum_{i=1}^{\infty}\sqrt{\lambda_i}\zeta_i(\theta)f_i(x) \tag{1.18}$$

where $f_i(x)$ and λ_i are the eigenvector functions and eigenvalues of the covariances $C(x_1,x_2)$ as the deterministic functions. The homogeneous Fredholm integral of the second kind specifies the prescribed eigenvalues and eigenvectors given by

$$\int_D C(x_1,x_2)f_i(x_1)dx_1=\lambda_i f_i(x_2) \tag{1.19}$$

Numerical solutions of Eq. (1.19) to determine the basis functions are introduced [4, 23] in Eq. (1.1). The computed eigenvectors satisfy the following equation as an orthogonal deterministic set of basis function given by

$$\int_D f_i(x)f_j(x)dx=\delta_{ij} \tag{1.20}$$

where δ_{ij} is the Kronecker-delta function. Furthermore, $\zeta_i(\theta)$ in Eq. (1.18) indicates an uncorrelated random variable set with zero mean and unit standard-deviation as:

$$\zeta_i(\theta) = \frac{1}{\sqrt{\lambda_i}} \int_D \left[A(x,\theta) - \bar{A}(x)\right] f_i(x) dx \tag{1.21}$$

Practically, the expansion in Eq. (1.18) is approximated using a finite number, M, of eigenvalues and eigenvectors as:

$$\tilde{A}(x,\theta) = \bar{A}(x) + \sum_{i=1}^{M} \sqrt{\lambda_i}\zeta_i(\theta) f_i(x) \tag{1.22}$$

Eq. (1.22) is used for simulation purposes by generating the set of random variables $\zeta_i(\theta)$ [4, 9, 23]. Although $\zeta_i(\theta)$ are Gaussian for Gaussian processes, they are should be non-Gaussian for non-Gaussian processes. However, to determine the non-Gaussian distribution, it is required to solve Eq. (1.21). Phoon et al. [24, 25] suggested iterative methodologies to solve Eq. (1.21). However, because of the Central Limit Theorem, an independent non-Gaussian sets easily tend to be closer to Gaussian than the required non-Gaussian $M \to \infty$ [26].

1.3 Non-Gaussian stochastic processes

This thesis is specifically concerned with modeling random processes that are non-Gaussian in nature. That is, the marginal density of the stochastic process does not

follow a Gaussian distribution and, more generally, the full probability structure of the process does not follow the joint Gaussian. The work here will consider two different means of modeling non-Gaussian processes as discussed in the following sections.

1.3.1 Translation process theory

Perhaps the most common means of modeling non-Gaussian stochastic processes utilizes Grigoriu's translation process theory [8] given by

$$Y(t) = g(X(t)) \tag{1.23}$$

with $X(t)$ and $Y(t)$ are a Gaussian and non-Gaussian process, respectively. The marginal non-Gaussian CDF $g(\cdot) = F_N^{-1}\{\Phi[\cdot]\}$ maps a Gaussian $X(t)$ to the prescribed non-Gaussian distribution.

For non-stationary processes, Ferrante et al. [27] extended the translation process theory for non-stationary cases as

$$Y(t) = g(X(t), t) = F_N^{-1}\{\Phi[X(t)], t\} \tag{1.24}$$

with the inverse time-dependent marginal non-Gaussian CDF $F_N^{-1}(\cdot, t)$ and the stationary and normalized Gaussian CDF $\Phi(\cdot)$. The result of translated ACF can be

calculated as

$$\begin{aligned} R_N(s,t) &= \mu(s)\mu(t) + \sigma(s)\sigma(t)\xi(s,t) \\ &= \int_{-\infty}^{\infty}\int_{-\infty}^{\infty} g(x_1,s)g(x_2,t)\phi\{x_1,x_2;\rho(s,t)\}\,dx_1\,dx_2 \end{aligned} \tag{1.25}$$

with the mean $\mu(t)$ and the standard deviation $\sigma(t)$ of the non-Gaussian process $Y(t)$ at varying time t. The correlation distortion, $\xi(s,t)$, means its non-Gaussian normalized ACF and $\phi\{\cdot,\cdot;\rho(s,t)\}$ is the joint Gaussian PDF with the normalized Gaussian ACF, $\rho(s,t)$, as

$$\phi\{x_1,x_2;\rho(s,t)\} = \frac{1}{\sqrt{2\pi(1-\rho(s,t)^2)}}\exp\left(-\frac{x_1^2+x_2^2-2\rho(s,t)x_1x_2}{2(1-\rho(s,t)^2)}\right). \tag{1.26}$$

For stationary and non-Gaussian processes with $\tau = s - t$, Eq. (1.25) simplified to

$$\begin{aligned} R_N(\tau) &= \mu^2 + \sigma^2\xi(\tau) \\ &= \int_{-\infty}^{\infty}\int_{-\infty}^{\infty} g(x_1)g(x_2)\phi\{x_1,x_2;\rho(\tau)\}\,dx_1\,dx_2 \end{aligned} \tag{1.27}$$

By using standard numerical quadrature rules such as quad2D function in MATLAB, we can solve Eq. (1.25) [28].

The translated ACFs, Eqs (1.25) or (1.27) can be mapped from an underlying Gaussian processes at all times, but, the inverse translation to estimate an unknown Gaussian ACF from a prescribed non-Gaussian PDF does not have an analytical solution occasionally. These incompatible cases with non-stationary translation processes

are introduced as the following two cases [27, 29, 30]. First, the positive semi-definite non-Gaussian ACF are not guaranteed in the inversion of Eq. (1.25). Second, part of the non-Gaussian normalized correlation $\xi(s,t)$ in Eqs. (1.25) and (1.27) are not placed on its admissible range $[\xi^{min}(s,t), \xi^{max}(s,t)]$. To resolve the prescribed cases with inadmissibility, Iterative Translation Approximation Methods were developed [22, 29, 9] and the recent methodology with K-L expansion is introduced in Chapter 2.

1.3.2 Higher-order correlations and higher-order spectra

Another means of modeling non-Gaussian stochastic processes commonly used in signal processing [31, 32] is through higher-order moments and/or spectra. The higher-order properties are fundamental factors of stochastic processes resulting from nonlinear systems that induce non-Gaussianity [31]. Combining these higher-order moments and spectra with non-Gaussianity in the processes is essential to realistic modeling and characterization of diverse physical system. Torquato [33] and several researchers [34, 35] utilized n-point correlations to explain material properties for random heterogeneous materialswhich are not explained only with the second order covariances of the processes/fields with inefficient optimization problems. Moreover, applications in nonlinear dynamics [36, 37, 38] shows that the higher-order proper-

ties are important including turbulence [39, 40, 41] and wave interaction [42, 43, 44]. Furthermore, astronomic data examination [45] and physics of plasma [46] are extensively studied with their characterization. However, the prescribed researches have been focused on interpretation and characterization of higher-order properties of non-Gaussian processes/fields. There had been no mathematical form to include the higher-order properties, therefore, we will focused on the development of stochastic processes modeling to integrate these properties in Chapter 3. Having motivated their importance, we now briefly review the specific mathematical properties of interest here.

1.3.2.1 Cumulant and moment functions

The definition of joint moments of order $r = k_1 + k_2 + \cdots + k_n$ for a real random vector $X = \{x_1, x_2, \cdots, x_n\}$ are given by [47, 14]

$$\begin{aligned} m_{k_1,k_2,\cdots,k_n} &\equiv E[x_1^{k_1} x_2^{k_2} \cdots x_n^{k_n}] \\ &= (-i)^r \frac{\partial^r \Phi(\omega_1, \omega_2, \cdots, \omega_n)}{\partial \omega_1^{k_1} \omega_2^{k_2} \cdots \partial \omega_n^{k_n}} \bigg|_{\omega_1=\omega_2=\cdots=\omega_n=0} \end{aligned} \tag{1.28}$$

and the joint cumulants of order r are defined by:

$$c_{k_1,k_2,\cdots,k_n} \equiv (-i)^r \frac{\partial^r \ln \Phi(\omega_1, \omega_2, \cdots, \omega_n)}{\partial \omega_1^{k_1} \omega_2^{k_2} \cdots \partial \omega_n^{k_n}} \bigg|_{\omega_1=\omega_2=\cdots=\omega_n=0} \tag{1.29}$$

where the joint characteristic function is

$$\Phi(\omega_1, \omega_2, \cdots, \omega_n) \equiv E\big[e^{i(\omega_1 x_1 + \omega_2 x_2 + \cdots + \omega_n x_n)}\big] \tag{1.30}$$

In addition, the moments and the cumulants are related as the following expressions [14] as

$$c_{k_1,k_2,\cdots,k_n} = \sum (-1)^{p-1}(p-1)! E\big[\prod_{i\in s_1} x_i\big] E\big[\prod_{i\in s_2} x_i\big] \cdots E\big[\prod_{i\in s_p} x_i\big] \tag{1.31}$$

where the summation extends over all groups $\{s_1, s_2, \cdots, s_p\}$ of the integers $k_1, k_2, \cdots, k_n$. In special, it is to be observed that each of cumulants higher than second order are zero when X is a jointly Gaussian random vector in contrast to the moments. Therefore, the cumulants of order $n > 2$ quantify the level of non-Gaussianity.

For a real stationary stochastic processes, $f(t)$, the moment and the cumulant can be indicated by

$$\begin{aligned} m[f(t), f(t+\tau_1), \cdots, f(t+\tau_{n-1})] &\equiv E[f(t)f(t+\tau_1)\cdots f(t+\tau_n)] \\ &= m_n^f(\tau_1, \tau_2, \cdots \tau_{n-1}) \\ c[f(t), f(t+\tau_1), \cdots, f(t+\tau_{n-1})] &\equiv c_n^f(\tau_1, \tau_2, \cdots \tau_{n-1}) \end{aligned} \tag{1.32}$$

The cumulant can be denoted by combining Eqs. (1.31) and (1.32) as

$$
\begin{aligned}
& c_1^f = m_1^f \\
& c_2^f(\tau) = m_2^f(\tau) - m_1^f \\
& c_3^f(\tau_1, \tau_2) = m_3^f(\tau_1, \tau_2) - m_1^f[m_2^f(\tau_1) + m_2^f(\tau_2) + m_2^f(\tau_2 - \tau_1)] + 2(m_1^f)^3 \\
& c_4^f(\tau_1, \tau_2, \tau_3) \\
& = m_4^f(\tau_1, \tau_2, \tau_3) - m_2^f(\tau_1)m_2^f(\tau_3 - \tau_2) - m_2^f(\tau_2)m_2^f(\tau_3 - \tau_1) - m_2^f(\tau_3)m_2^f(\tau_2 - \tau_1) \\
& - m_1^f[m_3^f(\tau_2 - \tau_1, \tau_3 - \tau_1) + m_3^f(\tau_2, \tau_3) + m_3^f(\tau_2, \tau_4) + m_3^f(\tau_1, \tau_2)] \\
& + (m_1^f)^2[m_2^f(\tau_1) + m_2^f(\tau_2) + m_2^f(\tau_3) + m_2^f(\tau_3 - \tau_1) + m_2^f(\tau_3 - \tau_2) + m_2^f(\tau_2 - \tau_1)] \\
& + 6(m_1^f)^4 \\
& \qquad \vdots
\end{aligned}
\tag{1.33}
$$

It is obvious that the moments and cumulants up to the third order are duplicated when $f(t)$ is a processes with zero mean. Similar to the property of cumulants of a jointly non-Gaussian random variable, all cumulants of the process higher than the second order represent non-Gaussian properties of the processes. For details, odd-ordered cumulant and even-ordered cumulants express asymmetric and symmetric non-linearities, respectively [48].

Furthermore, the statistics can be related the cumulants at $\tau_i = 0$ as

$$\begin{aligned} c_2^f(0) &= m_2^f(0) = E[f(t)^2] \\ c_3^f(0,0) &= m_3^f(0,0) = E[f(t)^3] \\ c_4^f(0,0,0) &= E[f(t)^4] - 3\{E[f(t)^2]\}^2 \end{aligned} \tag{1.34}$$

The skewness and kurtosis of the process are matched with the third and fourth-order cumulants at the origins. However, we need to make a point of that the cumulant functions provide richer characterization and information of the process than the singular values of the statistics.

1.3.2.2 Polyspectra

In the frequency domain, the n-th order polyspectrum (also referred as cumulant spectrum) of a process $f(t)$ is defined as the Fourier transform of its n-th order cumulants as [47]

$$\begin{aligned} &C_n^f(\omega_1, \omega_2, \cdots, \omega_{n-1}) \\ &= \frac{1}{(2\pi)^{n-1}} \int_{-\infty}^{\infty} \cdots \int_{-\infty}^{\infty} c_n^f(\tau_1, \tau_2, \cdots \tau_{n-1}) e^{-i(\omega_1\tau_1 + \omega_2\tau_2 + \cdots + \omega_{n-1}\tau_{n-1})} d\tau_1 d\tau_2 \cdots d\tau_{n-1} \end{aligned} \tag{1.35}$$

where $C_n^f(\omega_1, \omega_2, \cdots, \omega_{n-1})$ is a complex number.

As the first order polyspectrum, the power spectrum is a widely known quantity

to show the energy/power related with different frequency waves in the processes. In addition, the traditional SRM expands a stochastic process by matching the desired 2nd-order property.

The bispectrum, the second form of polyspectrum, also, has been researched extensively to explain physical phenomena [47, 15, 49, 48, 45] regarding quadratic phase coupling. The details of phase coupling are discussed the following section. The important properties of bispectrum possesses are reviewed briefly here. First, the bispectrum owns the following symmetries.

1.
$$B(\omega_1, \omega_2) = B(\omega_1 + 2\pi T, \omega_2 + 2\pi T) \tag{1.36}$$

2.
$$\begin{aligned} &B(\omega_1, \omega_2) = B(\omega_2, \omega_1) = B^*(-\omega_2, -\omega_1) = B^*(-\omega_1, -\omega_2) \\ &= B(-\omega_1 - \omega_2, \omega_2) = B(\omega_1, -\omega_1 - \omega_2) = B(-\omega_1 - \omega_2, \omega_1) \\ &= B(\omega_2, -\omega_1 - \omega_2) \end{aligned} \tag{1.37}$$

For thesis symmetries, the bispectrum can be depicted within the principal domain $\omega_2 \geq 0$, $\omega_1 \geq \omega_2$, $\omega_1 + \omega_2 \leq \pi T$ as depicted in Figure 1.1.

Bispectrum, as mentioned that it is a complex value, also includes unique property that the real and imaginary parts having different physical meaning. It was shown that the real and imaginary components of the bispectrum are deduced to the Fourier transform of symmetric and antisymmetric parts of the third-order cumulant, $s(\tau_1, \tau_2)$

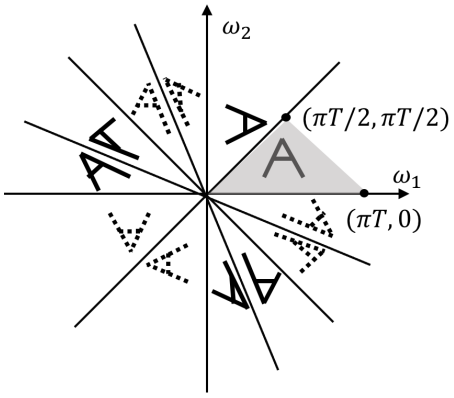

Figure 1.1: Symmetry properties of bispectrum.

and $a(\tau_1, \tau_2)$ as [50]

$$\begin{aligned} \Re B(\omega_1, \omega_2) &= \frac{1}{(2\pi)^2} \int_{-\infty}^{\infty} \int_{-\infty}^{\infty} s(\tau_1, \tau_2) e^{-i(\omega_1 \tau_1 + \omega_2 \tau_2)} d\tau_1 d\tau_2 \\ \Im B(\omega_1, \omega_2) &= \frac{-i}{(2\pi)^2} \int_{-\infty}^{\infty} \int_{-\infty}^{\infty} a(\tau_1, \tau_2) e^{-i(\omega_1 \tau_1 + \omega_2 \tau_2)} d\tau_1 d\tau_2 \end{aligned} \tag{1.38}$$

where

$$\begin{aligned} s(\tau_1, \tau_2) &= \frac{1}{2} \big\{ c_3^f(\tau_1, \tau_2) + c_3^f(-\tau_1, -\tau_2) \big\} \\ a(\tau_1, \tau_2) &= \frac{1}{2} \big\{ c_3^f(\tau_1, \tau_2) - c_3^f(-\tau_1, -\tau_2) \big\} \end{aligned} \tag{1.39}$$

Following the mentioned relationships, integrating the real and imaginary components of the bispectrum results in the skewness of the process and the derivative of the

process respectively [40, 42] as

$$\begin{aligned} E[f(t)^3] &= s(0,0) = c_3^f(0,0) \\ &= \int_{-\infty}^{\infty}\int_{-\infty}^{\infty} \Re B(\omega_1,\omega_2) d\omega_1 d\omega_2 \\ &= 6\int_{0}^{\infty}\int_{0}^{\infty} \Re B(\omega_1,\omega_2) d\omega_1 d\omega_2 \end{aligned} \tag{1.40}$$

$$\begin{aligned} & E\Big[\Big(\frac{\partial f(t)}{\partial t}\Big)^3\Big] \\ &= -\int_{-\infty}^{\infty}\int_{-\infty}^{\infty} \omega_1\omega_2(\omega_1+\omega_2)\Im B(\omega_1,\omega_2) d\omega_1 d\omega_2 \\ &= -6\int_{0}^{\infty}\int_{0}^{\infty} \omega_1\omega_2(\omega_1+\omega_2)\Im B(\omega_1,\omega_2) d\omega_1 d\omega_2 \end{aligned} \tag{1.41}$$

Finally, we can indicate bispectrum in terms of its magnitude and biphase, $\beta(\omega_1, \omega_2)$, as

$$B(\omega_1,\omega_2) = |B(\omega_1,\omega_2)| e^{i\beta(\omega_1,\omega_2)} \tag{1.42}$$

where

$$\beta(\omega_1,\omega_2) = \arctan\Big[\frac{\Im B(\omega_1,\omega_2)}{\Re B(\omega_1,\omega_2)}\Big] \tag{1.43}$$

In addition, trispectrum (also refered as the fourth-order cumulant spectra) can be defined as the Fourier transform of the fourth-order cumulant by Eq. (1.35). However,

the fourth-order cumulant are different from the the identical order moment as Eq. (1.34). Similar to the real and imaginary components of the bispectrum (Eq. (1.38)), the kurtosis and the trispectrum can be related to the one between the fourth-order cumulant with zero lag as [51]

$$\begin{aligned} c_4(0,0,0,0) &= E[f(t)^4] - 3 \cdot E[f(t)^2]^2 \\ &= \int_{-\infty}^{\infty}\int_{-\infty}^{\infty}\int_{-\infty}^{\infty} \Re T(\omega_1,\omega_2,\omega_3) d\omega_1 d\omega_2 d\omega_3 \end{aligned} \tag{1.44}$$

Lastly, similar to Eq. (1.42), a triphase, $\gamma(\omega_1,\omega_2,\omega_3)$ and a magnitude of the trispectrum can be utilized to represent the trispectrum as

$$T(\omega_1,\omega_2,\omega_3) = |T(\omega_1,\omega_2,\omega_3)| e^{i\gamma(\omega_1,\omega_2,\omega_3)} \tag{1.45}$$

where

$$\gamma(\omega_1,\omega_2,\omega_3) = \arctan\left[\frac{\Im T(\omega_1,\omega_2,\omega_3)}{\Re T(\omega_1,\omega_2,\omega_3)}\right] \tag{1.46}$$

1.3.2.3 Phase coupling and higher-order spectra

Higher-order moments/cumulants or higher-order spectra are used to detect and and quantify nonlinearities in stochastic processes. In a Fourier-basis, these higher-order properties show the interaction between distinct harmonic components causing contribution to the power at their sum and/or difference frequencies. Quadratic phase

coupling is the simplest interaction phenomenon and has been extensively studied [52, 53, 46, 54, 14]. 3rd-order cumulant and bispectrum was analytically calculated. The random process with quadratic phase coupling can be expressed as

$$f(t) = a\cos(\lambda_1 t - \theta_1) + b\cos(\lambda_2 t - \theta_2) + c\cos(\lambda_3 t - (\theta_1 + \theta_2)) \tag{1.47}$$

where frequencies are related as $\lambda_3 = \lambda_1 + \lambda_2$ and independent and identically uniformly distributed phase angles $\theta_i \sim U(-\pi, \pi]$ where $i \in 1, 2, 3$. At the third harmonic term, the quadratic phase coupling is placed. The 2nd-order cumulant(=moment) and power spectrum are calculated as

$$\begin{aligned} c_2(\tau) = R_2(\tau) &= E[f(t)f(t+\tau)] \\ &= \frac{a^2}{2}\cos(\lambda_1\tau) + \frac{b^2}{2}\cos(\lambda_2\tau) + \frac{c^2}{2}\cos(\lambda_3\tau) \end{aligned} \tag{1.48}$$

$$\begin{aligned} S(\omega) &= \frac{1}{2\pi}\int_{-\infty}^{\infty} c_2(\tau)e^{-i\omega\tau}d\tau \\ &= \frac{a^2}{4}[\delta(\omega-\lambda_1) + \delta(\omega+\lambda_1)] + \frac{b^2}{4}[\delta(\omega-\lambda_2) + \delta(\omega+\lambda_2)] \\ &+ \frac{c^2}{4}[\delta(\omega-\lambda_3) + \delta(\omega+\lambda_3)] \end{aligned} \tag{1.49}$$

The power spectrum of the simple example has 3 impulses with the coefficients $a^2/4$, $b^2/4$ and $c^2/4$, respectively as depicted in Figure 1.2a. The impulses are placed at the frequencies, λ_1, λ_2, and λ_3 in the region, $\omega > 0$. In view of power spectrum, the

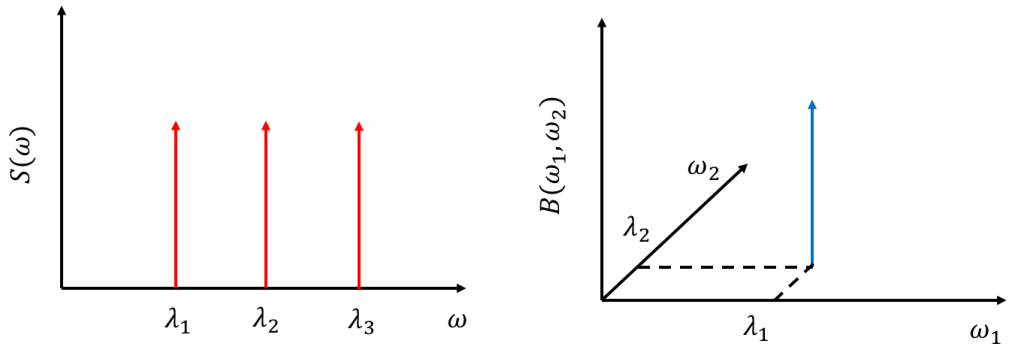

(a) **(b)**

Figure 1.2: (a) Power spectrum and (b) bispectrum for simple two-wave quadratic phase coupling.

quadratic phase coupling terms just identically performs with the independent terms.

The values of power spectrum causes the variance of Eq. (1.47) as

$$\text{Variance}[f(t)] = c_2(0) = R_2(0) = \int_{-\infty}^{\infty} S(\omega)d\omega = 2\Big(\frac{a^2}{4} + \frac{b^2}{4} + \frac{c^2}{4}\Big) \tag{1.50}$$

On the other hand, the 3rd-order cumulant(=moment) and bispectrum of the process is given as [54]

$$\begin{aligned} c_3(\tau_1, \tau_2) = R_3(\tau_1, \tau_2) = \\ = \frac{abc}{4}[\cos(\lambda_2\tau_1 + \lambda_1\tau_2) + \cos(\lambda_3\tau_1 - \lambda_1\tau_2) + \cos(\lambda_1\tau_1 + \lambda_2\tau_2) \\ + \cos(\lambda_3\tau_1 - \lambda_2\tau_2) + \cos(\lambda_1\tau_1 - \lambda_3\tau_2) + \cos(\lambda_2\tau_1 - \lambda_3\tau_2)] \end{aligned} \tag{1.51}$$

$$\begin{aligned} B(\omega_1, \omega_2) &= \frac{1}{(2\pi)^2} \int_{-\infty}^{\infty} \int_{-\infty}^{\infty} \big(c_3(\tau_1, \tau_2)\big) e^{-\omega_1 \tau_1} e^{-\omega_2 \tau_2} d\tau_1 d\tau_2 \\ &= \frac{abc}{8} [\delta(\omega_1 - \lambda_1, \omega_2 - \lambda_2) + \delta(\omega_1 + \lambda_1, \omega_2 + \lambda_2) \cdots] \end{aligned} \tag{1.52}$$

There are 12 impulses with same coefficients $\frac{abc}{8}$ in the bispectrum, Eq. (1.47), at (λ_1, λ_2) within the principal domain, $\omega_1 \geq \omega_2 \geq 0$ as Figure 1.2b. Compared to the power spectrum, the bispectrum represents the phase relations of harmonic components and contain it as the impulses at the coupled frequencies. Therefore, Eq. (1.47) has positive value of un-normalized skewness because of the bispectrum as

$$\begin{aligned} \text{Skew}[f(t)] = c_3(0,0) = R_3(0,0) &= \int_{-\infty}^{\infty} \int_{-\infty}^{\infty} B(\omega_1, \omega_2) d\omega_1 d\omega_2 \\ &= 12 \cdot \frac{abc}{8} \end{aligned} \tag{1.53}$$

Similar to the prescribed quadratic phase coupling example, a random process with cubic phase coupling at the last harmonic component can be expressed as

$$f(t) = a \cdot \cos(\lambda_1 t - \theta_1) + b \cos(\lambda_2 t - \theta_2) + c \cos(\lambda_3 t - \theta_3) + d \cos(\lambda_6 t - (\theta_1 + \theta_2 + \theta_3)) \tag{1.54}$$

The second-order cumulant(= moment) and power spectrum are given by

$$\begin{aligned} c_2(\tau) &= R_2(\tau) = E[f(t)f(t+\tau)] \\ &= \frac{a^2}{2}\cos(\lambda_1\tau) + \frac{b^2}{2}\cos(\lambda_2\tau) + \frac{c^2}{2}\cos(\lambda_3\tau) + \frac{d^2}{2}\cos(\lambda_6\tau) \end{aligned} \tag{1.55}$$

$$\begin{aligned} S(\omega) &= \frac{1}{2\pi}\int_{-\infty}^{\infty} R_2(\tau)e^{-i\omega\tau}d\tau \\ &= \frac{a^2}{4}[\delta(\omega-\lambda_1)+\delta(\omega+\lambda_1)] + \frac{b^2}{4}[\delta(\omega-\lambda_2)+\delta(\omega+\lambda_2)] \\ &+ \frac{c^2}{4}[\delta(\omega-\lambda_3)+\delta(\omega+\lambda_3)] + \frac{d^2}{4}[\delta(\omega-\lambda_6)+\delta(\omega+\lambda_6)] \end{aligned} \tag{1.56}$$

The power spectrum has 4 impulses with the values $a^2/4$, $b^2/4$, $c^2/4$, and $d^2/4$, respectively. Similar to the Eq. (1.48) and (1.49), the power spectrum suppresses the cubic phase relations of harmonic components and is not able to discriminate Eq. (1.54) from other processes without cubic phase coupling. The power spectrum and second order moment results in the variance of Eq. (1.54) as

$$\text{Variance}[f(t)] = c_2(0) = R_2(0) = \int_{-\infty}^{\infty} S(\omega)d\omega = 2\cdot\left(\frac{a^2}{4}+\frac{b^2}{4}+\frac{c^2}{4}+\frac{d^2}{4}\right) \tag{1.57}$$

However, the 4ourth-order cumulant which is not identical to the fourth-order moment

and depicts the cubic phase coupling obtained as

$$
\begin{aligned}
&c_4(\tau_1,\tau_2,\tau_3)\\
&= R_4(\tau_1,\tau_2,\tau_3) - R_2(\tau_1)\cdot R_2(\tau_2-\tau_3) - R_2(\tau_2)\cdot R_2(\tau_3-\tau_1) - R_2(\tau_3)\cdot R_2(\tau_1-\tau_2)\\
&= \frac{abcd}{8}[\cos(\lambda_2\tau_1+\lambda_1\tau_2-\lambda_6\tau_3)+\cos(\lambda_3\tau_1+\lambda_1\tau_2-\lambda_6\tau_3)+\cos(\lambda_1\tau_1+\lambda_2\tau_2-\lambda_6\tau_3)\\
&\quad+\cos(\lambda_3\tau_1+\lambda_2\tau_2-\lambda_6\tau_3)+\cos(\lambda_1\tau_1+\lambda_3\tau_2-\lambda_6\tau_3)+\cos(\lambda_2\tau_1+\lambda_3\tau_2-\lambda_6\tau_3)\\
&\quad+\cos(\lambda_6\tau_1-\lambda_2\tau_2-\lambda_3\tau_3)+\cos(\lambda_6\tau_1-\lambda_1\tau_2-\lambda_3\tau_3)+\cos(\lambda_6\tau_1-\lambda_3\tau_2-\lambda_2\tau_3)\\
&\quad+\cos(\lambda_6\tau_1-\lambda_1\tau_2-\lambda_2\tau_3)+\cos(\lambda_6\tau_1-\lambda_3\tau_2-\lambda_1\tau_3)+\cos(\lambda_6\tau_1-\lambda_2\tau_2-\lambda_1\tau_3)\\
&\quad+\cos(\lambda_2\tau_1-\lambda_6\tau_2+\lambda_1\tau_3)+\cos(\lambda_3\tau_1-\lambda_6\tau_2+\lambda_1\tau_3)+\cos(\lambda_3\tau_1+\lambda_2\tau_2+\lambda_1\tau_3)\\
&\quad+\cos(\lambda_2\tau_1+\lambda_3\tau_2+\lambda_1\tau_3)+\cos(\lambda_1\tau_1-\lambda_6\tau_2+\lambda_2\tau_3)+\cos(\lambda_3\tau_1-\lambda_6\tau_2+\lambda_2\tau_3)\\
&\quad+\cos(\lambda_3\tau_1+\lambda_1\tau_2+\lambda_2\tau_3)+\cos(\lambda_1\tau_1+\lambda_3\tau_2+\lambda_2\tau_3)+\cos(\lambda_1\tau_1-\lambda_6\tau_2+\lambda_3\tau_3)\\
&\quad+\cos(\lambda_2\tau_1-\lambda_6\tau_2+\lambda_3\tau_3)+\cos(\lambda_2\tau_1+\lambda_1\tau_2+\lambda_3\tau_3)+\cos(\lambda_1\tau_1+\lambda_2\tau_2+\lambda_3\tau_3)]\\
&-\frac{a^4}{8}[\cos(-\lambda_1\tau_1+\lambda_1\tau_2+\lambda_1\tau_3)+\cos(\lambda_1\tau_1-\lambda_1\tau_2-\lambda_1\tau_3)+\cos(\lambda_1\tau_1+\lambda_1\tau_2-\lambda_1\tau_3)]\\
&-\frac{b^4}{8}[\cos(-\lambda_2\tau_1+\lambda_2\tau_2+\lambda_2\tau_3)+\cos(\lambda_2\tau_1-\lambda_2\tau_2-\lambda_2\tau_3)+\cos(\lambda_2\tau_1+\lambda_2\tau_2-\lambda_2\tau_3)]\\
&-\frac{c^4}{8}[\cos(-\lambda_3\tau_1+\lambda_3\tau_2+\lambda_3\tau_3)+\cos(\lambda_3\tau_1-\lambda_3\tau_2-\lambda_3\tau_3)+\cos(\lambda_3\tau_1+\lambda_3\tau_2-\lambda_3\tau_3)]\\
&-\frac{d^4}{8}[\cos(-\lambda_6\tau_1+\lambda_6\tau_2+\lambda_6\tau_3)+\cos(\lambda_6\tau_1-\lambda_6\tau_2-\lambda_6\tau_3)+\cos(\lambda_6\tau_1+\lambda_6\tau_2-\lambda_6\tau_3)]
\end{aligned}
\tag{1.58}
$$

The trispectrum from the prescribed fourth-order cumulant is given by

$$\begin{aligned}
T(\omega_1,\omega_2,\omega_3) &= \frac{1}{(2\pi)^3}\int_{-\infty}^{\infty}\int_{-\infty}^{\infty}\int_{-\infty}^{\infty}\big(c_4(\tau_1,\tau_2,\tau_3)\big)e^{-\omega_1\tau_1}e^{-\omega_2\tau_2}e^{-\omega_3\tau_3}d\tau_1 d\tau_2 d\tau_3 \\
&= \frac{abcd}{16}[\delta(\omega_1-\lambda_1,\omega_2-\lambda_2,\omega_3-\lambda_3)+\delta(\omega_1+\lambda_1,\omega_2+\lambda_2,\omega_3+\lambda_3)+\cdots] \\
&- \frac{a^4}{16}[\delta(\omega_1+\lambda_1,\omega_2-\lambda_1,\omega_3-\lambda_1)+\delta(\omega_1-\lambda_1,\omega_2+\lambda_1,\omega_3+\lambda_1)+\cdots] \\
&- \frac{b^4}{16}[\delta(\omega_1+\lambda_2,\omega_2-\lambda_2,\omega_3-\lambda_2)+\delta(\omega_1-\lambda_2,\omega_2+\lambda_2,\omega_3+\lambda_2)+\cdots] \\
&- \frac{c^4}{16}[\delta(\omega_1+\lambda_3,\omega_2-\lambda_3,\omega_3-\lambda_3)+\delta(\omega_1-\lambda_3,\omega_2+\lambda_3,\omega_3+\lambda_3)+\cdots] \\
&- \frac{d^4}{16}[\delta(\omega_1+\lambda_6,\omega_2-\lambda_6,\omega_3-\lambda_6)+\delta(\omega_1-\lambda_6,\omega_2+\lambda_6,\omega_3+\lambda_6)+\cdots]
\end{aligned} \tag{1.59}$$

Inspection of Eq. (1.59) shows that the trispectrum has 48 components associated with cubic phase interactions of distinct harmonics (with magnitude $abcd/16$) and 6 components associated with "self-interactions" (3 wave coupling of waves with identical frequencies having magnitude $-a^4/16$, $-b^4/16$, $-c^4/16$, $-d^4/16$, respectively). The second terms exist even in the absence of wave interaction terms in the expansion. In other words, these self-interaction terms exist even in the classical SRM with asymptotic Gaussianity. The unnormalized kurtosis of Eq. (1.54) is given as

$$\begin{aligned}
\mathrm{Kurt}[f(t)] = c_4(0,0,0) &= \int_{-\infty}^{\infty}\int_{-\infty}^{\infty}\int_{-\infty}^{\infty} T(\omega_1,\omega_2,\omega_3)d\omega_1, d\omega_2, d\omega_3 \\
&= 48\cdot\frac{abcd}{16} - 6\cdot(\frac{a^4}{16}+\frac{b^4}{16}+\frac{c^4}{16}+\frac{d^4}{16})
\end{aligned} \tag{1.60}$$

To understand the "self-interactions" or "asymtonically diminishing" terms, let

us consider a process $f(t)$ represented by the classical Gaussian SRM of Eq. (1.17). The trispectrum of classical SRM is

$$\begin{aligned} &T(\omega_1, \omega_2, \omega_3) \\ &= -\sum_{k=0}^{\infty} \frac{A_k^4}{4}[\delta(\omega_1 + \lambda_k, \omega_2 - \lambda_k, \omega_3 - \lambda_k) + \delta(\omega_1 - \lambda_k, \omega_2 + \lambda_k, \omega_3 + \lambda_k) + \cdots] \end{aligned} \tag{1.61}$$

where there are every 6 peaks per the harmonic term, respectively. As an aside, the bispectrum of $f(t)$ is zero because there is no quadratic phase coupling. The unnormalized kurtosis of $f(t)$ from the classical SRM with the harmonic terms can be represented as

$$\begin{aligned} \text{Kurt}[f(t)] = c_4(0,0,0) &= \int_{-\infty}^{\infty}\int_{-\infty}^{\infty}\int_{-\infty}^{\infty} T(\omega_1, \omega_2, \omega_3) d\omega_1, d\omega_2, d\omega_3 \\ &= -6\sum_{k=0}^{\infty}(\frac{A_k^4}{4}) \end{aligned} \tag{1.62}$$

The original kurtosis of classical SRM is given by

$$\begin{aligned} \text{Kurtosis}[f(t)] = \frac{E[f(t)^4]}{E[f(t)^2]^2} &= \frac{c_4(0,0,0) + 3 \cdot c_2(0)^2}{c_2(0)^2} = \frac{-6\sum_{k=0}^{\infty}(\frac{A_k^4}{4})}{\sigma^4} + 3 \\ &= -\frac{3}{2}\frac{\sum_{k=0}^{\infty} A_k^4}{\sigma^4} + 3 = 3 \end{aligned} \tag{1.63}$$

because the limit can be calculated as [3]

$$\begin{aligned}\lim_{N\to\infty}\sum_{k=0}^{N-1}A_k^4 &= \lim_{N\to\infty}\sum_{k=0}^{N-1}[2S(\omega_k)\Delta\omega]^{4/2} \\ &= \sqrt{2}(\omega_u)^2\lim_{N\to\infty}\sum_{k=0}^{N-1}\left(\frac{S(\omega_k)}{N}\right)^2 \\ &\leq \sqrt{2}(\omega_u)^2\lim_{N\to\infty}N\cdot\frac{S_{max}^2}{N^2} \\ &= \sqrt{2}(\omega_u\cdot S_{max})^2\lim_{N\to\infty}\frac{1}{N}=0\end{aligned} \tag{1.64}$$

where ω_u is upper cut-off frequency of $S(\omega)$ and S_{max} is maximum of power spectrum $S(\omega)$. Therefore, we notice that the kurtosis of Eq. (1.17) asymptotically converges to 3, and the SRM is asymptotically Gaussian.

Chapter 2

Iterative translation approximation method for non-stationary and non-Gaussian processes

As an existing family of procedures called the Iterative Translation Approximation Method (ITAM) to handle inadmissibility of translation processes, a new methodology is presented for simulating non-Gaussian and non-stationary stochastic processes using Karhunen-Loève (KL) expansion and translation process theory [9]. The proposed method advances the ITAM by iteratively updating the non-stationary covariance function. Because the original ITAM requires estimation of evolutionary spectrum from the covariance function for which no analytical relation exists, the presented method without the prescribed estimation improves the accuracy with efficient com-

putational cost for non-stationary processes. Several stationary and non-stationary examples are examined.

2.1 ITAM with spectral representation

Translation process model is advantageous in plenty of civil engineering problems. For example, the extreme values of the non-Gaussian processes are essential in reliability analysis, therefore, the translation process matching the non-Gaussian distribution and the prescribed ACF is appropriated in spite of its inadmissible cases mentioned in Section 1.3.1.

To solve the inadmissibility, the ITAM was introduced to simulate stationary and non-Gaussian processes by upgrading the underlying Gaussian PSDF in view of SRM [29]. Furthermore, the ITAM was expanded to represent non-stationary and non-Gaussian processes by iteratively updating the underlying Gaussian ES [29] as

$$S_G^{(i+1)}(\omega,t) = \left[\frac{S_N^T(\omega,t)}{S_N^{(i)}(\omega,t)}\right]^{\beta} S_G^{(i)}(\omega,t) \tag{2.1}$$

where $S_N^T(\omega,t)$ is a target non-Gaussian and non-stationary ES, $S_N^{(i)}(\omega,t)$ is the estimated non-Gaussian ES at the ith iteration. $S_G^{(i)}(\omega,t)$ and $S_G^{(i+1)}(\omega,t)$ are the underlying Gaussian ES at iteration i and $i+1$ respectively. The exponent parameter β is chosen to adjust convergence speed.

There are several strong advantages in the ITAM. First, it converges fast within

ten iterations in general. Second, it is computationally light and easy to implement. Third, the updated underlying Gaussian ES satisfy the condition of PSD. However, there are primary limitation of the ITAM with ES is that it needs estimation of the ES from the non-stationary ACF for non-stationary processes since Priestly defined that the ES is not defined by the non-stationary ACF [55]. Although a method to calculate a unique ES from the non-stationary ACF under several conditions was proposed [56], it is computationally expensive. Moreover, an approximation quantity named as pseudo-autocorrelation that assumes local stationary are introduced in the ITAM [29]. As a result, the prescribed ITAM for non-stationary and non-Gaussian processes costed expensive calculation with relatively lower accuracy.

2.2 ITAM with Karhunen-Loéve expansion

The presented method with K-L expansion detours the estimation of ES by directly updating the underlying non-stationary ACF repeatedly and is denoted as ITAM-KL. The flowchart of ITAM-KL is provided in Figure 2.1 as well. The following sections explain the particulars of the proposed methodology.

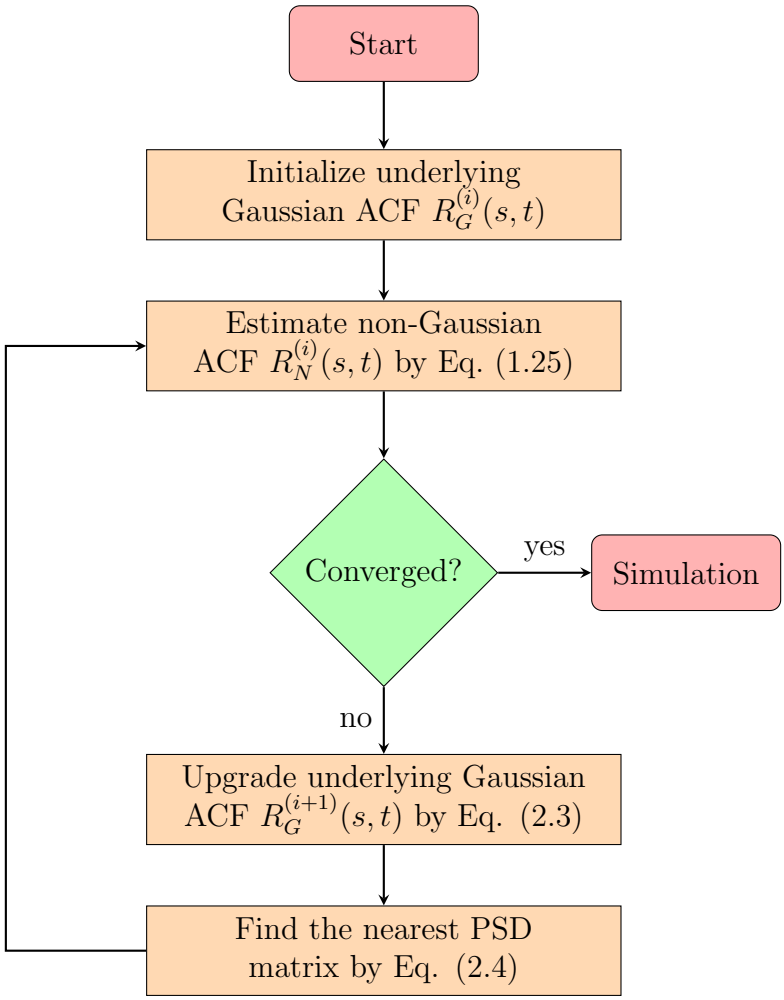

Figure 2.1: Flowchart of proposed methodology: ITAM-KL.

2.2.1 Initialize underlying Gaussian ACF

With a target incompatible pair of non-stationary autocorrelation and marginal non-Gaussian CDF, choose an initial arbitrary underlying Gaussian ACF. The initial ACF must satisfy every condition of ACF. In practical, the initial ACF can be chosen by the target non-Gaussian ACF.

2.2.2 Compute the non-Gaussian ACF

Secondly, the non-Gaussian and non-stationary ACF is estimated from the underlying Gaussian based on translation process using Eq. (1.25). The normalized Gaussian correlation function in Eq. (1.25) is calculated as

$$\rho^{(i)}(s,t) = \frac{R_G^{(i)}(s,t)}{\sqrt{R_G^{(i)}(t,t) \cdot R_G^{(i)}(s,s)}} \tag{2.2}$$

2.2.3 Upgrade underlying Gaussian ACF

Given that the procedure is not converged at i-th iteration, the underlying Gaussian ACF is upgraded for $i+1$th iteration as

$$R_G^{(i+1)}(s,t) = \left(\frac{R_N^T(s,t)}{R_N^{(i)}(s,t)}\right) R_G^{(i)}(s,t) \tag{2.3}$$

Here is no exponent parameter β in the conventional ITAM because it will produce imaginary numbers when the signs of $R_N^T(s,t)$ and $R_G^{(i)}(s,t)$ are opposite in Eq. (2.1). Moreover, the upgraded Gaussian ACF is not strictly PSD such as the updated ES in the original ITAM. Therefore, we require an step for preserving the PSD property of the updated Gaussian ACF at every iteration.

2.2.4 Find nearest positive semi-definite ACF

Higham [57] suggested a methodology to compute its nearest correlation matrix of an arbitrary real and symmetric matrix A in Frobenius norm by solving

$$\begin{aligned} &\min \frac{1}{2}\|A - \hat{A}\|^2 \\ &\text{s.t. } A = \hat{A}^T, \text{diag}(\hat{A}) = e, \hat{A} \geq 0 \end{aligned} \tag{2.4}$$

where $\hat{A}$ is the nearest PSD matrix and e is the unit vector. Furthermore, Qi and Sun [58] proposed a quadratically convergent Newton method for maintaining the nearest correlation matrix of the updated ACF by dualizing Eq. (2.4) to a convex optimization problem. Even though they are several methods for computing the nearest PSD matrix [59], ITAM-KL employed the method of Qi and Sum mentioned in the Appendix A.

This step of maintaining PSD correlation is iteratively applied after upgrading underlying ACF. Even though the computed non-Gaussian and non-stationary ACF becomes closer to the target without this iterative step, the converged underlying Gaussian ACF would be negative-definite. Because of the negative eigenvalues of the underlying ACF, the K-L expansion generates significant numerical errors.

. Even though the computed non-Gaussian and non-stationary ACF is closer to the target without this step, the converged underlying ACF is not PSD (and, therefore, not a valid ACF). In this case, the underlying Gaussian ACF has negative

eigenvalues and simulation with the K-L expansion produces considerable numerical errors. This effect is considered additional in Section 2.5.

2.2.5 Check relative difference and iterate

The relative difference between the target non-stationary and non-Gaussian ACF and the estimated one is calculated as

$$\epsilon_{(i)} = 100\sqrt{\frac{\sum_{n=0}^{N-1}\sum_{m=0}^{N-1}\left[R_N^{(i)}(s_n,t_m) - R_N^T(s_n,t_m)\right]^2}{\sum_{n=0}^{N-1}\sum_{m=0}^{N-1}\left[R_N^T(s_n,t_m)\right]^2}} \tag{2.5}$$

where N is the number of discretized time steps. Corresponding to the level of the relative difference. the iterative flow of ITAM K-L will continue or stop.

2.2.6 Simulation using K-L Expansion

When ITAM K-L converges in an final underlying Gaussian ACF, translation process maps the prescribed Gaussian ACF to the target non-Gaussian and non-stationary ACF closely. At first, K-L expansion with the underlying Gaussian ACF (Eq. (1.22)) simulates Gaussian and non-stationary samples. Finally, the sample functions can be mapped to the prescribed non-Gaussian and non-stationary processes (Eq. (1.24)).

2.2.7 Comments on numerical implementation

For numerical execution, there is few restrictions in view of that we do not truncate the K-L expansion - whole eigenvalue and eigenfunctions of ACF are kept. The truncation and discretization of K-L expansion was studied [5]. Consequently, when we only consider to select the degree of discretization of the ACF, there are a some of numerical limits arisen in the representation. The accuracy of the presented ITAM-KL approach is without regard to the the truncation. However, the truncation of the ACF is strongly related to the computational cost. Therefore, as the discretization become finer, it requires exponentially increased computational cost related to the number of evaluation of Eq. (1.25).

2.3 Numerical examples

A number of numerical examples of stationary/non-stationary and strongly/weakly non-Gaussian processes are examined to check the availability of the presented method, ITAM-KL. Furthermore, examples includes the two types of incompatibility in the translation processes mentioned in Section 1.3.1. This section utilized the identical and reshaped numerical examples exploited by Phoon et al. [24].

2.3.1 Stationary and non-Gaussian processes

The target stationary and non-Gaussian ACFs as numerical examples are considered:

$$\begin{aligned} C_1(s,t) &= \exp(-|s-t|) \\ C_2(s,t) &= \exp(-|s-t|^2) \\ C_3(s,t) &= \exp(-|s-t|) \cdot \cos[4\pi(s-t)] \\ C_4(s,t) &= \exp(-|s-t|^2) \cdot \cos[4\pi(s-t)] \end{aligned} \tag{2.6}$$

which are defined within range $s, t \in [0, 2]$.

As the target non-Gaussian distributions, two different zero mean and unit variated marginal non-Gaussian CDFs are utilized to investigate the accuracy and efficiency of the presented ITAM-KL for weakly and strongly non-Gaussian processes.

First, the beta distribution CDF is

$$F(y; p, q) = \frac{\Gamma(p+q)}{\Gamma(p)\Gamma(q)} \int_0^u z^{p-1}(1-z)^{q-1} dz \tag{2.7}$$

where $\Gamma(\cdot)$ is the gamma function and $u = \frac{y - y_{\min}}{y_{\max} - y_{\min}}$ with upper and lower bounds $y_{\min}$ and $y_{\max}$. The parameters in the given unit variate and zero mean CDF are chosen as $p = 4$ and $q = 2$, and the upper and lower bound are $y_{min} = -3.74$ and $y_{max} = 1.87$. As described in the plots of the PDF and the correlation distortion in Figure 2.2, the beta distribution is weakly non-Gaussian.

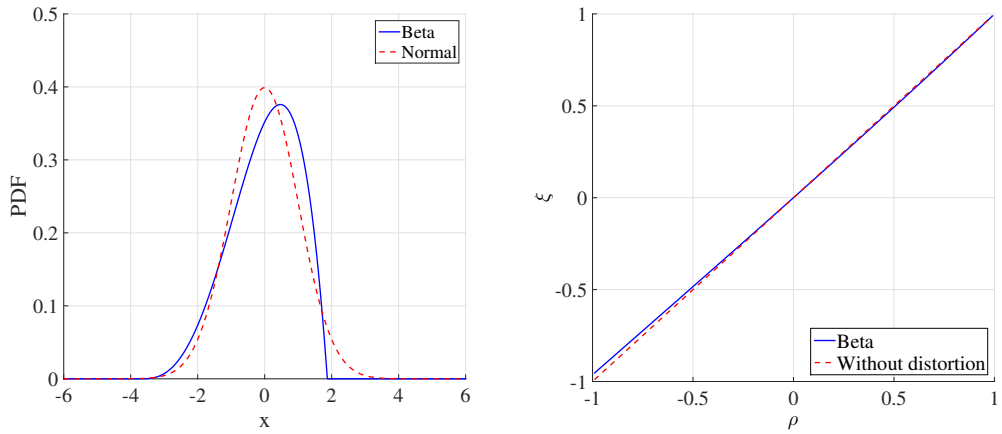

(a) **(b)**

Figure 2.2: Weakly non-Gaussian and stationary beta (a) PDF and (b) its correlation distortion.

The results of non-Gaussian and stationary ACFs with the beta distribution are described with their own target ACFs and the underlying ACFs in Figure 2.3. In this case with the weakly non-Gaussian distribution, the inadmissibility of the translation process does not strong. To estimate the effectiveness of ITAM-KL, the relative difference from Eq. (5.12) are calculated in Table 2.1. The maximum relative difference is only 1.94%.

Secondly, the shifted lognormal distribution is considered and its CDF is

$$F(y;\alpha,\beta,\delta) = \Phi\left(\frac{\ln(y-\delta)-\alpha}{\beta}\right) \tag{2.8}$$

The parameters of the shifted lognormal CDF are chosen as $\alpha = -0.7707$, $\beta = 1$, and $\delta = -0.7628$ to make the CDF the mean zero and unit standard deviation distribution. As plotted in Figure 2.4, the corresponding PDF is strongly non-Gaussian with

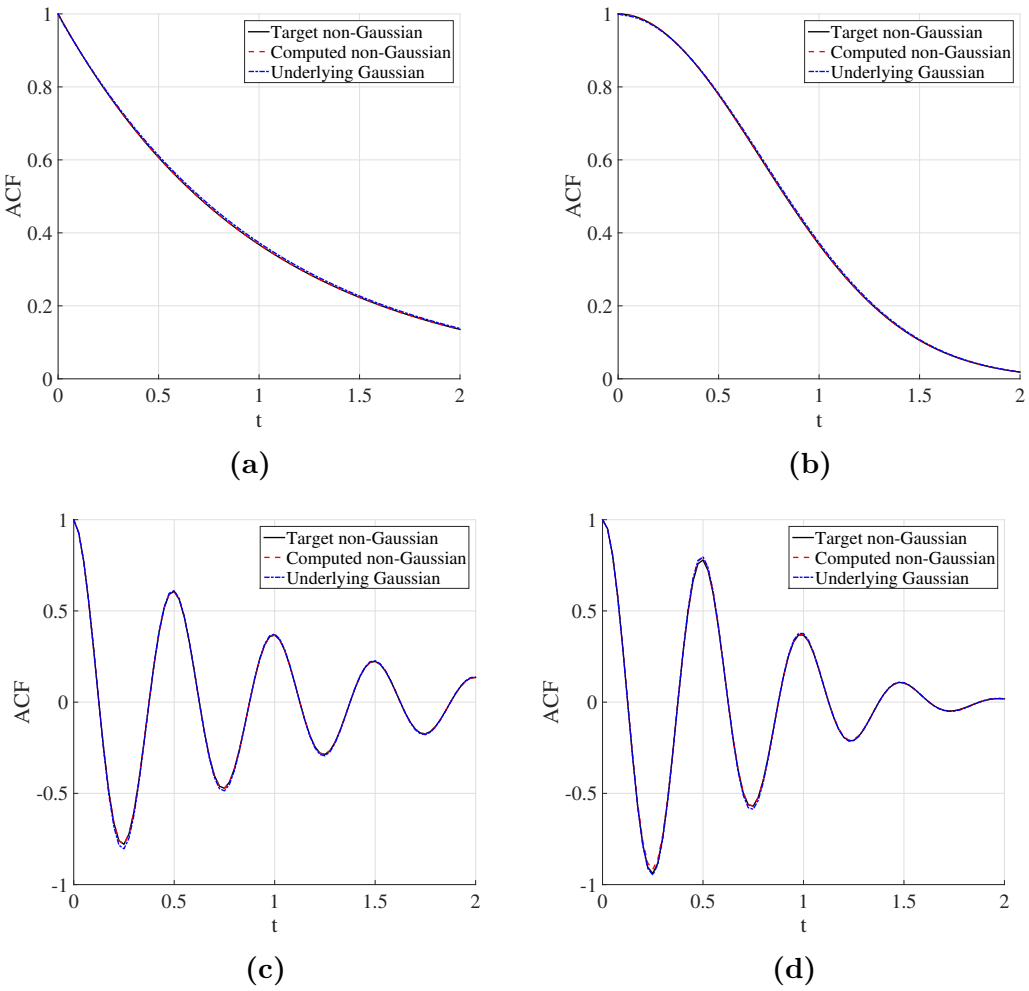

Figure 2.3: Underlying Gaussian, target non-Gaussian and ITAM computed non-Gaussian ACFs for (a) C_1, (b) C_2, (c) C_3, and (d) C_4 with weakly non-Gaussian beta distribution.

the broad inadmissible range in its correlation distortion.

The results for the lognormal distribution are plotted in Figure 2.5 with the estimated non-Gaussian ACFs, the target non-Gaussian ACFs, and the corresponding underlying Gaussian ACFs. Contrast to the beta distribution, the degree of correlation distortion of the translation is extreme. Nevertheless, the proposed ITAM-KL

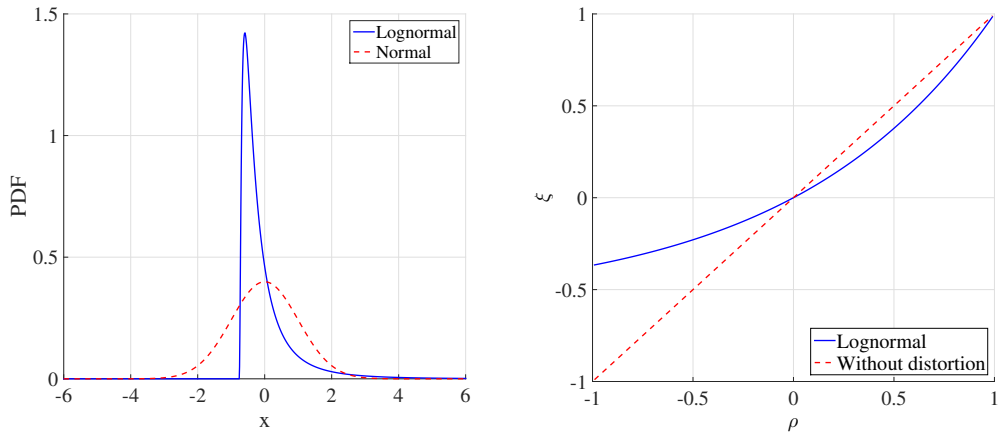

Figure 2.4: Strongly non-Gaussian and stationary shifted lognormal (a) PDF and (b) its correlation distortion.

generate accurate results for ACFs C_1 and C_2 with the respective differences of 0.014% and 0.228%. Although the translation of the strongly non-Gaussian distribution has serious negative distortion, the relative differences are small because the ACFs C_1 and C_2 holds only positive correlation. However, the ACFs C_3 and C_4 possessing negative correlation have relatively bigger errors of 35.30% and 39.92%, respectively. Although the relative differences between the estimated non-Gaussian ACFs and target ACFs are extensive, the general shapes of the target ACFs are preserved in the computed ACFs. The differences of ITAM-KL for ACFs, $C_1 - C_4$ with the lognormal distribution are listed in Table 2.1. Also, the corresponding computational cost with a single 2.3 GHz Intel Core 17 processeor are provided. Moreover, all number of iterations across all ITAM-KL and the maximum number of the finding nearest PSD ACF (referred as Max. N.-CG iter.) also are in Table 2.1.

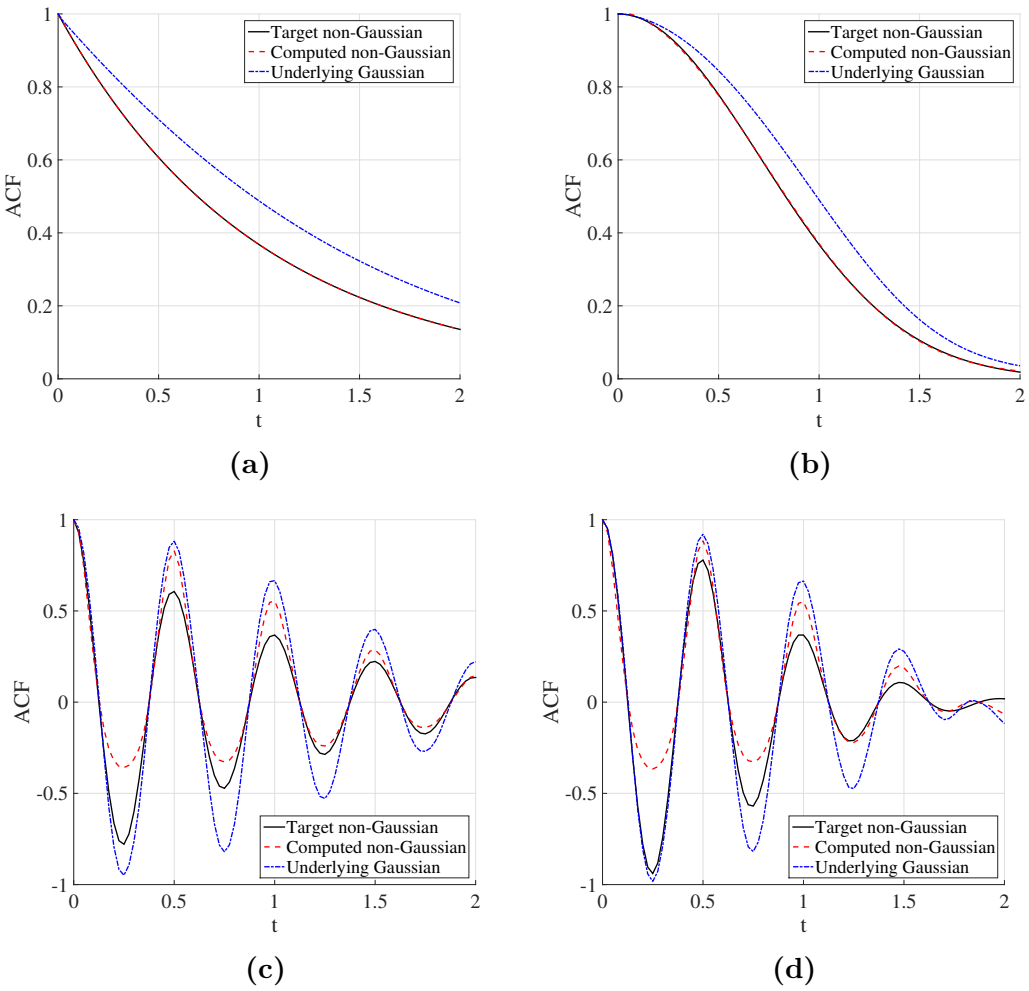

Figure 2.5: Underlying Gaussian, target non-Gaussian, and ITAM computed non-Gaussian ACFs for (a) C_1, (b) C_2, (c) C_3, and (d) C_4 with strongly non-Gaussian shifted lognormal distribution.

2.3.2 Non-stationary and non-Gaussian processes

As non-stationary and non-Gaussian examples, the following target covariances are examined as

$$\begin{aligned} C_5(s,t) &= \min(s,t) \\ C_6(s,t) &= 4[\min(s,t) - s\,t] \\ C_7(s,t) &= \min(s,t)\,\cos[4\pi(s-t)] \\ C_8(s,t) &= 4[\min(s,t) - s\,t]\,\cos[4\pi(s-t)] \end{aligned} \tag{2.9}$$

where the domain of the AXFs are identically $s, t \in [0,1]$ and the maximum variance is one. The plots of these target time-varying covariance matrices are presented in Figure 2.6.

Similar to the stationary numerical examples, two different non-Gaussian and non-stationary distributions with zero mean are considered, but their variance are time-dependent according to their own target covariance functions. First, the non-stationary beta distribution (Eq. (2.7)) with $u = \frac{y-y_{\min}}{y_{\max}-y_{\min}}$, $y_{\min} = \mu_b(t) - \sigma_b(t)\sqrt{\frac{p(p+q+1)}{q}}$, and $y_{\max} = \mu_b(t) + \sigma_b(t)\sqrt{\frac{q(p+q+1)}{p}}$ is examined. The distribution parameters are chosen to be $p = 4$ and $q = 2$ for the CDFs with the mean $\mu_b(t) = 0$ and the time-varying variance $\sigma_b(t)^2 = C(t,t)$ for all t. For the non-stationary and weakgly non-Gaussian beta distribution, the results of the proposed ITAM-KL at time $t = 0.5$ with target non-Gaussian, computed non-Gaussian and underlying Gaussian ACFs are plotted in

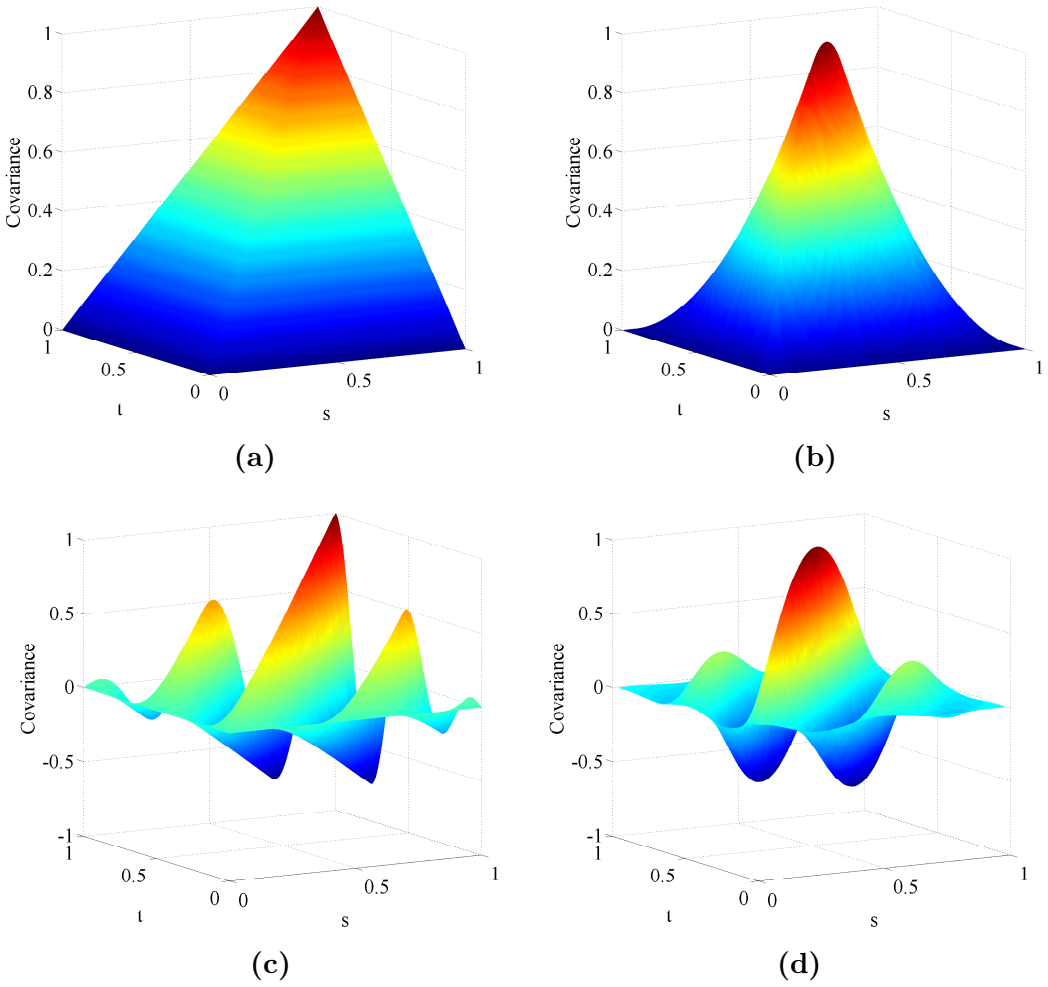

Figure 2.6: Target non-stationary covariances: (a) C_5, (b) C_6, (c) C_7, and (d) C_8.

Figure 2.7. The relative difference are negligible as mentioned in Table 2.1.

Secondly, the non-stationary and strongly non-Gaussian shifted lognormal distribution is examined (Eq. (2.8)). The distribution parameters are defined as time-varying α, δ and constant $\beta = 1$. In special, the parameter α and δ are functions of t and are chosen by making the mean $\mu_l(t) = 0$ and the variance $\sigma_l^2(t)$ matching the target time-dependent variance. Therefore, the mean and the variance of the

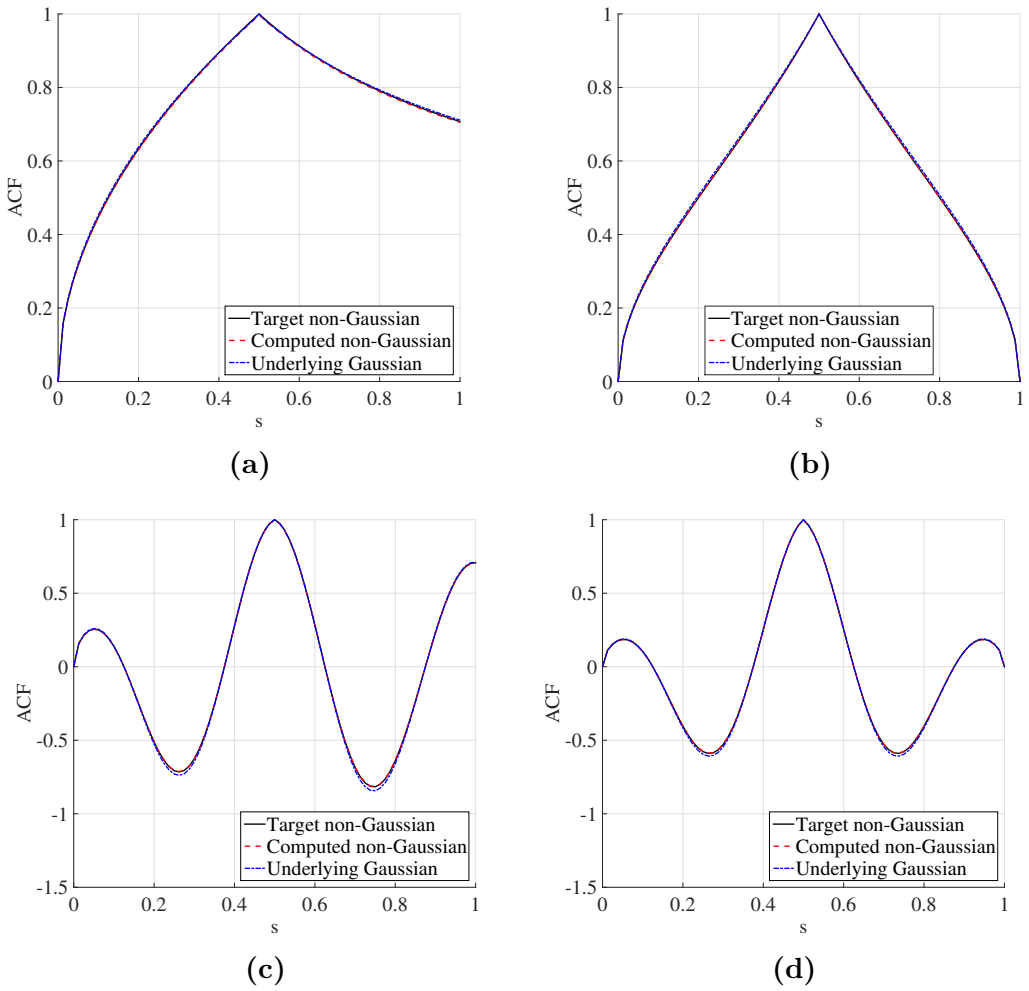

Figure 2.7: Underlying Gaussian, target non-Gaussian, and ITAM computed non-Gaussian normalized ACFs of (a) C_5, (b) C_6, (c) C_7, and (d) C_8 with non-stationary beta distribution at time $t = 0.5$.

non-stationary lognormal distribution are given by

$$\mu_l(t) = \delta(t) + \exp\left[\alpha(t) + \frac{\beta^2}{2}\right] \tag{2.10}$$

$$\sigma_l^2(t) = [\exp(\beta^2) - 1] \cdot \exp[2\alpha(t) + \beta^2] \tag{2.11}$$

The results of ITAM-KL for the non-stationary lognormal distributions are depicted in Figure 2.8 at $t = 0.5$. We can recognize the highly accurate result in the covariances C_5 and C_6 with smaller relative differences of only 0.016% and 0.014% respectively. Nonetheless, the differences in the covariances C_7 and C_8 are relatively larger because of their negative l correlations. Even though severe incompatibility between the covariances and the non-stationary CDFs are emerged, the main characteristics of covariances are preserved in the computed covariances. The summary of the non-stationary results are provided in Table 2.1

2.4 Comparison with ITAM-SRM

One of the most important advantage of the presented method compared to the conventional ITAM-SRM fro non-stationary processes is that it eliminates the computationally heavy and inaccurate step to estimate ES. The proposed ITAM-KL also increase the accuracy in view of the relative difference. Compared with the ITAM-SRM [29], an example with strongly non-Gaussian marginal distribution and non-stationary ES from the previous work is evaluated. The target non-Gaussian ES is given by

$$S_N(\omega, t) = e^{-\left(\frac{\omega - \omega_0(t)}{2}\right)^2} \tag{2.12}$$

where the parameter $\omega_0(t)$ is

$$\omega_0(t) = 10 + 20t \tag{2.13}$$

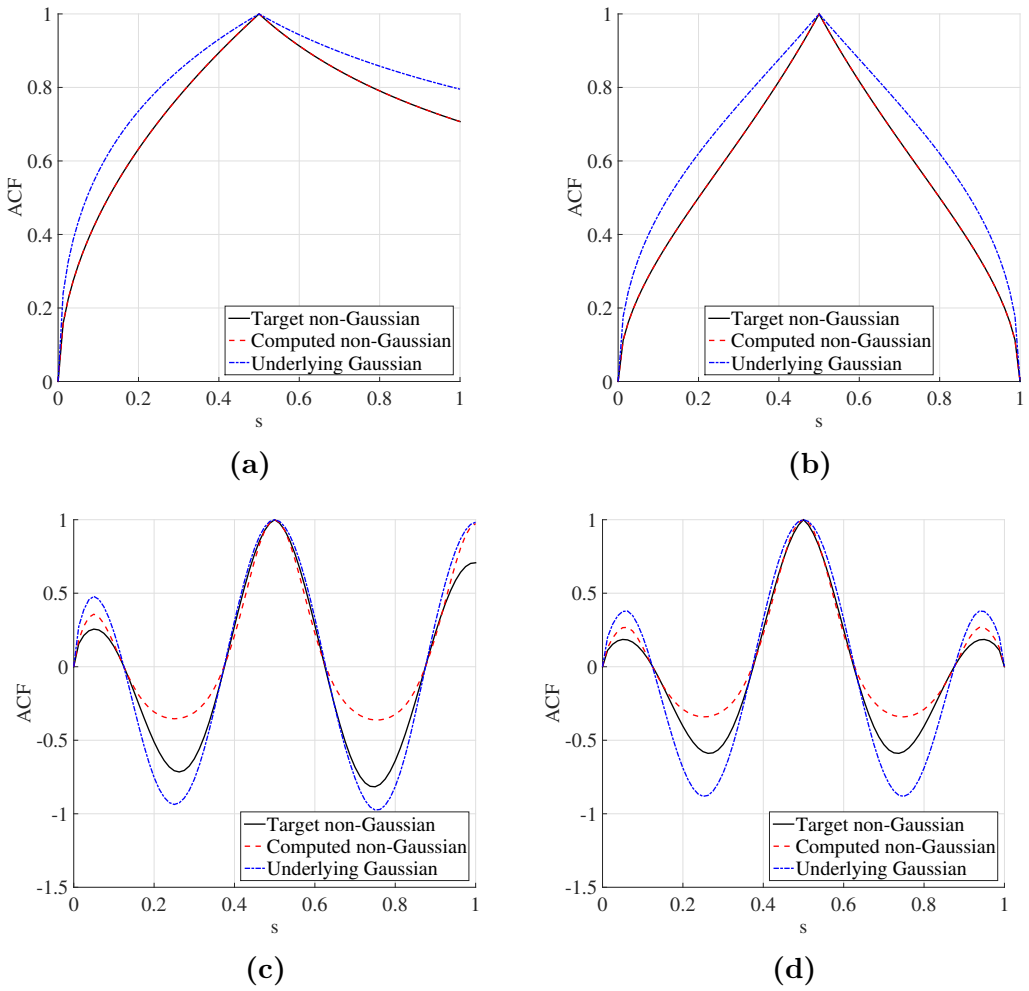

Figure 2.8: Underlying Gaussian, target non-Gaussian, and ITAM computed non-Gaussian normalized ACFs of (a) C_5, (b) C_6, (c) C_7, and (d) C_8 with non-stationary shifted lognormal distribution at time $t = 0.5$.

The equivalent non-Gaussian and non-stationary ACF is computed as [55]

$$R_N(s,t) = \int_{-\infty}^{\infty} \sqrt{S_N(\omega,s)S_N(\omega,t)}e^{i\omega t}d\omega \tag{2.14}$$

The non-stationary and non-Gaussian ES and ACF are plotted in Figure 2.9.

As non-Gaussian and non-stationary distributions, two different beta CDFs with

Table 2.1: Relative differences and computational costs for weakly (beta) and strongly (lognormal) non-Gaussian distributions applied to stationary and non-stationary processes.

Target	Beta distribution			
	Rel. diff. ϵ (%)	ITAM-KL iter.	CPU Time (sec)	Max. N.-CG iter.
Stationary ($\Delta x = 0.0250$, 81×81 matrices)				
C_1	0.0000	3	667	0
C_2	0.0599	4	1529	1
C_3	0.0000	3	562	0
C_4	1.9372	3	573	3
Non-Stationary ($\Delta x = 0.0125$, 81×81 matrices)				
C_5	0.0024	7	1773	0
C_6	0.0007	6	1156	0
C_7	0.0007	6	1165	0
C_8	0.0009	6	1016	0
Target	Lognormal distribution			
	Rel. diff. ϵ (%)	ITAM-KL iter.	CPU Time (sec)	Max. N.-CG iter.
Stationary ($\Delta x = 0.0250$, 81×81 matrices)				
C_1	0.0146	10	964	0
C_2	0.2277	11	2076	3
C_3	35.393	5	374	5
C_4	39.925	4	316	5
Non-Stationary ($\Delta x = 0.0125$, 81×81 matrices)				
C_5	0.0159	14	1584	0
C_6	0.0142	10	851	0
C_7	34.450	4	341	5
C_8	22.685	5	379	4

zero mean and unit variance are considered and defined as

$$f(y; a, b, c, d) = \frac{\Gamma(c+d)}{\Gamma(c)\Gamma(d)(b-a)^{c+d-1}}(y-a)^{c-1}(b-y)^{d-1} \tag{2.15}$$

Firstly, an "U-shaped" beta distribution with parameters $a = -1.1$, $b = 1.7$, $c = 0.342$, and $d = 0.528$ is considered. Secondly, a "L-shaped" beta distribution with

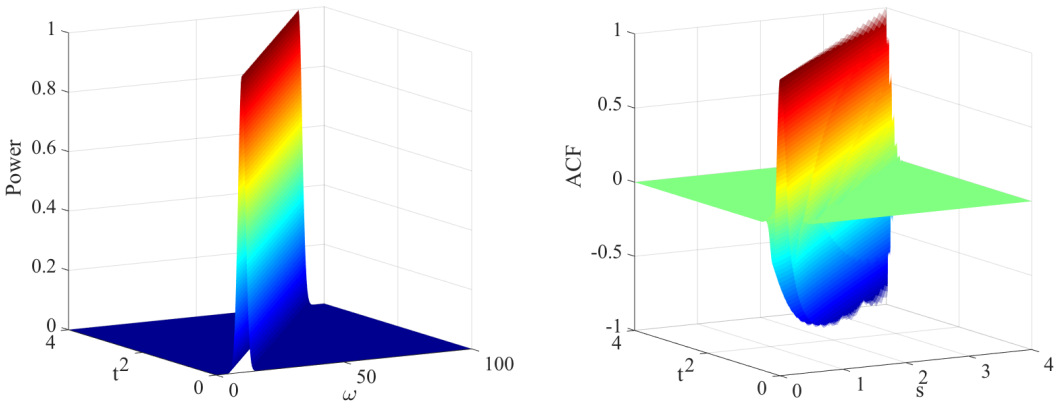

(a) **(b)**

Figure 2.9: Target non-Gaussian and non-stationary (a) ES and (b) ACF.

parameters $a = -0.457$, $b = 28.45$, $c = 0.1895$, and $d = 11.795$ is examined. Their own upper and lower bounded are given by $y_{min} = a$ and $y_{max} = b$. The plots of the PDFs and correlation distortions are depicted in Figure 2.10.

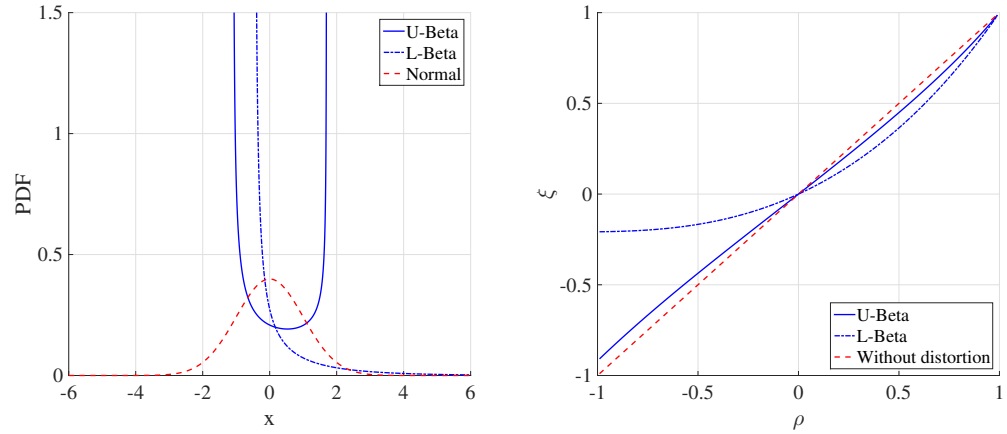

(a) **(b)**

Figure 2.10: Two different beta (a) PDFs and (b) these correlation distortions.

The estimated non-Gaussian ESs and ACFs for the prescribed beta distributions are computed based on the ITAM-SRM and ITAM-KL and the relative difference at

different time $t = 0$, $t = 1$, and $t = 2$ are listed in Table 2.2. It is evident that the relative differences with the proposed ITAM with K-L expansion are much smaller the the one with the ITAM-SRM. Furthermore, the converged non-Gaussian ACFs using the two different ITAMs are plotted in Figure 2.11.

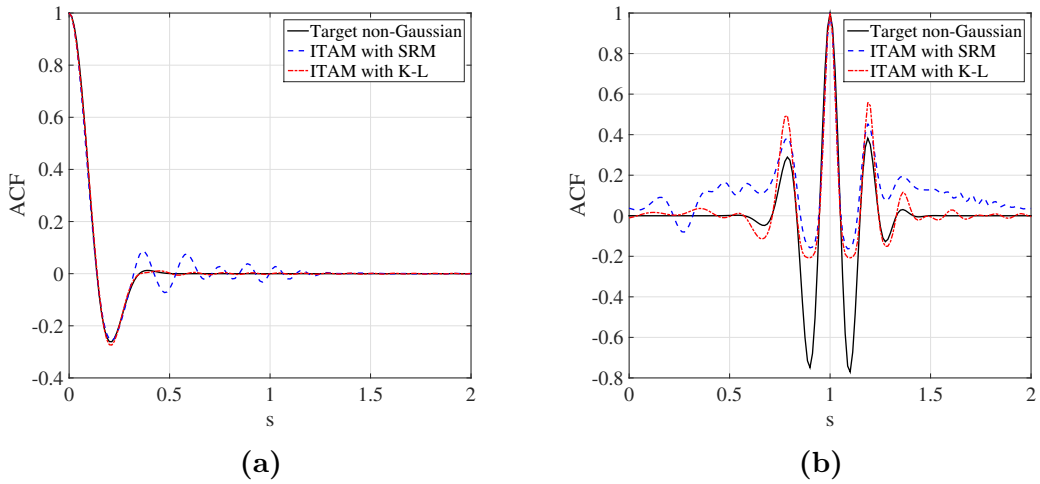

Figure 2.11: Comparison of computed non-Gaussian ACFs using ITAM-KL and ITAM-SRM with (a) U-beta distribution at time $t = 0$ and (b) L-beta distribution at time $t = 1$.

2.5 Effect of the finding nearest PSD matrix of underlying ACF

As mentioned before, the importance of the step of finding nearest PSD matrix of underlying Gaussian ACF in the proposed ITAM-KL are considered. This stage keeps the underlying Gaussian ACF PSD and ensures the compatibility of translation process. However, someone may prefer to iterative update the ACF without

Table 2.2: Comparison of relative differences between the standard ITAM with SRM and the upgraded ITAM with the K-L expansion.

	Relative difference ϵ (%)			
	U-beta distribution		L-beta distribution	
Time	ITAM with SRM	ITAM with K-L	ITAM with SRM	ITAM with K-L
$t = 0$	12.798	2.4433	57.627	12.655
$t = 1$	9.3529	5.8626	69.647	52.139
$t = 2$	7.9026	6.3818	68.608	51.672

the prescribed step and simulate the process only with the positive eigenvalues and their eigenfunctions. But, the mentioned approach without finding PSD ACF cause significant difference between the target non-Gaussian ACF and the estimated non-Gaussian ACF from the stochastic samples.

In Figure 2.12a, the converged normalized non-Gaussian ACFs with and without finding the nearest PSD ACF are depicted. Even though both results seem to be matched well with the target, the non-PSD solution much converge to the target ACF. Nevertheless, Figure 2.12b presenting the estimated ACFs from the sample functions shows us that simply ignoring the non-negative eigenvalues by not search the nearest PSD ACF during the iterations causes considerable error in the simulation. Furthermore, the ignoring PSD yields the realization with inaccurate variance $\sigma^2_{\text{without PSD}} \approx 3.3322$) with 100,000 samples compared to the other one

($\sigma^2_{\text{with PSD}} \approx 1.0062$).

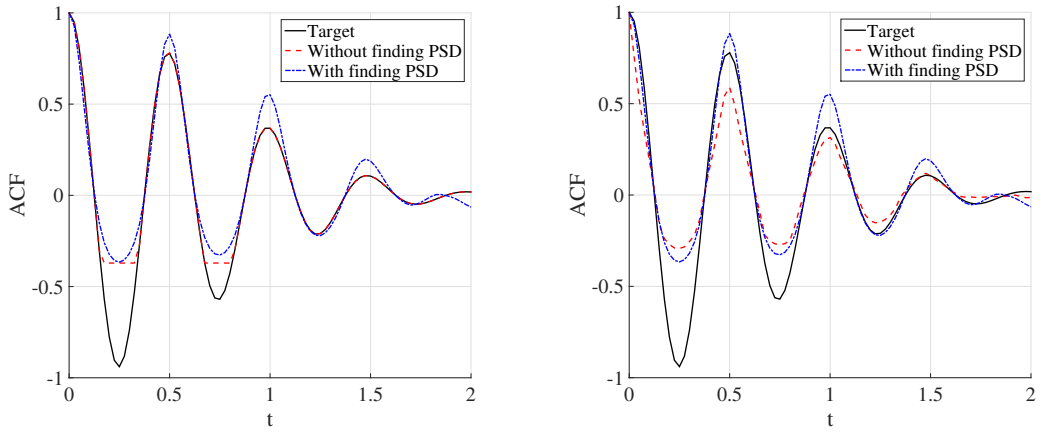

Figure 2.12: (a) Computed normalized non-Gaussian ACFs after iterations with and without finding the nearest PSD ACF. (b) Estimated normalized non-Gaussian ACFs from sample functions produced using the ACFs in (a) with the K-L expansion.

The previous results show that the step searching the nearest PSD ACF is indispensable. However, is it required at every end of iteration or can we only apply this step once at the last iteration? Table 2.3 shows the accuracy of the two procedures on the numerical examples in Section 2.3.1 and 2.3.2. It is shown that finding the nearest PSD at every iteration is superior for every case ($C_1 - C_8$). Therefore, given the inexpensive cost of finding the nearest PSD matrix, it is recommended to search the nearest PSD at every iteration although the both scheme are valid to satisfy the PSD condition of ACFs.

Table 2.3: Comparison of relative differences between the target and computed ACFs by finding the nearest PSD ACF at each iteration and finding it once at the end of iterations for a shifted lognormal distribution.

	Relative difference ϵ (%)	
Target	Finding PSD at each iteration	Finding PSD once
Stationary		
C_1	0.0146	0.0146
C_2	0.2277	0.2388
C_3	35.393	36.596
C_4	39.925	40.028
Non-stationary		
C_5	0.0159	0.0159
C_6	0.0142	0.0142
C_7	34.450	35.217
C_8	22.685	23.380

2.6 Conclusions

A new methodology have been proposed for simulation of strongly non-Gaussian and non-stationary stochastic process. The proposed methodology belongs to the scope of the ITAM and is demonstrated to improve the accuracy and computational efficiency of the ITAM for non-stationary processes. Diverse marginal distribution

with weakly/strongly non-Gaussian are considered as numerical examples. The results show that the proposed methodology is competent for both stationary and non-stationary processes with different incompatibility of translation process. It possesses several advantages when compared with the conventional simulation methods. First, the convergence speed is very fast and the accuracy of matching with the target ACFs is high. Secondly, estimation of ES in the original ITAM for non-stationary processes is alleviated. Thirdly, the results possesses the marginal non-Gaussian distribution perfectly because of translation process. Lastly, it is straightforward to apply the ITAM-KL in diverse situations.

Chapter 3

Bispectral representation method

The prescribed spectral representation method is generalized for simulation of asymmetrically nonlinear stochastic processes with skewed higher-order properties [10]. New orthogonal increments for the spectral process in the Cramér spectral representation are proposed to include wave interaction and satisfy the orthogonal conditions up to thrid-order. To define the orthogonal increments, two new quantities - partial bicoherence and pure power spectrum - that decouple the contribution of the quadratic wave interactions and single wave powers in the power spectrum. Several numerical examples of diverse processes with different forms of power spectra and bispectra are considered to examine the proposed method. Also, turbulent wind velocities form large eddy simulations are simulated with the proposed methodology.

3.1 Partial bicoherence and pure power spectrum

Bicoherence is appropriate normalized form to evaluate the magnitude of the bispectrum (mentioned in Eq. (1.42)). The most common definition of the bicoherence derived by Kim and Powers [46] is given by

$$b^2(\omega_1, \omega_2) = \frac{|B(\omega_1, \omega_2)|^2}{E[|F(\omega_1)F(\omega_2)|^2]S(\omega_1 + \omega_2)} \tag{3.1}$$

where $F(\omega)$ are the Fourier coefficients of the process $f(t)$. The bicoherence is bounded on the range $[0, 1]$ by Schwartz's inequality and represent the fraction of energy associated with quadratic phase coupling. However, Hinich and Wolinskey [60] argued that the prescribed bicoherence is not strictly correct and is only appropriate for stochastic processes with narrow-band frequencies. When there is broadband coupling, this normalization is contaminated [39].

Therefore, we require a new feature to define the proportion of the bispectral power that comes form the quadratic wave interactions with two frequencies ω_i and ω_j seperately. To do so, we introduce new qualities named as the partial bicoherence b_p (similar to the partial coherence of Bendat and Piersor [61]) and the pure power

spectrum S_p are given by

$$b_p^2(\omega_i, \omega_j) = \frac{|B(\omega_i, \omega_j)|^2}{S_p(\omega_i) S_p(\omega_j) S(\omega_i + \omega_j)} \tag{3.2}$$

where

$$S_p(\omega_k) = S(\omega_k) \left[1 - \sum_{\substack{i+j=k \\ i \geq j \geq 0}} b_p^2(\omega_i, \omega_j) \right] \tag{3.3}$$

This partial bicoherence separates the fraction of power in the wave with frequency $\omega_k = \omega_i + \omega_j$ that comes from the two wave interactions with frequency ω_i and ω_j only by eliminating contributions from other combinations of two frequencies and an independent part at frequency ω_k.

There is a valuable property of the partial bicoherence that $0 \leq \sum_{\substack{i+j=k \\ i \geq j \geq 0}} b_p^2(\omega_i, \omega_j) \leq 1$ with the summation $\sum_{\substack{i+j=k \\ i \geq j \geq 0}} b_p^2(\omega_i, \omega_j)$ that represents total influence of all quadratic wave interactions on the power at frequency ω_k. Concurrently, the pure power spectrum in Eq. (3.3) represents the power spectrum of the process without all quadratic wave interactions. This partial bicoherence become identical with the bicoherence of Kim and powers with simple quadratic phase coupling only with three wave (such as Eq. (1.47)). Although Eqs. (3.2) and (3.3) looks like circular definitions between the partial bicoherence and pure power spectrum, we can constructed both of them in a term-by-term fashion as starting at the lowest frequencies and increasing.

3.2 Simulation of higher-order processes by spectral representation

3.2.1 Third-order processes

We propose a higher-order spectral representation based expansion for the simulation of stochastic processes. The spectral representation of Eq. (1.5) shows its capacity to represent third-order processes with the orthogonal conditions, Eqs. (1.7) and (1.8). To derive the corresponding orthogonal increments for this higher-order representation, we utilize the partial bicoherence and pure power spectrum defined in Eqs. (3.2) and (3.3). For the simulation, we provide a discretized form of the partial bicoherence as

$$b_p^2(\omega_i, \omega_j) = \frac{B^2(\omega_i, \omega_j)\Delta\omega_i^2\Delta\omega_j^2}{S_p(\omega_i)\Delta\omega_i S_p(\omega_j)\Delta\omega_j S(\omega_i+\omega_j)\Delta(\omega_i+\omega_j)} \tag{3.4}$$

As mentioned before, we expand the standard orthogonal increments in the spectral representation given Eq. (1.16) in terms of the independent part only related with the pure power spectrum $du_P(\cdot)$ and $dv_P(\cdot)$, and the interacting part arisen from wave interactions (with the partial bicoherence), $du_I(\cdot)$ and $dv_I(\cdot)$, for the third-order rep-

resentation as

$$\begin{aligned} du(\omega_k) &= du_P(\omega_k) + du_I(\omega_k) \\ dv(\omega_k) &= dv_P(\omega_k) + dv_I(\omega_k) \end{aligned} \tag{3.5}$$

where

$$\begin{aligned} du_P(\omega_k) &= \sqrt{2 \cdot 2S_p(\omega_k)\Delta\omega_k}\cos\phi_k = \sqrt{2 \cdot 2S(\omega_k)\Delta\omega_k\left[1 - \sum_{i+j=k}^{i\geq j\geq 0} b_p^2(\omega_i,\omega_j)\right]}\cos\phi_k \\ dv_P(\omega_k) &= \sqrt{2 \cdot 2S_p(\omega_k)\Delta\omega_k}\sin\phi_k = \sqrt{2 \cdot 2S(\omega_k)\Delta\omega_k\left[1 - \sum_{i+j=k}^{i\geq j\geq 0} b_p^2(\omega_i,\omega_j)\right]}\sin\phi_k \end{aligned} \tag{3.6}$$

and

$$\begin{aligned} du_I(\omega_k) &= \sqrt{2 \cdot 2S(\omega_k)\Delta\omega_k}\left\{\sum_{i+j=k}^{i\geq j\geq 0}\left|b_p^2(\omega_i,\omega_j)\right|\cos\left[\phi_i + \phi_j + \beta(\omega_i,\omega_j)\right]\right\} \\ dv_I(\omega_k) &= \sqrt{2 \cdot 2S(\omega_k)\Delta\omega_k}\left\{\sum_{i+j=k}^{i\geq j\geq 0}\left|b_p^2(\omega_i,\omega_j)\right|\sin\left[\phi_i + \phi_j + \beta(\omega_i,\omega_j)\right]\right\} \end{aligned} \tag{3.7}$$

where $\beta(\omega_i,\omega_j)$ is the biphase given by Eq. (1.43). Examination of Eqs. (1.16) and (3.6) shows that $du_P(\omega_k)$ and $dv_P(\omega_k)$ are consistent with the classical orthogonal increments based on the pure power spectrum, while the increments $du_I(\omega_k)$ and $dv_I(\omega_k)$ express the quadratic wave interactions.

Applying the new orthogonal increments to the spectral representation of Eq.

(1.11) provide a new third-order spectral representation as

$$\begin{aligned} f(t) &= \sqrt{2}\sum_{k=0}^{\infty}\sqrt{2S_p(\omega_k)\Delta\omega_k}\cos(\omega_k t-\phi_k) \\ &+\sqrt{2}\sum_{k=0}^{\infty}\sum_{i+j=m}^{i\geq j\geq 0}\sqrt{2S(\omega_i+\omega_j)\Delta(\omega_i+\omega_j)}\big|b_p(\omega_i,\omega_j)\big| \\ &\cdot\cos[(\omega_i+\omega_j)t-(\phi_i+\phi_j+\beta(\omega_i,\omega_j))] \end{aligned} \tag{3.8}$$

that can simulate of the stochastic processes with asymmetric nonlinearities and we will mention this representation as bispectral representation method (shortly in BSRM). Furthermore, the sample functions generated from Eq. (3.8) own both the prescribed power spectrum and bispectrum in ensemble. In Appendix B, it is proven that the presented orthogonal increments fulfill all the orthogonal conditions of the spectral process up to third-order.

3.2.2 Fourth and higher-order processes

Simulations of stochastic processes including fourth-order spectra (with cubic phase coupling and symmetric non-linearities) have not been explicitly developed to date. However, the process for achieving these expansions will follow the similar prescribed steps with higher-order wave interaction terms in the orthogonal increments and we need to modify all of lower-order terms. For example, in the fourth-order case, the orthogonal increments should be divided to three components. The first term will stand for the independent terms without any effects of two and three wave interac-

tions. The second components will denote the pure two-wave interactions without the effects of three wave interactions. Then, the final term will explicitly represent the tree-wave interactions.

3.3 Numerical examples

We apply the proposed methodology for simulation of third-order skewed stochastic processes with the diverse forms of power spectra and bispectral including analytical results.

3.3.1 Quadratic phase coupling: real and imaginary bispectrum

As the first example, we examine two stochastic processes with simple quadratic coupling only with four harmonic terms. Both of the processes share identical power spectrum as

$$\begin{aligned} S(\omega) = &\frac{1}{4}\delta(\omega - 2\pi \cdot 10) + \frac{1}{4}\delta(\omega - 2\pi \cdot 20) \\ &+ \frac{1}{4}\delta(\omega - 2\pi \cdot 30) + \frac{1}{4}\delta(\omega - 2\pi \cdot 40) \quad \text{for} \quad \omega \geq 0 \end{aligned} \tag{3.9}$$

and depicted in Figure 3.1a. However, they possess their own bispectra. The firs process, $f_r(t)$, only has a real bispectrum defined as

$$B(\omega_1,\omega_2) = \frac{1/\sqrt{2}}{8}\delta(\omega_1 - 2\pi\cdot 20, \omega_2 - 2\pi\cdot 10) + \frac{1/\sqrt{2}}{8}\delta(\omega_1 - 2\pi\cdot 30, \omega_2 - 2\pi\cdot 10) \quad \text{for} \;\; \omega_1 \geq \omega_2 \geq 0 \tag{3.10}$$

and the second process, $f_i(t)$, only has a imaginary bispectrum given by

$$B(\omega_1,\omega_2) = \frac{i/\sqrt{2}}{8}\delta(\omega_1 - 2\pi\cdot 20, \omega_2 - 2\pi\cdot 10) + \frac{i/\sqrt{2}}{8}\delta(\omega_1 - 2\pi\cdot 30, \omega_2 - 2\pi\cdot 10) \quad \text{for} \;\; \omega_1 \geq \omega_2 \geq 0 \tag{3.11}$$

and both of the bispectra are depicted in Figure 3.1, too. The squared partial bicoherence, Eq. (3.2), and the pure power spectra, Eq. (3.3) are identical for both processes and are given by:

$$b_p^2(\omega_1,\omega_2) = \begin{cases} 0.5, & \text{if } \omega_1 = 2\pi\cdot 20,\ \omega_2 = 2\pi\cdot 10 \\ 1, & \text{if } \omega_1 = 2\pi\cdot 30,\ \omega_2 = 2\pi\cdot 10 \\ 0, & \text{otherwise} \end{cases} \quad \text{for} \;\; \omega_1 \geq \omega_2 \geq 0 \tag{3.12}$$

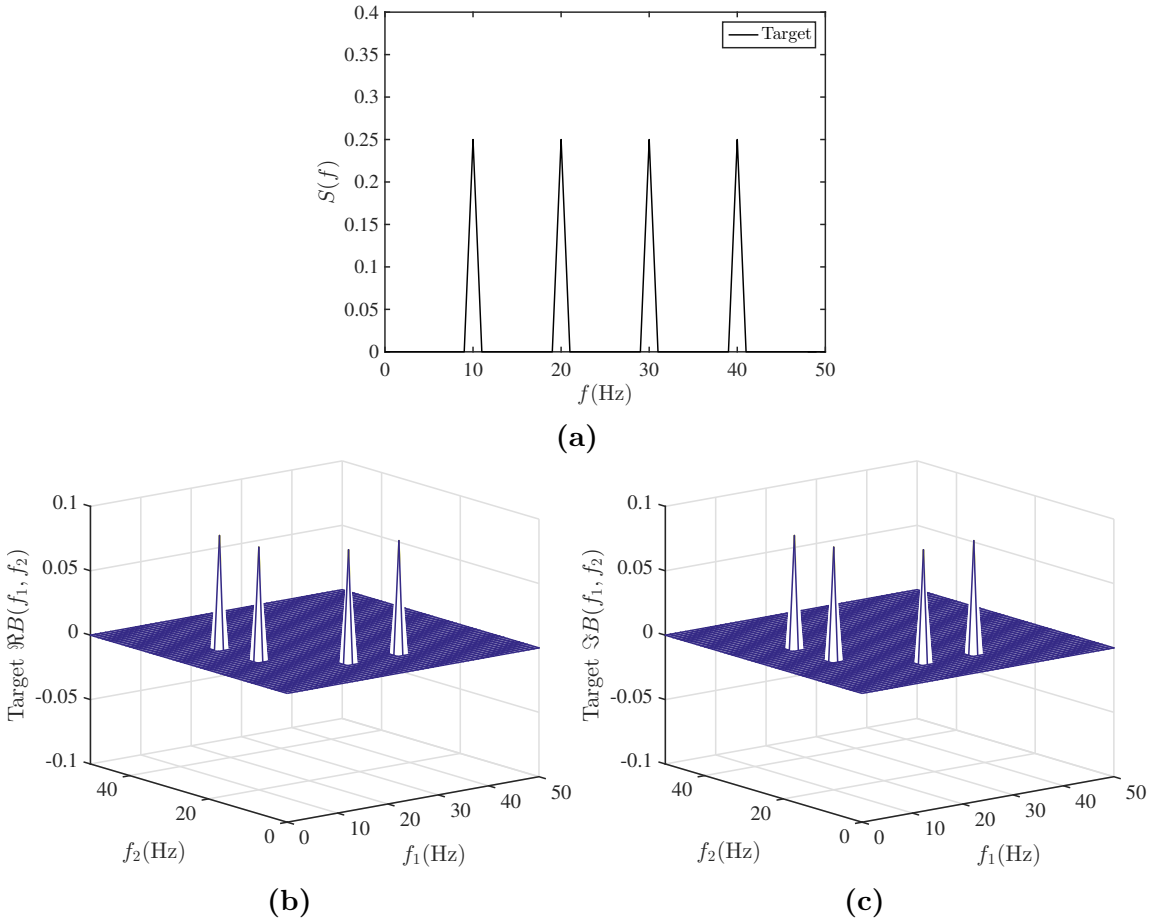

Figure 3.1: (a) Power spectrum, (b) real bispectrum of $f_r(t)$ and (c) imaginary bispectrum of $f_i(t)$ for two simple quadratic phase coupling processes.

and

$$S_p(\omega) = \frac{1}{4}\delta(\omega - 2\pi \cdot 10) + \frac{1}{4}\delta(\omega - 2\pi \cdot 20) + \frac{1}{8}\delta(\omega - 2\pi \cdot 30) \quad \text{for} \quad \omega \geq 0 \tag{3.13}$$

However, they own different biphases at the coupled frequencies: $\beta(40\pi, 20\pi) = \beta(60\pi, 20\pi) = 0$ for the first process with real bispectrum and $\beta(40\pi, 20\pi) = \beta(60\pi, 20\pi) = \pi/2$ for the second process with imaginary bispectrum. With the proposed represen-

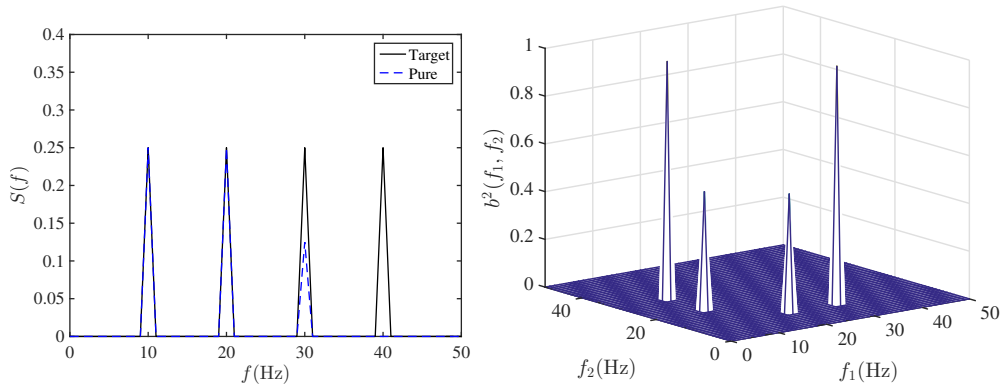

(a) **(b)**

Figure 3.2: (a) Pure power spectrum and (b) squared partial bicoherence for two simple quadratic phase coupling processes.

tation, these processes can be simulated using the forms of expansion given by

$$\begin{aligned} f_r(t) &= \cos(2\pi \cdot 10t - \phi_1) + \cos(2\pi \cdot 20t - \phi_2) \\ &+ \frac{1}{\sqrt{2}}\cos(2\pi \cdot 30t - \phi_3) + \frac{1}{\sqrt{2}}\cos[2\pi \cdot 30t - (\phi_1 + \phi_2)] \\ &+ \cos[2\pi \cdot 40t - (\phi_1 + \phi_3)] \end{aligned} \tag{3.14}$$

for the first process with real bispectrum and

$$\begin{aligned} f_i(t) &= \cos(2\pi \cdot 10t - \phi_1) + \cos(2\pi \cdot 20t - \phi_2) \\ &+ \frac{1}{\sqrt{2}}\cos(2\pi \cdot 30t - \phi_3) + \frac{1}{\sqrt{2}}\sin[2\pi \cdot 30t - (\phi_1 + \phi_2)] \\ &+ \sin[2\pi \cdot 40t - (\phi_1 + \phi_3)] \end{aligned} \tag{3.15}$$

for the second process with imaginary bispectrum. By contrast, the traditional SRM for this process is given by

$$\begin{aligned} f_0(t) = &\cos(2\pi \cdot 10t - \phi_1) + \cos(2\pi \cdot 20t - \phi_2) \\ &+ \cos(2\pi \cdot 30t - \phi_3) + \cos(2\pi \cdot 40t - \phi_4) \end{aligned} \tag{3.16}$$

without any phase coupling. Firstly, we can recognize the BSRM is very simple and similar to the classical SRM. However, it includes more information beyond the second-order properties of the processes.

In Figure 3.3, representative sample functions and their derivatives for the processes, $f_r(t)$ and $f_i(t)$ are shown and compared with the sample function of the original SRM with identical phase angle set, $f_0(t)$. Based on the prescribed properties of real and imaginary bispectrum (Eqs. (1.40) and (1.41)), the two processes with BSRM have different asymmetric types. Firstly, the real bispectrum process $f_r(t)$ has strongly skewed, but its derivative process $\frac{\partial f_r(t)}{\partial t}$ still are symmetric. Against the previous result, the process $f_i(T)$ remains symmetric while its time-derivative $\frac{\partial f_i(t)}{\partial t}$ is negatively skewed. On the other hand, the classical SRM processes $f_0(t)$ and $\frac{\partial f_0(t)}{\partial t}$ are symmetric. Furthermore, the statistics are provided in Table 3.1 with the target variance and skewness of $f_r(t)$, $f_i(t)$, $\frac{\partial f_r(t)}{\partial t}$, and $\frac{\partial f_i(t)}{\partial t}$ compared with their estimated values from 50,000 sample functions. Lastly, the estimated power spectra and bispectra for $f_r(t)$ and $f_i(t)$ are shown in Figure 3.4 and well match with their own targets depicted in Figure 3.1.

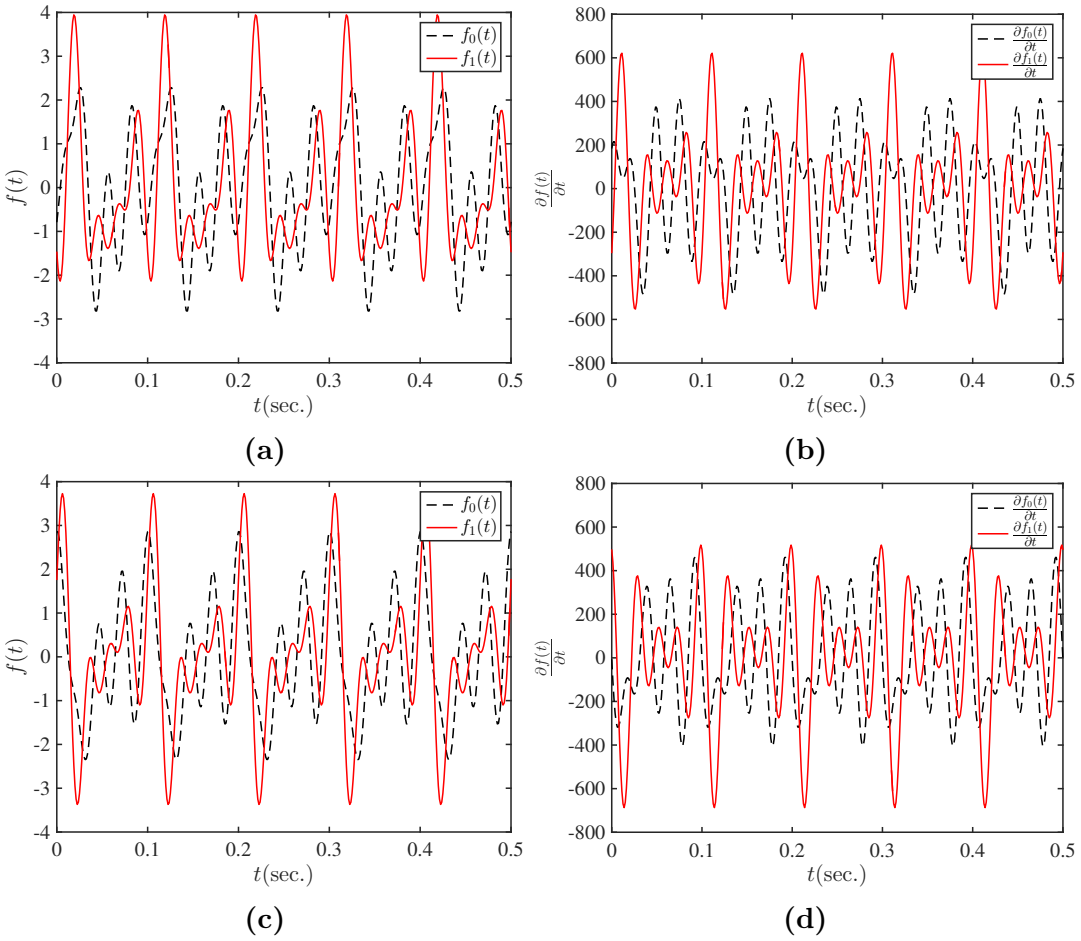

Figure 3.3: Representative sample functions of the simple quadratic phase coupling process generated using the proposed method and the classical SRM and their time derivatives having (a,b) real and (c,d) imaginary bispectra.

3.3.2 Skewed non-Gaussian white noise

In the previous section, the processes only with distinct frequencies and their phase coupling are considered. However, most stochastic processes of interest have a continuous shape in frequency domain with broadband wave couplings. Hence, we considered a band-limited skewed non-Gaussian white noise process with power

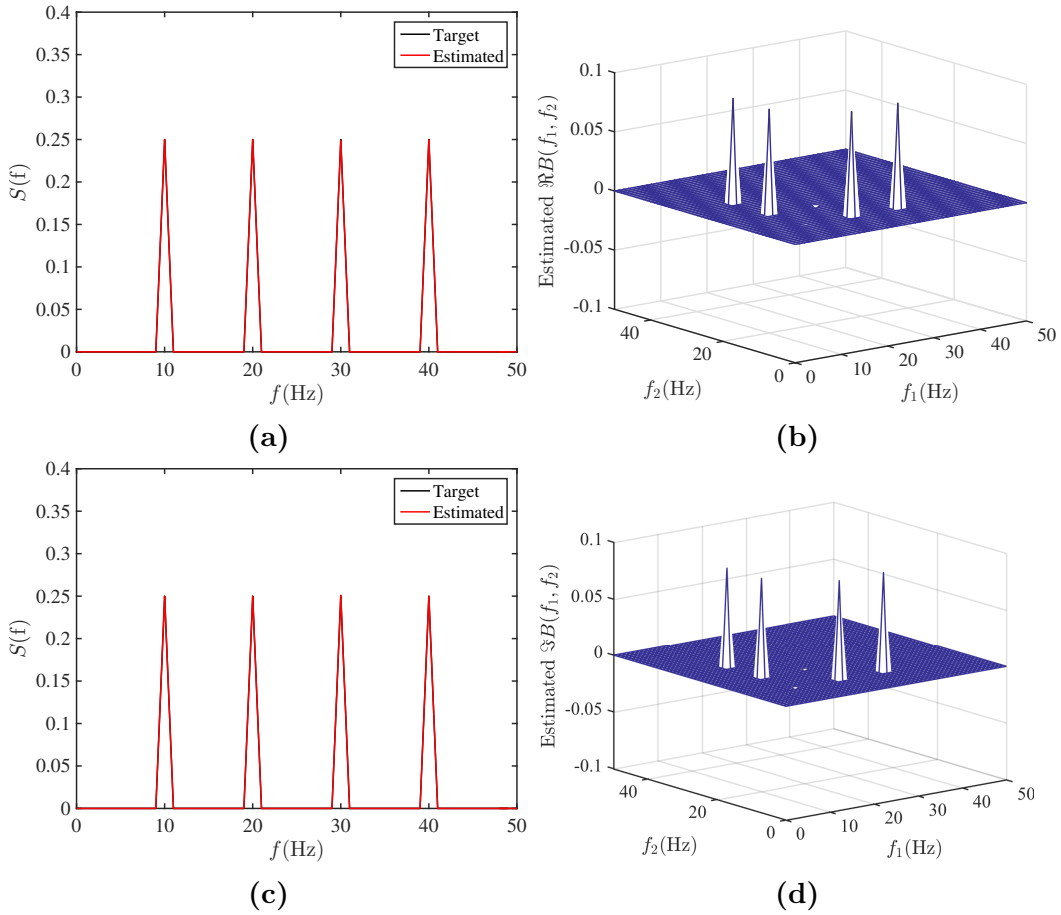

Figure 3.4: (a,b) Estimated power spectrum and real bispectrum for quadratic phase coupling process with real bispectrum,$f_r(t)$. (b,d) Estimated power spectrum and imaginary bispectrum for quadratic phase coupling process with imaginary bispctrum, $f_i(t)$. Estimates computed from 50,000 sample generated using proposed method.

spectrum given by

$$S(\omega) = 14 \quad \text{for} \quad \omega_1 \leq 2\pi \cdot 5 \tag{3.17}$$

and bispectrum

$$B(\omega_1, \omega_2) = 20 - 20i \quad \text{for} \quad \omega_1 \leq 2\pi \cdot 2.5, \ \omega_2 \leq 2\pi \cdot 2.5 \tag{3.18}$$

All the power spectrum, real and imaginary part of bispectrum are depicted in Figure 5.17. Given the prescribed power spectrum and bispectrum, the squared partial

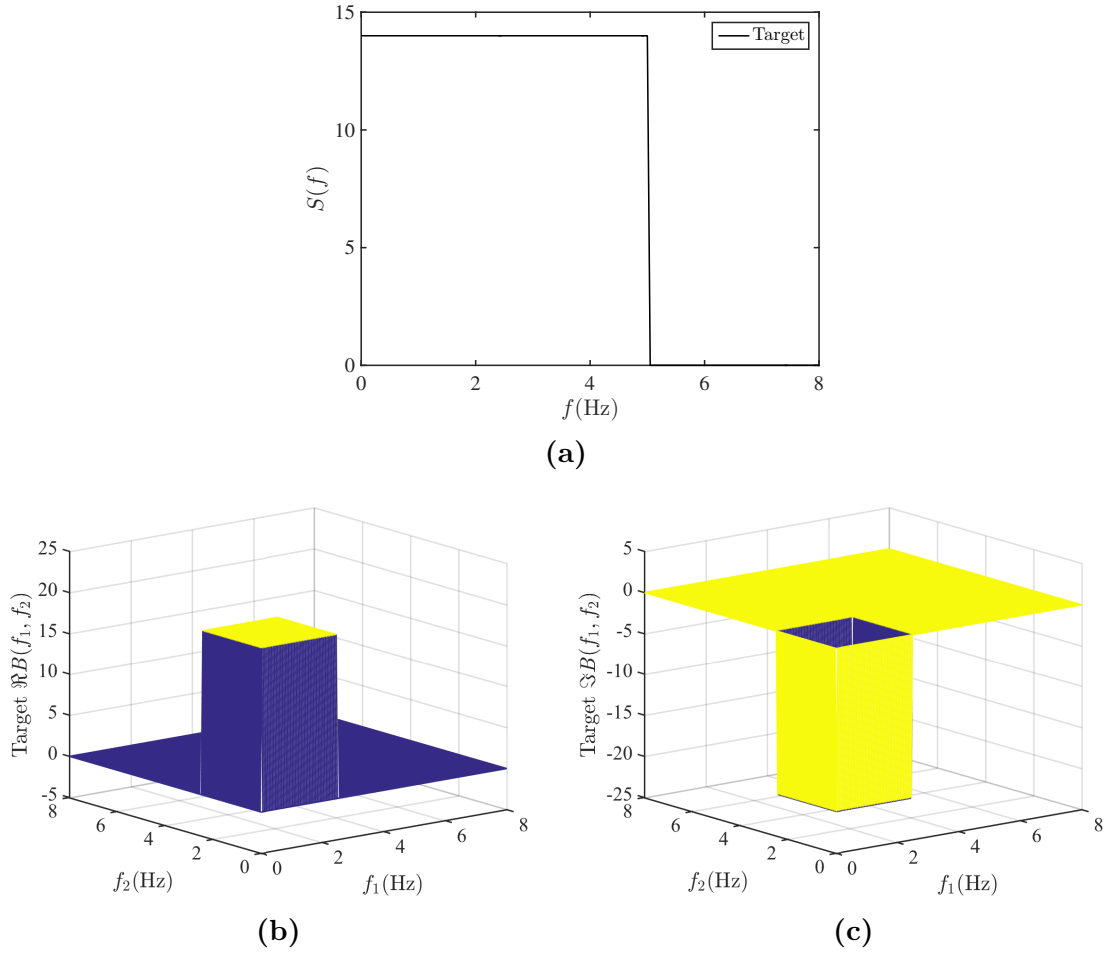

Figure 3.5: (a) Power spectrum, (b) real and (c) imaginary bispectrum for non-Gaussian white noise process.

bicoherence and pure power spectrum of the process are calculated and depicted in Figure 5.18. Note that a considerable part of the power in the power spectrum from the quadratic coupling (or the bispectrum) are shown by the hollowed wedge shape in the pure power spectrum in Figure 5.18a.

In Figure 3.7, representative sample function and its derivative of the skewed

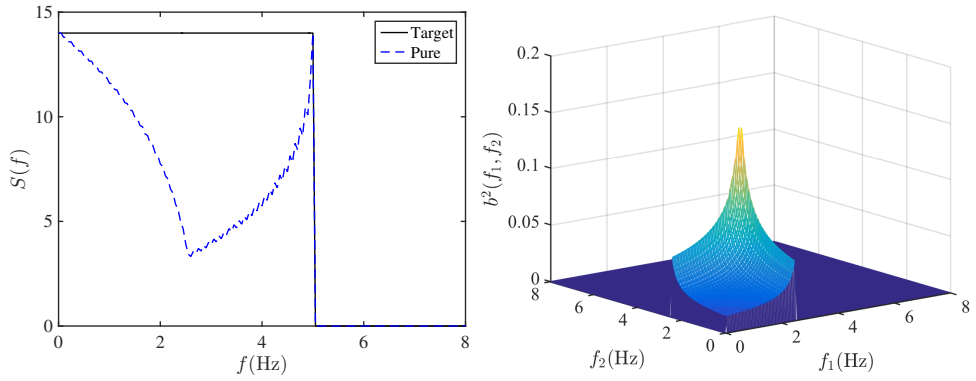

(a) **(b)**

Figure 3.6: (a) Pure power spectrum and (b) squared partial bicoherence for non-Gaussian white noise process.

white noise process with the proposed BSRM are presented and compared with the samples with the conventional SRM . From the comparison, we can notice the positive

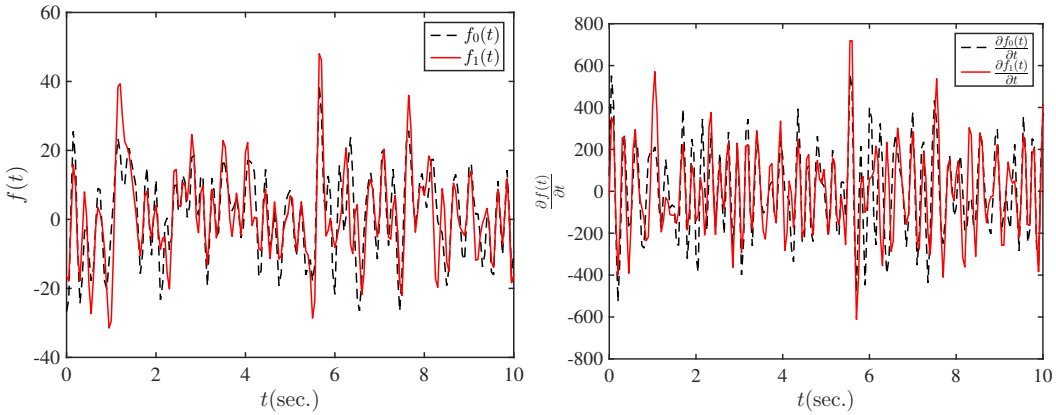

(a) **(b)**

Figure 3.7: (a) Representative sample functions and their (b) time derivatives of skewed non-Gaussian white noise process $f_w(t)$ generated using the proposed method and the classical SRM.

skewness in the sample and its derivative from BSRM. Notify that the estimated power spectrum form 50,000 samples of the BSRM match perfectly with the target power spectrum and even in terms of both components of bispectrum as provided in Figure

3.8. Furthermore, the statistics of the target, BSRM, SRM process are compared in Table 3.1 and the results of BSRM are remarkably accurate.

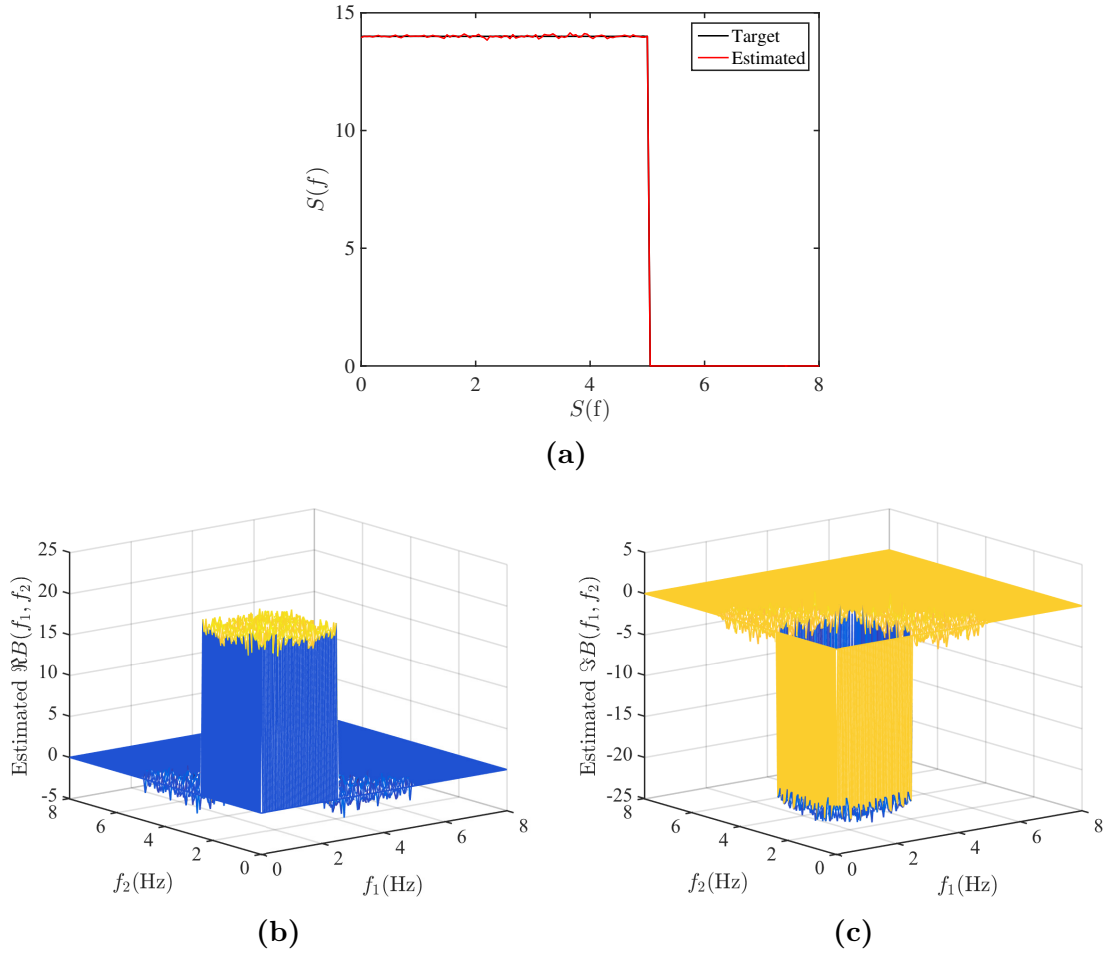

Figure 3.8: (a) Estimated power spectrum, (b) real and (c) imaginary bispectra of non-Gaussian white noise process from 50,000 sample functions generated using the proposed method.

3.3.3 Peaked broadband process

As final numerical example, another broadband process $f_p(t)$ having peaks in both the power spectrum and bispectrum is considered. The power spectrum of the process

are given by

$$S(\omega) = \frac{40}{\sqrt{2\pi \cdot 0.25}} e^{-\frac{(\omega - 2\pi \cdot 2)^2}{2 \cdot 0.25}} \tag{3.19}$$

and the bispectrum is

$$\begin{aligned} B(\omega_1, \omega_2) = &- \frac{20}{2\pi \cdot 0.0625} e^{-\frac{1}{2 \cdot 0.0625}((\omega_1 - 2\pi \cdot 1.25)^2 + (\omega_2 - 2\pi \cdot 1.25)^2)} \\ &+ i \cdot \frac{20}{2\pi \cdot 0.0625} e^{-\frac{1}{2 \cdot 0.0625}((\omega_1 - 2\pi \cdot 1.25)^2 + (\omega_2 - 2\pi \cdot 1.25)^2)} \end{aligned} \tag{3.20}$$

and their plots are presented in Figure 3.9. Moreover, the squared partial bicoherence and pure power spectrum are calculated and depicted in Figure 3.10.

Sample functions of the peak and broadband process $f_p(t)$ and its derivative are plotted in Figure 3.11 compared with samples with SRM. There is substantial difference between the BSRM and SRM at the peaks within the samples and their derivatives. Both results from BSRM have negative skewness and their statistics are summarized in Table 3.1. Moreover, Figure 3.12 shows that the estimated power spectrum and bispectrum from 50,000 sample functions with BSRM are matched perfectly in ensemble.

3.3.4 Application to wind velocity generation from CFD data

We utilize the presented method, BSRM, to simulate wind velocities from statistical properties of data generated from large eddy simulations (LES) of the atmospheric

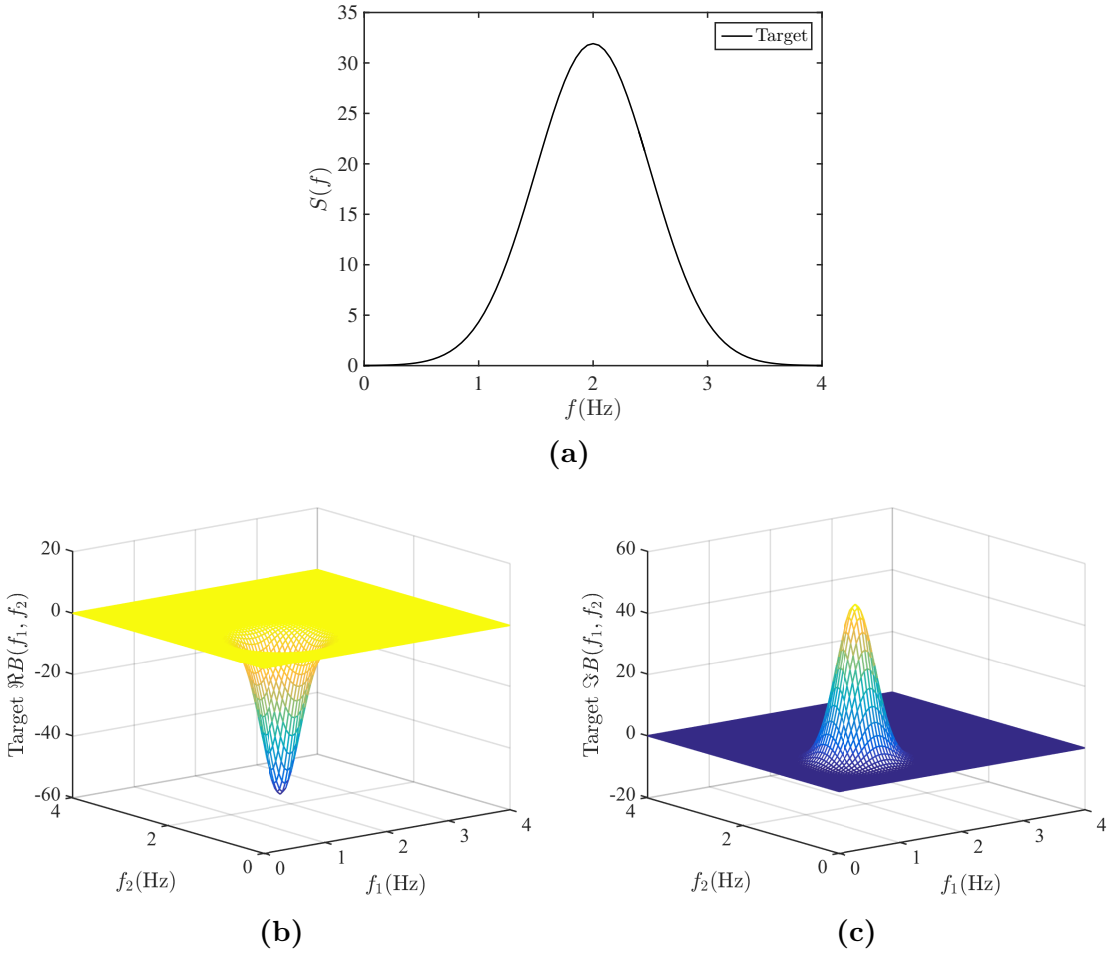

Figure 3.9: (a) Power spectrum, (b) real and (c) imaginary bispectra for the peaked broadband process.

boundary layer. The data are supported by Yeo and Shi at the National Institute of Standards and Technology [62].

3.3.5 Summary and statistical analysis of LES study

LES is well-developed tool for the study of atmospheric flow in which governed by the Navier-Stokes equations and solved numerically above critical length-scale such

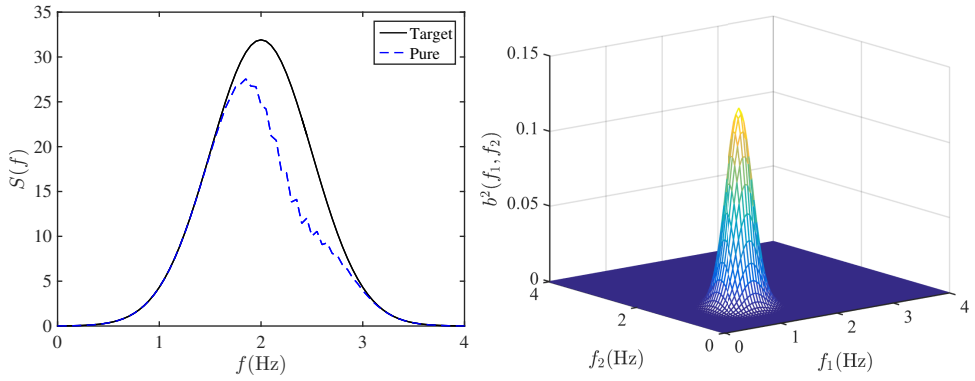

(a) **(b)**

Figure 3.10: (a) Pure power spectrum and (b) squared partial bicoherence for the peaked broadband process.

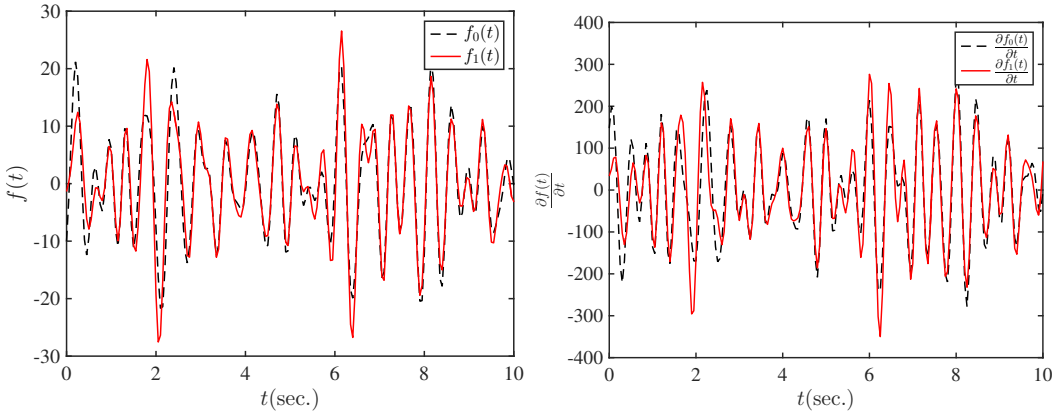

(a) **(b)**

Figure 3.11: Sample functions (a) of the peaked broadband process and (b) their derivatives generated using the proposed method and the classical SRM.

as a grid scale. Synthetic wind velocities from the LES are statistically characterized up to the third-order properties. Although simulation with the proposed methodology does not represent perfect atmospheric flow, the results possess the given power spectra and bispectra of the wind velocities from the LES.

In this example, Sin and Yeo described an atmospheric boundary layer of height

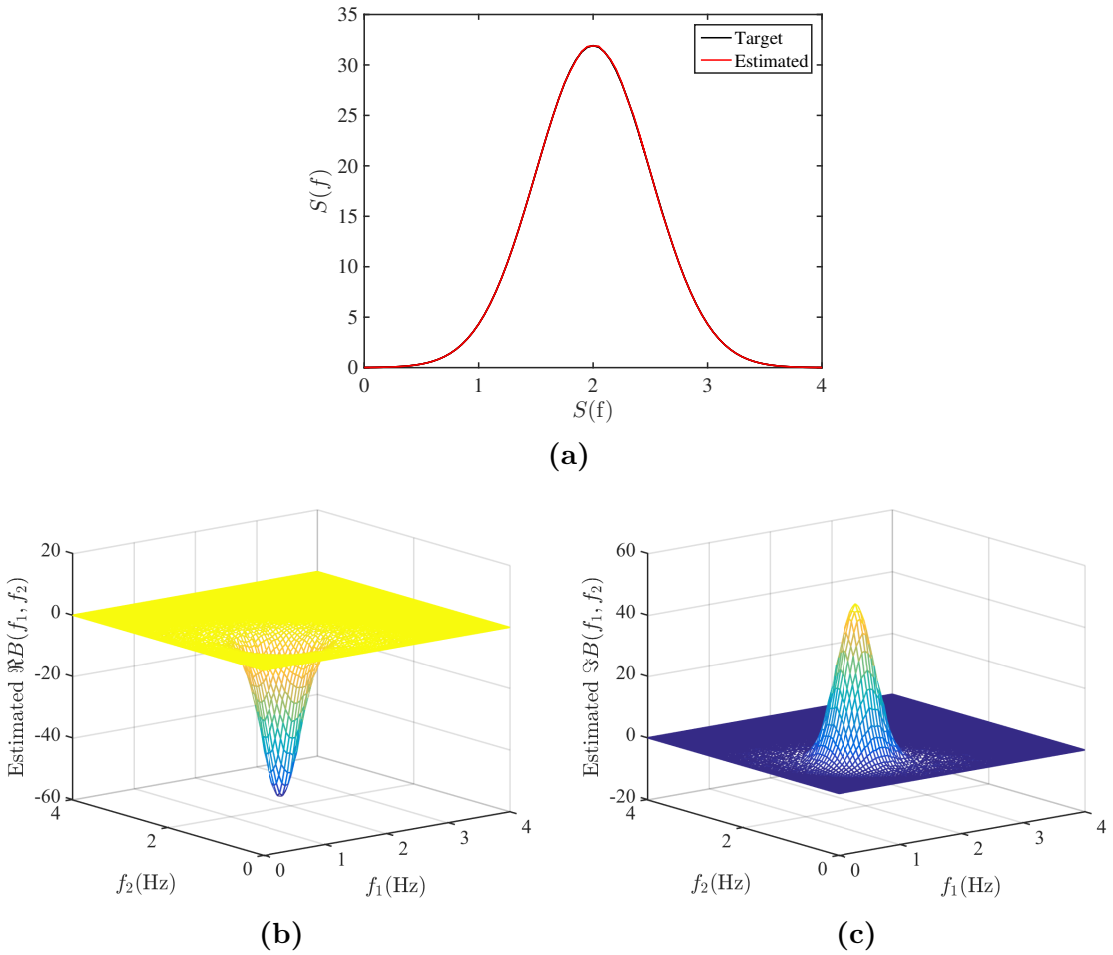

Figure 3.12: (a) Estimated power spectrum, (b) real, and (c) imaginary bispectra from 50,000 sample functions of the peaked broadband process generated using the proposed method.

1km (computational extents $H = 10$m, which is 1:100 scaled. The model over open terrain with assumed roughness length $z_0 = 0.03$m (in the model $z_0 \cong 0.0003$m). The Flow of the atmospheric layer is in the computational domain as depicted in Figure 3.13a until a stationary condition is achieved. Velocity contours at different heights are presented in Figure 3.13b. From this synthetic flow field, stream-wise wind velocities are withdrawn at a point at height $h = 1$ and the time histories and the

Table 3.1: Target and estimated moments of stochastic processes and their derivatives from 50,000 sample functions generated using the proposed method and the classical SRM.

		Quadratic phase coupling Real bispectrum - $f_r(t)$			Quadratic phase coupling Imag. bispectrum - $f_i(t)$		
		Target	Sim.	SRM	Target	Sim	SRM
$f(t)$	Variance	2	1.9991	2.0000	2	1.9999	2.0000
	Skewness	0.7500	0.7497	-0.0006	0	0.0010	-0.0006
$\frac{\partial f(t)}{\partial t}$	Variance	59218	58859	58859	59218	58855	58859
	Skewness	0	0.0017	-0.0005	-0.3378	-0.3291	-0.0005

		Skewed white noise - $f_w(t)$			Peaked braodband - $f_p(t)$		
		Target	Sim.	SRM	Target	Sim	SRM
$f(t)$	Variance	140	140.71	140.70	80	80.00	80.04
	Skewness	0.4528	0.4468	-0.0002	-0.1677	-0.1681	-0.0004
$\frac{\partial f(t)}{\partial t}$	Variance	46751	41266	41260	13423	12865	12858
	Skewness	0.1022	0.1113	-0.0002	-0.0793	-0.0789	0.0001

estimated PDF are plotted in Figure 3.14. We can recognize the wind velocity time history clearly have a negative skewness. Also, the second-order statistical properties including autocovariance and power spectrum are given in Figure 3.15. Moreover, the third-order characteristics including the third-order cumulant and bispectrum are plotted in Figure 3.16 using open source Matlab code, Higher Order Spectra Analysis [63]. In this examination, the original single history with duration 146 sec. with discrete time step 1/250 sec. is divided to 146 individual histories with duration 1 sec. This dividing procedure provides smooth polysectral estimates.

By applying the proposed BSRM, we simulate the skewed wind time histories with the power spectrum (Figure 3.15b) and bispectrum (Figures 3.16b - 3.16c). One of the

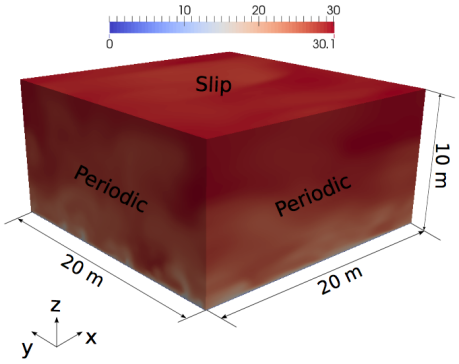

(a)

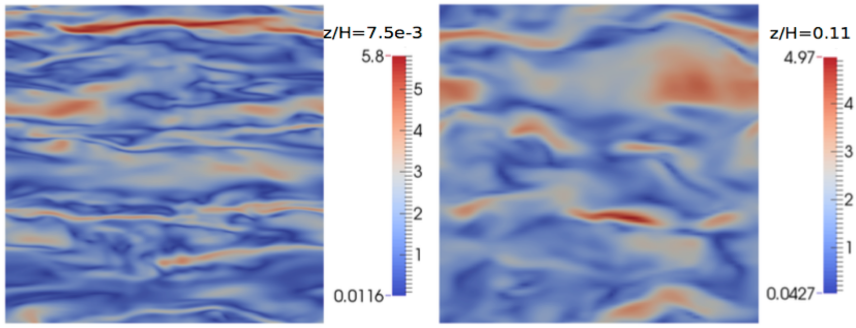

(b)

Figure 3.13: (a) Geometry of the LES computational domain with colored velocity magnitude and (b) velocity counters at $z/H = 7.5e^{-3}$ and $z/H = 0.11$.

.

generated samples are plotted in Figure 3.17 and compared with the sample functions from the classical SRM. From their estimated PDFs, we can see the differences in the tails.

The statistics of all synthetic wind velocities are compared in Table 3.2 and the process with BSRM not only matched the target variance but for the target skewness. The estimated third order correlations form the BSRM sample functions are plotted in Figure 3.18. The results tell us the proposed methodology generates skewed stochastic

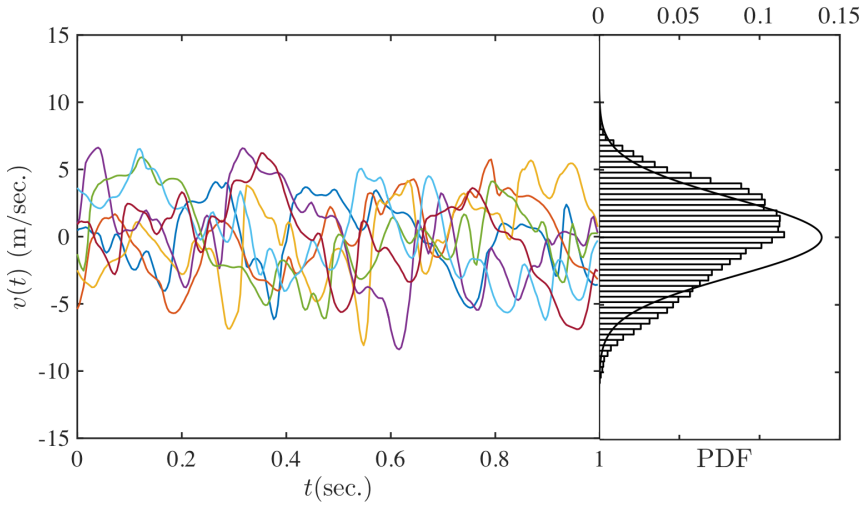

Figure 3.14: Wind velocity histories extracted from the LES model and the empirical PDF.

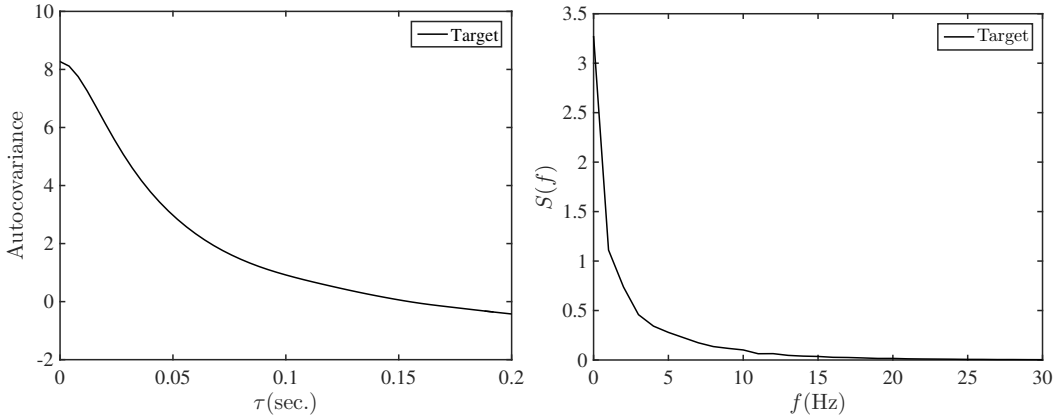

(a) **(b)**

Figure 3.15: (a) Autocovariance, (b) power spectrum of LES modeled wind turbulence.

samples with high accuracy in terms of second and third order properties.

Although the third-order characterization with BSRM is successful, the asymmetric non-Gaussianity with lower kurtosis than three in the PDFs still are not included. This indicates us fourth order characteristics in the wind velocities are also impor-

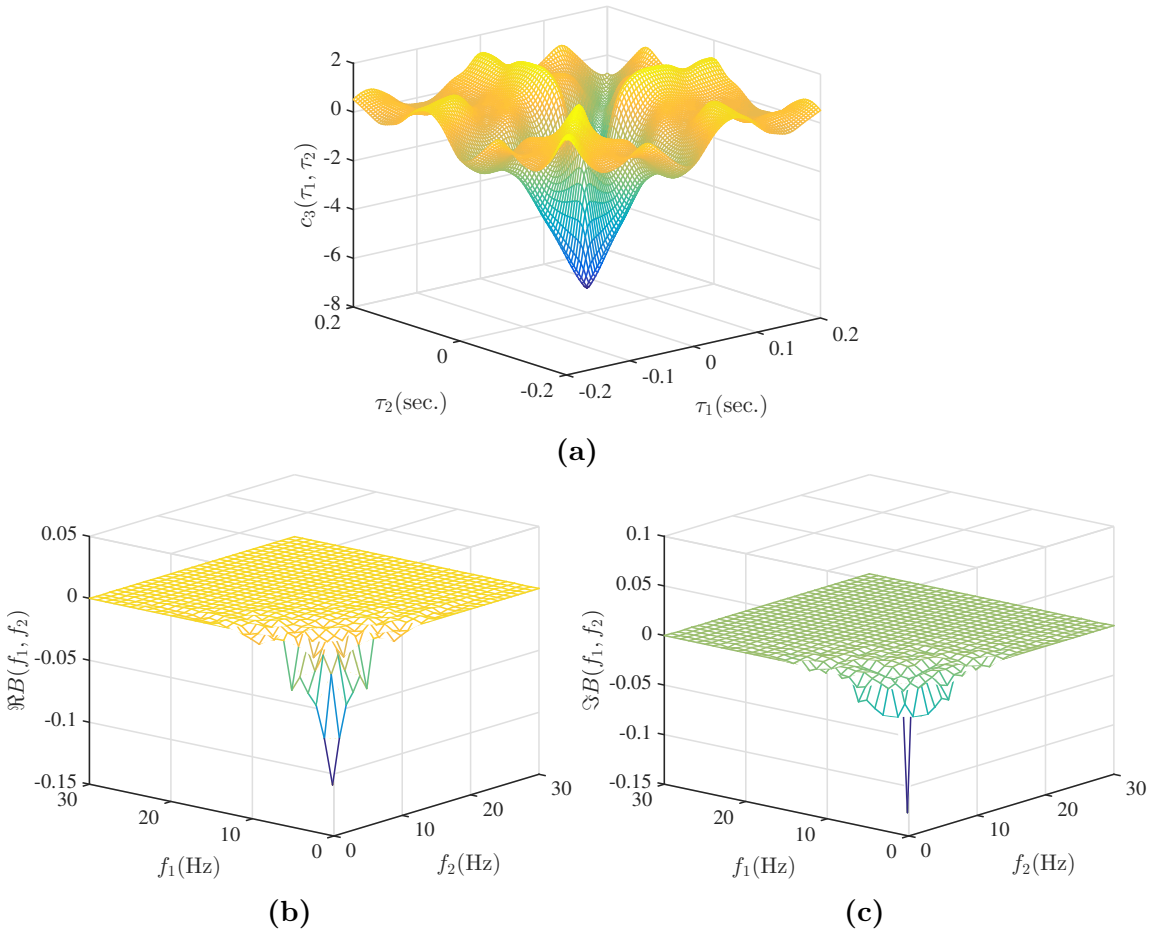

Figure 3.16: (a) Third-order cumulant function, (d) real and (c) imaginary bispectra of LES modeled wind turbulence.

tant. It becomes a huge motivation to further generalize the presented BSRM to higher-order.

Table 3.2: Target and estimated moments of the wind velocity process from 10,000 sample functions generated using the proposed method and the SRM.

	Target	Sim.	SRM
Variance	8.2717	8.2600	8.2605
Skewness	-0.2959	-0.2928	-0.0054
Kurtosis	2.7276	3.0772	2.9850

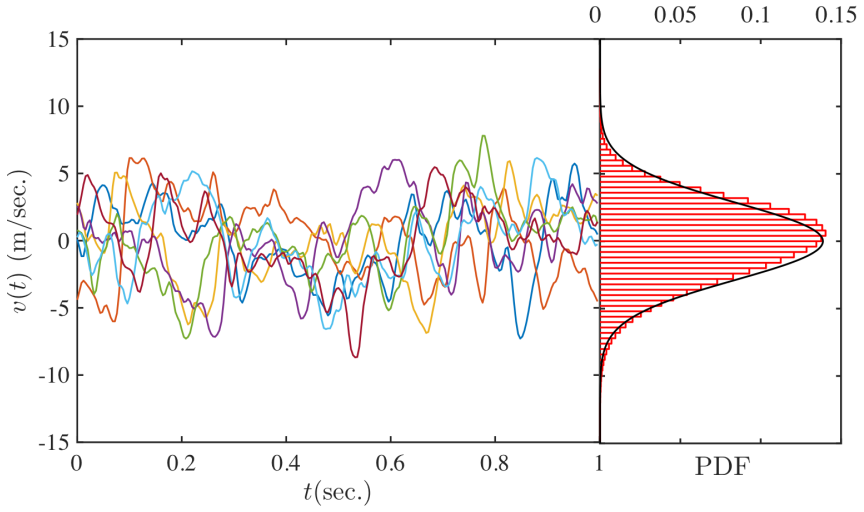

(a)

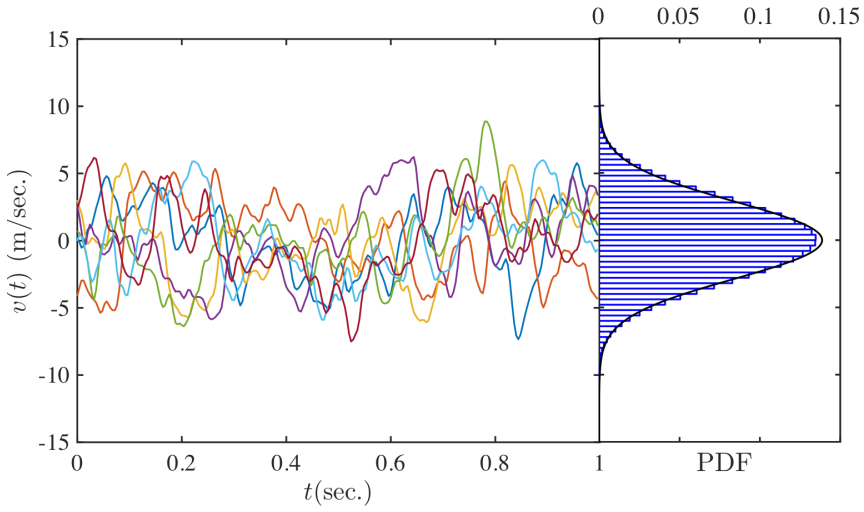

(b)

Figure 3.17: Simulated wind velocity histories and their PDFs generated using (a) the proposed method and (b) the SRM.

3.4 Conclusions

In this work, a third-order simulation methodology has been derived from the Cramér spectral representation that serves as an extension of the classical Spectral

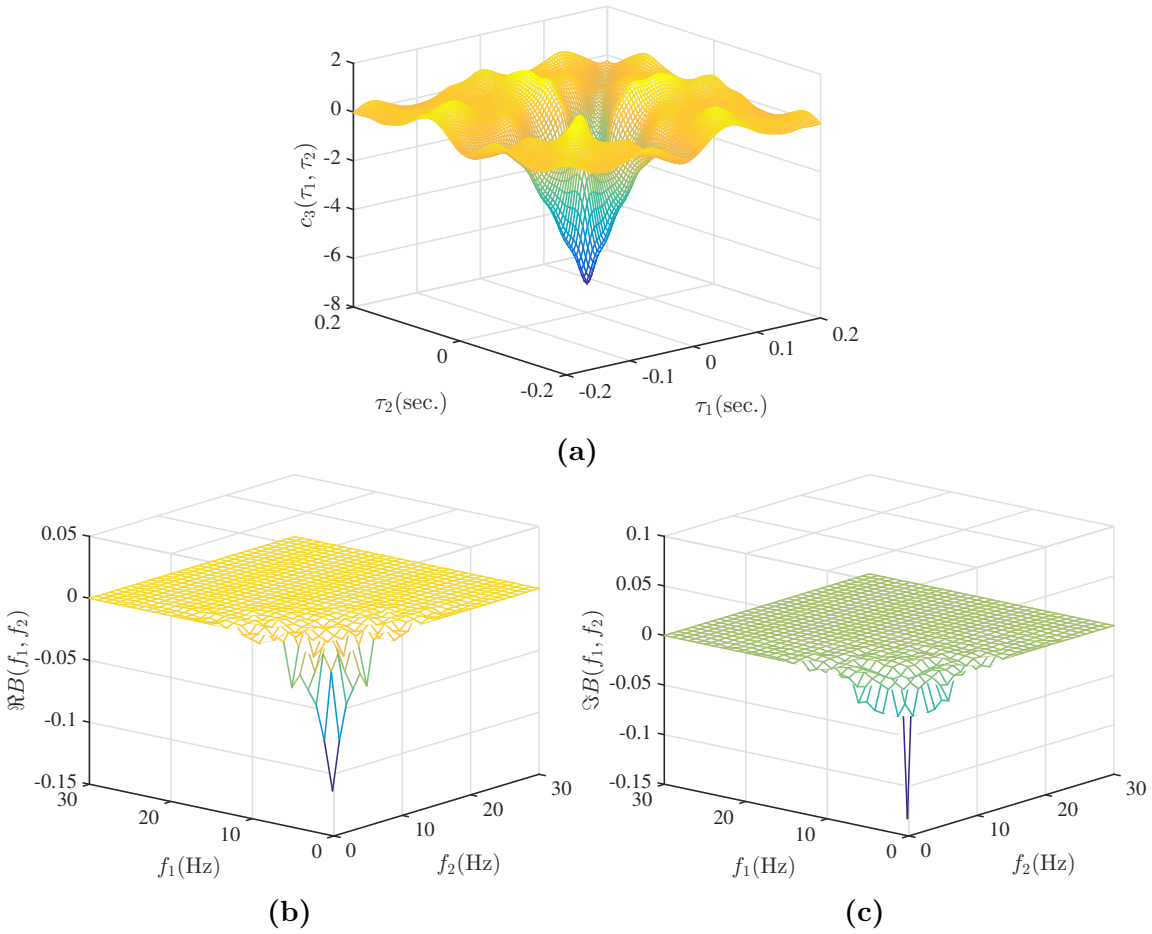

Figure 3.18: (a) Estimated third-order cumulant, (b) real and (c) imaginary bispectra from 10,000 samples functions of the wind velocity process generated using the proposed method.

Representation Method. The method is derived by defining an orthogonal spectral process that includes contributions from nonlinear wave interactions while maintaining the prescribed orthogonality conditions up to third order. This is achieve through the definition of two new quantities, the pure power spectrum and the partial bicoherence, that enable the single wave and wave interaction components to be decoupled. Extension of the method to fourth and higher-order processes is discussed. Several

numerical examples are provided to show the capabilities of the methodology to accurately simulate processes from a known power spectrum and bispectrum. Finally, the method is applied to the generation of wind velocity histories based on a statistical characterization of Large Eddy Simulations of the atmospheric boundary layer.

Chapter 4

Phase difference distributions in higher-order stochastic processes

Many stochastic processes exhibit features that are not well-characterized by independent wave components. These processes are often referred to as nonlinear in the literature as they involve wave interactions that cannot be expressed through simple linear models. These nonlinearities, in turn, induce non-Gaussianity in stochastic processes with many wave components. The means of characterizing these nonlinearities have been largely expressed through higher-order moments (cumulants) spectra as discussed in the previous chapter. It follows logically, and somewhat intuitively, that those properties should derive from dependancies in phase of the wave components but, to date, no direct connection has been made between the joint distribution of the phases (or quantities derived from these, e.q. conditional distributions or joint

moments) and the higher-order properties of the process. This chapter offers the first such explicit analytical connection of these qualities.

4.1 Circular probability distributions and their properties

In this section, we differentiate between probability measures defined on the real line and circular probability measures whose support lies on the circumference of a unit circle [64, 65, 66]. As will be shown, it is convenient (and somewhat intuitive) to consider random phases in the SRM to have circular distributions. For example, the conventional interpretation of random phases in the SRM, Eq. (1.14), is that they are uniform on the line $(-\pi, \pi]$. An equivalent interpretation is that they are uniformly distributed on a unit circle. Adopting the second interpretation, we now explore some properties of circular distributions.

Since each point on the circumference of the unit circle represents a direction, a circular distribution is a way of assigning probabilities to different directions (i.e. defining a directional distribution of angles). Let $f(\theta)$ be the probability density function of a continuous circular random variable Θ. The pdf $f(\theta)$ has the following

basic properties:

$$\begin{aligned} & f(\theta) \geq 0; \ \forall \theta \\ & \int_{-\pi}^{\pi} f(\theta) d\theta = 1 \\ & f(\theta) = f(\theta + k \cdot 2\pi); \forall k \in \mathbb{I} \end{aligned} \tag{4.1}$$

where $\mathbb{I}$ denotes the set of integers.

A circular distribution can also be described via its characteristic function. The value of the characteristic function at an integer p is called the p-th trigonometric moment of θ and is given by

$$\phi_\theta(p) \equiv E[e^{ip\theta}] = \int_{-\pi}^{\pi} e^{ip\theta} dF(\theta) = \rho_p e^{i\mu_p} \text{ where } p = 0, \pm 1, \pm 2, \cdots \tag{4.2}$$

The amplitude of the trigonometric moment can be bounded by Lyapunov's inequality as

$$|\phi_\theta(p)| = \rho_p = |E(e^{ip\theta})| \leq E(|e^{ip\theta}|) = 1 \tag{4.3}$$

In particular, consider the first trigonometric moment given by

$$\phi_\theta(1) = E[e^{i\theta}] = \rho_1 e^{i\mu_1}; \tag{4.4}$$

where $\rho_1 \in [0, 1]$ is the mean resultant length and $\mu_1 \in (-\pi, \pi]$ is the mean direction

determined from

$$\begin{aligned} \rho_1 &= |E[e^{i\theta}]| \\ \mu_1 &= \tan^{-1}\left(\frac{\Im E[e^{i\theta}]}{\Re E[e^{i\theta}]}\right) \end{aligned} \tag{4.5}$$

The mean resultant length represents the magnitude of the expected value of all unit radial vectors distributed on the unit circle with directions distributed as $f(\theta)$, while the mean direction is the mean angle of these vectors. The circular variance defined as $v = 1 - \rho_1$ is a measure of the dispersion of θ analogous to the variance of a linear RV. Furthermore, the characteristic function of the sum of independent circular random variables is given by the following. Let $\theta_1, \cdots, \theta_n$ be independent circular, the characteristic function of $S_n = \theta_1 + \cdots + \theta_n$ is given by

$$\phi_{S_n}(p) = \prod_{i=1}^{n} \phi_i(p) \tag{4.6}$$

4.1.1 Circular uniform distribution

Three of the most popular circular probability models are the circular uniform, von Mises, and wrapped Cauchy distributions. The circular uniform distribution has probability density function given by

$$f_U(\theta) = \frac{1}{2\pi}; \theta \in (-\pi, \pi] \tag{4.7}$$

That is, all directions of θ are equally distributed and it is no concentration. Its trigonometric moments, $\phi_\theta(p)$ of all orders are zero except zero-th order, $\phi_\theta(0) = 1$. Because of the unique characteristic function of the circular uniform random variable, the summation of a circular uniform random variable with any other independent random variables is uniformly distributed by Eq. (4.6).Accordingly, the first trigonometric moments of the circular uniform distribution are given in the following Table 4.1. The circular uniform distribution is non-directional and its mean direction, μ_1, does not exist. The mean resultant length, ρ_1, is zero, which means the circular variance has its maximum value, $v = 1$. The circular uniform distribution is identical to the linear uniform distribution with range, $(-\pi, \pi]$, therefore, it can be used for the independent random phases in the classical SRM for Gaussian processes.

Trigonometric Moments	
Mean direction (μ_1)	undefined
Mean resultant length (ρ_1)	0

Table 4.1: Trigonometric moments of circular uniform distribution.

As we will see, when the distribution of phase angles is not circular uniform, it means that there is a certain concentration and direction of the phases, and a stochastic process generated by the SRM is non-Gaussian. Therefore, to model more general phase relationships in stochastic processes, it is useful to consider more general families of circular distributions. The following two distributions can be used to model phases in such cases: the von Mises and wrapped Cauchy distributions.

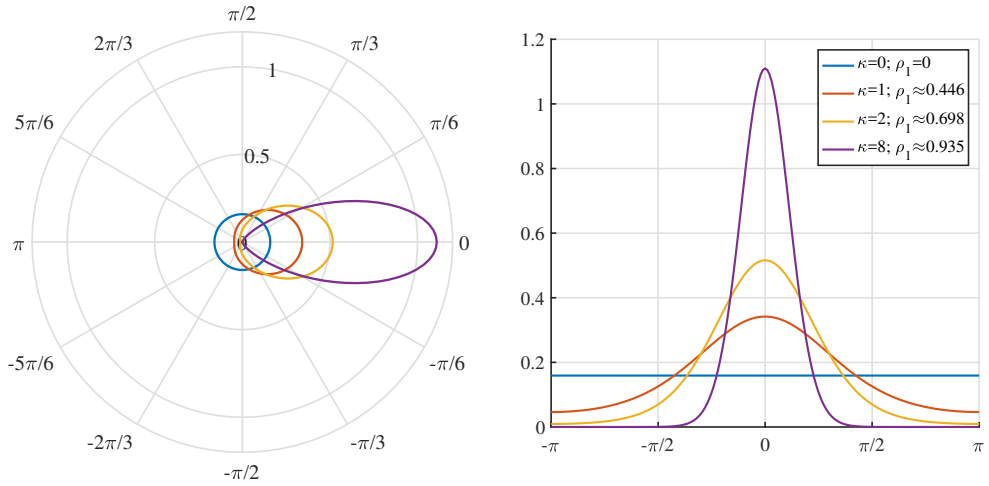

(a) **(b)**

Figure 4.1: Von Mises distributions in (a) polar and (b) Cartesian coordinates with zero mean direction and various mean resultant lengths.

4.1.2 Von Mises distribution

The von Mises distribution [67] (shown in Figure 4.1) is a symmetric and unimodal circular distribution with probability density given by

$$f_{VM}(\theta;\mu_1,\kappa) = \frac{e^{\kappa\cos(\theta-\mu_1)}}{2\pi I_0(\kappa)}; \theta \in (-\pi,\pi], \mu_1 \in (-\pi,\pi], \kappa \geq 0 \tag{4.8}$$

where μ is a direction parameter (equal to mean direction) , κ is a scale parameter, and I_0 is the modified Bessel function of the first kind having order $p = 0$ which follows the general form given by

$$I_p(\kappa) = \frac{1}{2\pi}\int_0^{2\pi} e^{\kappa\cos(\theta)}\cos(p\cdot\theta)d\theta; p \in \mathbb{I} \tag{4.9}$$

The von Mises distribution has been well studied with a strong emphasis on pa-

rameter estimation [68, 69, 70] and its p-th order trigonometric moments are given by

$$\phi_p(\theta; \mu_1, \kappa) = \frac{I_p(\kappa)}{I_0(\kappa)} e^{ip\mu_1} \tag{4.10}$$

Specifically, the first trigonometric moments are given in Table 4.2. Given the moment

Trigonometric Moments	
Mean direction (μ_1)	μ_1
Mean resultant length (ρ_1)	$\frac{I_1(\kappa)}{I_0(\kappa)}$

Table 4.2: Trigonometric moments of the von Mises distribution.

form in Eq. (4.10), the von Mises distribution can be difficult to use for our purposes. Because the modified Bessel function has no analytical inverse, we cannot easily identify the parameter κ for a given mean resultant length.

4.1.3 Wrapped Cauchy distribution

An easier distribution to work with is the wrapped Cauchy distribution shown in Figure 4.2. The wrapped Cauchy distribution has pdf given by

$$f_{WC}(\theta; \mu_1, \rho_1) = \frac{1}{2\pi} \frac{1 - \rho_1^2}{1 + \rho_1^2 - 2\rho_1 \cos(\theta - \mu_1)}; \theta \in (-\pi, \pi], \mu_1 \in (-\pi, \pi], 0 \leq \rho_1 \leq 1 \tag{4.11}$$

and is directly parameterized by mean direction μ_1 and mean resultant length ρ_1, also shown in Table 4.3. The wrapped Cauchy distribution is also symmetric and unimodal. Moreover, the convolution of wrapped Cauchy distributions, $f_{WC}(\mu_1, \rho_1)$

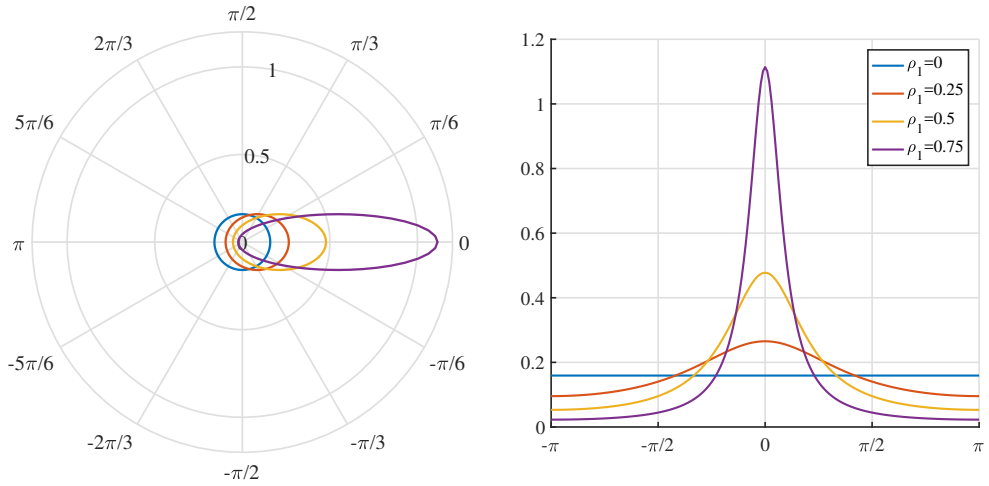

(a) **(b)**

Figure 4.2: Wrapped Cauchy distributions in (a) polar and (b) Cartesian coordinates with zero mean direction and various mean resultant lengths.

and $f_{WC}(\bar{\mu}_1, \bar{\rho}_1)$ is $f_{WC}(\mu_1 + \bar{\mu}_1\ , \rho_1 \cdot \bar{\rho}_1)$.

Trigonometric Moments	
Mean direction (μ_1)	μ_1
Mean resultant length (ρ_1)	ρ_1

Table 4.3: Trigonometric moments of wrapped Cauchy distribution.

4.2 Relating higher-order spectra and circular phase difference distributions

In this section, we derive an analytical relation between higher-order spectra and phase dependencies in the SRM under specific conditions. In particular, it will be shown how the orthogonality conditions of the Cramér spectral representation can be used to relate higher-order spectra to the trigonometric moments of circular phase

difference distributions when a certain form of orthogonal increments are assumed.

Recall from Section 1.1, that there are two widely used forms of the SRM having orthogonal increments given in Eqs. (1.13) and (1.16) respectively. Consider the form given in Eq. (1.16) where the orthogonality derives from randomness in phase angles θ_k. Again, recall that when $\theta_k \sim f_U(-\pi, \pi]$ (circular uniform), processes generated by the SRM [3] are Gaussian.

The k-th order cumulant of the process represented by Eq. (1.17) can be expressed purely in term of the k-th trigonometric cumulants of the phase relations which in turn depends only on the relationship of the random phases. Applying the orthogonal increments from Eq. (1.16) to the orthogonality conditions in Eq. (1.4) yields

$$c[dz(\omega_1)dz(\omega_2)\cdots dz^*(\omega_k)] = \delta(\omega_1+\omega_2+\cdots-\omega_k)\cdot\frac{\prod_{i=1}^{k}A_i}{\sqrt{2^k}}\cdot c\left[e^{-i(\theta_1+\theta_2+\cdots-\theta_k)}\right] \tag{4.12}$$

When θ_i are independent and circular uniform random variables, it is straight forward to show that the higher-order cumulants of the processe are equal to zero, because $\theta_1+\theta_2+\cdots-\theta_k$ also has a circular uniform distribution. Consequently, the process is Gaussian as the number of phases increases to infinity. But, more generally, Eq. (4.12) implies that the cumulants of the process, $c[dz(\omega_1)dz(\omega_2)\cdots dz^*(\omega_k)]$ are related to conditional dependencies in the phases. That is, if θ_1, θ_2, $\cdots$, θ_k are not independent, then $\theta_1+\theta_2+\cdots-\theta_k$ will not be circular uniform and higher-order cumulants will be non-zero (i.e. the process will be non-Gaussian). To illustrate this point, consider

the first four cumulants as follows.

The first-order cumulant (moment), or mean, from Eq. (1.16) is given by

$$c[dz(\omega)] = E[dz(\omega)] = E[\frac{A_k}{\sqrt{2}}e^{-\theta_k}] = 0 \tag{4.13}$$

where $dz(\omega) = \frac{1}{2}[du(\omega) + idv(\omega)]$.

The second-order cumulant (moment) is given by

$$c[dz(\omega_1)dz^*(\omega_2)] = E[dz(\omega_1)dz^*(\omega_2)] = \delta(\omega_1 - \omega_2) \cdot \frac{A_1A_2}{\sqrt{4}} \cdot E[e^{-i(\theta_1-\theta_2)}] = S(\omega_1)\Delta\omega_1 \tag{4.14}$$

and relates the orthogonal increments to the power spectral density $S(\omega_1)$. That is, under the condition, $\omega_1 = \omega_2$ (implied by $\delta(\omega_1 - \omega_2)$), we have $\theta_1 = \theta_2$ and hence $E[e^{-(\theta_1-\theta_2)}] = 1$.

The third-order cumulant (moment) is given by

$$\begin{aligned} c[dz(\omega_1)dz(\omega_2)dz^*(\omega_3)] &= E[dz(\omega_1)dz(\omega_2)dz^*(\omega_3)] \\ &= \delta(\omega_1 + \omega_2 - \omega_3) \cdot \frac{A_1A_2A_3}{\sqrt{8}} \cdot E[e^{-i(\theta_1+\theta_2-\theta_3)}] \\ &= B(\omega_1, \omega_2)\Delta\omega_1\Delta\omega_2 \end{aligned} \tag{4.15}$$

which we now see relates the first trigonometric moment of the phase difference $\theta_3 -$

$(\theta_1 + \theta_2)$ to the bispectrum. This is seen directly by rearranging Eq. (4.15) as

$$\phi_{\theta_3-(\theta_1+\theta_2)}(1) = E[e^{i(\theta_3-(\theta_1+\theta_2))}] = \frac{\sqrt{8}B(\omega_1,\omega_2)\Delta\omega_1\Delta\omega_2}{A_1A_2A_3} \text{ for } \omega_3 = \omega_1 + \omega_2 \quad (4.16)$$

In other words, for frequencies related as $\omega_3 = \omega_1 + \omega_2$, the first trigonometric moment of the circular distribution of the phase difference $\theta_3 - (\theta_1 + \theta_2)$ can be determined exactly from the bispectrum $B(\omega_1, \omega_2)$.

Lastly, the fourth-order cumulant can be related similarly to the trispectrum by

$$\begin{aligned} c[dz(\omega_1)dz(\omega_2)dz(\omega_3)dz^*(\omega_4)] &= \delta(\omega_1+\omega_2+\omega_3-\omega_4)\cdot\frac{A_1A_2A_3A_4}{\sqrt{16}} \\ &\quad\cdot c_4[e^{-i(\theta_1+\theta_2+\theta_3-\theta_4)}] \\ &= T(\omega_1,\omega_2,\omega_3)\Delta\omega_1\Delta\omega_2\Delta\omega_3 \end{aligned} \quad (4.17)$$

where

$$\begin{aligned} c[e^{-i(\theta_1+\theta_2+\theta_3-\theta_4)}] &= E[e^{-i(\theta_1+\theta_2+\theta_3-\theta_4)}] - E[e^{-i(\theta_1+\theta_2)}]E[e^{-i(\theta_3-\theta_4)}] \\ &\quad - E[e^{-i(\theta_2+\theta_3)}]E[e^{-i(\theta_1-\theta_4)}] - E[e^{-i(\theta_1+\theta_3)}]E[e^{-i(\theta_2-\theta_4)}] \end{aligned} \quad (4.18)$$

Notice, however, that as shown in Eq. (4.18) the cumulant and moment are not equivalent. The cumulant thus induces several expectations. Under the condition

that $\omega_1 \neq \omega_2$, $\omega_2 \neq \omega_3$, and $\omega_1 \neq \omega_3$, this relation simplifies as

$$c[e^{-i(\theta_1+\theta_2+\theta_3-\theta_4)}] = E[e^{-i(\theta_1+\theta_2+\theta_3-\theta_4)}] \text{ for } \omega_1+\omega_2 \neq 0, \omega_2+\omega_3 \neq 0, \omega_1+\omega_3 \neq 0 \tag{4.19}$$

Thus, under the condition in Eq. (4.19), again a straightforward relation can be expressed between the trigonometric moment of the circular distributed phase difference $\theta_4 - (\theta_1 + \theta_2 + \theta_3)$ and the trispectrum of the process as

$$\phi_{\theta_4-(\theta_1+\theta_2+\theta_3)}(1) = E[e^{i(\theta_4-(\theta_1+\theta_2+\theta_3))}] = \frac{\sqrt{16}T(\omega_1,\omega_2,\omega_3)\Delta\omega_1\Delta\omega_2\Delta\omega_3}{A_1A_2A_3A_4} \quad \text{for } \omega_4 = \omega_1+\omega_2+\omega_3 \tag{4.20}$$

Eqs. (4.17) - (4.20) imply that the trispectrum can be obtained from the phase dependency $\theta_4 - (\theta_1 + \theta_2 + \theta_3)$ except when $\omega_1 = -\omega_2 = -\omega_3 = \omega_4$ or $\omega_1 = \omega_2 = -\omega_3 = \omega_4$ or $-\omega_1 = \omega_2 = \omega_3 = \omega_4$. The values of the tispectrum under the conditions, $\omega_1 = -\omega_2 = -\omega_3 = \omega_4$ or $\omega_1 = \omega_2 = -\omega_3 = \omega_4$ or $-\omega_1 = \omega_2 = \omega_3 = \omega_4$, are asymptotically diminishing and therefore do not contribute to the kurtosis in the limit as mentioned at Section 1.3.2.3. Consequently, the 4th order condition of Cramér's representation under the conditions stated above can be related to the trispectrum values of the processes which alter their kurtosis. The prescribed equations show that when we have non-zero values of $E[e^{i\theta_3-(\theta_1+\theta_2)}]$ and $E[e^{i(\theta_4-(\theta_1+\theta_2+\theta_3)}]$ (the first trigonometric moment of $\theta_3 - (\theta_1 + \theta_2)$ and $\theta_4 - (\theta_1 + \theta_2 + \theta_3)$), the stochastic process

will have non-zero bispectrum or trispectrum and it will be non-Gaussian.

Perhaps a more intuitive understanding of these relations can be gained by looking at the higher-order phases and coherences. Recall the definitions of biphase and triphase in Eq. (1.43). Utilizing the relations in Eqs. (4.16)) and (4.20), the biphase and triphase of the stochastic process can be related to the trigonometric moments of the phase differences by

$$\beta(\omega_1, \omega_2) = \tan^{-1}\left[\frac{\Im E[e^{-i(\theta_1+\theta_2-\theta_3)}]}{\Re E[e^{-i(\theta_1+\theta_2-\theta_3)}]}\right] \tag{4.21}$$

$$\begin{aligned}\gamma(\omega_1, \omega_2, \omega_3) &= \tan^{-1}\left[\frac{\Im c[e^{-i(\theta_1+\theta_2+\theta_3-\theta_4)}]}{\Re c[e^{-i(\theta_1+\theta_2+\theta_3-\theta_4)}]}\right] \\ &= \tan^{-1}\left[\frac{\Im E[e^{-i(\theta_1+\theta_2+\theta_3-\theta_4)}]}{\Re E[e^{-i(\theta_1+\theta_2+\theta_3-\theta_4)}]}\right] \\ &\text{for } \omega_1+\omega_2 \neq 0, \omega_2+\omega_3 \neq 0, \omega_1+\omega_3 \neq 0\end{aligned} \tag{4.22}$$

From Eq. (4.5), we recognized that the bisphase and triphase of the stochastic process are equal to the mean directions of the phase differences, $\theta_3 - (\theta_1 + \theta_3)$ and $\theta_4 - (\theta_1 + \theta_2 + \theta_3)$, respectively.

Recalling the squared discretized bicoherences of Brillinger and Rosenblatt [71], b_1^2 and, Kim and Powers [46], b_2^2 in Eqs. (3.4), and applying the relations in Eqs.

(4.16) and (4.20) yields

$$b_1^2(\omega_1,\omega_2) = \frac{\left|\left[\frac{A_1A_2A_3}{\sqrt{8}}E\big[e^{-i(\theta_1+\theta_2-\theta_3)}\big]\right]\right|^2}{E\left[\frac{A_1}{\sqrt{2}}e^{-i\theta_1}\frac{A_1}{\sqrt{2}}e^{i\theta_1}\right]E\left[\frac{A_2}{\sqrt{2}}e^{-i\theta_2}\frac{A_2}{\sqrt{2}}e^{i\theta_2}\right]E\left[\frac{A_3}{\sqrt{2}}e^{-i\theta_3}\frac{A_3}{\sqrt{2}}e^{i\theta_3}\right]} = \left|E\big[e^{i(\theta_3-(\theta_1+\theta_2)}\big]\right|^2 \tag{4.23}$$

$$b_2^2(\omega_1,\omega_2) = \frac{\left|\left[\frac{A_1A_2A_3}{\sqrt{8}}E\big[e^{-i(\theta_1+\theta_2-\theta_3)}\big]\right]\right|^2}{E\left[\frac{A_1A_2}{\sqrt{4}}e^{-i(\theta_1+\theta_2)}\frac{A_1A_2}{\sqrt{4}}e^{i(\theta_1+\theta_2)}\right]E\left[\frac{A_3}{\sqrt{2}}e^{-i\theta_3}\frac{A_3}{\sqrt{2}}e^{i\theta_3}\right]} = \left|E\big[e^{i(\theta_3-(\theta_1+\theta_2)}\big]\right|^2 \tag{4.24}$$

That is, both bicoherences are equivalent under the assumed orthogonal increments and are equal to the squared mean resultant length of the phase difference $\theta_3-(\theta_1+\theta_2)$.

Next, consider the squared discretized tricoherences by Haubrich [72], t_1^2 and Kim and Powers [46], t_2^2. Again, under the assumed orthogonal increments with conditions given in Eq. (4.18), applying the relations in Eq. (4.20) yields

$$\begin{aligned} t_1^2(\omega_1,\omega_2,\omega_3) &= \frac{\left|\left[\frac{A_1A_2A_3A_4}{\sqrt{16}}c_4\big[e^{-i(\theta_1+\theta_2+\theta_3-\theta_4)}\big]\right]\right|^2}{E\left[\frac{A_1}{\sqrt{2}}e^{-i\theta_1}\frac{A_1}{\sqrt{2}}e^{i\theta_1}\right]E\left[\frac{A_2}{\sqrt{2}}e^{-i\theta_2}\frac{A_2}{\sqrt{2}}e^{i\theta_2}\right]E\left[\frac{A_3}{\sqrt{2}}e^{-i\theta_3}\frac{A_3}{\sqrt{2}}e^{i\theta_4}\right]E\left[\frac{A_4}{\sqrt{2}}e^{-i\theta_4}\frac{A_4}{\sqrt{2}}e^{i\theta_4}\right]} \\ &= \left|c_4\big[e^{i(\theta_4-(\theta_1+\theta_2+\theta_3))}\big]\right|^2 \\ &= \left|E\big[e^{i(\theta_4-(\theta_1+\theta_2+\theta_3))}\big]\right|^2 \text{ for } \omega_1+\omega_2\neq 0, \omega_2+\omega_3\neq 0, \omega_1+\omega_3\neq 0 \end{aligned} \tag{4.25}$$

$$
\begin{aligned}
t_2^2(\omega_1,\omega_2,\omega_3) &= \frac{\left|\left[\frac{A_1A_2A_3A_4}{\sqrt{16}}c_4\left[e^{-i(\theta_1+\theta_2+\theta_3-\theta_4)}\right]\right]\right|^2}{E\left[\frac{A_1A_2A_3}{\sqrt{8}}e^{-i(\theta_1+\theta_2+\theta_3)}\frac{A_1A_2A_3}{\sqrt{8}}e^{i(\theta_1+\theta_2+\theta_3)}\right]E\left[\frac{A_4}{\sqrt{2}}e^{-i\theta_4}\frac{A_4}{\sqrt{2}}e^{i\theta_4}\right]} \\
&= \left|c_4\left[e^{i(\theta_4-(\theta_1+\theta_2+\theta_3))}\right]\right|^2 \\
&= \left|E\left[e^{i(\theta_4-(\theta_1+\theta_2+\theta_3))}\right]\right|^2 \text{ for } \omega_1+\omega_2\neq 0, \omega_2+\omega_3\neq 0, \omega_1+\omega_3\neq 0
\end{aligned}
\tag{4.26}
$$

Again, the squared tricoherences are identical to the squared mean resultant length of the phase differences $\theta_4-(\theta_1+\theta_2+\theta_3)$.

It is important to reiterate the importance of these results. The expressions given above provide a first glimpse into the nature of the complex wave interactions that result in stochastic process non-linearities. Specifically, it has been shown that, under certain conditions, the higher-order spectra can be directly related to the joint circular distribution of the phases in the stochastic process through the trigonometric moments of phase differences of different degrees. This generalizes the notion of independent circular phase components in Fourier-type expansions of stochastic processes to enable the use of non-unifrom models (e.g. von Mises or wrapped Cauchy) to integrate phase dependencies. Explicit examples of its application will be considered in the following section

4.3 Simple Examples

In this section, two simple stochastic processes with quadratic and cubic phase coupling respectively are modeled by explicitly utilizing the circular phase angle difference distributions discussed in the previous section. Specifically, the phase difference distributions are selected to possess the mean directions and mean resultant lengths implied by a specified bispectrum/trispectrum.

4.3.1 Three waves stochastic process with quadratic phase coupling

Consider a stochastic process with quadratic phase coupling at discrete frequencies having power spectrum and bispectrum given by

$$S(\omega) = \frac{1}{4}\delta(\omega - 2\pi \cdot 10) + \frac{1}{4}\delta(\omega - 2\pi \cdot 20) + \frac{1}{4}\delta(\omega - 2\pi \cdot 30) \quad \text{for} \quad \omega \geq 0 \tag{4.27}$$

$$B(\omega_1, \omega_2) = \frac{1/\sqrt{2}}{8}\delta(\omega_1 - 2\pi \cdot 20, \omega_2 - 2\pi \cdot 10) \quad \text{for} \quad \omega_1 \geq \omega_2 \geq 0 \tag{4.28}$$

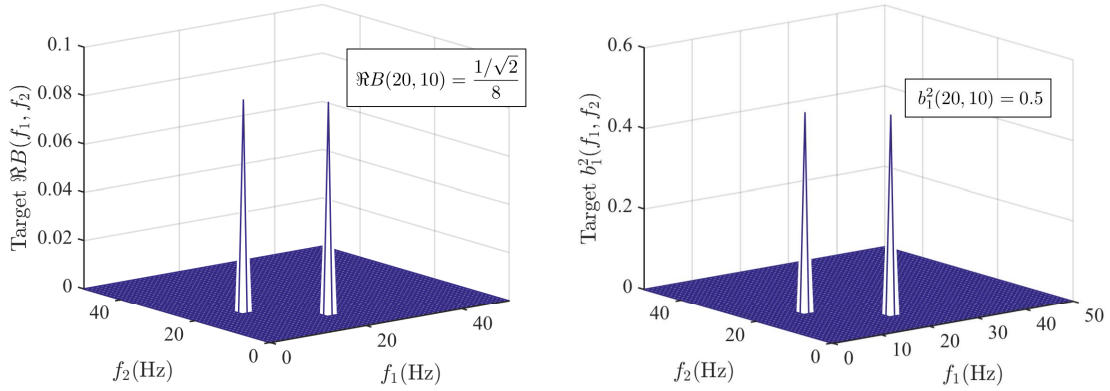

Figure 4.3: Target (a) real bispectrum, $\Re B$, and (b) squared bicoherence, b_1^2.

The squared bicoherences according to Eq. (4.23) and (4.24) can be calculated as

$$b_1^2(\omega_1, \omega_2) = b_2^2(\omega_1, \omega_2) = \begin{cases} 0.5, & \text{if } \omega_1 = 2\pi \cdot 20,\ \omega_2 = 2\pi \cdot 10 \\ 0, & \text{otherwise} \end{cases} \quad \text{for } \ \omega_1 \geq \omega_2 \geq 0 \tag{4.29}$$

The target bispectrum and bicoherence are plotted in Figure 4.3.

The biphase at the coupled frequencies is $\beta(2\pi \cdot 20, 2\pi \cdot 10) = 0$. The process can be expanded as

$$f(t) = \cos(2\pi \cdot 10t - \theta_1) + \cos(2\pi \cdot 20t - \theta_2) + \cos(2\pi \cdot 30t - \theta_3) \tag{4.30}$$

Because of the quadratic phase coupling the phases, $\{\theta_1, \theta_2, \theta_3\}$ are dependent. From the derivations above, it follows that θ_1 and θ_2 are, indeed, independent $U(-\pi, \pi]$

while θ_3 is not. Specifically, the quantity $\theta_3 - (\theta_1 + \theta_2)$ has mean direction $\mu_1 = 0$ and mean resultant length $\rho_1 = b_1(2\pi \cdot 20, 2\pi \cdot 10) = \sqrt{0.5}$. To match these quantities, we consider $\theta_3 - (\theta_1 + \theta_2)$ to follow a wrapped Cauchy distribution with parameters $\mu_1 = 0$ and $\rho_1 = \sqrt{2}$. To generate phases angles following the prescribed distributions, first, θ_1 and θ_2 are independently generated with uniform circular distribution. Next, the random variable $\theta_* = \theta_3 - (\theta_1 + \theta_2)$ is generated from the given wrapped Cauchy distribution. Finally, $\theta_3 = \theta_* + \theta_1 + \theta_2$ is obtained as the dependent random variable. Following the proof in Section 4.1, θ_3 is uniformly distributed. These distributions are shown from 50,000 random samples in Figure 4.4.

Using the phases shown in Figure 4.4, 50,000 realizations of the process are generated and one such realization is shown in Figure 4.5. Figure 4.6 shows the estimated real bispectrum and squared bicoherence from the 50,000 realizations given in Eqs. (4.28) and (4.29). Given the target bispectrum, the process has positive skewness given by

$$\text{Skewness}[f(t)] = \frac{\int_{-\infty}^{\infty}\int_{-\infty}^{\infty} B(\omega_1, \omega_2) d\omega_1 d\omega_2}{(\int_{-\infty}^{\infty} S(\omega) d\omega)^{3/2}} = \frac{1}{\sqrt{3}} \tag{4.31}$$

The true and estimated moments from the 50,000 realizations are compared in Table 4.4, showing very good agreement.

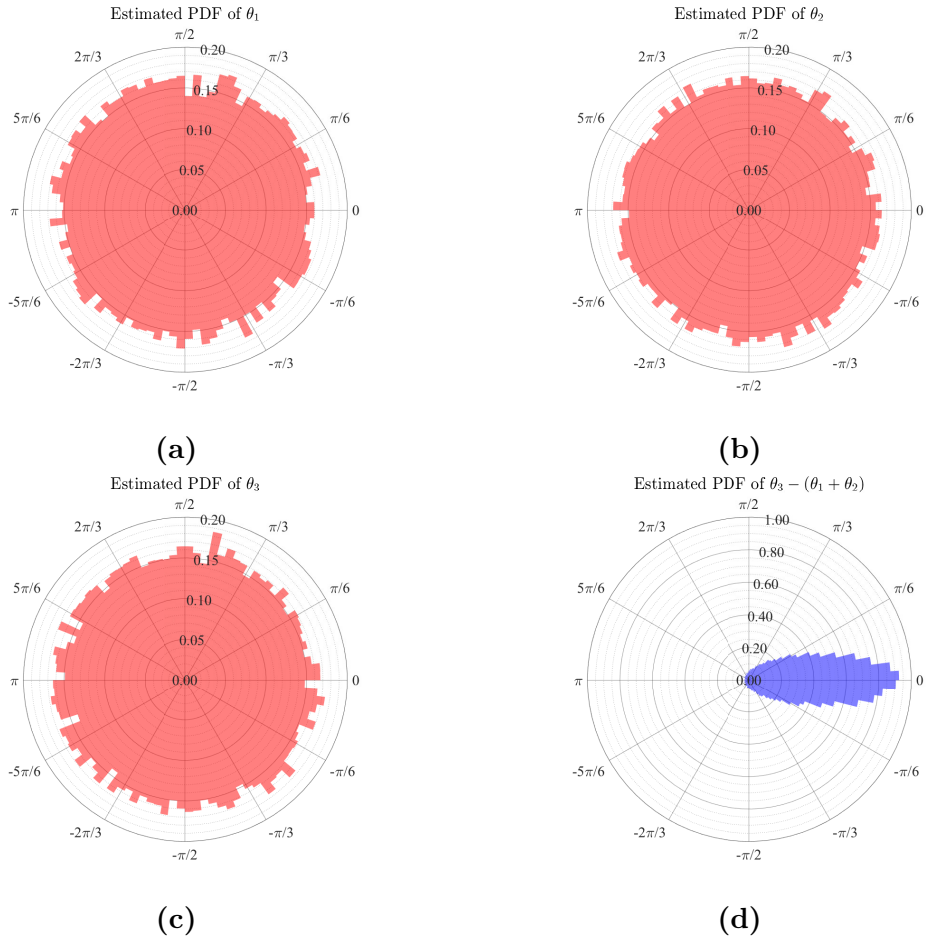

Figure 4.4: Estimated PDFs of random phase angles; (a) θ_1, (b) θ_2, (c) θ_3, and quadratic phase difference; (d) $\theta_3 - (\theta_1 + \theta_2)$.

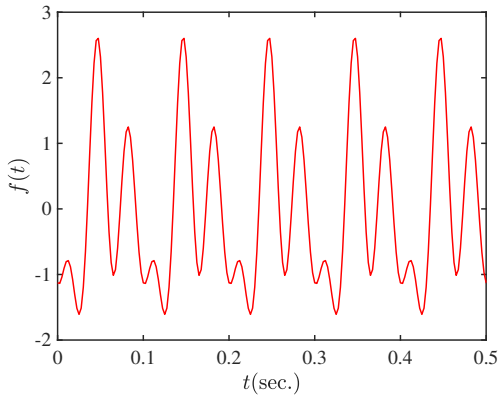

Figure 4.5: Representative sample function of the three wave process with quadratic phase coupling.

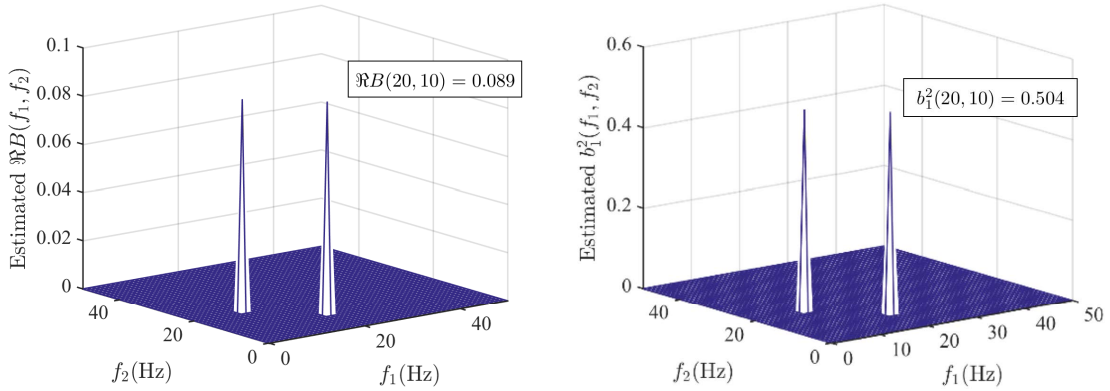

(a) **(b)**

Figure 4.6: Estimated (a) real bispectrum, $\Re B$, and (b) squared bicoherence, b_1^2.

$f(t)$	Target	Estimated
Variance	$3/2$	1.500
Skewness	$1/\sqrt{3}$	0.5776

Table 4.4: Target and estimated moments of the three wave stochastic process with quadratic phase coupling.

4.3.2 Four wave stochastic process with cubic phase coupling

Consider next process with cubic phase coupling between discrete frequencies. The target power spectrum and trispectrum are given by

$$S(\omega) = \frac{1}{4}\delta(\omega - 2\pi \cdot 5) + \frac{1}{4}\delta(\omega - 2\pi \cdot 10) + \frac{1}{4}\delta(\omega - 2\pi \cdot 15) + \frac{1}{4}\delta(\omega - 2\pi \cdot 30) \quad \text{for } \omega \geq 0 \tag{4.32}$$

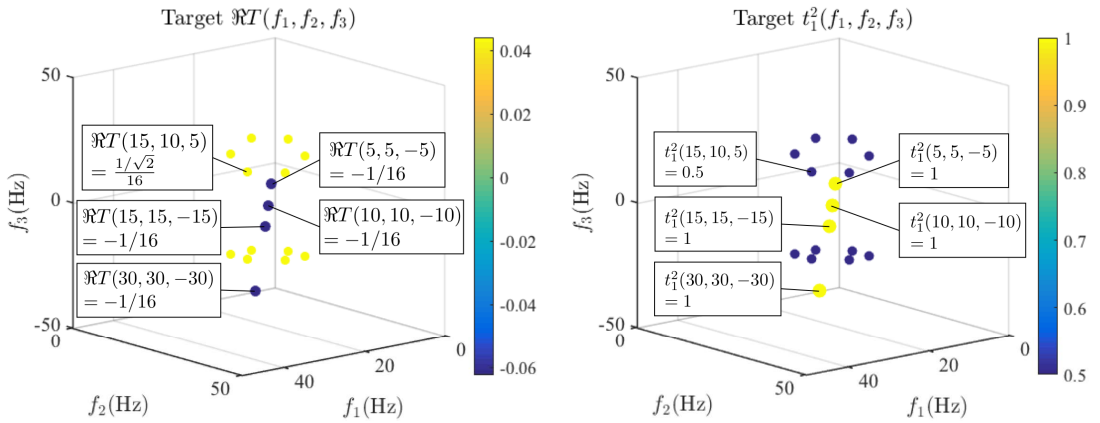

(a) **(b)**

Figure 4.7: Target (a) real trispectrum, $\Re T$, and (b)squared tricoherences, t_1^2.

$$T(\omega_1, \omega_2, \omega_3) = \frac{1/\sqrt{2}}{16}\delta(\omega_1 - 2\pi \cdot 15, \omega_2 - 2\pi \cdot 10, \omega_3 - 2\pi \cdot 5) \quad \text{for} \quad \omega_1 \geq \omega_2 \geq \omega_3 \geq 0 \tag{4.33}$$

where the trispectrum is only defined in the domain, $\omega_1 \geq \omega_2 \geq \omega_3 \geq 0$, to exclude the asymptotically diminishing terms of the trispectrum mentioned in Section 1.3.2.3. Furthermore, the target tricoherences (Eq. (4.25)) and (4.26)) are computed as

$$t_1^2(\omega_1, \omega_2) = t_2^2(\omega_1, \omega_2) = \begin{cases} 0.5, & \text{if } \omega_1 = 2\pi \cdot 15,\ \omega_2 = 2\pi \cdot 10,\ \omega_3 = 2\pi \cdot 5 \\ 0, & \text{otherwise} \end{cases} \quad \text{for} \quad \omega_1 \geq \omega_2 \geq \omega_3 \geq 0 \tag{4.34}$$

and the triphase at the coupled frequencies is $\gamma(2\pi \cdot 15, 2\pi \cdot 10, 2\pi \cdot 5) = 0$. The target trispectrum and tricoherence are plotted in Figure 4.7. Similar to the quadratic

coupling case, we can expand the process as

$$f(t) = \cos(2\pi \cdot 5t - \theta_1) + \cos(2\pi \cdot 10t - \theta_2) + \cos(2\pi \cdot 15t - \theta_3) + \cos(2\pi \cdot 30t - \theta_4) \tag{4.35}$$

In this case, we have $\theta_1, \theta_2, \theta_3 \sim f_U(-\pi, \pi]$, and $\theta_4 - (\theta_1 + \theta_2 + \theta_3) \sim f_{WC}(\mu_1, \rho_1)$ with $\mu_1 = \gamma(2\pi \cdot 15, 2\pi \cdot 10, 2\pi \cdot 5) = 0$ and $\rho_1 = t_1(2\pi \cdot 15, 2\pi \cdot 10, 2\pi \cdot 5) = \sqrt{0.5}$. Like the prescribed PDFs in the quadratic coupling example, each individual random phase is uniformly distributed, but the difference $\theta_4 - (\theta_1 + \theta_2 + \theta_3)$ is assumed to follow wrapped Cauchy distribution with $\mu_1 = 1$ and $\rho_1 = \sqrt{0.5}$. Similar to the previous example, θ_1, θ_2, and θ_3 are independently generated following a circular uniform distribution. Next, $\theta_{**} = \theta_4 - (\theta_1 + \theta_2 + \theta_3)$ is produced with the given wrapped Cauchy distribution. Finally, we can obtain $\theta_4 = \theta_1 + \theta_2 + \theta_3 + \theta_{**}$ and, again, marginal distribution of θ_4 is circular uniform. The estimated circular PDFs of the phases angles and their differences from 50,000 samples are given in Figure 4.8. From these phase angles, 50,000 realizations of the stochastic process are generated from Eq. (4.35). One such realization is shown in Figure 4.9.

The estimated real trispectrum and its squared tricoherences in the 1st and 8th octants from the 50,000 realizations are depicted in Figure 4.10. These quantities match their targets in Figure 4.7 very accurately. However, the estimated quantities in Figure 4.10 also include several symmetries and self-cubic phase couplings that are not present in Eq. (4.33) as well as the terms $T(5, 5, -5)$, $T(10, 10, -10)$, $T(15, 15, -15)$

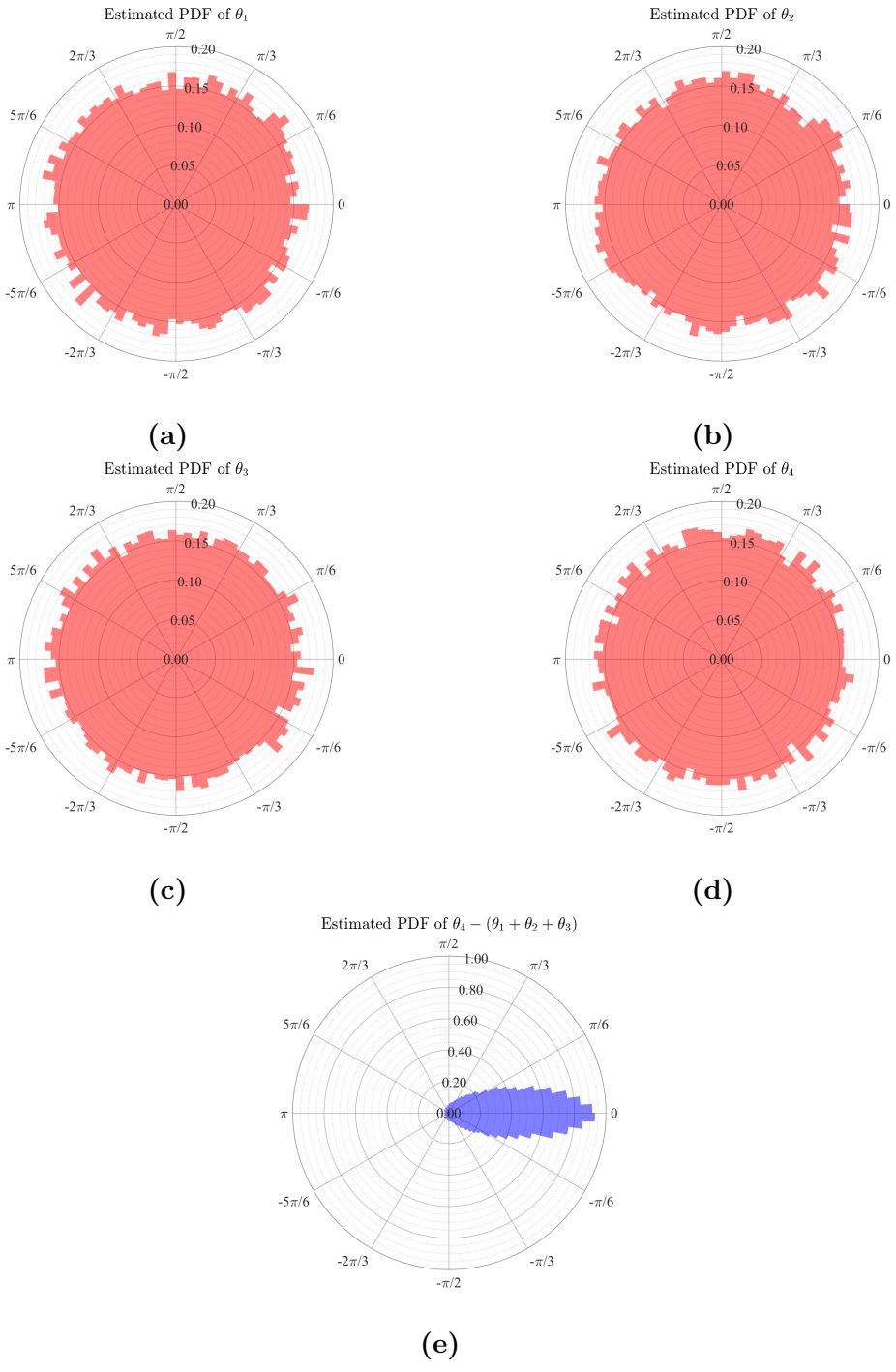

Figure 4.8: Estimated PDFs of random phase angles; (a) θ_1, (b) θ_2, (c) θ_3, (d) θ_4, and cubic phase difference; (e) $\theta_4 - (\theta_1 + \theta_2 + \theta_3)$.

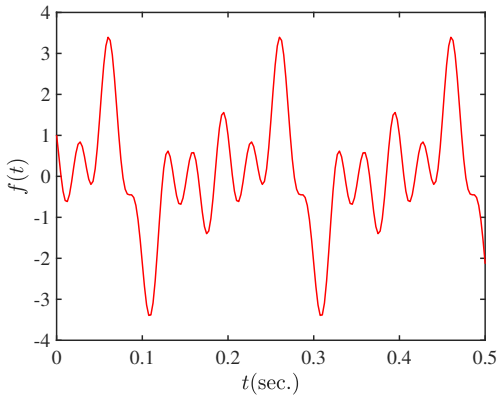

Figure 4.9: Representative sample function of a four wave process with cubic phase difference.

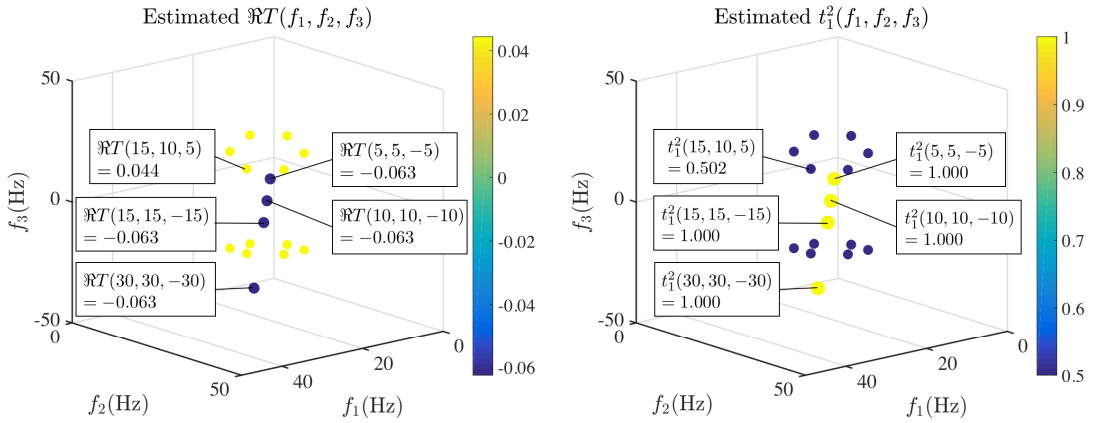

(a) **(b)**

Figure 4.10: Estimated (a) real trispectrum, $\Re T$, and (b) squared tricoherences, t_1^2.

and $T(30, 30, -30)$ that arise from individual components.

The target unnormalized kurtosis is computed by integrating the trispectrum as Eq. (1.60) as

$$Kurt[f(t)] = \int_{-\infty}^{\infty}\int_{-\infty}^{\infty}\int_{-\infty}^{\infty} T(\omega_1, \omega_2, \omega_3)d\omega_1 d\omega_2 d\omega_3 = 48 \cdot \frac{1/\sqrt{2}}{16} - 6 \cdot \frac{4}{16} \quad (4.36)$$

and the target kurtosis becomes

$$\text{Kurtosis}[f(t)] = \frac{Kurt[f(t)]}{(\int_{-\infty}^{\infty} S(\omega)d\omega)^2} + 3 = \frac{3(\sqrt{2}-1)}{8} + 3 \quad (4.37)$$

The target and estimated moments from the 50,000 realizations are compared in Table 4.5.

$f(t)$	Target	Estimated
Variance	2	2.000
Kurtosis	$3 + 3(\sqrt{2}-1)/8$	3.3718

Table 4.5: Target and estimated moments of the four wave stochastic process with cubic phase coupling.

4.4 Practical challenges to relating HOS and phase difference distributions

For general stochastic processes with continuous spectra, the proposed method cannot be directly applied for the reasons described in this section. Therefore, the current application is limited to simple processes with a small number of distinct/discrete frequencies. A further generalization/application of the relations derived here requires further investigation.

Specifically, there are two practical challenges to relating general (continuous) higher-order spectra(HOS) and phase-difference distributions. The first limitation is that any frequency exhibiting phase coupling can only result from the coupling of two unique frequencies. That is, cases where different frequency combinations yield a common frequency (e.g. $\omega_2 + \omega_2 = \omega_4$ and $\omega_1 + \omega_3 = \omega_4$) cannot be related as proposed. Consider, for example, the following process

$$f(t) = A\cos(\omega_1 t - \theta_1) + B\cos(\omega_2 t - \theta_2) + C\cos(\omega_3 t - \theta_3) + D\cos(\omega_4 t - \theta_4) \quad (4.38)$$

In this process, the proposed relations suggest that both the phase differences $\theta_* = \theta_4 - (\theta_2 + \theta_2)$ and $\theta_{**} = \theta_4 - (\theta_1 + \theta_3)$ must be simultaneously specified. However, simulating θ_4 to match both trigonometric moments proves incompatible. Let us assume the phase differences be distributed as wrapped Cauchy distributions with

the given the first trigonometric moments as $\theta_* \sim f_{WC}(\mu_1, \rho_1)$ and $\theta_{**} \sim f_{WC}(\bar{\mu}_1, \bar{\rho}_1)$. Next, we can combine the phase differences as

$$\theta_* - \theta_{**} = \theta_3 - \theta_1 \tag{4.39}$$

According to the convolutional property of wrapped Cauchy distribution mentioned in Section 4.1, the marginal distribution of $\theta_* - \theta_{**}$ is $f_{WC}(\mu_1 - \bar{\mu}_1, \rho_1 \cdot \bar{\rho}_1)$. Because θ_1 and θ_3 are independently circular uniform distributed, however, $\theta_3 - \theta_1$ is also circular uniform distributed. Therefore, Eq. (4.39) is incompatible.

The second limitation arises when the processes has "ested" phase coupling, when a coupled frequency couples with another frequency, which couples with another frequency. For example, the phase differences are given only at coupled frequencies ($\omega_1 + \omega_1 = \omega_2$, $\omega_1 + \omega_2 = \omega_3$ and $\omega_1 + \omega_3 = \omega_4$) as

$$\begin{aligned} \theta_* &= \theta_2 - (\theta_1 + \theta_1) \sim f_{WC}(\mu_1, \rho_1) \\ \theta_{**} &= \theta_3 - (\theta_1 + \theta_2) \sim f_{WC}(\bar{\mu}_1, \bar{\rho}_1) \\ \theta_{***} &= \theta_4 - (\theta_1 + \theta_3) \sim f_{WC}(\bar{\bar{\mu}}_1, \bar{\bar{\rho}}_1) \end{aligned} \tag{4.40}$$

We can generate each phase difference from representative wrapped Cauchy distribution, yet, undesigned quadratic phase coupling at (ω_2, ω_2) is generated as

$$\theta_4 - (\theta_2 + \theta_2) = \theta_{***} + 2 \cdot \theta_{**} - 2 \cdot \theta_* \sim f_{WC}(\mu_1 + 2\bar{\mu}_1 - 2\bar{\bar{\mu}}_1, \rho_1 \cdot \bar{\rho}_1^2 \cdot \bar{\bar{\rho}}_1^2) \tag{4.41}$$

However, the method is capable of simulating processes with several phase couplings with all distinct frequencies that avoid the two prescribed cases. Consider a stochastic process with quadratic phase couplings at distinct frequency-pairs as follows. The target power spectrum and bispectrum are given by

$$
\begin{aligned}
&S(\omega) = \\
&\frac{1}{4}[\delta(\omega - 2\pi \cdot 0.6) + \delta(\omega - 2\pi \cdot 0.7) + \delta(\omega - 2\pi \cdot 0.8) + \delta(\omega - 2\pi \cdot 0.9) + \delta(\omega - 2\pi \cdot 1.0) \\
&+ \delta(\omega - 2\pi \cdot 1.1) + \delta(\omega - 2\pi \cdot 1.3) + \delta(\omega - 2\pi \cdot 1.5) + \delta(\omega - 2\pi \cdot 1.7) + \delta(\omega - 2\pi \cdot 1.9) \\
&+ \delta(\omega - 2\pi \cdot 2.1) + \delta(\omega - 2\pi \cdot 2.2) + \delta(\omega - 2\pi \cdot 2.3) + \delta(\omega - 2\pi \cdot 2.4) + \delta(\omega - 2\pi \cdot 2.5)] \\
&\qquad\qquad\qquad\qquad\qquad\qquad\qquad\qquad\qquad\qquad \text{for } \omega \geq 0
\end{aligned}
\tag{4.42}
$$

$$
\begin{aligned}
B(\omega_1, \omega_2) = &\frac{1/\sqrt{2}}{8}[\delta(\omega_1 - 2\pi \cdot 1.9, \omega_2 - 2\pi \cdot 0.6) + \delta(\omega_1 - 2\pi \cdot 1.7, \omega_2 - 2\pi \cdot 0.7) \\
&+ \delta(\omega_1 - 2\pi \cdot 1.5, \omega_2 - 2\pi \cdot 0.8) + \delta(\omega_1 - 2\pi \cdot 1.3, \omega_2 - 2\pi \cdot 0.9) \\
&+ \delta(\omega_1 - 2\pi \cdot 1.1, \omega_2 - 2\pi \cdot 1.0)] \qquad\qquad \text{for } \omega_2 \geq \omega_1 \geq 0
\end{aligned}
\tag{4.43}
$$

The associated squared bicoherence has identical values of $\sqrt{0.5}$ at frequency-pairs, $(2\pi \cdot 1.9, 2\pi \cdot 0.6)$, $(2\pi \cdot 1.7, 2\pi \cdot 0.7)$, $(2\pi \cdot 1.5, 2\pi \cdot 0.8)$, $(2\pi \cdot 1.3, 2\pi \cdot 0.9)$, and $(2\pi \cdot$

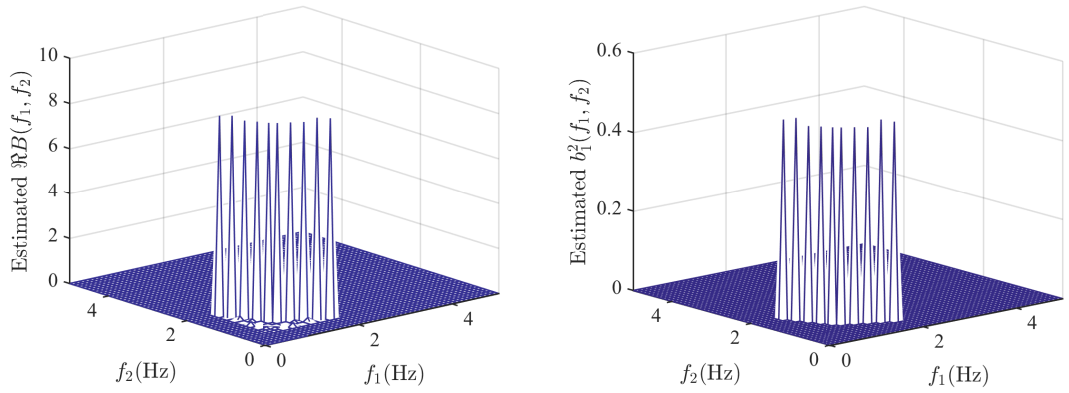

(a) **(b)**

Figure 4.11: Estimated (a) real bispectrum, $\Re B$, and (b) squared bicoherence, b_1^2.

$1.1, 2\pi \cdot 1.0)$. Therefore, we can generate the process as

$$\begin{aligned} f(t) = &\cos(2\pi \cdot 0.6t - \theta_1) + \cos(2\pi \cdot 1.9t - \theta_2) + \cos(2\pi \cdot 2.5t - \theta_3) \\ &+ \cos(2\pi \cdot 0.7t - \theta_4) + \cos(2\pi \cdot 1.7t - \theta_5) + \cos(2\pi \cdot 2.4t - \theta_6) \\ &+ \cos(2\pi \cdot 0.8t - \theta_7) + \cos(2\pi \cdot 1.5t - \theta_8) + \cos(2\pi \cdot 2.3t - \theta_9) \\ &+ \cos(2\pi \cdot 0.9t - \theta_{10}) + \cos(2\pi \cdot 1.3t - \theta_{11}) + \cos(2\pi \cdot 2.2t - \theta_{12}) \\ &+ \cos(2\pi \cdot 1.0t - \theta_{13}) + \cos(2\pi \cdot 1.1t - \theta_{14}) + \cos(2\pi \cdot 2.1t - \theta_{15}) \end{aligned} \tag{4.44}$$

with $\theta_{i+2} - (\theta_i + \theta_{i+1}) \sim WC(0, \sqrt{0.5})$ for $i \in \{1, 4, 7, 10, 13\}$. In this case, every frequency in the expansion is distinct; there are no over-constrained phases (first limited case) and there are no nested phase coupling (second limited case). We can generate quadratic phase coupling at the target pairs. Given 50,000 realizations of Eq. (4.44), the process has estimated bispectrum and squared bicoherence depicted in Figure 4.11 and one realization is shown in Figure 4.12. Finally, the estimated

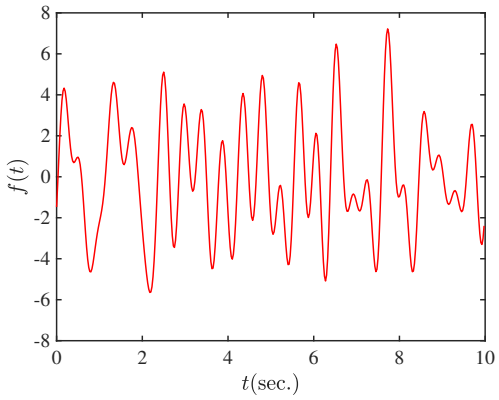

Figure 4.12: Representative sample function of several quadratic phase couplings.

variance and skewness of the realizations are compared with their target values in Table 5.2 showing very good agreement.

$f(t)$	Target	Estimated
Variance	$15/2$	7.500
Skewness	$1/\sqrt{15}$	0.2582

Table 4.6: Target and estimated moments of a stochastic process with five distinct quadratic phase coupling.

4.5 Conclusion

A new approach to identify and generate higher-order stochastic processes with circular phase angle difference distribution is introduced. The first trigonometric of the circular distribution defines the higher-order spectra including bispectrum and trispectrum, and the connection is derived by orthogonal conditions of Cramér representation. Here are numerical generation example for the discrete frequencies. As a future work, the realization of continuous higher-order spectra should be researched

to construct stochastic processes representation.

Chapter 5

Applications in nonlinear structural dynamics

The objective of this chapter is to study the effects of higher-order stochastic excitation on the response of nonlinear structures and compare the results with the response observed from existing second-order methods (SRM and ITAM). Two type of nonlinear properties are considered in this chapter; material and geometric nonlinearities. First, a simple elastic-plastic structure with steel rod is subjected to wind pressure. I generate 10,000 wind pressure time histories using the ITAM and BSRM based on the characterization of wind pressures from wind tunnel test data. Significant differences in the inelastic response are observed, and a connection is made between these differences and the higher-order properties of the wind pressure process. Secondly, the aerodynamic simulation of a long-span bridge with coupled self-excited

and buffeting forces are considered with 5,000 wind fluctuation time histories using SRM, ITAM, and BSRM. The geometric nonlinearity of aerodynamic forces cause extraordinary results on the simulation. Statistical properties and higher-order properties of the aerodynamic forces and displacement are examined.

5.1 Dynamics of a hanging billboard subject to extreme wind loads

In this section, I utilize data from wind tunnel tests conducted at Tokyo Polytechnic University [73] to characterize a wind pressure stochastic process and represent this process using both the ITAM and BSRM. The resulting simulations from both methods are then applied to a nonlinear single degree of freedom structure, and some observations on the structural performance are made. Extensive wind tunnel tests have been conducted at Tokyo Polytechnic University to study wind flow around structures of various type. Among the structures were 22 different high-rise building models with 1/400 length scale, 1/3 velocity scale, and temporal scale 3/400. I extracted wind pressures coefficient histories, from one structure with the ratio of breadth, depth, and height as 0.1m: 0.1m: 0.5m, exposure factor is 1/4, and 0 degree angle of wind at one of the 443 measurement locations. Statistics of the wind pressure histories are plotted in Figure 5.1. Among the wind pressures, One of the history is choosen from a measurement which located near the center-bottom of the windward

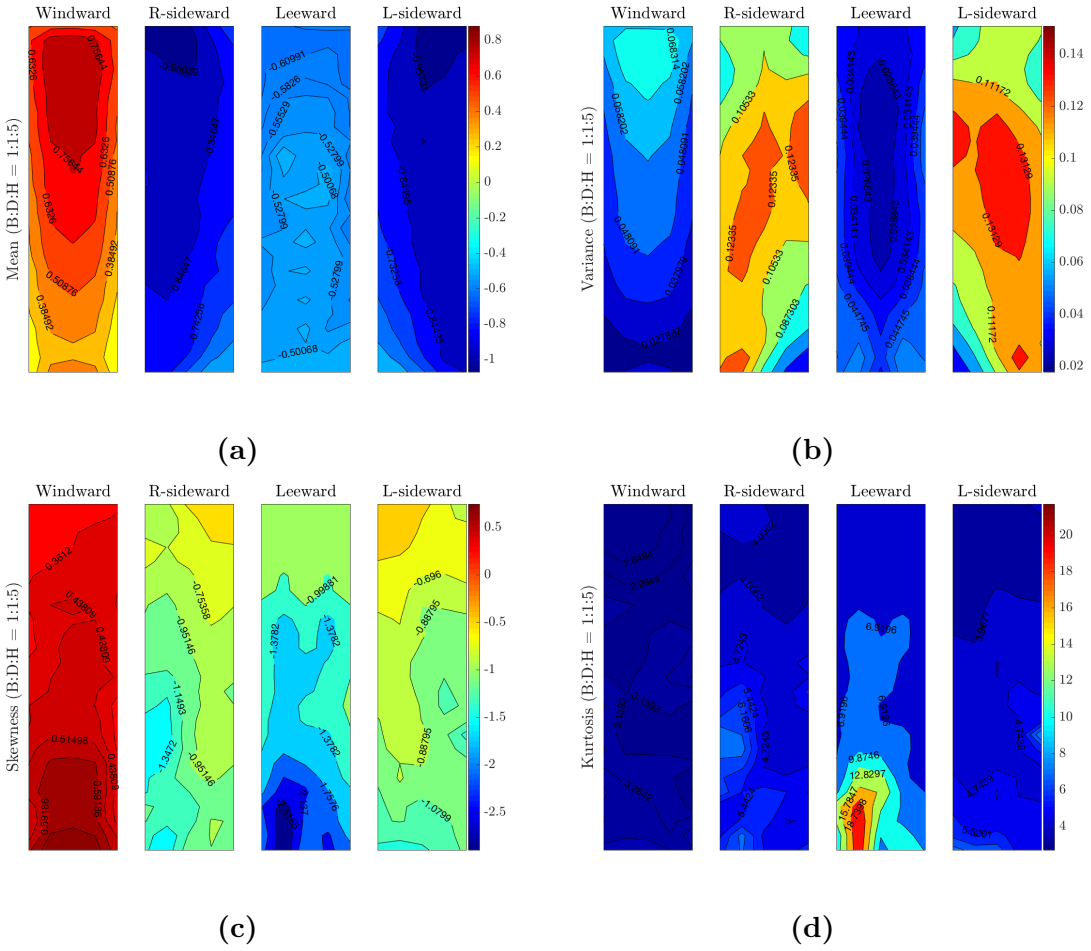

Figure 5.1: Statistics of wind pressure; (a) mean, (b) variance, (c) skewness, and (d) kurtosis.

surface, and is shown in Figure 5.2. This location is selected because it represents a possible location for a sign structure with the highest skewness of wind pressure. The duration of the time history of the data is 15 sec. with time step 0.001 sec.

After characterizing the process from the time history data (i.e. estimating the power spectrum, bispectrum, and marginal PDF), the ITAM and BSRM are utilized to generated 10,000 samples of the wind pressure process. For the ITAM, a lognormal

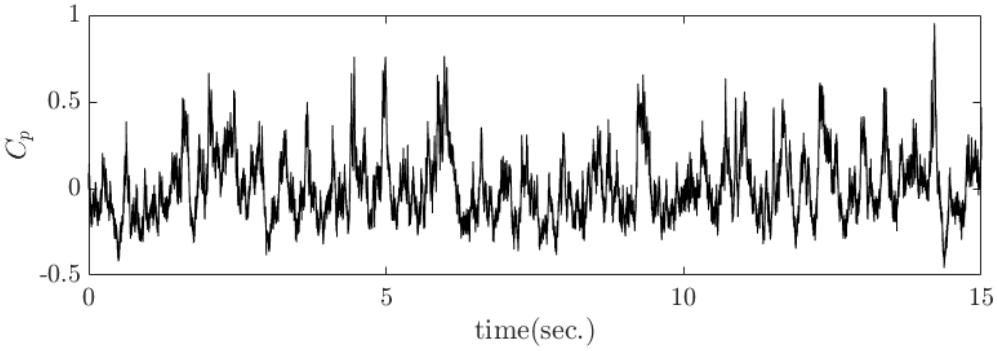

Figure 5.2: Time history of zero mean wind pressure located at the center-bottorm of the windward surface.

distribution given as

$$f(x) = \frac{1}{\sqrt{2\pi\sigma_N^2}(x-\bar{\mu})} \exp\Big[-\frac{(\log(x-\bar{\mu})-\mu_N)^2}{2\sigma_N^2}\Big]; x \geq \bar{\mu} \tag{5.1}$$

is selected to represent the marginal PDF of the zero-mean wind pressure coefficient histories. The parameters are estimated from the data as $\sigma_N = 0.2011$, $\mu_N = -0.1228$ with $\bar{\mu} = -0.9025$. The quantities are scaled with the temporal scale to model real wind conditions such that the duration of the generated samples is 2000 sec.

Samples of the zero-mean wind pressure coefficient histories generated using the ITAM and BSRM with identical phase angles are plotted in Figure 5.3. The empirical PDFs of the zero-mean wind pressure coefficient from the data, ITAM simulations, and BSRM simulations are shown in Figure 5.4. The statistics of the data, ITAM simulations and SRM simulations are given in Table 5.1. All of the PDF have similar skewness although there are noticeable differences in the tails. The ITAM and BSRM have similar upper tails but these tails are heavier than the data suggests they should

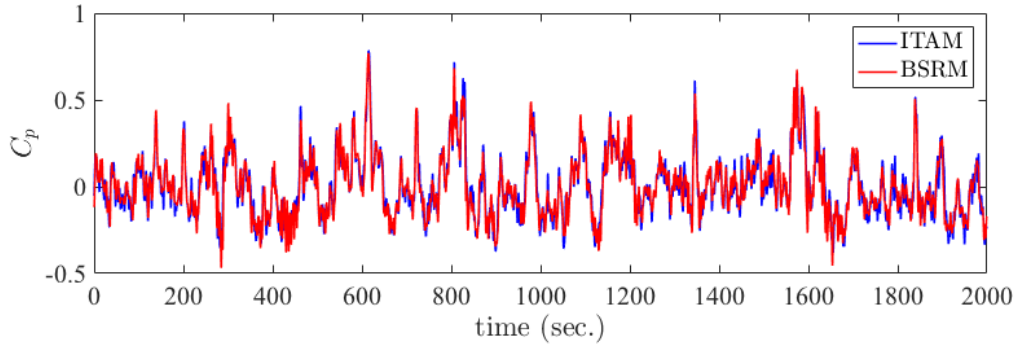

Figure 5.3: Zero mean wind pressure coefficient histories of ITAM simulations and BSRM simulations.

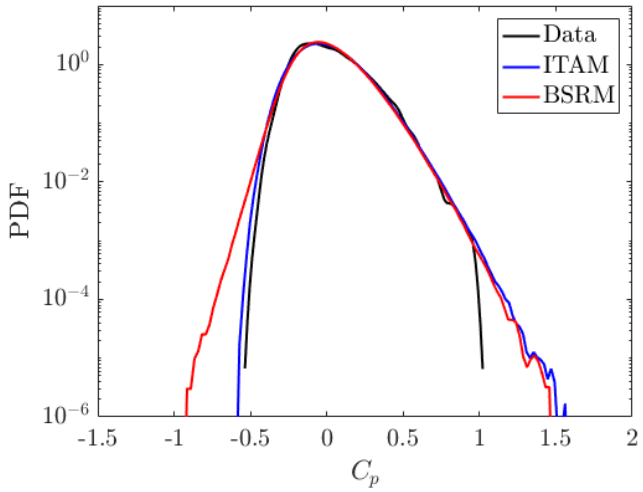

Figure 5.4: Empirical probability densities of the zero mean wind pressure coefficient of wind tunnel test data, IITAM simulations and BSRM simulations.

be. For the ITAM, this implies that the lognormal model is not a perfect fit. For the BSRM, this implies that higher than 3rd-order properties may be necessary for accurate characterization such that, for example, the process can match kurtosis and other traits that describe the tails. In the lower tail, the ITAM provides a better fit than the BSRM. This is expected to be less important though because yielding of the structure will predominantly result from high pressure events occurring in

Method	Standard dev.	Skewness	Kurtosis
Data	0.1834	0.6268	3.464
ITAM	0.1841	0.6142	3.653
BSRM	0.1792	0.6171	3.796

Table 5.1: Statistics of the zero mean wind pressure coefficient histories from wind tunnel test data, ITAM simulations and BSRM simulations.

the upper tail. Nonetheless, this mismatch may influence the dynamics by creating unexpectedly small pressures (or even suction pressures) that are not consistent with the data.

The estimated power spectra from the wind pressure data and the ITAM and BSRM simulations are shown in Figure 5.5. The BSRM simulations match the power spectrum of the wind pressure data with very high accuracy. Meanwhile, the ITAM shows a slight increase in power in the low-frequency range as a result of translation process incompatibility [22].

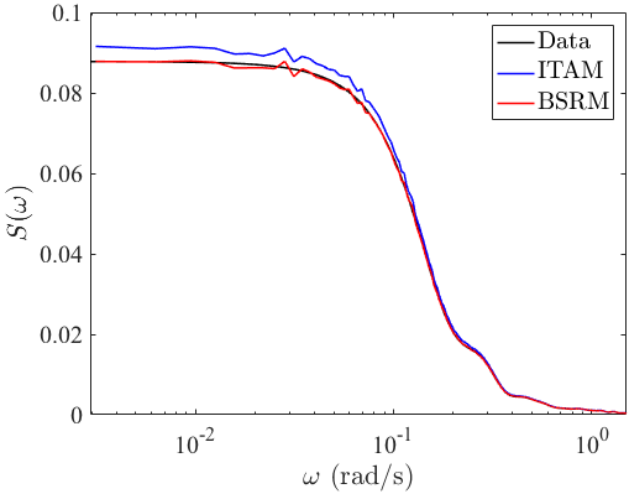

Figure 5.5: Power spectra of the zero mean wind pressure coefficient from wind tunnel test data, ITAM simulations and BSRM simulations.

Lastly, the bispectra of the wind pressure coefficient histories from the data, ITAM, and BSRM are estimated and compared. The complex bispectrum of the wind tunnel test data is dominated by the real part because there is no skewness at derivatives of the time histories, and the magnitude of bispectrum is shown in Figure 5.5. Like the power spectrum, the amplitude in the low frequency range is much higher than at higher frequency meaning there are significant interactions between low frequency waves.

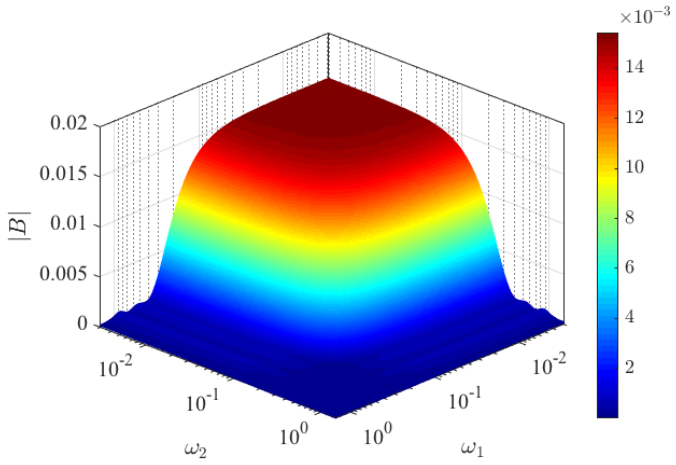

Figure 5.6: Amplitude of the wind pressure coefficient bispectrum from wind tunnel test data.

Figure 5.7 shows a comparison between the amplitude bispectrum estimates from the data and the ITAM and BSRM simulations at three different frequencies. Here, I see noticeable discrepancies between the BSRM and ITAM. The BSRM simulations show a good match with the data. The ITAM, on the other hand, shows increased amplitude in the bispectrum at low frequencies and decreased amplitude at high frequencies. Note that the ITAM is not expected to match the bispectrum. This

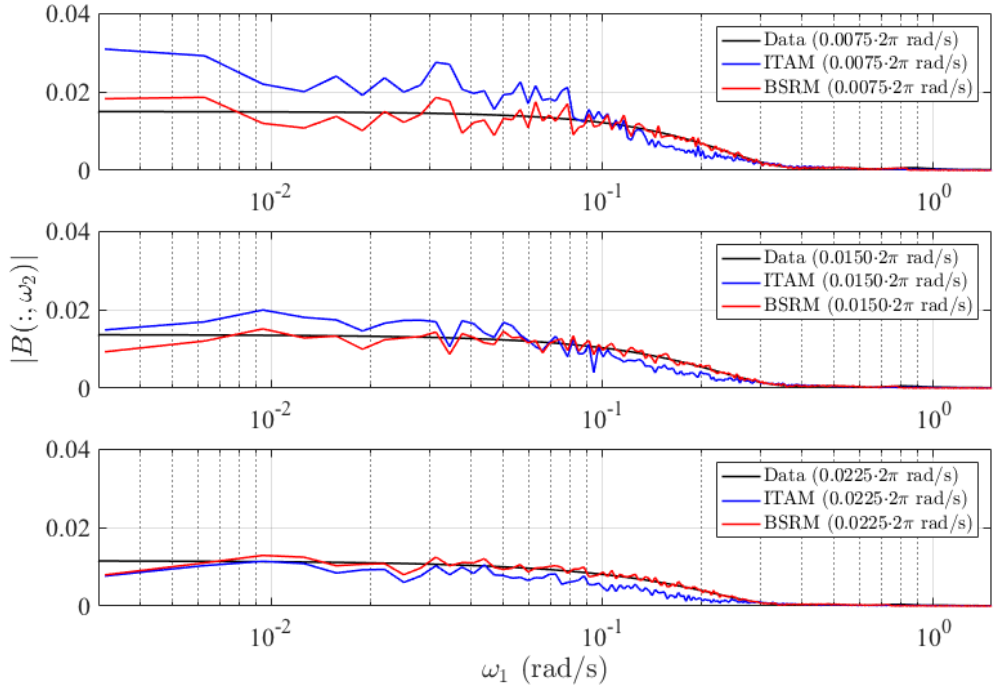

Figure 5.7: Comparison of estimated amplitude Bispectra for the zero mean wind tunnel test data, ITAM simulations, and BSRM simulations at $\omega_2 = 0.0075 \cdot 2\pi$, $\omega_2 = 0.0150 \cdot 2\pi$, and $\omega_1 = 0.0225 \cdot 2\pi$.

implies that the ITAM simulations have stronger 3-point correlations than the data and the BSRM simulations at low frequencies and weaker 3-point correlations at high frequencies.

The peak pressure of the wind histories with the different simulations are compared in Figure 5.8. Similar to the result of the proability distributions (Figure 5.4), the maximum pressure of the ITAM is higher than the BSRM, even they possess similar skewness. The result shows that approaches by matching only the skewness of the stochastic processes can not explain the details of the processes including the extreme values. The effect of the differences in the peak pressure affect the displacements

consequently, and the outcomes of the structural dynamics are will be considered in the next subsection.

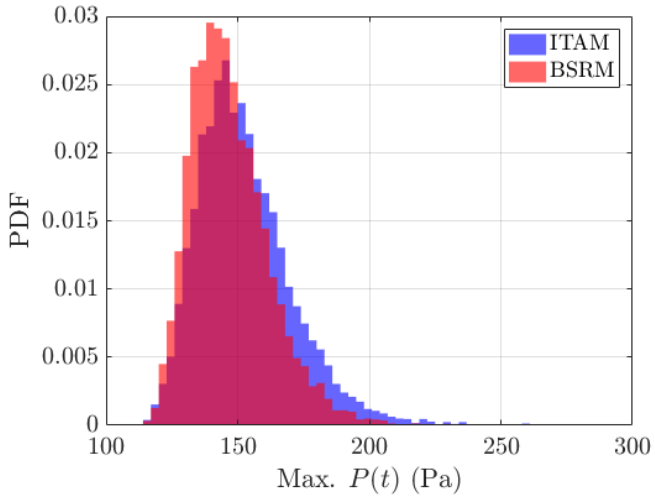

Figure 5.8: Peak pressure of ITAM and BSRM simulations.

5.1.1 Stochastic wind-structure dynamic simulation

In this section, the wind pressures generated using ITAM and BSRM are applied to a simple nonlinear structure. The time-varying wind force on the structure is calculated as

$$f_p(t) = \frac{1}{2}\rho[C_p(t) + \bar{C}_p]A_p\bar{U}^2 \tag{5.2}$$

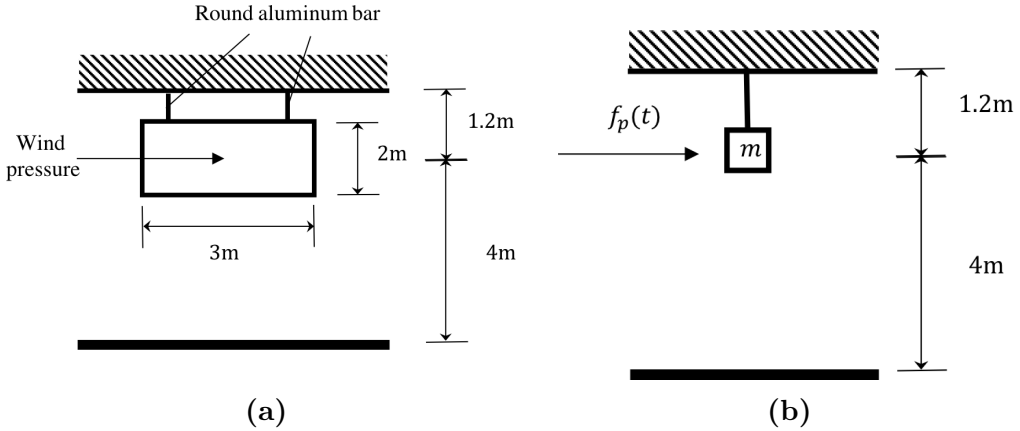

Figure 5.9: (a) Hanging billboard supported by aluminum bars under wind load and (b) its idealized lumped mass structure.

where $\rho = 1.23\text{kg/m}^3$ is the density of air, $C_p(t)$ is the simulated zero-mean wind pressure coefficient history, $\bar{C}_p = 0.44$ is the mean pressure coefficient from wind tunnel test data, A_p is the surface area perpendicular to the direction of the wind, and $\bar{U} = 14.04\text{m/sec}$ is the average wind speed at height 4m.

I consider a hanging billboard supported by aluminum rods as shown in Figure 5.9a which is idealized by a lumped mass structure in Figure 5.9b with mass $m = 1000kg$. The length of the aluminum bars is $L = 1.2m$, the diameter of circular aluminum bar is $d = 2.8cm$, and the tributary surface area for load in each rod is $A_p = 3m^2$.

The rods are Aluminum 6061-T6 and modeled as elastic perfectly-plastic with yield stress $\sigma_y = 240MPa$ and elastic modulus $E = 69GPa$ resulting in an elastic stiffness for the SDOF structure of $k = 7312N/m$. The damping ratio is $\xi = 0.02$.

I are specifically interested in studying the differences in the nonlinear (yielding) response of the structure between the ITAM and BSRM simulations. To do this,

I subjected the structure to the 10,000 generated wind pressures (as defined above) and observed the behavior of the process immediately before and during each yielding event. Specifically, I observe the peak pressure that results in the yielding event and the associated impulse defined as:

$$I = \int_{t_d} P(t)dt \tag{5.3}$$

where t_d is time window between the mean upcrossing prior to yield and the yield event. The peak pressure is the maximum wind pressure in the time window t_d.

From these simulations, it was observed that structure yielded 5062 times from the 10,000 ITAM simulation and 2187 times from the 10,000 BSRM simulations. Why, when the wind pressure processes possess nominally the same variance and skewness and have almost identical upper tails (Figure 5.4), do they yield such drastically different response with the ITAM causing the structure to yield more than twice as often as the BSRM? It appears that this can be explained by the amplification of the bispectrum by the ITAM illustrated in Figure 5.5.

Consider this from the perspective of the peak pressure and impulse. Figure 5.10 shows the joint probability distribution of the peak pressure and impulse for the yielding events from both ITAM and BSRM. Notice that the spread in peak pressure is similar between the two methods (the ITAM has slightly larger spread in peak pressure). The ITAM, however, has a much larger spread in terms of impulse

with much more frequent high impulse events. This means that, while the histories from both methods yield comparable pressures, there is more energy being delivered by the ITAM histories. In other words, the ITAM model produces wind gusts that have a longer duration of sustained high pressure. This added energy, I believe, is a direct result of the strong 3-point correlation (amplified bispectrum) in the ITAM simulations.

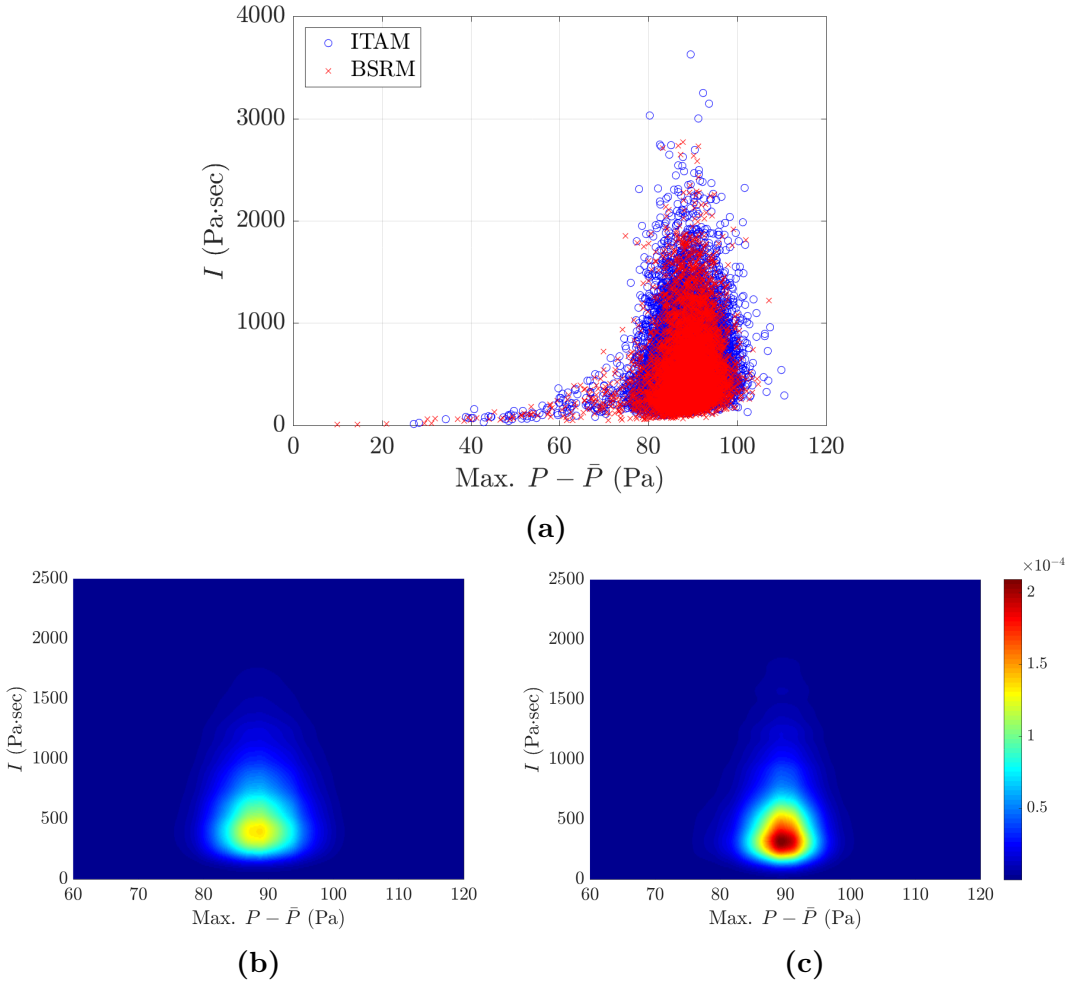

Figure 5.10: (a) Peak pressure-impulse diagram of ITAM and BSRM and estimated probability density of (b) ITAM and (c) BSRM.

The number of yieldings of the aluminum bars between the simulations are compared in Figure 5.11a. We can see that ITAM simulations have the greater number of yielding than the BSRM. Because of the stronger positive tail of the ITAM simulations, it causes the yielding more than the result of the BSRM. Figure 5.11b shows the maximum values of displacement have similar trend compare to the number of the yielding; the more yielding in the ITAM simulations causes the stronger tail in the displacements.

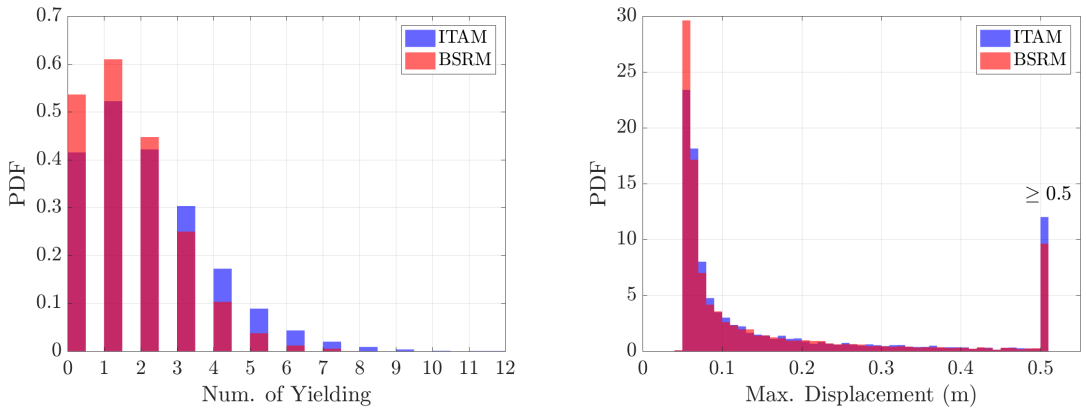

Figure 5.11: (a) Number of yielding and (b) Peak displacements of ITAM and BSRM simulations.

The distributions of the temporal displacements are considered in Figure 5.12. After the transient period of the displacements, we can see the divergence of the difference between the distributions of the displacements as time passed. Specially, the distribution between the displacement at 500 second has not distinct, but the tails of the displacement of the ITAM simulations are growing faster than the BSRM.

This result highlights the potential importance of matching higher-order properties

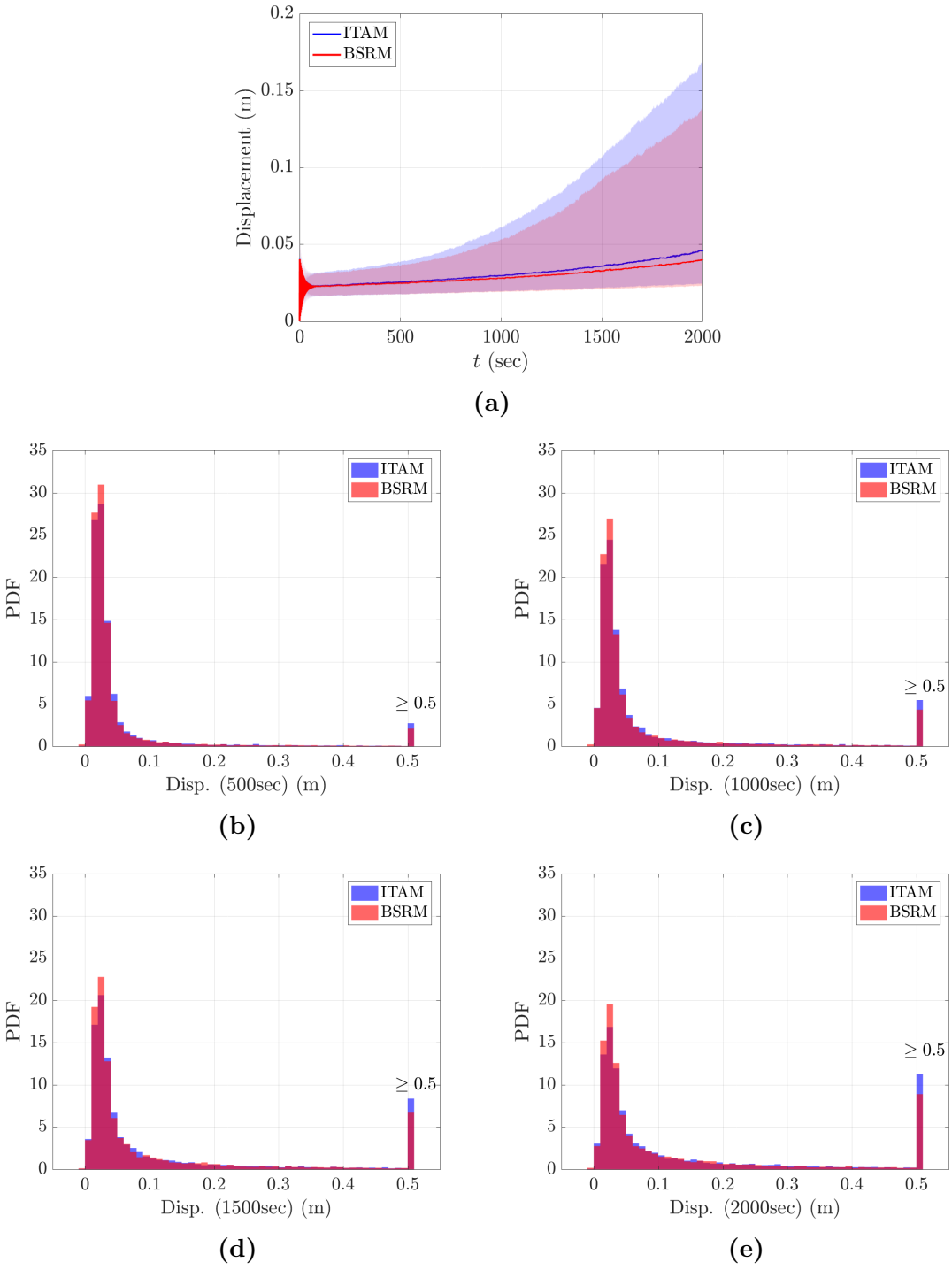

Figure 5.12: (a) Median, 25th percentile and 75th percentile of displacement and displacements at time (a) 500sec, (b) 1000sec, (c) 1500sec, (d) 2000sec.

in the excitation for non-linear structures subject to stochastic dynamic excitation. While not conclusive at this point, it seems to indicate that higher-order spectra can greatly influence the structural response. Moreover, additional studies are necessary to provide a more realistic link to test data. In both models, simplifying assumptions are made that cause discrepancies between the simulations and the test data so I cannot currently assess which model is a better representation of the true pressures. It is nevertheless important to observe how seemingly small changes in the representation of a stochastic process can have major consequences on the structural response emphasizing the importance of identifying and utilizing the best possible modeling practices and recognizing the potential limitations of those models.

5.2 Buffeting response analysis of a bridge deck

In this subsection, the time domain analysis of coupled self-excited forces and unsteady characteristics of buffeting forces [74] in the aerodynamic simulation are examined with non-Gaussian wind fluctuations simulated with the SRM, ITAM, and BSRM. The time domain analysis is more appropriate to analyze the effect of non-linear interactions between wind and structures. [75, 76, 77] Frequency-dependent unsteady aerodynamic forces and nonlinear interactions of aerodynamic and forces are utilized to estimate the response of the system. The governing equations of the

simulation at the static equilibrium position are given excluding the the static aerodynamic forces as

$$\mathbf{M}\ddot{\mathbf{Z}}(t) + \mathbf{C}\mathbf{Z}(t) + \mathbf{K}\mathbf{Z}(t) = \mathbf{F_{se}}(t) + \mathbf{F_b}(t) \tag{5.4}$$

where $\mathbf{M}$, $\mathbf{C}$, and $\mathbf{K}$ are mass, damping, and stiffness matrices, $\mathbf{Z}(t)$ is displacement vector with vertical, lateral and torsional components as $[h(t), p(t), \alpha(t)]^T$, $\mathbf{F_{se}}$ and $\mathbf{F_b}$ indicates self-excited force vector and buffeting force vector with lift, drag, and pitching moment as $[L_{se}, D_{se}, M_{se}]^T$ and $[L_b, D_b, M_b]^T$, respectively. Figure 5.13 indicates the prescribed aerodynamic forces, the displacements, and wind which U is mean wind velocity, and $u(t)$ and $v(t)$ are lateral and vertical components of wind fluctuations on the bridge dec.

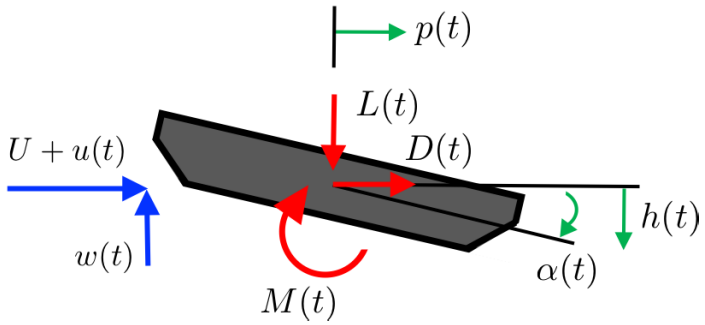

Figure 5.13: Configuration of aerodynamic displacements and wind fluctuations on bridge section.

5.2.1 Self-excited and buffeting forces

For harmonic motion, the aerodynamic self-excited forces per unit span are described with flutter derivatives [78], parameters to define the motion-induced aerodynamic forces in the theoretical model and identified by means of wind tunnel test, as [79]

$$\begin{aligned}
L_{se}(t) &= \frac{1}{2}\rho U^2(2b)\Big(kH_1^*\frac{\dot{h}}{U} + kH_2^*\frac{b\dot{\alpha}}{U} + k^2H_3^*\alpha + k^2H_4^*\frac{h}{b} + kH_5^*\frac{\dot{p}}{U} + k^2H_6^*\frac{p}{b}\Big) \\
D_{se}(t) &= \frac{1}{2}\rho U^2(2b)\Big(kP_1^*\frac{\dot{p}}{U} + kP_2^*\frac{b\dot{\alpha}}{U} + k^2P_3^*\alpha + k^2P_4^*\frac{p}{b} + kP_5^*\frac{\dot{h}}{U} + k^2P_6^*\frac{h}{b}\Big) \\
M_{se}(t) &= \frac{1}{2}\rho U^2(2b^2)\Big(kA_1^*\frac{\dot{h}}{U} + kA_2^*\frac{b\dot{\alpha}}{U} + k^2A_3^*\alpha + k^2A_4^*\frac{h}{b} + kA_5^*\frac{\dot{p}}{U} + k^2A_6^*\frac{p}{b}\Big)
\end{aligned} \tag{5.5}$$

where ρ is the air density, U is the mean wind velocity, $k = \omega b/U$ is the reduced frequency, $B = 2b$ is width of the bridge deck, ω is the circular frequency of vibration, H_i^*, P_i^*, and A_i^* ,$i \in \{1, \cdots, 6\}$ are flutter derivatives, independent from frequency. h, p, and α are vertical, lateral, horizontal components of the displacement.

For arbitrary structural displacements, the three components of self-excited forces, $F_{se}(t)$, per unit span can be presented regarding convolution integrals as [80]

$$\begin{aligned}
L_{se}(t) &= \frac{1}{2}\rho U^2\int_{-\infty}^{t}\big(I_{L_{seh}}(t-\tau)h(\tau) + I_{L_{sep}}(t-\tau)p(\tau) + I_{L_{se\alpha}}\alpha(\tau)\big)d\tau \\
D_{se}(t) &= \frac{1}{2}\rho U^2\int_{-\infty}^{t}\big(I_{D_{seh}}(t-\tau)h(\tau) + I_{D_{sep}}(t-\tau)p(\tau) + I_{D_{se\alpha}}\alpha(\tau)\big)d\tau \\
M_{se}(t) &= \frac{1}{2}\rho U^2\int_{-\infty}^{t}\big(I_{M_{seh}}(t-\tau)h(\tau) + I_{M_{sep}}(t-\tau)p(\tau) + I_{M_{se\alpha}}\alpha(\tau)\big)d\tau
\end{aligned} \tag{5.6}$$

where I is the impulse function of the self-excited force, F_{se}. Aerodynamic transfer

functions between the aerodynamic impulse function and the flutter derivatives are given by the Fourier transform of Eq. (5.6) and the corresponding terms in Eq. (5.5) as [80, 81]

$$\begin{aligned}
\bar{I}_{L_{se,h}} &= 2k^2(H_4^* + iH_1^*) \\
\bar{I}_{L_{se,p}} &= 2k^2(H_6^* + iH_5^*) \\
\bar{I}_{L_{se,\alpha}} &= 2k^2b(H_3^* + iH_2^*) \\
\bar{I}_{D_{se,h}} &= 2k^2(P_6^* + iP_5^*) \\
\bar{I}_{D_{se,p}} &= 2k^2(P_4^* + iH_1^*) \\
\bar{I}_{D_{se,\alpha}} &= 2k^2b(P_3^* + iP_2^*) \\
\bar{I}_{M_{se,h}} &= 2k^2b(A_4^* + iA_1^*) \\
\bar{I}_{M_{se,p}} &= 2k^2b(A_6^* + iA_5^*) \\
\bar{I}_{L_{se,\alpha}} &= 2k^2b^2(A_3^* + iA_2^*)
\end{aligned} \tag{5.7}$$

where the overbar denotes the Fourier transform and i means imaginary unit. Again, $k = \omega b/U$ is the reduced frequency, and b is the half of bridge deck width. In the frequency domain, the self-excited forces can be represented as a product of the transfer function, Eq. (5.7), and the corresponding displacements.

As time domain analysis of aerodynamic forces, the continuous functions of aerodynamic impulse are required. However, the flutter derivatives are estimated as discrete values of the reduced frequency, k, with limited geometric configurations of

deck in the wind tunnel tests. Therefore, the rational function approximation can estimates the continuous form of the flutter derivates for the self-excited forces [82]. Corresponding to the lift, drag, and pitching moment induced by each component of displacements, continuous approximations of the aerodynamic transfer function are calculated as

$$
\begin{aligned}
\bar{I}_{L_{se,h}}(i\omega) &= A_{Lh,1} + A_{Lh,2}\cdot\frac{i\omega b}{U} + A_{Lh,3}\cdot\left(\frac{i\omega b}{U}\right)^2 + \sum_{l=1}^{m}\frac{A_{Lh,l+3}\cdot i\omega}{i\omega+\frac{d_l U}{b}}\\
\bar{I}_{L_{se,p}}(i\omega) &= A_{Lp,1} + A_{Lp,2}\cdot\frac{i\omega b}{U} + A_{Lp,3}\cdot\left(\frac{i\omega b}{U}\right)^2 + \sum_{l=1}^{m}\frac{A_{Lp,l+3}\cdot i\omega}{i\omega+\frac{d_l U}{b}}\\
\bar{I}_{L_{se,\alpha}}(i\omega) &= A_{L\alpha,1} + A_{L\alpha,2}\cdot\frac{i\omega b}{U} + A_{L\alpha,3}\cdot\left(\frac{i\omega b}{U}\right)^2 + \sum_{l=1}^{m}\frac{A_{L\alpha,l+3}\cdot i\omega}{i\omega+\frac{d_l U}{b}}\\
\bar{I}_{D_{se,h}}(i\omega) &= A_{Dh,1} + A_{Dh,2}\cdot\frac{i\omega b}{U} + A_{Dh,3}\cdot\left(\frac{i\omega b}{U}\right)^2 + \sum_{l=1}^{m}\frac{A_{Dh,l+3}\cdot i\omega}{i\omega+\frac{d_l U}{b}}\\
\bar{I}_{D_{se,p}}(i\omega) &= A_{Dp,1} + A_{Dp,2}\cdot\frac{i\omega b}{U} + A_{Dp,3}\cdot\left(\frac{i\omega b}{U}\right)^2 + \sum_{l=1}^{m}\frac{A_{Dp,l+3}\cdot i\omega}{i\omega+\frac{d_l U}{b}}\\
\bar{I}_{D_{se,\alpha}}(i\omega) &= A_{D\alpha,1} + A_{D\alpha,2}\cdot\frac{i\omega b}{U} + A_{D\alpha,3}\cdot\left(\frac{i\omega b}{U}\right)^2 + \sum_{l=1}^{m}\frac{A_{D\alpha,l+3}\cdot i\omega}{i\omega+\frac{d_l U}{b}}\\
\bar{I}_{M_{se,h}}(i\omega) &= A_{Mh,1} + A_{Mh,2}\cdot\frac{i\omega b}{U} + A_{Mh,3}\cdot\left(\frac{i\omega b}{U}\right)^2 + \sum_{l=1}^{m}\frac{A_{Mh,l+3}\cdot i\omega}{i\omega+\frac{d_l U}{b}}\\
\bar{I}_{M_{se,p}}(i\omega) &= A_{Mp,1} + A_{Mp,2}\cdot\frac{i\omega b}{U} + A_{Mp,3}\cdot\left(\frac{i\omega b}{U}\right)^2 + \sum_{l=1}^{m}\frac{A_{Mp,l+3}\cdot i\omega}{i\omega+\frac{d_l U}{b}}\\
\bar{I}_{L_{se,\alpha}}(i\omega) &= A_{M\alpha,1} + A_{M\alpha,2}\cdot\frac{i\omega b}{U} + A_{M\alpha,3}\cdot\left(\frac{i\omega b}{U}\right)^2 + \sum_{l=1}^{m}\frac{A_{M\alpha,l+3}\cdot i\omega}{i\omega+\frac{d_l U}{b}}
\end{aligned}
\tag{5.8}
$$

with frequency independent coefficients, $A_{(\cdot),1}$, $A_{(\cdot),2}$, $A_{(\cdot),3}$, $A_{(\cdot),l+3}$, and $d_l(\geq 0)$.

The preceding rational function representation of the aerodynamic transfer func-

tions can be extended into the Laplace domain, and the inverse Laplace transform yields the aerodynamic impulse function as

$$
\begin{aligned}
I_{L_{se,h}}(t) &= A_{Lh,1}\delta(t) + A_{Lh,2}\frac{b}{U}\dot{\delta}(t) + A_{Lh,3}\frac{b^2}{U^2}\ddot{\delta}(t) + \sum_{l=1}^{m}\int_{-\infty}^{t} A_{Lh,l+3}\cdot e^{\left(-\frac{d_l U}{b}(t-\tau)\dot{\delta}(\tau)\right)}d\tau \\
I_{L_{se,p}}(t) &= A_{Lp,1}\delta(t) + A_{Lp,2}\frac{b}{U}\dot{\delta}(t) + A_{Lp,3}\frac{b^2}{U^2}\ddot{\delta}(t) + \sum_{l=1}^{m}\int_{-\infty}^{t} A_{Lp,l+3}\cdot e^{\left(-\frac{d_l U}{b}(t-\tau)\dot{\delta}(\tau)\right)}d\tau \\
I_{L_{se,\alpha}}(t) &= A_{L\alpha,1}\delta(t) + A_{L\alpha,2}\frac{b}{U}\dot{\delta}(t) + A_{L\alpha,3}\frac{b^2}{U^2}\ddot{\delta}(t) + \sum_{l=1}^{m}\int_{-\infty}^{t} A_{L\alpha,l+3}\cdot e^{\left(-\frac{d_l U}{b}(t-\tau)\dot{\delta}(\tau)\right)}d\tau \\
I_{D_{se,h}}(t) &= A_{Dh,1}\delta(t) + A_{Dh,2}\frac{b}{U}\dot{\delta}(t) + A_{Dh,3}\frac{b^2}{U^2}\ddot{\delta}(t) + \sum_{l=1}^{m}\int_{-\infty}^{t} A_{Dh,l+3}\cdot e^{\left(-\frac{d_l U}{b}(t-\tau)\dot{\delta}(\tau)\right)}d\tau \\
I_{D_{se,p}}(t) &= A_{Dp,1}\delta(t) + A_{Dp,2}\frac{b}{U}\dot{\delta}(t) + A_{Dp,3}\frac{b^2}{U^2}\ddot{\delta}(t) + \sum_{l=1}^{m}\int_{-\infty}^{t} A_{Dp,l+3}\cdot e^{\left(-\frac{d_l U}{b}(t-\tau)\dot{\delta}(\tau)\right)}d\tau \\
I_{D_{se,\alpha}}(t) &= A_{D\alpha,1}\delta(t) + A_{D\alpha,2}\frac{b}{U}\dot{\delta}(t) + A_{D\alpha,3}\frac{b^2}{U^2}\ddot{\delta}(t) + \sum_{l=1}^{m}\int_{-\infty}^{t} A_{D\alpha,l+3}\cdot e^{\left(-\frac{d_l U}{b}(t-\tau)\dot{\delta}(\tau)\right)}d\tau \\
I_{M_{se,h}}(t) &= A_{Mh,1}\delta(t) + A_{Mh,2}\frac{b}{U}\dot{\delta}(t) + A_{Mh,3}\frac{b^2}{U^2}\ddot{\delta}(t) + \sum_{l=1}^{m}\int_{-\infty}^{t} A_{h,l+3}\cdot e^{\left(-\frac{d_l U}{b}(t-\tau)\dot{\delta}(\tau)\right)}d\tau \\
I_{M_{se,p}}(t) &= A_{Mp,1}\delta(t) + A_{Mp,2}\frac{b}{U}\dot{\delta}(t) + A_{Mp,3}\frac{b^2}{U^2}\ddot{\delta}(t) + \sum_{l=1}^{m}\int_{-\infty}^{t} A_{Mp,l+3}\cdot e^{\left(-\frac{d_l U}{b}(t-\tau)\dot{\delta}(\tau)\right)}d\tau \\
I_{M_{se,\alpha}}(t) &= A_{M\alpha,1}\delta(t) + A_{M\alpha,2}\frac{b}{U}\dot{\delta}(t) + A_{M\alpha,3}\frac{b^2}{U^2}\ddot{\delta}(t) + \sum_{l=1}^{m}\int_{-\infty}^{t} A_{M\alpha,l+3}\cdot e^{\left(-\frac{d_l U}{b}(t-\tau)\dot{\delta}(\tau)\right)}d\tau
\end{aligned}
\tag{5.9}
$$

where $\delta(t)$ is Dirac delta functions. Thus, the self-excited forces induced by arbitrary

each component of the displacement can be expressed as

$$
\begin{aligned}
L_{se,h}(t) &= \frac{1}{2}\rho U^2\Big(A_{Lh,1}h(t) + A_{Lh,2}\frac{b}{U}\dot{h}(t) + A_{Lh,3}\frac{b^2}{U^2}\ddot{h}(t) + \sum_{l=1}^{m}\phi_{Lh,l}(t)\Big)\\
L_{se,p}(t) &= \frac{1}{2}\rho U^2\Big(A_{Lp,1}p(t) + A_{Lp,2}\frac{b}{U}\dot{p}(t) + A_{Lp,3}\frac{b^2}{U^2}\ddot{p}(t) + \sum_{l=1}^{m}\phi_{Lp,l}(t)\Big)\\
L_{se,\alpha}(t) &= \frac{1}{2}\rho U^2\Big(A_{L\alpha,1}\alpha(t) + A_{L\alpha,2}\frac{b}{U}\dot{\alpha}(t) + A_{L\alpha,3}\frac{b^2}{U^2}\ddot{\alpha}(t) + \sum_{l=1}^{m}\phi_{L\alpha,l}(t)\Big)\\
D_{se,h}(t) &= \frac{1}{2}\rho U^2\Big(A_{Dh,1}h(t) + A_{Dh,2}\frac{b}{U}\dot{h}(t) + A_{Dh,3}\frac{b^2}{U^2}\ddot{h}(t) + \sum_{l=1}^{m}\phi_{Dh,l}(t)\Big)\\
D_{se,p}(t) &= \frac{1}{2}\rho U^2\Big(A_{Dp,1}p(t) + A_{Dp,2}\frac{b}{U}\dot{p}(t) + A_{Dp,3}\frac{b^2}{U^2}\ddot{p}(t) + \sum_{l=1}^{m}\phi_{Dp,l}(t)\Big)\\
D_{se,\alpha}(t) &= \frac{1}{2}\rho U^2\Big(A_{D\alpha,1}\alpha(t) + A_{D\alpha,2}\frac{b}{U}\dot{\alpha}(t) + A_{D\alpha,3}\frac{b^2}{U^2}\ddot{\alpha}(t) + \sum_{l=1}^{m}\phi_{D\alpha,l}(t)\Big)\\
M_{se,h}(t) &= \frac{1}{2}\rho U^2\Big(A_{Mh,1}h(t) + A_{Mh,2}\frac{b}{U}\dot{h}(t) + A_{Mh,3}\frac{b^2}{U^2}\ddot{h}(t) + \sum_{l=1}^{m}\phi_{Mh,l}(t)\Big)\\
M_{se,p}(t) &= \frac{1}{2}\rho U^2\Big(A_{Mp,1}p(t) + A_{Mp,2}\frac{b}{U}\dot{p}(t) + A_{Mp,3}\frac{b^2}{U^2}\ddot{p}(t) + \sum_{l=1}^{m}\phi_{Mp,l}(t)\Big)\\
M_{se,\alpha}(t) &= \frac{1}{2}\rho U^2\Big(A_{M\alpha,1}\alpha(t) + A_{M\alpha,2}\frac{b}{U}\dot{\alpha}(t) + A_{M\alpha,3}\frac{b^2}{U^2}\ddot{\alpha}(t) + \sum_{l=1}^{m}\phi_{M\alpha,l}(t)\Big)
\end{aligned}
\tag{5.10}
$$

where

$$
\begin{aligned}
\dot{\phi}_{(\cdot)h,l}(t) &= -\frac{d_l U}{b}\phi_{(\cdot)h,l}(t) + A_{(\cdot)h,l+3}\dot{h}(t)\\
\dot{\phi}_{(\cdot)p,l}(t) &= -\frac{d_l U}{b}\phi_{(\cdot)p,l}(t) + A_{(\cdot)p,l+3}\dot{p}(t)\\
\dot{\phi}_{(\cdot)\alpha,l}(t) &= -\frac{d_l U}{b}\phi_{(\cdot)\alpha,l}(t) + A_{(\cdot)\alpha,l+3}\dot{\alpha}(t)
\end{aligned}
\tag{5.11}
$$

Similar to the prescribed procedure for the self-excited forces, convolutional integrals involving the aerodynamic impulse functions and fluctuating wind velocities

expresses the buffeting forces, F_b, per unit span corresponding to arbitrary wind fluctuations as [83, 74]

$$\begin{aligned} L_b(t) &= -\frac{1}{2}\rho U^2 \int_{-\infty}^{t} \big(I_{L_{bu}}(t-\tau)\frac{u(\tau)}{U} + I_{L_{bw}}(t-\tau)\frac{w(\tau)}{U}\big)d\tau \\ D_b(t) &= \frac{1}{2}\rho U^2 \int_{-\infty}^{t} \big(I_{D_{bu}}(t-\tau)\frac{u(\tau)}{U} + I_{D_{bw}}(t-\tau)\frac{w(\tau)}{U}\big)d\tau \\ M_b(t) &= \frac{1}{2}\rho U^2 \int_{-\infty}^{t} \big(I_{M_{bu}}(t-\tau)\frac{u(\tau)}{U} + I_{M_{bw}}(t-\tau)\frac{w(\tau)}{U}\big)d\tau \end{aligned} \tag{5.12}$$

where I indicates the impulse functions of buffeting forces. Similar to Eq. 5.5, The buffeting forces per unit span are commonly expressed as [84, 83, 85]

$$\begin{aligned} L_b(t) &= -\frac{1}{2}\rho U^2 (2b)\Big(2C_L\chi_{L_{bu}}\frac{u(t)}{U} + (C'_L + C_D)\chi_{L_{bw}}\frac{w(t)}{U}\Big) \\ D_b(t) &= \frac{1}{2}\rho U^2 (2b)\Big(2C_D\chi_{D_{bu}}\frac{u(t)}{U} + C'_D\chi_{D_{bw}}\frac{w(t)}{U}\Big) \\ M_b(t) &= \frac{1}{2}\rho U^2 (2b)^2\Big(2C_M\chi_{M_{bu}}\frac{u(t)}{U} + C'_M\chi_{M_{bw}}\frac{w(t)}{U}\Big) \end{aligned} \tag{5.13}$$

where $\chi_{L_{bw}}$, $\chi_{L_{bu}}$, $\chi_{D_{bw}}$, $\chi_{D_{bu}}$, $\chi_{M_{bw}}$, $\chi_{M_{bu}}$ are the transfer functions between the buffeting forces and wind fluctuations. The absolute values of the transfer functions are called as aerodynamic admittance functions.

Similar to the approach for the self-excited forces as Eq. (5.6), the aerodynamic transfer functions are related to the Fourier transform of the impulse function of the

buffeting forces as [85]

$$\begin{aligned}
\bar{I}_{L_{bu}} &= 4bC_L\chi_{L_{bu}} \\
\bar{I}_{L_{bw}} &= 2b(C'_L + C_D)\chi_{L_{bw}} \\
\bar{I}_{D_{bu}} &= 4bC_D\chi_{D_{bu}} \\
\bar{I}_{D_{bw}} &= 2bC'_D\chi_{D_{bw}} \\
\bar{I}_{L_{bu}} &= 8b^2C_M\chi_{M_{bu}} \\
\bar{I}_{L_{bw}} &= 4b^2C'_M\chi_{M_{bw}}
\end{aligned} \tag{5.14}$$

Similarly, the rational function approximation of the aerodynamic transfer functions can be shown as [74, 86]

$$\begin{aligned}
\chi_{L_{bu}} &= A_{Lbu,1} + \sum_{l=1}^{m_{Lbu}} \frac{A_{Lbu,l+1}i\omega}{i\omega + \frac{d_{Lbu,l}U}{b}} \\
\chi_{L_{bw}} &= A_{Lbw,1} + \sum_{l=1}^{m_{Lbw}} \frac{A_{Lbw,l+1}i\omega}{i\omega + \frac{d_{Lbw,l}U}{b}} \\
\chi_{D_{bu}} &= A_{Dbu,1} + \sum_{l=1}^{m_{Lbu}} \frac{A_{Dbu,l+1}i\omega}{i\omega + \frac{d_{Dbu,l}U}{b}} \\
\chi_{D_{bw}} &= A_{Dbw,1} + \sum_{l=1}^{m_{Dbw}} \frac{A_{Dbw,l+1}i\omega}{i\omega + +\frac{d_{Dbw,l}U}{b}} \\
\chi_{M_{bu}} &= A_{Mbu,1} + \sum_{l=1}^{m_{Mbu}} \frac{A_{Mbu,l+1}i\omega}{i\omega + +\frac{d_{Mbu,l}U}{b}} \\
\chi_{M_{bw}} &= A_{Mbw,1} + \sum_{l=1}^{m_{Mbw}} \frac{A_{Mbw,l+1}i\omega}{i\omega + \frac{d_{Mbw,l}U}{b}}
\end{aligned} \tag{5.15}$$

with frequency independent coefficients, $A_{(\cdot),1}$, $A_{(\cdot),2}$, $A_{(\cdot),3}$, $A_{(\cdot),l+3}$, and $d_{(\cdot),l}(\geq 0)$.

Accordingly, aerodynamic impulse functions of buffeting forces are represented by the inverse Laplace transform such as Eq. (5.20) and the buffeting forces from the impulse functions induced by each component of wind fluctuation can be given as [74]

$$
\begin{aligned}
L_{bu}(t) &= -\frac{1}{2}\rho U^2 \cdot 4bC_L\Big((A_{Lbu,1} + \sum_{l=1}^{m_{Lbu}} A_{Lbu,l+1})\frac{u(t)}{U} - \sum_{l=1}^{m_{Lbu}} \frac{d_{Lbu,l}U}{b}\phi_{Lbu,l}(t)\Big) \\
L_{bw}(t) &= -\frac{1}{2}\rho U^2 \cdot 2b(C'_L + C_D)\Big((A_{Lbw,1} + \sum_{l=1}^{m_{Lbw}} A_{Lbw,l+1})\frac{w(t)}{U} - \sum_{l=1}^{m_{Lbw}} \frac{d_{Lbw,l}U}{b}\phi_{Lbw,l}(t)\Big) \\
D_{bu}(t) &= \frac{1}{2}\rho U^2 \cdot 4bC_D\Big((A_{Dbu,1} + \sum_{l=1}^{m_{Dbu}} A_{Dbu,l+1})\frac{u(t)}{U} - \sum_{l=1}^{m_{Dbu}} \frac{d_{Dbu,l}U}{b}\phi_{Dbu,l}(t)\Big) \\
D_{bw}(t) &= \frac{1}{2}\rho U^2 \cdot 2bC'_D\Big((A_{Dbw,1} + \sum_{l=1}^{m_{Dbw}} A_{Dbw,l+1})\frac{w(t)}{U} - \sum_{l=1}^{m_{Dbw}} \frac{d_{Dbw,l}U}{b}\phi_{Dbw,l}(t)\Big) \\
M_{bu}(t) &= \frac{1}{2}\rho U^2 \cdot 8b^2C_M\Big((A_{Mbu,1} + \sum_{l=1}^{m_{Mbu}} A_{Mbu,l+1})\frac{u(t)}{U} - \sum_{l=1}^{m_{Mbu}} \frac{d_{Mbu,l}U}{b}\phi_{Mbu,l}(t)\Big) \\
M_{bw}(t) &= \frac{1}{2}\rho U^2 \cdot 4bC'_M\Big((A_{Mbw,1} + \sum_{l=1}^{m_{Mbw}} A_{Mbw,l+1})\frac{w(t)}{U} - \sum_{l=1}^{m_{Mbw}} \frac{d_{Mbw,l}U}{b}\phi_{Mbw,l}(t)\Big)
\end{aligned}
\tag{5.16}
$$

where

$$
\begin{aligned}
\dot{\phi}_{(\cdot)u,l}(t) &= -\frac{d_{(\cdot)u,l}U}{b}\phi_{(\cdot)u,l}(t) + A_{(\cdot)u,l+1}\frac{u(t)}{U} \\
\dot{\phi}_{(\cdot)w,l}(t) &= -\frac{d_{(\cdot)w,l}U}{b}\phi_{(\cdot)w,l}(t) + A_{(\cdot)w,l+1}\frac{w(t)}{U}
\end{aligned}
\tag{5.17}
$$

and $A_{w,1}$, $A_{w,l+1}$, $d_{w,l}$ are frequency independent coefficients, $\phi_{w,l}$ are additional variables.

To analyze the coupled aerodynamic forces, Aksahi-Kaikyo bridge was simplified to a section model of a bridge deck subjected to the aerodynamic forces. The

primary dimension of the bridge is given in Table 5.2. Base on the configuration, the diagonal components of the mass matrix, $\mathbf{M}$ in Eq (5.4) are decided by $[43.79\ \text{tf/m}, 43.79\ \text{tf/m}, 9826\ \text{tf}\cdot\text{m}^2/\text{m}]^T$. The stiffness and dampling matrix are given as $\mathbf{K} = \mathbf{M}\cdot\text{diag}(\omega_1^2, \omega_2^2, \omega_3^2)$ and $\mathbf{C} = \mathbf{M}\cdot 2\lambda\cdot\text{diag}(\omega_1, \omega_2, \omega_3)$, respectively. The damping ratio, λ, of the structure is assumed as 0.02.

Main span (m)		1990
Girder section (m)	Width (B)	35.5
	Height (D)	14.0
Dead load (tf/m)		43.79
Polar moment of inertia ($\text{tf}\cdot\text{m}^2/\text{m}$)		9826
Natural frequency (rad/s)	1st lateral bending (ω_1)	0.2450
	1st vertical bending (ω_2)	0.4021
	1st torsional (ω_3)	0.9425

Table 5.2: Structural dynamic dimension of Akashi-Kaikyo bridge.

For the aerodynamic parameters, the flutter derivates are evaluated using the Theordorsen function [87, 88] which is given as

$$C(k) = \frac{H_1^{(2)}(k)}{H_1^{(2)}(k) + iH_0^{(2)}(k)} \tag{5.18}$$

where $H_i^{(j)}$ is Hankel function, identical to Bessel function of third kind. Therefore,

when $C(k) = F(k) + iG(k)$, the flutter derivates are assumed as

$$\begin{aligned}
A_1^*(k) &= \frac{\pi F(k)}{4k} \\
A_2^*(k) &= -\frac{\pi}{16k}(1 - F(k) - \frac{2G(k)}{k}) \\
A_3^*(k) &= \frac{\pi}{8k^2}(\frac{k^2}{8} + F(k) - \frac{kG(k)}{2}) \\
A_4^*(k) &= -\frac{\pi G(k)}{4k} \\
H_1^*(k) &= -\frac{\pi F(k)}{k} \\
H_2^*(k) &= -\frac{\pi}{4k}(1 + F(k) + \frac{2G(k)}{k}) \\
H_3^*(k) &= -\frac{\pi}{2k^2}(F(k) - \frac{kG(k)}{2}) \\
H_4^*(k) &= \frac{\pi}{2}(1 + \frac{2G(k)}{k})
\end{aligned} \tag{5.19}$$

Furthermore, the other derivates are based on the quasi-steady theory [77] with the aerodynamic parameters as

$$\begin{aligned}
P_1^*(k) &= -\frac{2C_D}{k} \\
P_2^*(k) &= \frac{C_L - C_D'}{2k} \\
P_3^*(k) &= \frac{C_D'}{k^2} \\
P_5^*(k) &= \frac{C_D' - C_L}{k} \\
H_5^*(k) &= \frac{2C_L}{k} \\
A_5^*(k) &= -\frac{4C_M}{k}
\end{aligned} \tag{5.20}$$

and $P_4^* = P_6^* = H_6^* = A_6^* = 0$ and C_L, C_D, C_M are mean lift, drag, moment coefficient,

respectively, and $C'_L = dC_L/d\alpha$, $C'_D = dC_D/d\alpha$, $C'_M = dC_M/d\alpha$. The coefficients are assumed to be as $C_D = 0.3230$, $C'_D = 0$, $C_L = 0.0942$, $C'_L = 1.905$, and $C_M = 0.0104$, $C'_M = 0.2717$ [74]. The prescribed flutter derivates are plotted in Figures 5.14, 5.15, and 5.16. The rational function approximations of the given transfer functions (Eqs. (5.19) and (5.20)) are compared with their own targets in Figure 5.17, respectively. $\chi_{L_{bu}}$, $\chi_{L_{bw}}$, $\chi_{M_{bu}}$, $\chi_{M_{bu}}$ are given by Sears functions [89] as

$$\chi_{Sears}(k) = \frac{J_0(k)K_1(ik) + iJ_1(k)K_0(ik)}{K_1(ik) + k_0(ik)} \tag{5.21}$$

where J_0, J_1 are Bessel functions of first kind and K_0, K_1 are modified Bessel functions of second kind. $\chi_{D_{bu}}$ and $\chi_{D_{bw}}$ are based on Davenport's function [84] as

$$\chi^2_{Davenport} = \frac{2}{c^2}(c - 1 + e^{-c}) \tag{5.22}$$

where $c = \lambda f D/U$, D is section depth, and λ is a decay factor assumed to be 8 [74].

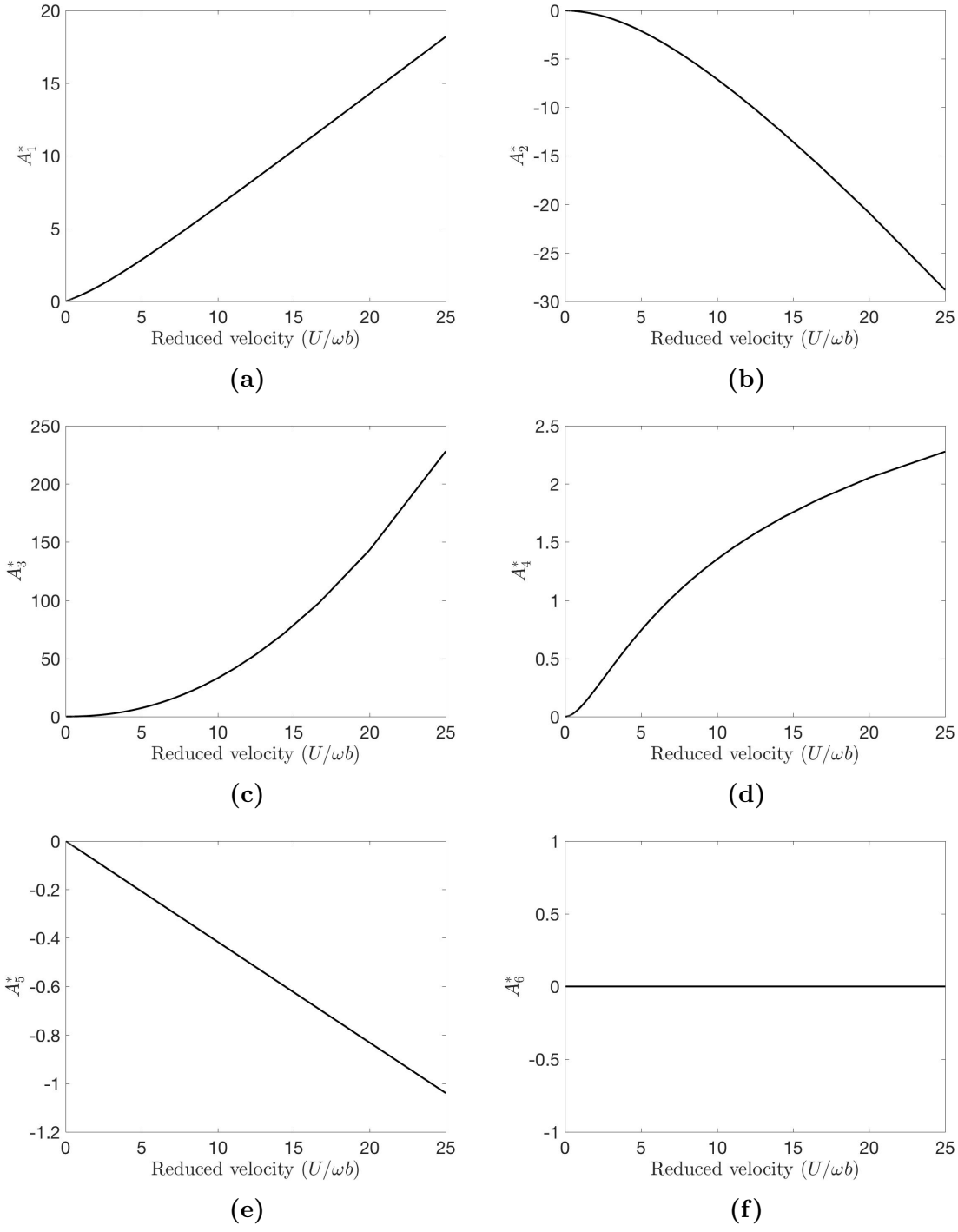

Figure 5.14: Flutter derivatives; (a) A_1^*, (b) A_2^*, (c) A_3^*, (d) A_4^*, (e) A_5^*, (f) A_6^*.

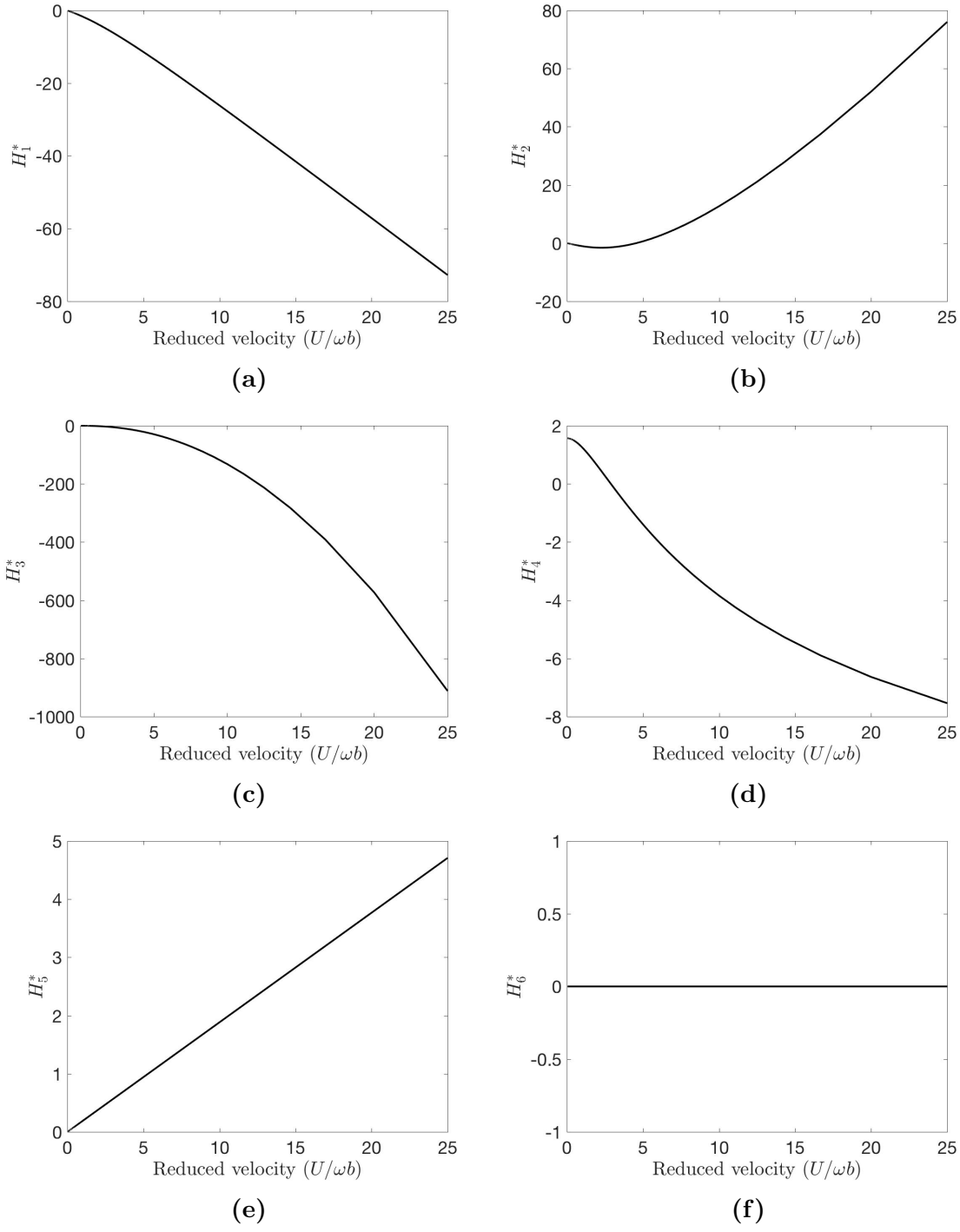

Figure 5.15: Flutter derivatives; (a) H_1^*, (b) H_2^*, (c) H_3^*, (d) H_4^*, (e) H_5^*, (f) H_6^*.

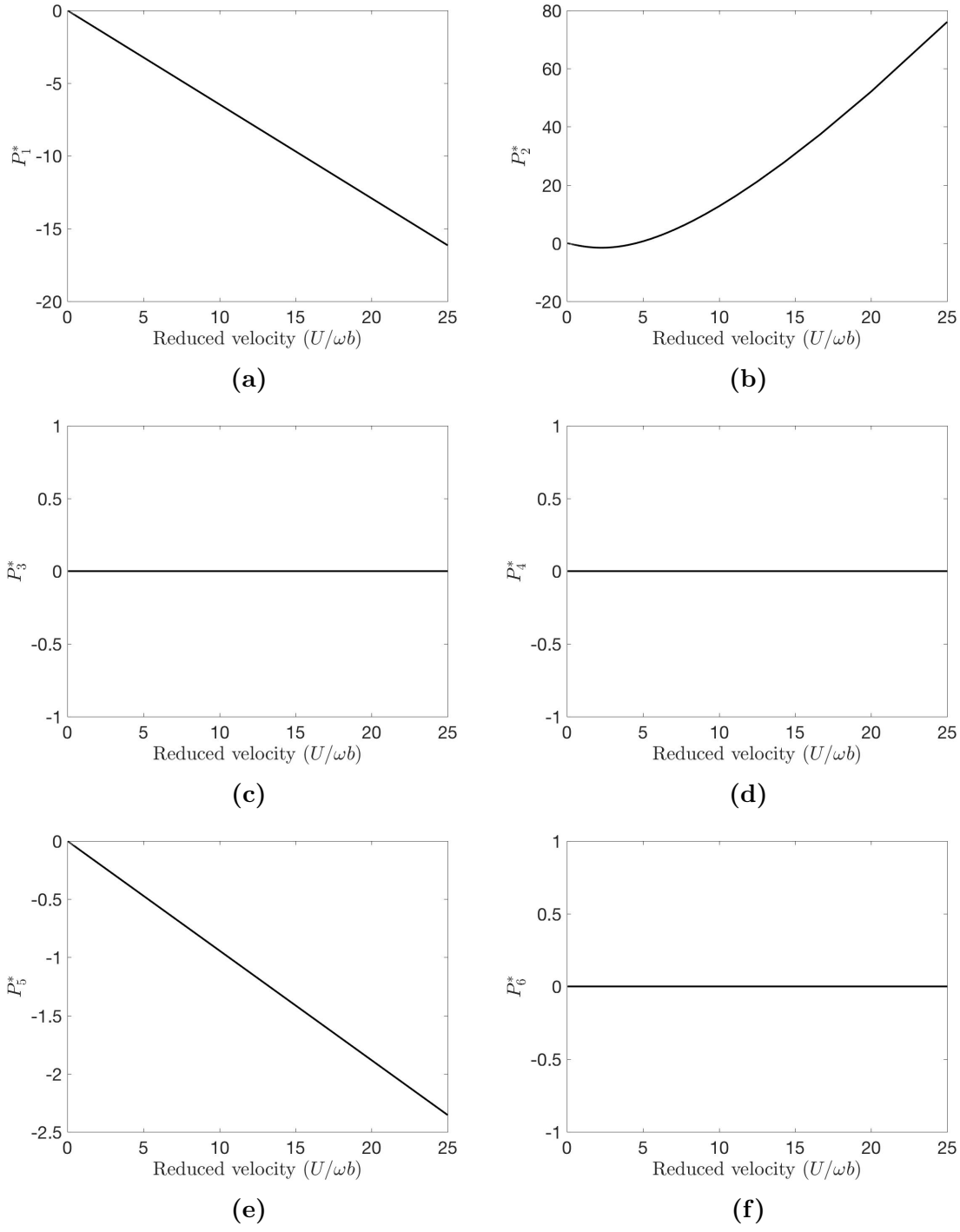

Figure 5.16: Flutter derivatives; (a) P_1^*, (b) P_2^*, (c) P_3^*, (d) P_4^*, (e) P_5^*, (f) P_6^*.

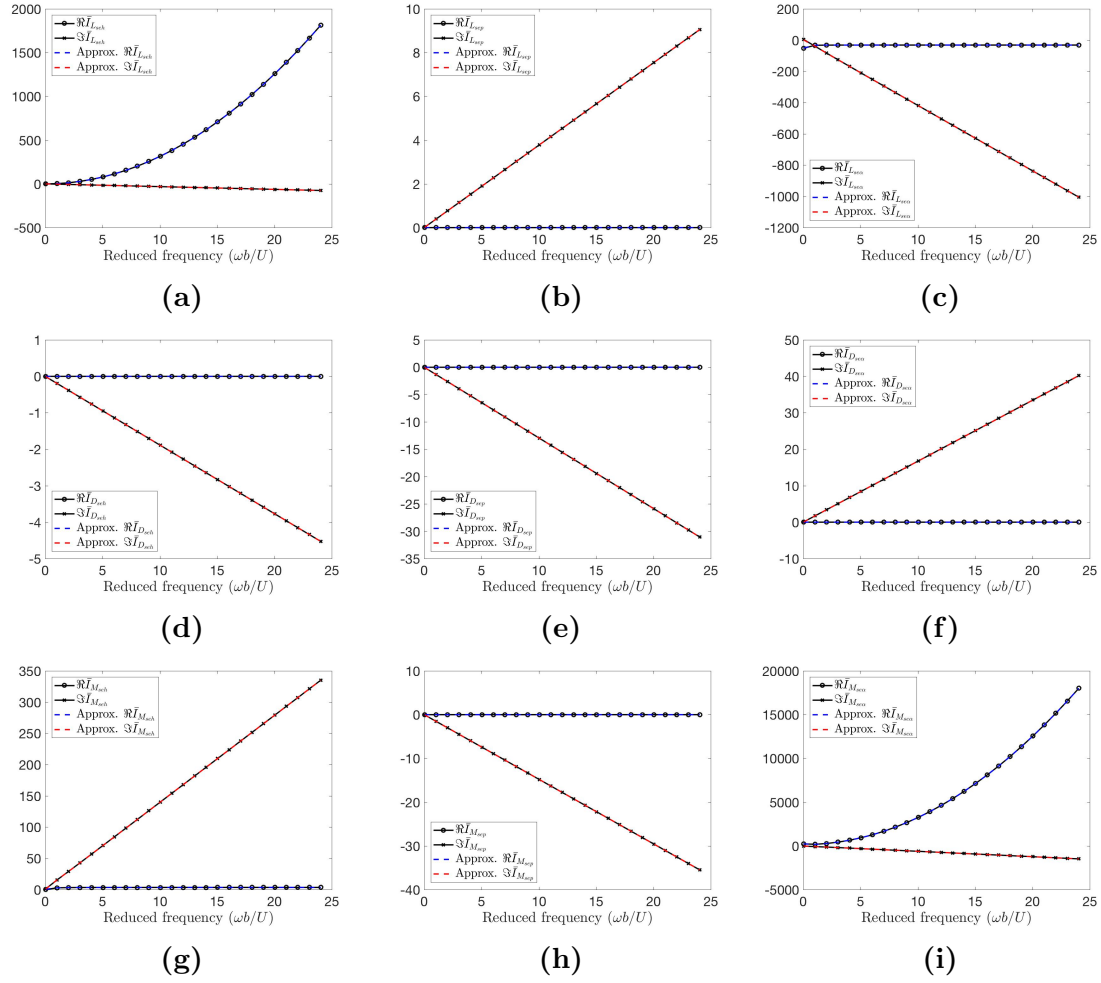

Figure 5.17: Target and rational function representations of aerodynamic transfer functions of self-excited forces; (a) $\bar{I}_{L_{seh}}$, (b) $\bar{I}_{L_{sep}}$, (c) $\bar{I}_{L_{se\alpha}}$, (d) $\bar{I}_{D_{seh}}$, (e) $\bar{I}_{D_{sep}}$, (f) $\bar{I}_{D_{se\alpha}}$, (g) $\bar{I}_{M_{seh}}$, (h) $\bar{I}_{M_{sep}}$, (i) $\bar{I}_{M_{se\alpha}}$.

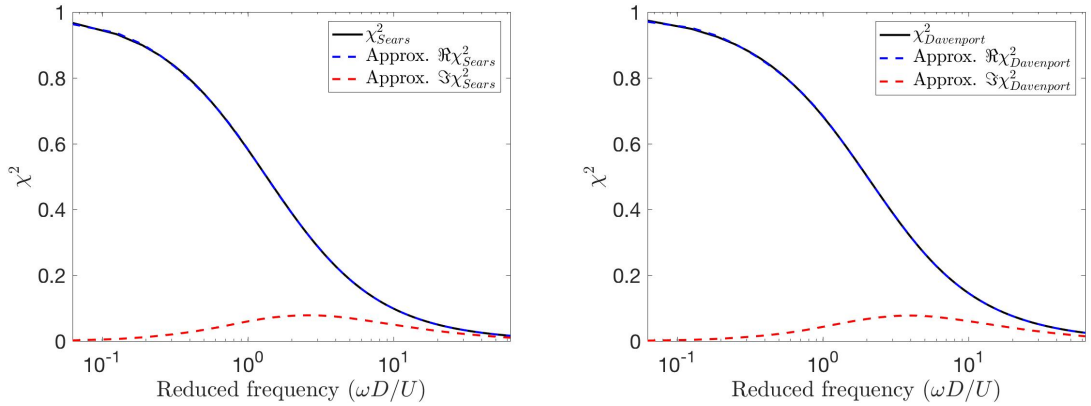

Figure 5.18: Target and rational function representations of admittance functions of buffeting forces; (a) Sears function, (b) Davenport's function.

5.2.2 Stochastic simulation of wind fluctuations

Target power spectrums for the lateral and vertical wind fluctuations are given by the von Kármán spectra [85] as follows

$$\begin{aligned} S_u^T(f) &= 0.5 \cdot \frac{\sigma_u^2 \cdot 4(f \cdot L_u/U)}{f \cdot (1 + 70.78(f \cdot L_u/U)^2)^{5/6}} \\ S_w^T(f) &= 0.5 \cdot 2(f \cdot L_w^y/U) \frac{\sigma_w^2 \cdot (1 + 188.88(f \cdot L_w/U)^2}{f \cdot (1 + 70.78(f \cdot L_w/U)^2)^{11/6}} \end{aligned} \tag{5.23}$$

where σ_u and σ_w are standard deviations of the lateral and vertical components of the wind fluctuations respectively and L_u and L_w are turbulence integral scales which measures the correlation distance of the lateral and vertical components in the along-wind direction; The coefficients are assumed to be as $\sigma_u = 0.1 \cdot U$, $\sigma_w = 0.05 \cdot U$, and the integral lengths are $L_u = 80$m, $L_w = 40$m. The prescribed power spectrums are illustrated in Figure 5.19. Furthermore, the coherence function between the lateral

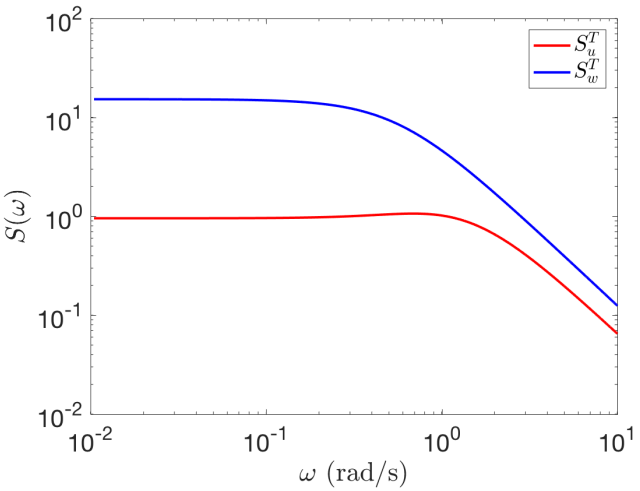

Figure 5.19: Target power spectra for lateral and vertical wind fluctuations.

and vertical components is assumed to be as unity by sharing identical phase angles and the targer cross-power spectrum is given as

$$S_{u,w}^T(f) = \sqrt{S_u(f)S_w(f)} \tag{5.24}$$

Wind velocities $u(t)$ and $w(t)$ are simulated in three ways; using the SRM, ITAM and BSRM. In all cases 5,000 time histories are generated based on Eq. (5.25). First, the SRM is used to generate wind velocity fluctuation histories in each direction using Eq. (1.17). Secondly, the ITAM with SRM is used to generated non-Gaussian wind fluctuations with marginal log-normal distributions having skewness 0.7 with PDF given by

$$f_r(x) = \frac{1}{\sqrt{2\pi\sigma_N^2}(x-\bar{\mu})} \exp\Big[-\frac{(\log(x-\bar{\mu})-\mu_N)^2}{2\sigma_N^2}\Big]; x \geq \bar{\mu}, r \in \{u, w\} \tag{5.25}$$

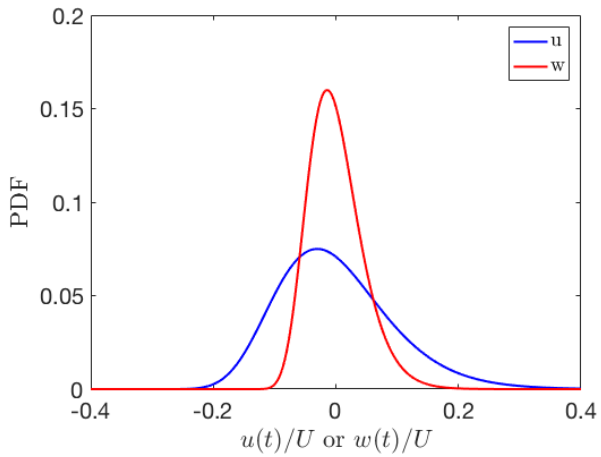

Figure 5.20: Target lognormal PDFs with skewness 0.7 for lateral (u) and vertical (w) wind fluctuations.

where $\sigma_N = 0.2264$, $\mu_N = 0.5 \cdot \log(\frac{\sigma_r^2}{\exp(\sigma_N^2)-1} - 0.5\sigma_N^2)$, $\bar{\mu} = -\exp(\mu_N + 0.5\sigma_N^2)$. The skewness of the distributions are identically 0.7 and the variances match those prescribed in Eq. (5.23). The PDFs are plotted in Figure 5.20. Lastly, the BSRM from Eq. (3.8) is used to generate wind fluctuations with identical skewness as those from the ITAM. To achieve this, the partial bicoherence is prescribed as

$$b_p^2(\omega_1, \omega_2) = C \cdot \exp\left[-\lambda(\omega_1 + \omega_2)\right] \tag{5.26}$$

where $C = 1/720$ and $\lambda = 0.1$ for both vertical and horizontal components. Figure 5.21 shows the partial bicoherence. From Eqs. (5.23) and (5.26), the pure power spectra for each wind fluctuations are computed and shown in Figure 5.22. When the pure power spectrum is decided, the target bispectra of wind fluctuations are expressed in Figure 5.23.

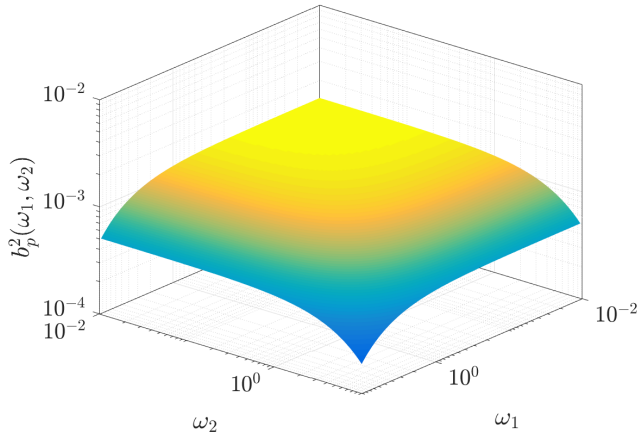

Figure 5.21: Target pure bicoherence of wind fluctuations.

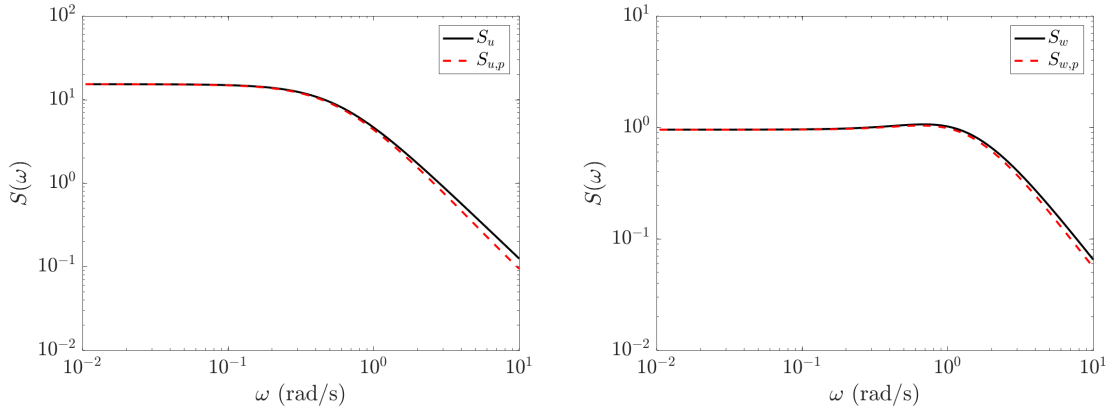

(a) **(b)**

Figure 5.22: Target power spectra and pure power spectra of (a) lateral and (b) vertical wind fluctuations.

Again, 5,000 time histories for each wind fluctuation are generated with the given methodologies. For direct comparison, the random phase are kept constant across the different simulation methods as mentioned. Examples of simulated wind fluctuations at mean wind velocity $U = 60$m/s are shown in Figure 5.24. When viewed in their total length of 600 sec., the difference between ITAM and BSRM simulations are

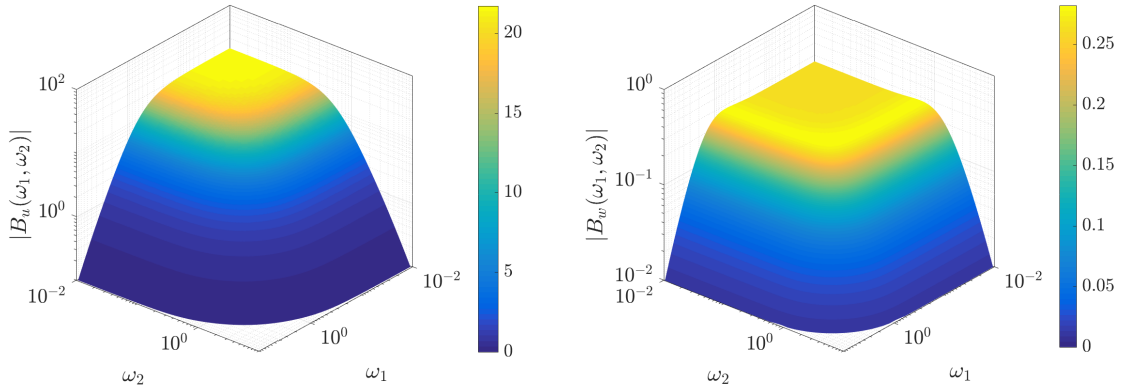

(a) **(b)**

Figure 5.23: Amplitude of target bispectra for (a) lateral and (b) vertical wind fluctuations.

minimal. However, the difference become apparent when a closer view is taken as Figure 5.25 which shows a 10 second segment of the histories. As described in Figures 5.26a, 5.26b, and 5.26c, the estimated power spectra from the SRM, ITAM, and BSRM histories matched the target power spectra. Moreover, the cross-power spectra are matched the target one in Figure 5.26d. In the examples considered here, the lateral wind fluctuation, u, of BSRM has lower tails than the one of ITAM, but, there is relatively small difference in the vertical fluctuations, w.

The distributions of the histories depicted in the Gaussian probability plots of the samples in Figure 5.27. As expected probability plots of SRM follow the straight line of a Gaussian distribution. However, the marginal probability plots of the ITAM and BSRM have positive skewness. These plots show differences in the tails between the realizations of the ITAM and BSRM. Even though the skewness of ITAM and BSRM are the same, the ITAM simulations have a lower bound since the follow a lognormal

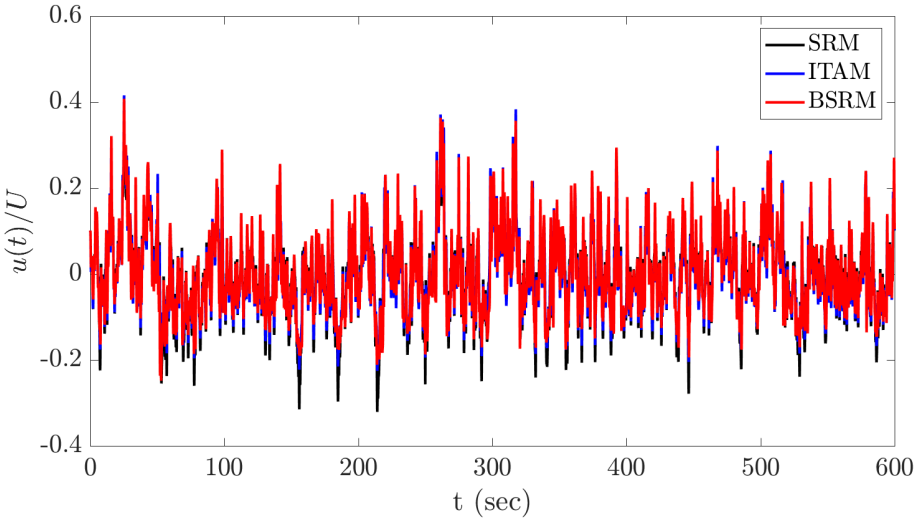

(a)

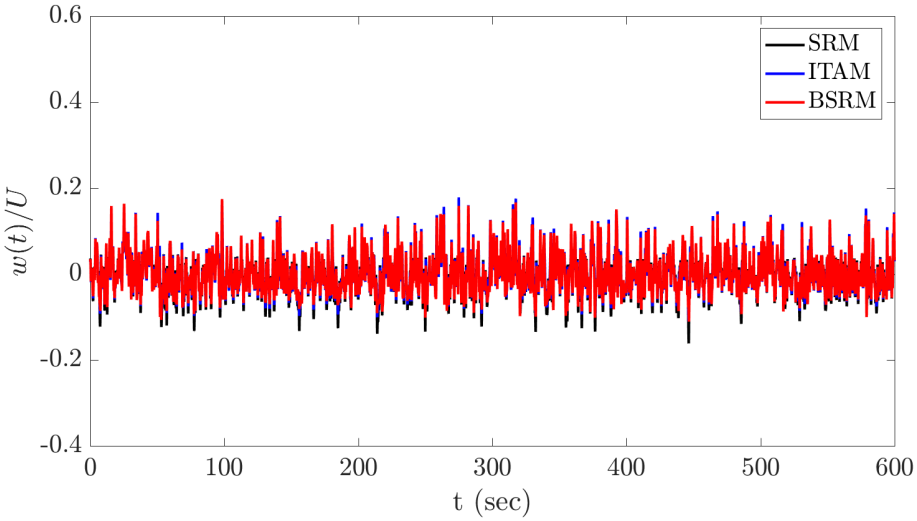

(b)

Figure 5.24: Examples of simulated (a) lateral and (b) vertical wind fluctuations with SRM, ITAM, BSRM simulations.

distribution. Meanwhile, there is no lower bound in the BSRM simulations, therefore, they have a heavier lower tail. The upper tails of ITAM simulations are also sightly heavier. The maximum values of the wind fluctuations are compared in Figure 5.28. Because of the skewness and heaviness of the upper tails, the ITAM has the largest

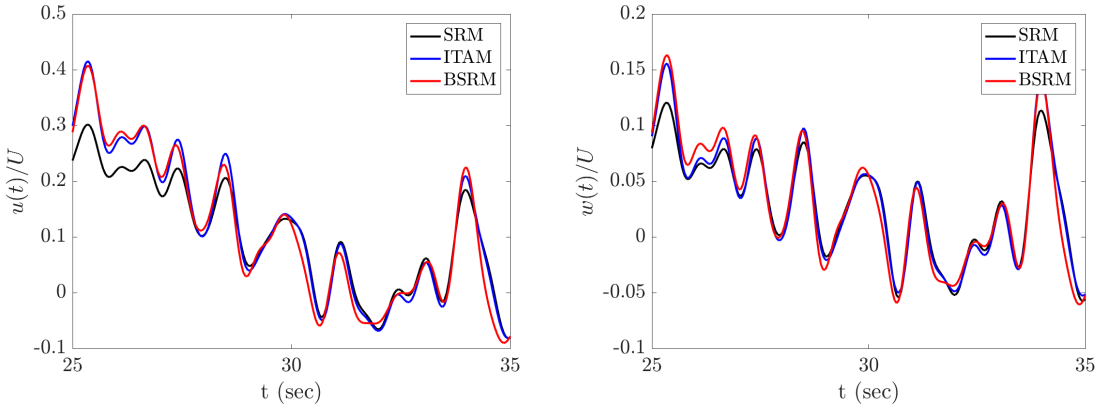

Figure 5.25: Comparisons of (a) lateral and (b) vertical wind fluctuations between SRM, ITAM and BSRM simulations in a short period, $t \in [25, 35]$.

peak values in both components of wind fluctuations

Bispectral analysis on wind fluctuations are performed and the amplitudes of estimated bispectra are plotted in Figures 5.29 and 5.30 and compared with the target bispectra. First, the SRM realizations have much smaller bispectrum than the ITAM and BSRM because of their symmetric distribution. In the estimated bispectra from the ITAM and BSRM, we see that recognize the low-frequency part of the ITAM bispectrum in Figure 5.29d is slightly higher than the one from the BSRM in Figure 5.29f. However, the bispectra of the vertical component from the ITAM and BSRM in Figures 5.30d and 5.30f are close to each other. Table 5.3 provides a summary of the statistics of these wind fluctuations. By sharing the similar variance among the SRM, ITAM, and BSRM simulations, there are only identical skewness for the ITAM and BSRM. Similarly, the kurtosis of the SRM is close to be Gaussian, however, the one of the ITAM and BSRM have different values from three. [!ht]

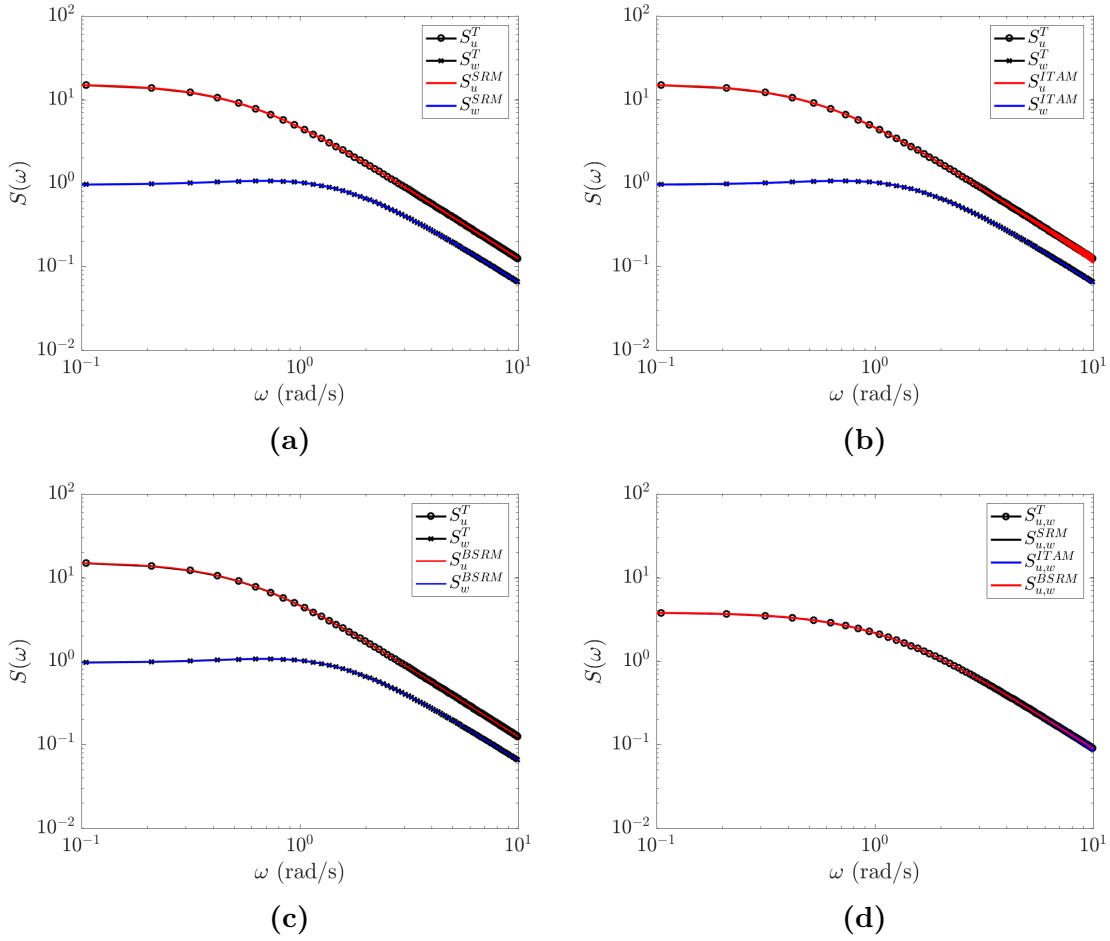

Figure 5.26: Power spectra of lateral and vertical wind fluctuations with (a) SRM, (b) ITAM, (c) BSRM and (d) their own cross-power spectra.

5.2.3 Simulated self-excited and buffeting forces

The simulated wind time histories on the bridge deck model were utilized to calculate the displacement responses from the aerodynamic coupling of self-excited and buffeting forces. Examples of the self-excited forces per unit length computed using Eqs. (5.20) are plotted in Figures 5.31a, 5.31c, and 5.31e. Figures 5.31b, 5.31d, and 5.31f show Gaussian probability plots of the lift, drag, and torsional self-excited

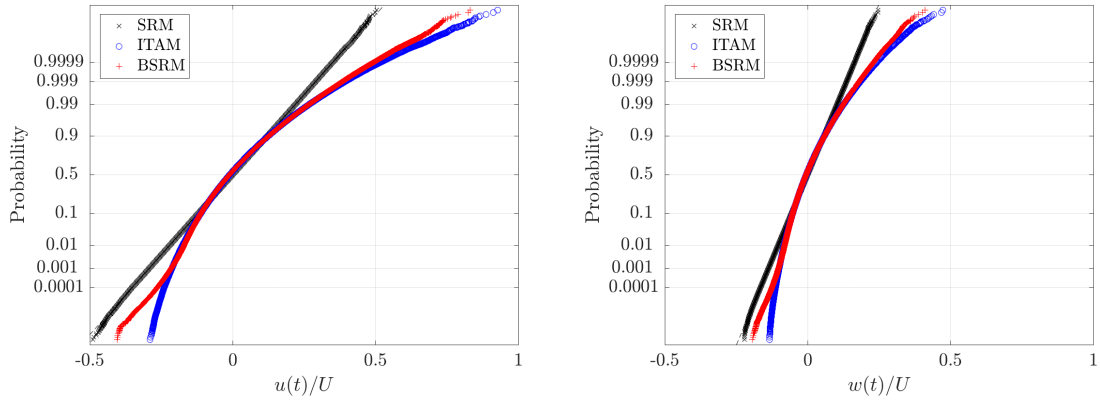

Figure 5.27: Gaussian probability plots for (a) lateral and (b) vertical wind fluctuations.

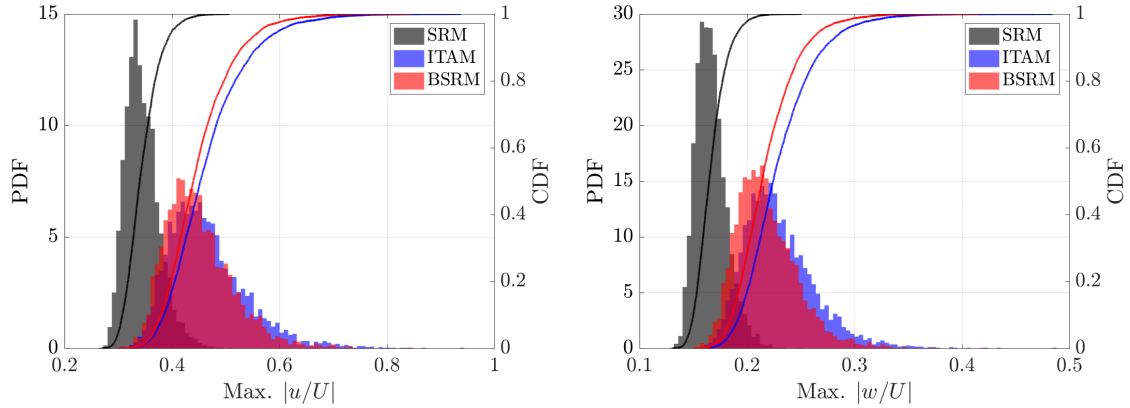

Figure 5.28: Peak wind fluctuations; (a) lateral and (b) vertical components.

Component	Method	Standard dev.	Skewness	Kurtosis
u	SRM	5.6742	0.0002	2.9924
	ITAM	5.6736	0.6970	3.8629
	BSRM	5.6742	0.7009	3.7277
w	SRM	2.6590	0.0006	2.9964
	ITAM	2.6590	0.6990	3.8733
	BSRM	2.6591	0.6927	3.7297

Table 5.3: Statistics of simulated wind fluctuation time histories.

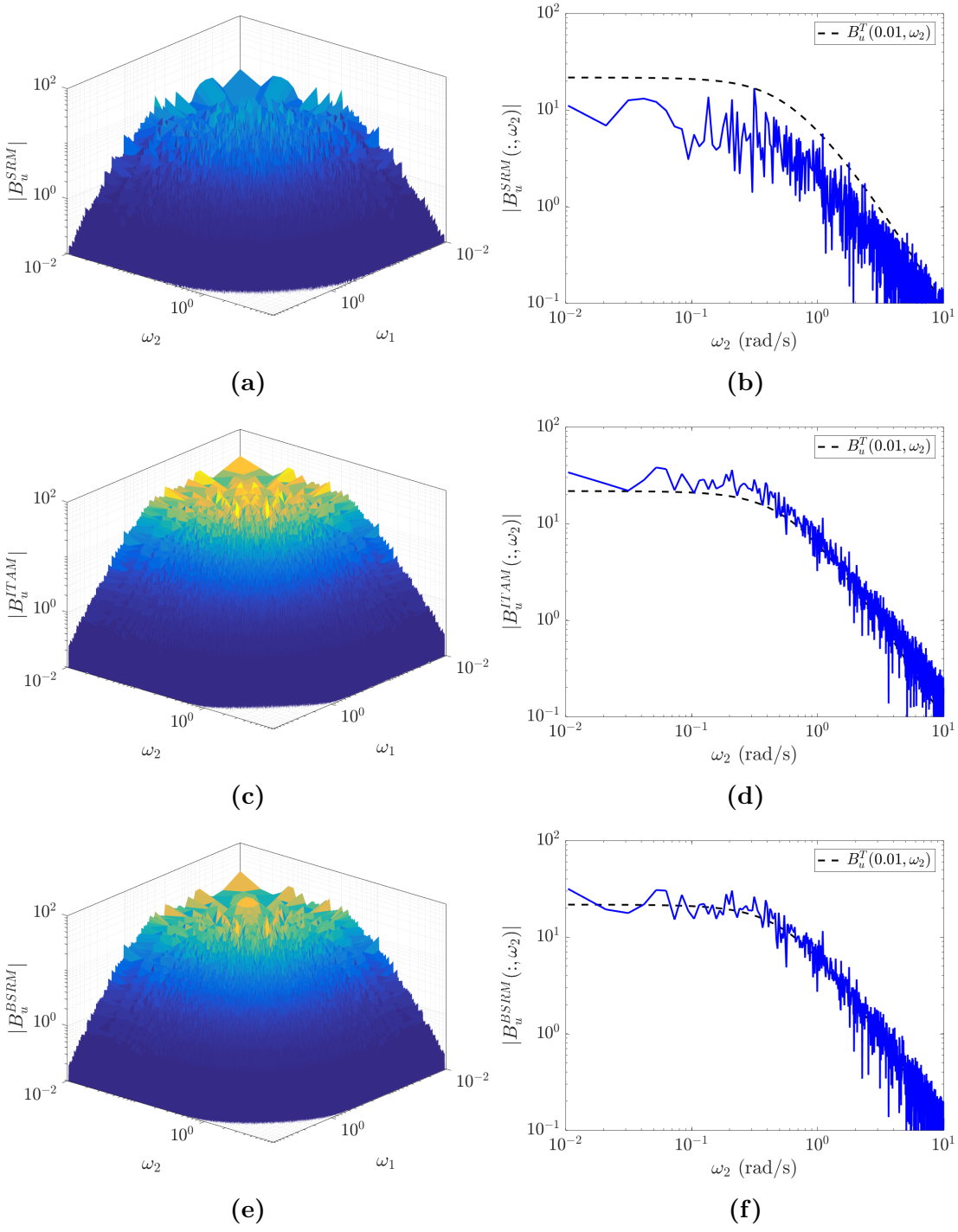

Figure 5.29: Estimated amplitudes of bispectra of lateral wind fluctuations from (a, b) SRM, (c, d) ITAM, and (e, f) BSRM.

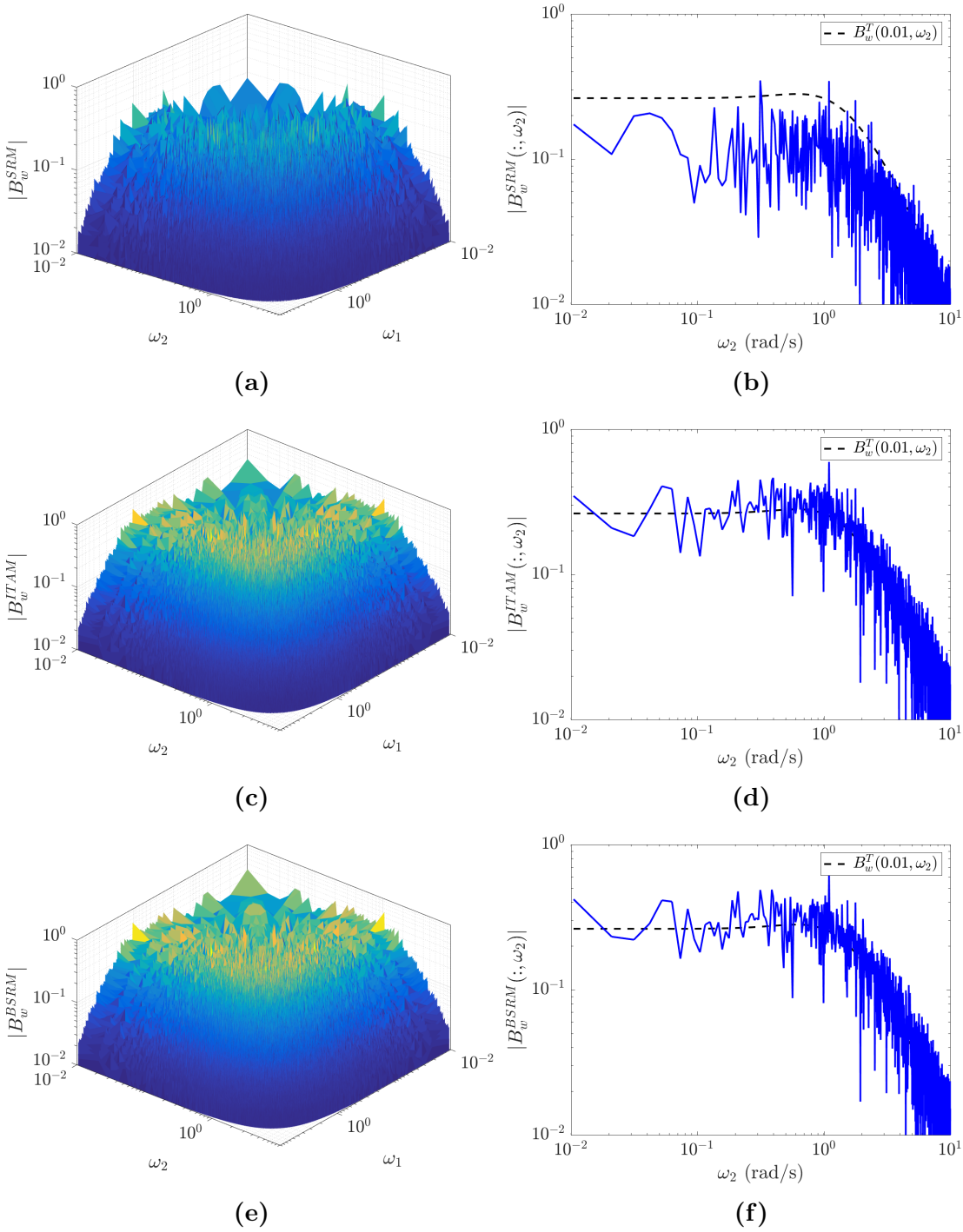

Figure 5.30: Estimated amplitudes of bispectra of vertical wind fluctuations from (a, b) SRM, (c, d) ITAM, and (e, f) BSRM.

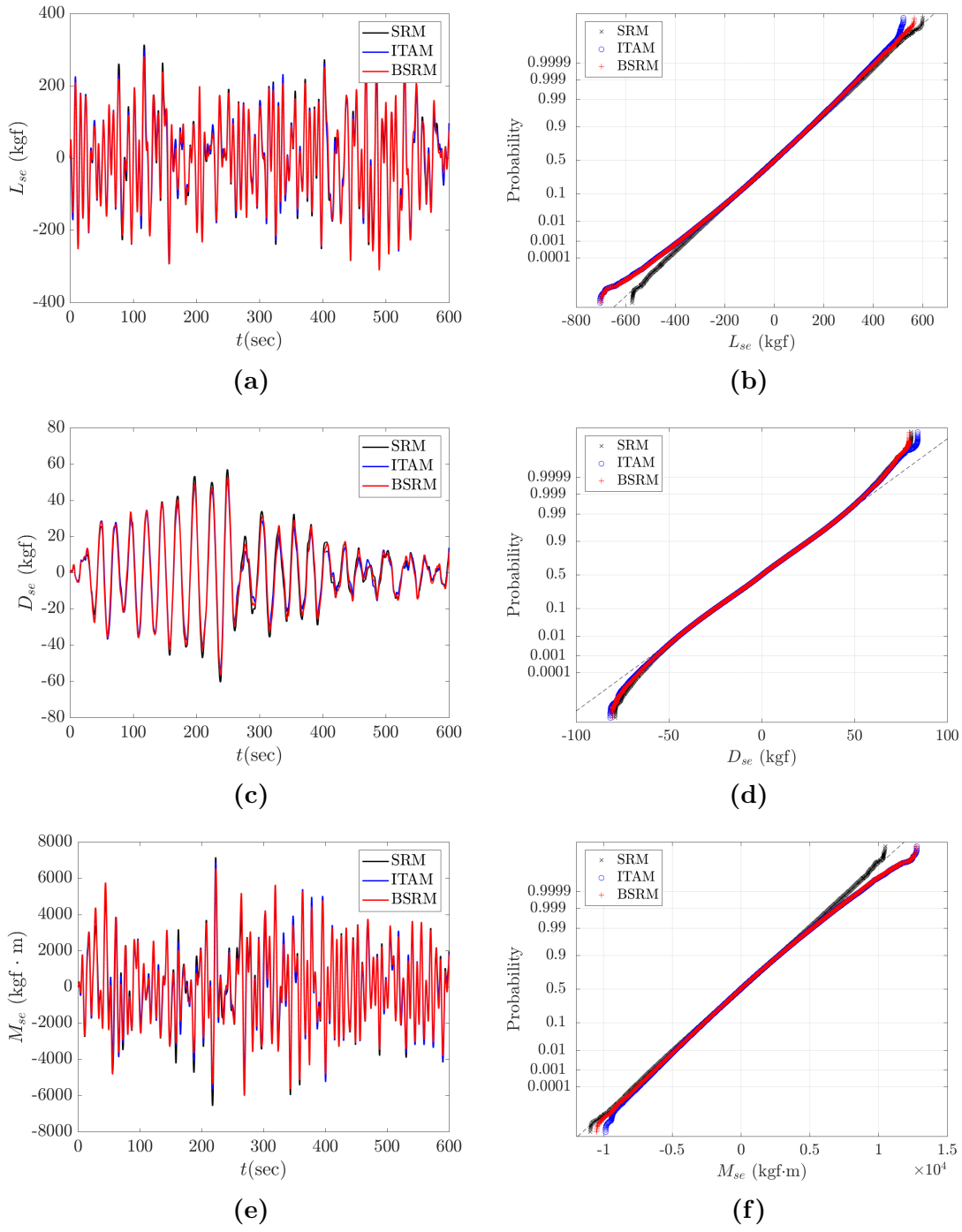

Figure 5.31: Samples and probability plots of self-excited forces; (a, b) $L_{se}(t)$, (c, d) $D_{se}(t)$, (e, f) $M_{se}(t)$.

forces from the SRM, ITAM, and BSRM velocities. The lift and moment of self-excited forces are skewed by the skewness of wind fluctuations generated by ITAM and BSRM, although the drag forces are not affected by the skewness. In addition, the distributions functions of peak values of the peak forces are shown in in Figure 5.32. The peak lift and moment are dependent of the nonlinearity of the wind fluctuations, but the drag forces do not appear to change significantly with non-Gaussian wind velocities. Similar to the Gaussian probability plots, the mean of peak values of the lift and moment is higher than the drag.

The estimated power spectra of the self-excited forces are presented in Figure 5.33. The power spectra describe the relationships with the natural frequencies of the bridge and the self-excited forces. All of the power spectra are indistinguishable meaning they do not depend on the velocity simulation method. However, the estimated bispectra of the forces in Figure 5.34 show same difference in the intensities of phase coupling. The bispectra of the self-excited forces generated by ITAM and BSRM have stronger non-linear coupling forces from the SRM. Furthermore, the peaks of the amplitudes of bispectra are located at $(0.40\text{rad/s}, 0.40\text{rad/s})$ and $(0.24\text{rad/s}, 0.24\text{rad/s})$, corresponding to the first torsional and vertical bending natural frequencies of the bridge model. it represents that there are strong quadratic phase coupling between the pairs of their own frequency-waves and their doubled frequency-waves such as 0.40rad/s and 0.80rad/s and 0.24rad/s and 0.48rad/s. Compared to the following bispectra of displacements in Figure 5.43 which have peaks at the edges

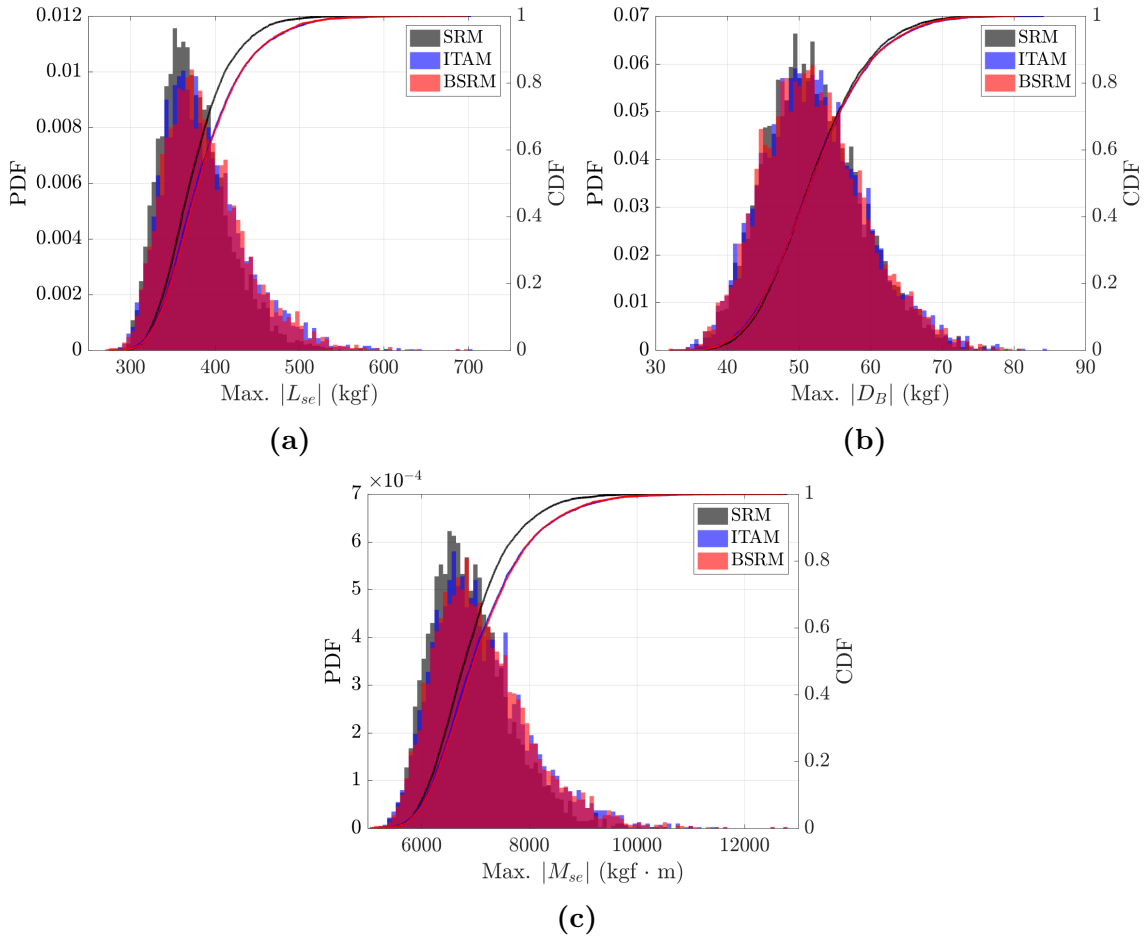

Figure 5.32: Probability plots of peak self-excited forces; (a) L_{se}, (b) D_{se}, (c) M_{se}.

of the bispectrum, we can think that the geometric non-linearity of the aerodynamic simulations causes this differences in higher-order spectra of the excitations and the displacements. Threfore, the estimation of bispectrum could be used to discriminate between the effects of he nonlinear dynamic systems including their excitations. A summary of the statistics of the self-excited forces is given in Table 5.4. At first, we can see the drag self-excited forces with every methodology are lower kurtosis than three as described in Figure 5.31d; they have weaker tails than the Gaussian distri-

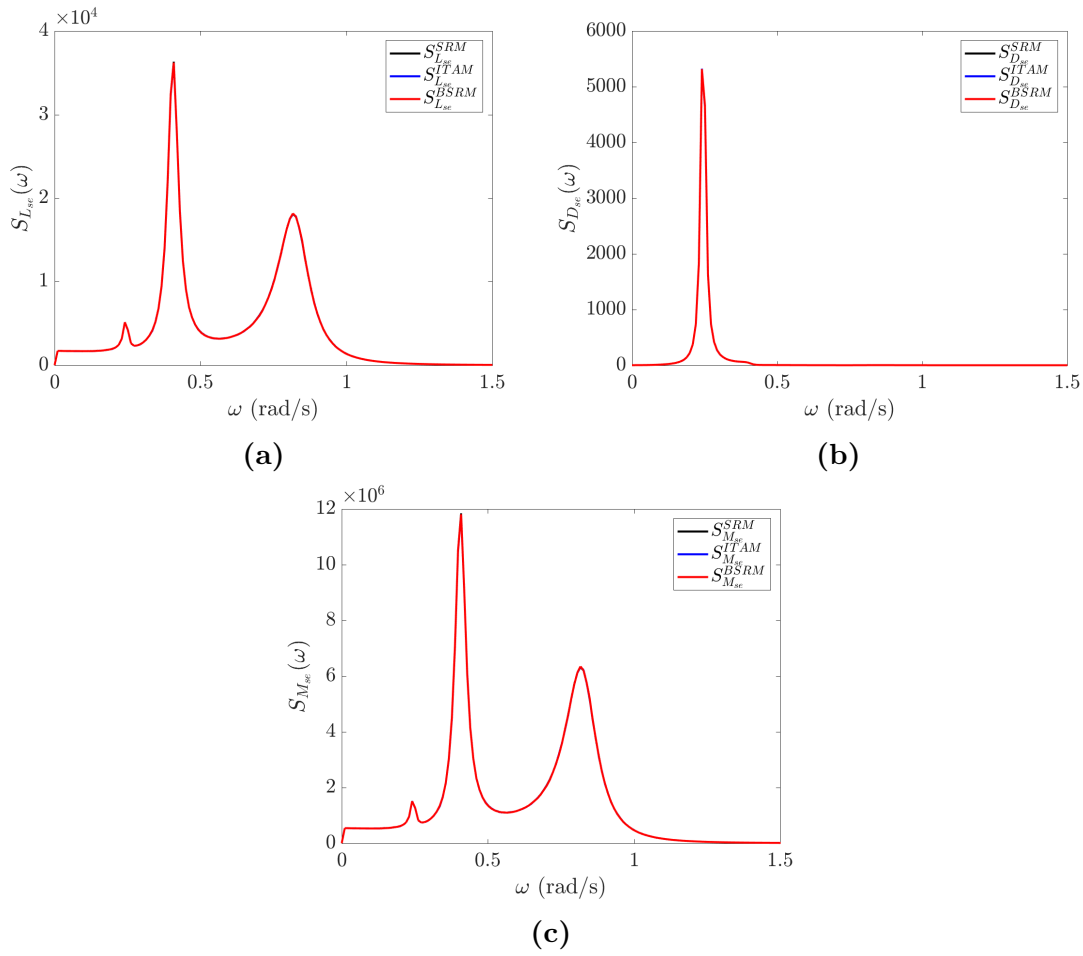

Figure 5.33: Estimated power spectra of self-excited forces; (a) L_{se}, (b) D_{se}, (c) M_{se}.

bution. Also, it shows that the self-excited ITAM and BSRM forces are more skewed than the SRM in the every components.

The buffeting forces are generated by the wind fluctuation components using Eqs. (5.16). Samples of the buffeting forces per unit length from the SRM, ITAM and BSRM wind velocities are given in Figure 5.35. The buffeting forces acting on the deck follow the similar trends of wind fluctuations (Figure 5.27) in the view of probability plot as presented in Figures 5.35b, 5.35d, 5.35f; the ITAM and BSRM has stronger

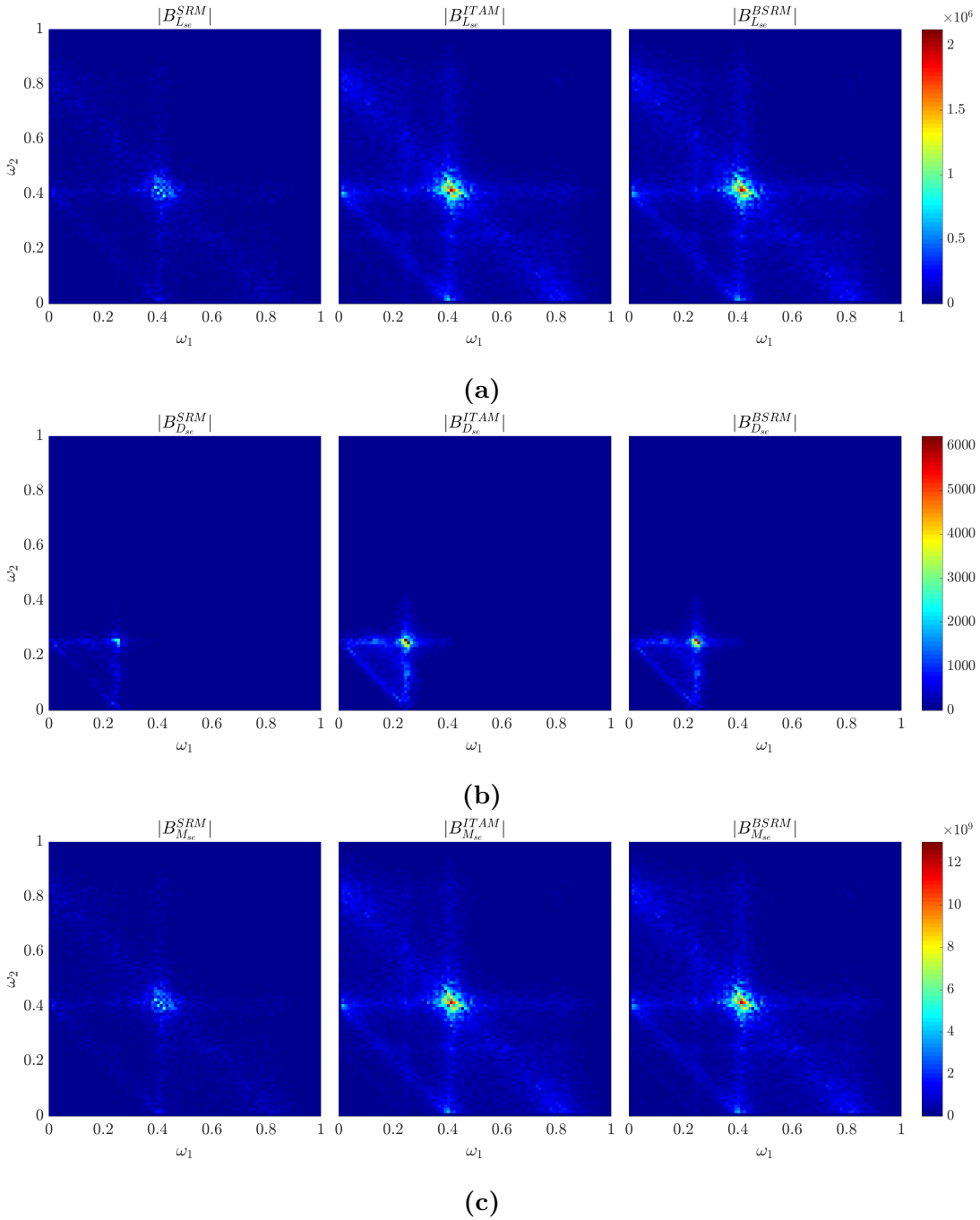

Figure 5.34: Estimated bispectra of self-excited forces; (a) L_{se}, (b) D_{se}, (c) M_{se}.

upper tails than the SRM in the view of marginal distribution and the BSRM has no lower bound compared to the ITAM in the all of directions. The buffeting forces

Component	Method	Standard dev.	Skewness	Kurtosis
L_{se}	SRM	115.5	-0.0037	2.988
	ITAM	115.5	-0.1429	3.085
	BSRM	115.5	-0.1409	3.092
D_{se}	SRM	19.33	-0.0013	2.882
	ITAM	19.34	-0.0091	2.889
	BSRM	19.35	-0.0071	2.882
M_{se}	SRM	2112	0.0039	2.990
	ITAM	2118	0.1320	3.085
	BSRM	2119	0.1302	3.092

Table 5.4: Statistics of self-excited forces.

from the SRM have Gaussian distribution, however, the ones of ITAM andB SRM buffeting forces are strongly skewed.

The PDFs and CDFs of the peak values of buffeting forces are shown in Figure 5.36, and the ITAM results have the strongest upper tails than the other simulations similar to the peak values of wind fluctuations (Figure 5.28). Furthermore, the differences in the drag buffeting forces are bigger than the lift and the moments.

The estimated power spectra of buffeting forces are illustrated in Figure 5.37 and shown as continuous spectra and identical to each other. However, it is worth mentioning the difference in computed bispectra in Figure 5.38; similar to the prescribed bispectra in self-excited forces (Figure 5.34), there are considerable distinctions among the different methodologies. Because of the unskewed buffeting forces of the SRM, their bispectrums are close to zero, but, the results of the ITAM and BSRM shows stronger amplitude of bispectra. These two results are similar in the lift and pitching moments, however, there is big difference in the drag buffeting forces. It is show-

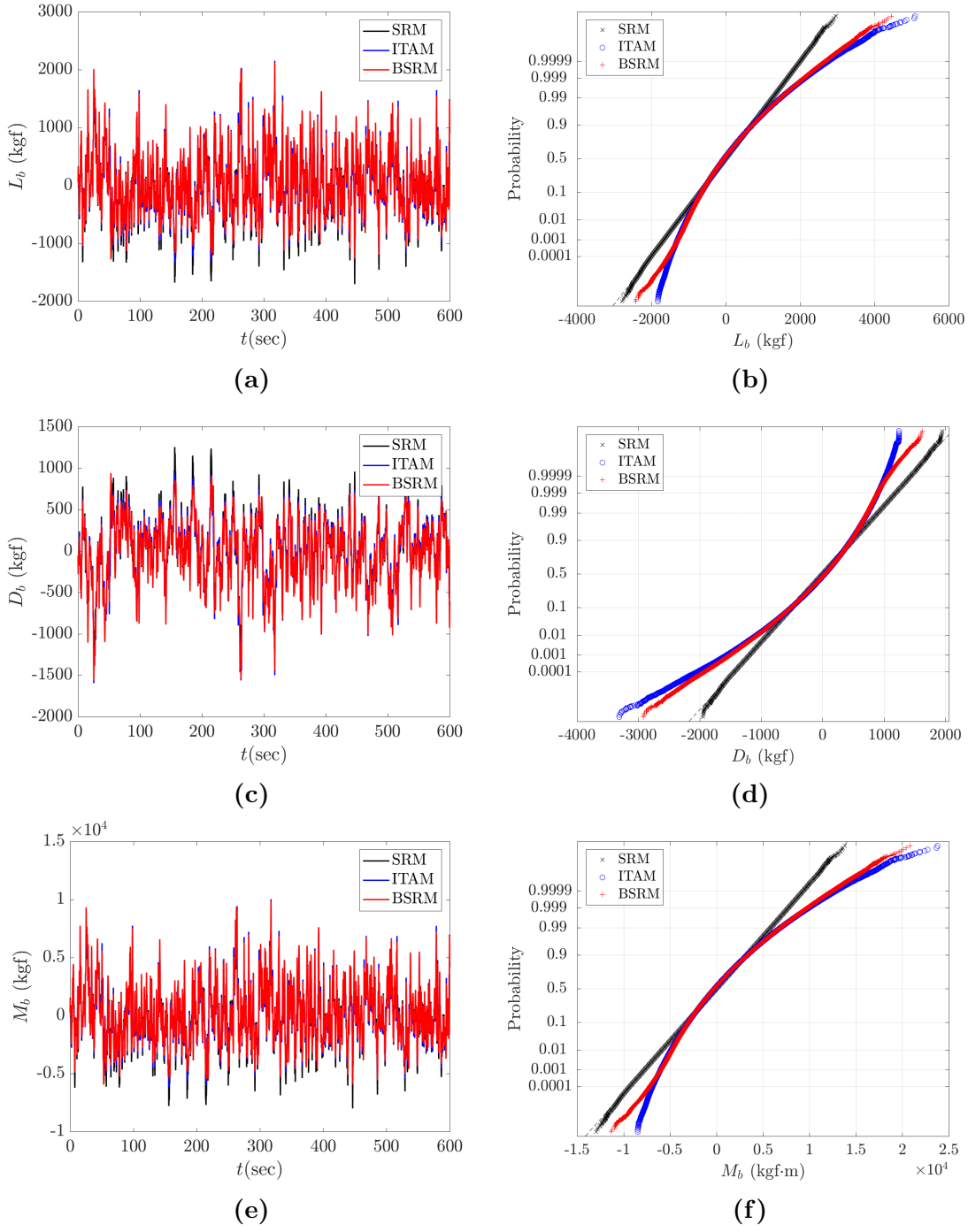

Figure 5.35: Samples and probability plots of buffeting forces; (a, b) L_b, (c, d) D_b, (e, f) M_b.

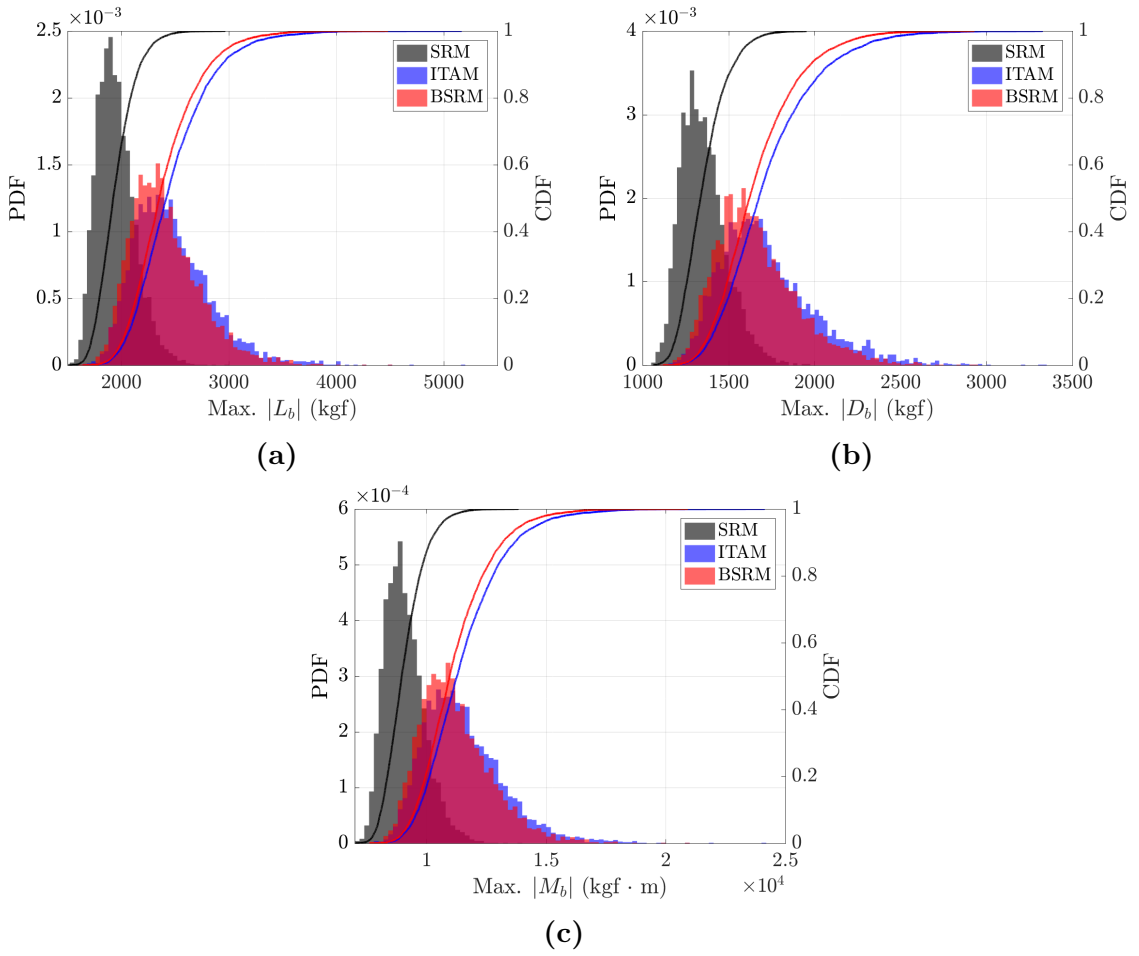

Figure 5.36: Probability plots of peak buffeting forces; (a) L_b, (b) D_b, (c) M_b.

ing that the higher bispectrum in low-frequencies of the lateral wind velocities of the ITAM (Figure 5.26c makes the stronger bispectrum of the drag buffeting forces compared to the BSRM. This difference causes relatively bigger skewness in the buffeting forces from the ITAM, -0.6117, than the BSRM, -0.5776 compared to the other components. The statistical summary of buffeting forces are given in Table 5.5.

Probability distributions of the peak total forces are plotted in Figure 5.39. The buffeting forces, F_b, per unit span are more significant than the self-excited forces,

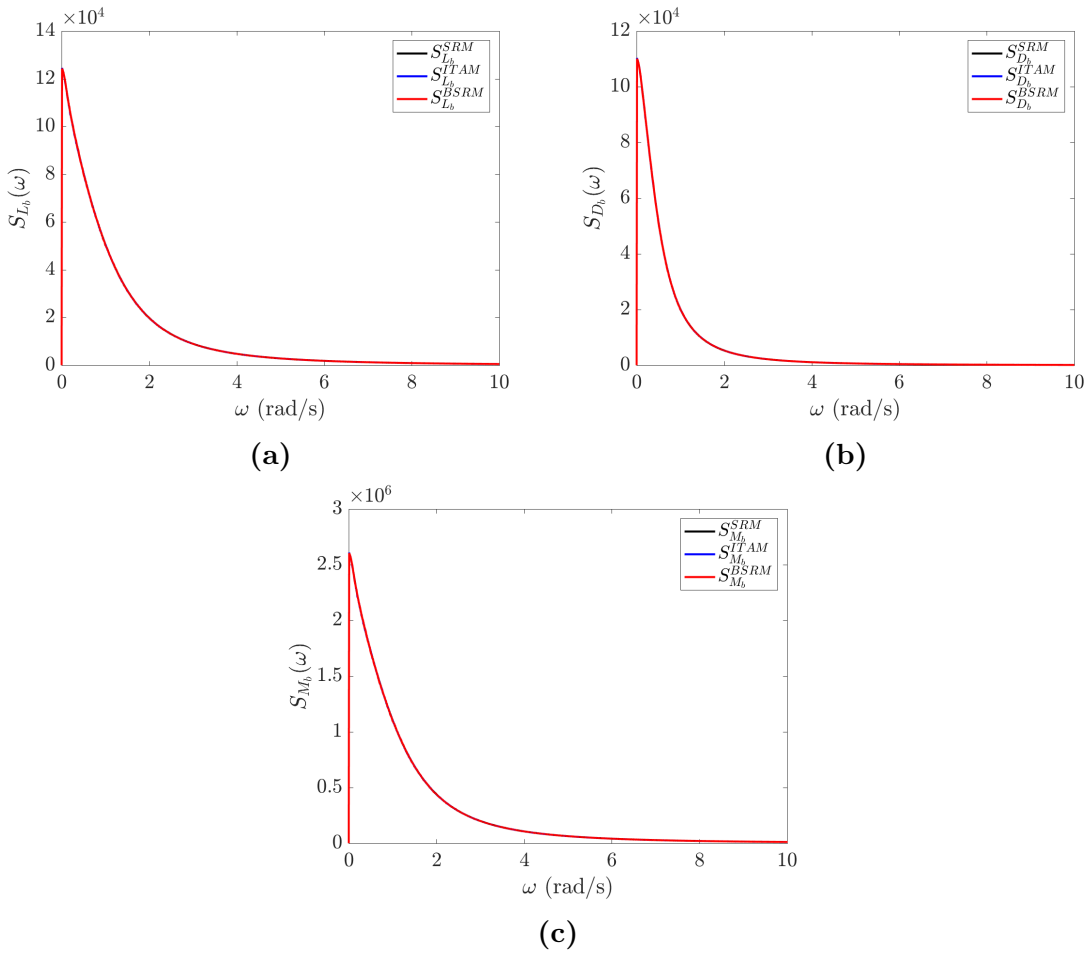

Figure 5.37: Estimated power spectra of buffeting forces; (a) L_b, (b) D_b, (c) M_b

Component	Method	Standard dev.	Skewness	Kurtosis
L_b	SRM	536.0	0.0005	2.994
	ITAM	539.7	0.5601	3.572
	BSRM	539.9	0.5739	3.490
D_b	SRM	387.3	-0.0000	2.988
	ITAM	387.2	-0.6117	3.665
	BSRM	387.3	-0.5776	3.475
M_b	SRM	2513	0.0004	2.994
	ITAM	2512	0.5603	3.573
	BSRM	2522	0.5743	3.492

Table 5.5: Statistics of buffeting forces.

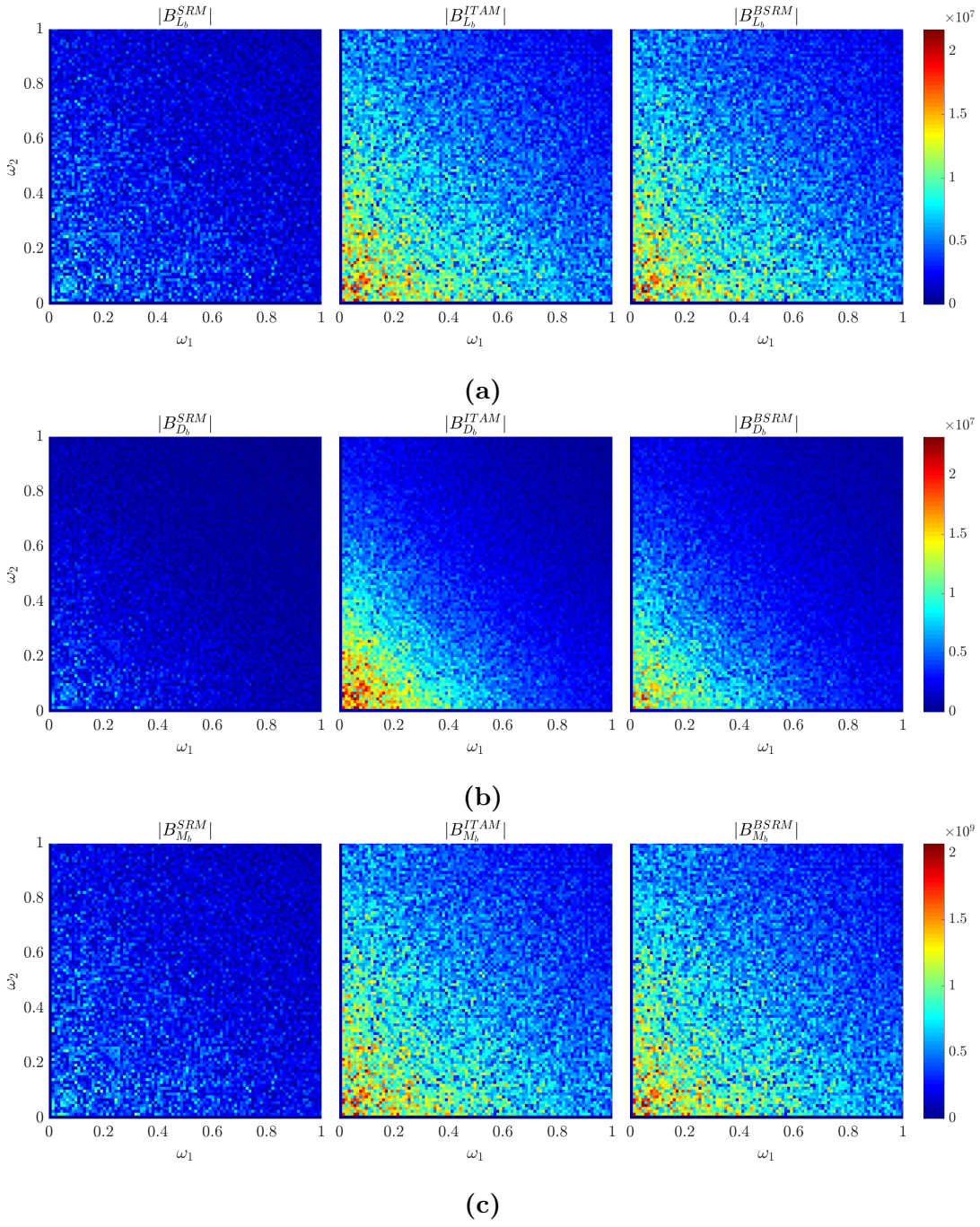

Figure 5.38: Estimated bispectra of buffeting forces; (a) L_b, (b) D_b, (c) M_b.

F_{se}, and the distributions of the peak buffeting forces in Figure 5.36 affects on the distribution of the peak total forces further than the one of the peak self-excited

forces. However, the gaps in the peak total forces between the ITAM are BSRM are relatively reduced from the difference in the peak self-excited forces.

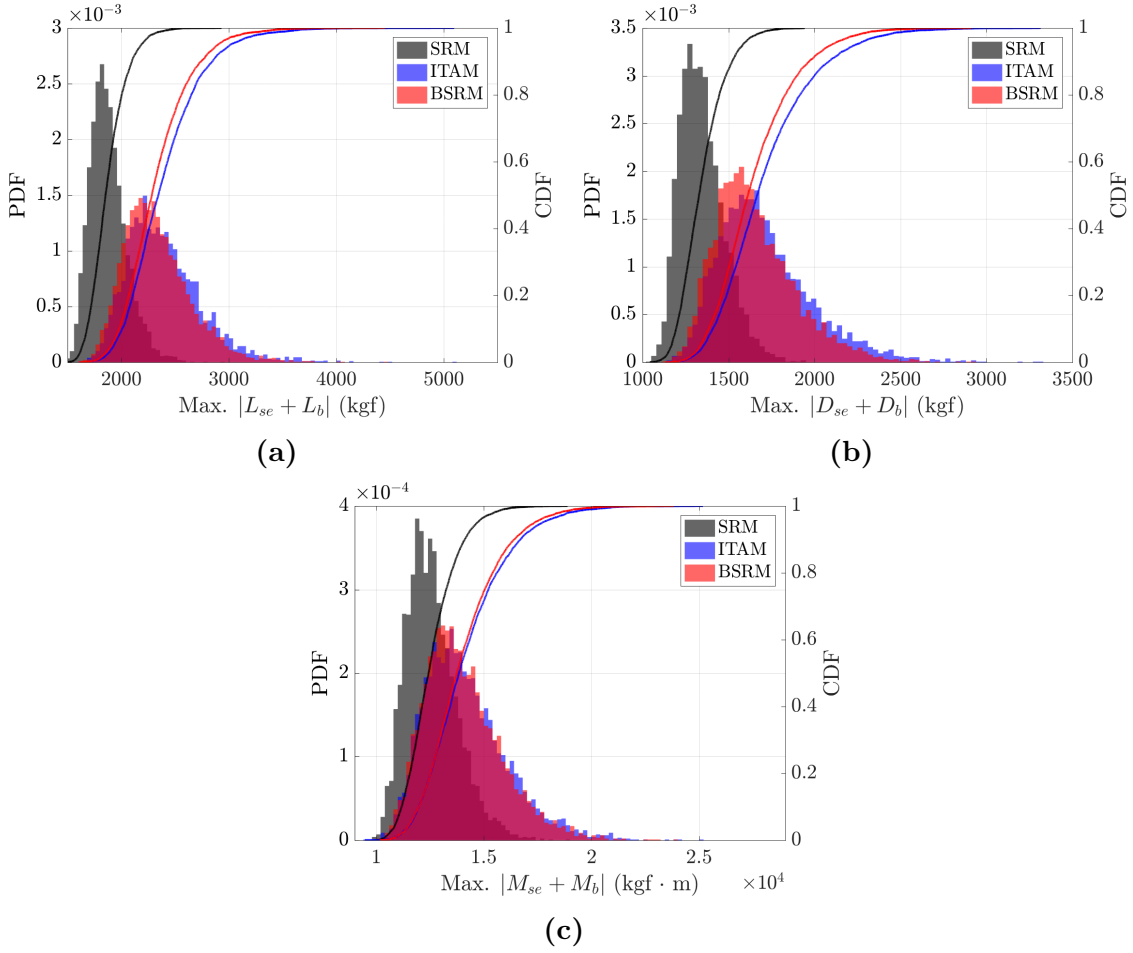

Figure 5.39: Probability plots of total peak forces; (a) $L_{se} + L_b$, (b) $D_{se} + D_b$, (c) $M_{se} + M_b$.

5.2.4 Analysis of simulated displacements

At last, examples of the aerodynamic responses of the deck are plotted in Figure 5.40. In the probability plots of the displacements, we can recognized weaker tails in

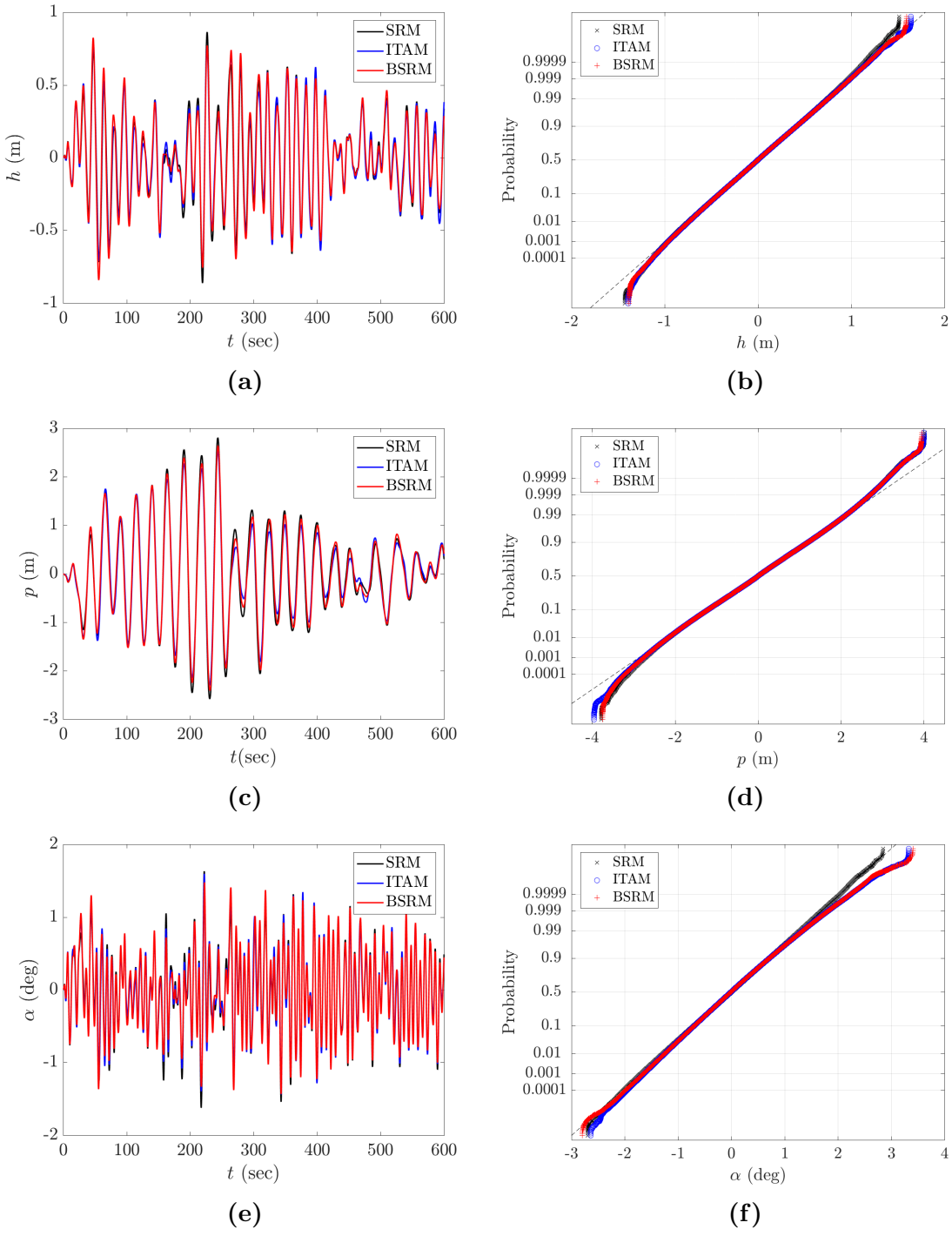

Figure 5.40: Samples and probability plots of displacements; (a, b) h, (c, d) p, (d, e) α.

the vertical and lateral displacements than the Gaussian distribution. However, the skewness in the torsional displacements (Figure 5.40f), it shows that the importance of accurate representation of wind fluctuations including skewness because it causes the divergence of the torsional and vertical displacements easily [74]. Figure 5.41 shows that the stronger skewness in the peak torsional displacements of the ITAM and BSRM simulations than the SRM, it also mentions us why we needs non-Gaussian simulations for aerodynamic applications.

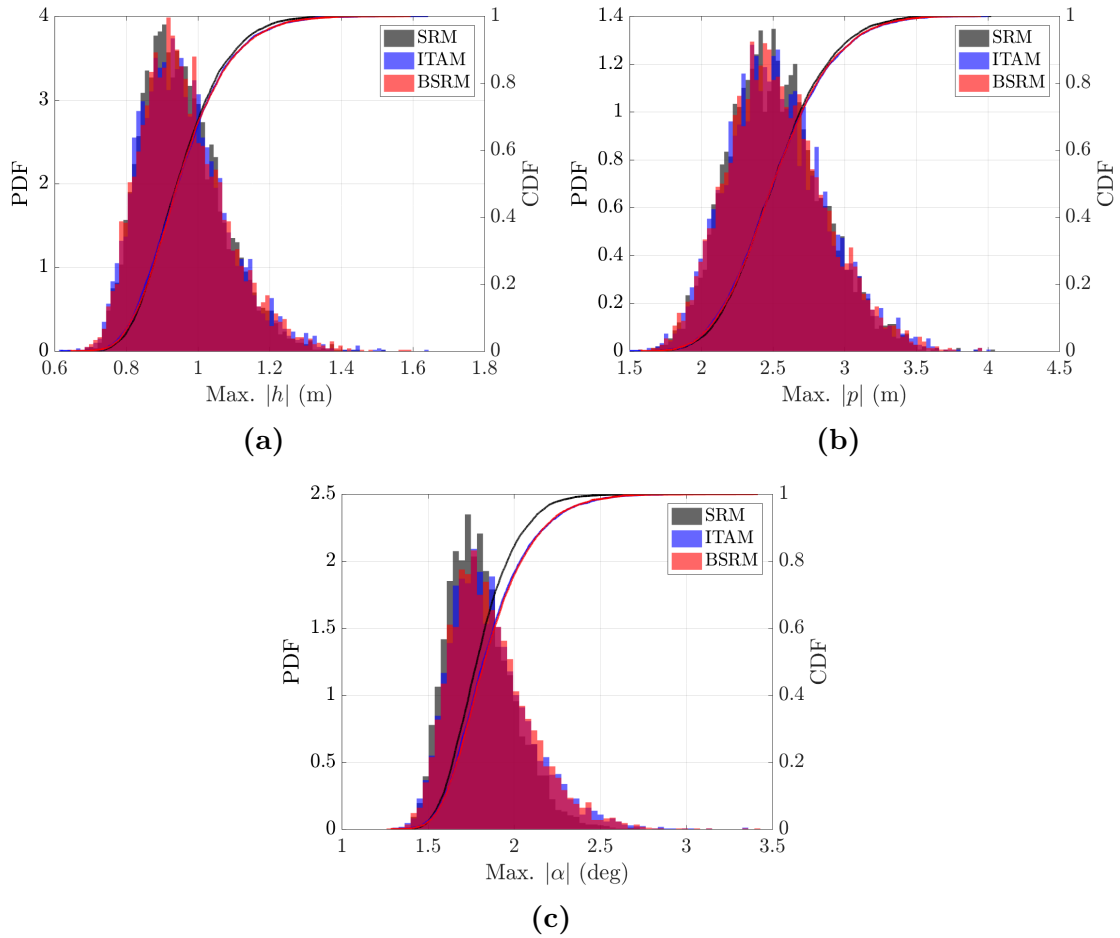

Figure 5.41: Peak displacements; (a) h, (b) p, (c) α.

In Figure 5.42, the power spectra of the buffeting responses are closed to each other. According to the their own natural frequency (Table 5.2), but, the power spectra of torsional displacements are combined with all of the natural frequencies. The estimated bispectra of the responses are plotted in Figure 5.43. As mentioned

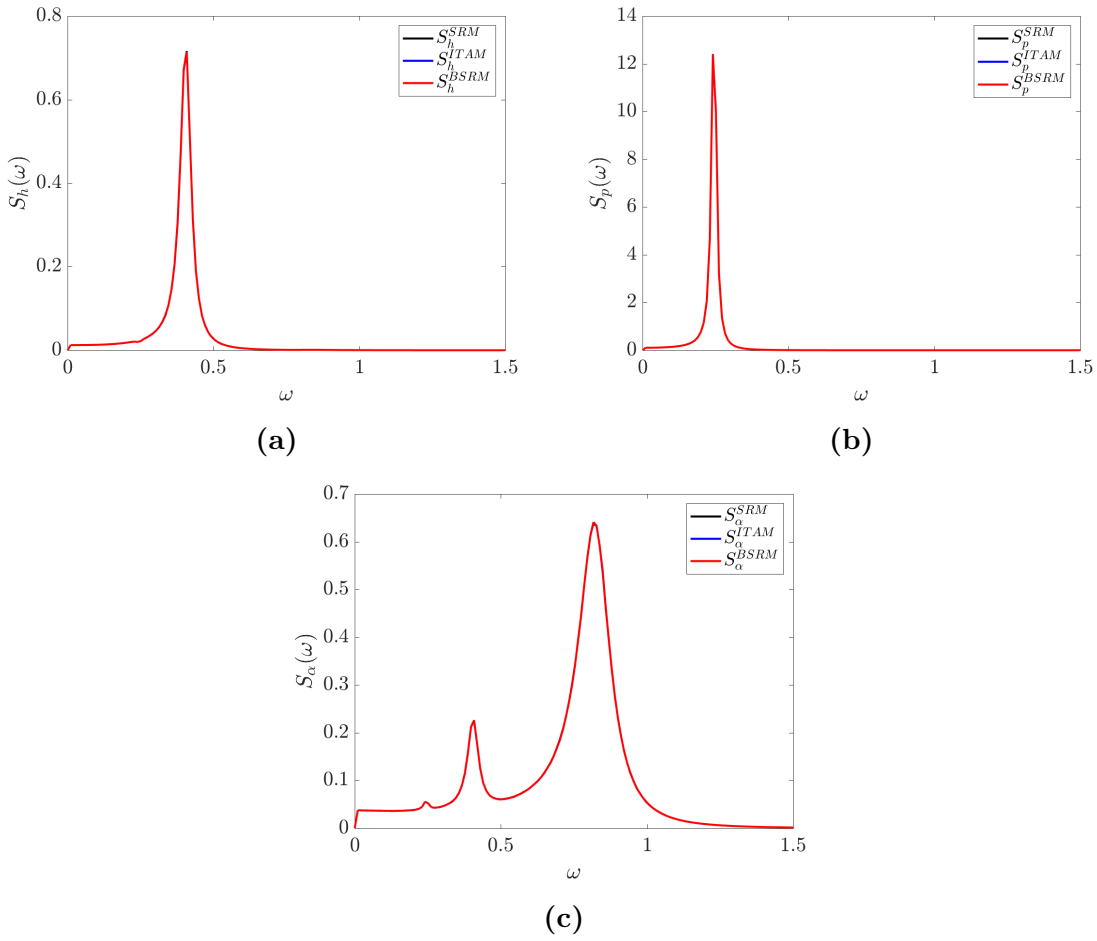

Figure 5.42: Estimated power spectra of displacements; (a) h, (b) p, (c) α.

before, in contrast to the bispectra of self-excited forces in Figure 5.34, the peaks amplitude of bispectra are not placed at the diagonals of the bispectra, but the ω_1 and ω_2 axes. The nonlinearity of the system cause the difference in the higher-order

frequency domain. Also, the amplitudes of the bisepctra are relatively lower than the ones of the self-excited and buffeting forces.

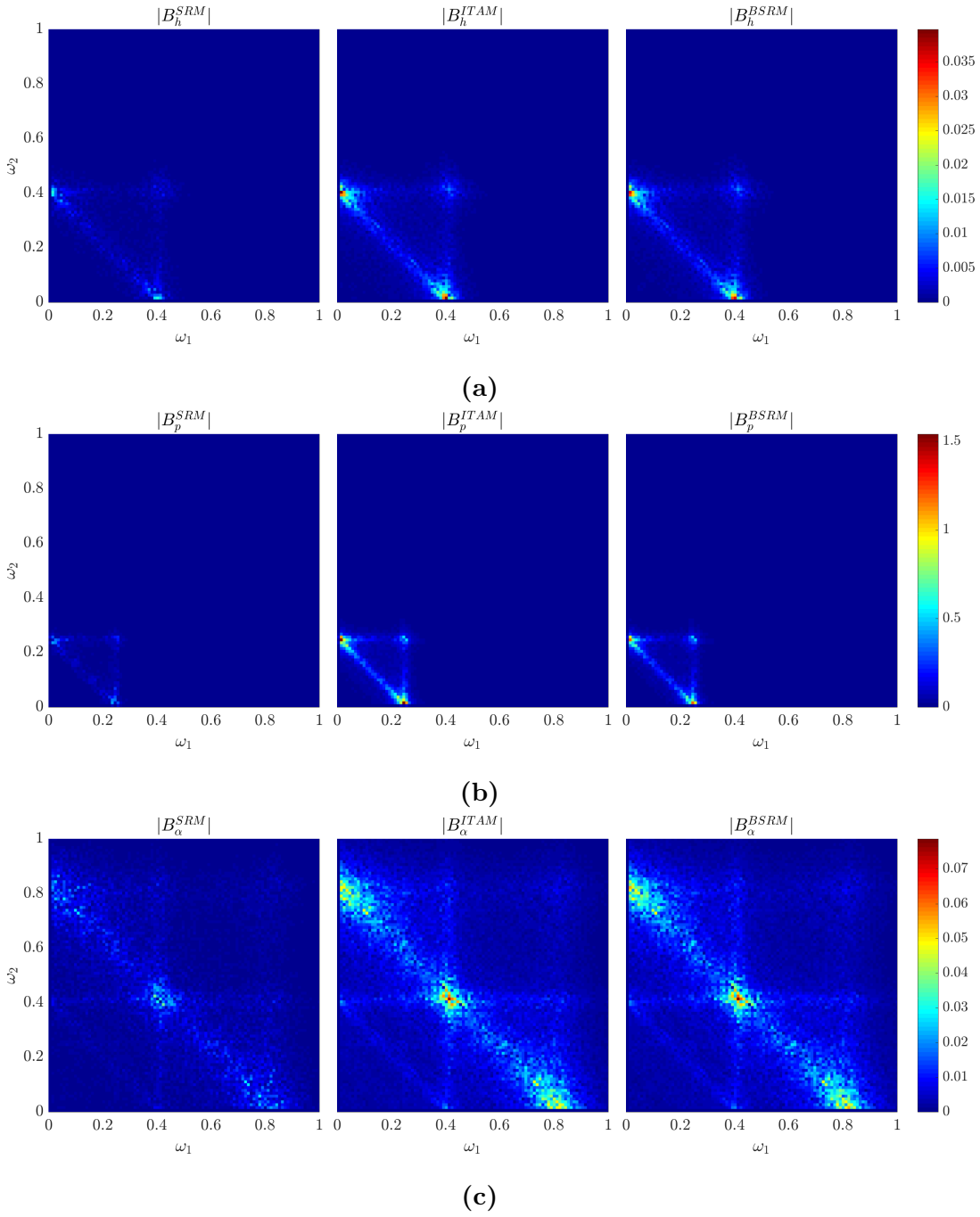

(a)

(b)

(c)

Figure 5.43: Estimated bispectra of displacements; (a) h, (b) p, (c) α.

Component	Method	Standard dev.	Skewness	Kurtosis
h	SRM	0.3207	0.0032	2.948
	ITAM	0.3205	0.0373	3.665
	BSRM	0.3208	0.0366	2.980
p	SRM	0.9297	-0.0018	2.866
	ITAM	0.9302	-0.0182	2.897
	BSRM	0.9307	-0.0150	2.890
α	SRM	0.5515	0.0008	2.988
	ITAM	0.5512	0.1170	3.082
	BSRM	0.5514	0.1162	3.092

Table 5.6: Statistics of displacements.

The probability distributions of the root mean squares (RMS) of displacements are illustrated in Figure 5.44. The RMS of displacements represents the variation in the kinetic energy due to wind fluctuations of the wind time histories [90]. We can recognize that there are enormous differences between the RMS of the SRM and the ITAM/BSRM. Specially, the variance of the displacements of the ITAM and BSRM are much bigger than the SRM even they possess identical power spectra such as Figure 5.42 . Lastly, the statistics of the aerodynamic displacements are represented in Table 5.6.

5.3 Conclusion

The generation of higher-order stochastic processes and its application to nonlinear stochastic structural dynamics are investigated. The BSRM, a new form of higher-order spectral expansion, is utilized to generate wind pressures and velocities and is compared with the existing second-order SRM and ITAM. Based on a dataset of wind

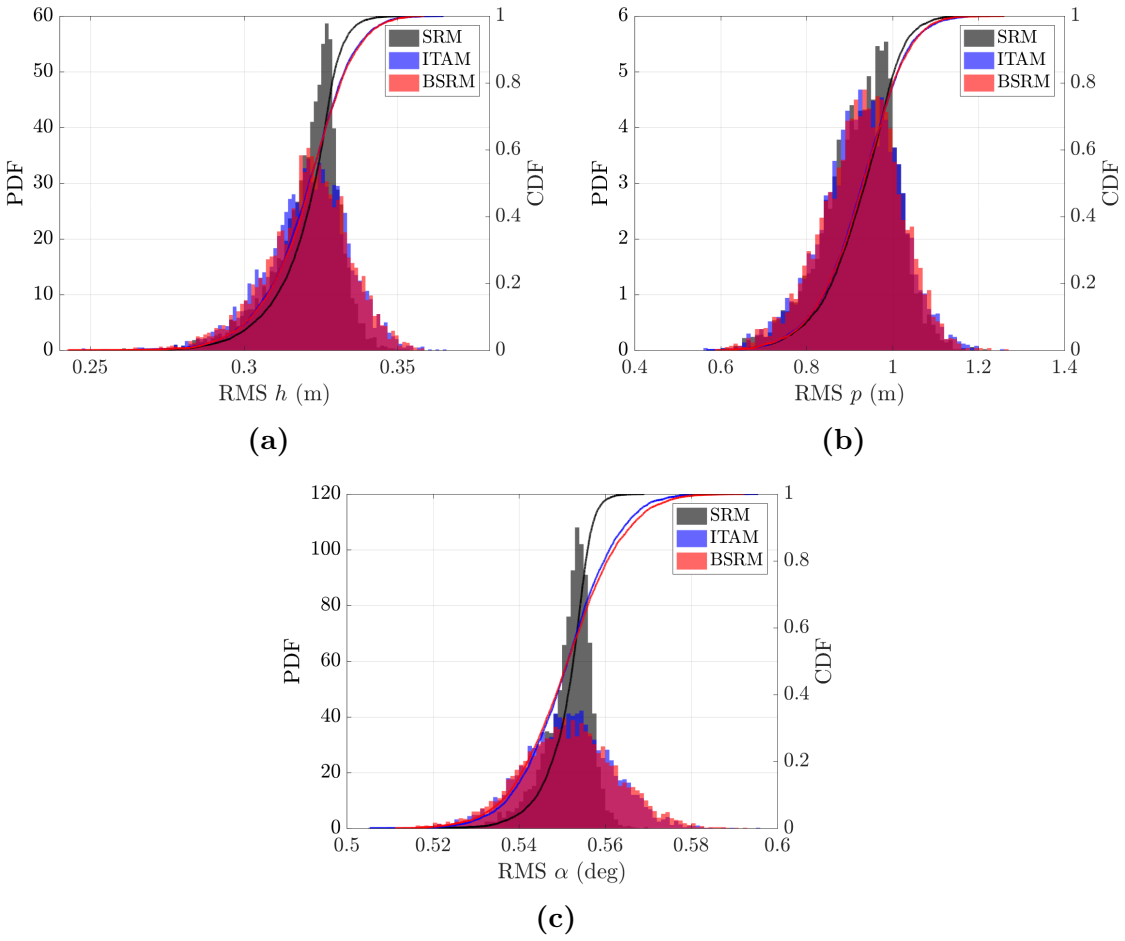

Figure 5.44: Root mean squares of displacements; (a) h, (b) p, (c) α.

tunnel tests on the high-rise building, wind pressure histories are generated using the ITAM and BSRM and utilized to consider the influence of higher-order correlations on the response of an elastic-plastic single degree of freedom structure. Very different responses are observed which appear to be attributed to differences in the bispectra of the simulated histories. Similarly, the wind fluctuations for coupled self-excited and unsteady buffeting loads are generated with the prescribed methods. The skewness and the bispectra of the wind fluctuations in ITAM and BSRM affect the stochastic

properties of the buffeting responses of the bridge deck.

Chapter 6

Summary and future works

This thesis presents novel techniques for simulation of non-Gaussian/non-stationary stochastic processes which are following a prescribed target second-order spectrum by matching a marginal distribution or a third-order spectrum. There has been much research in the past few decades to represent stochastic properties precisely of time histories of wind fluctuations, earthquakes and so on. The introduction of existing representations and definition of high-order spectra, and the efforts to represent the processes are briefly introduced in Chapter 1.

In Chapter 2, the author extended the ITAM to simulation using the K-L expansion for representing non-stationarity. There were primary limitations of the standard ITAM for non-stationary processes; it required estimation of an ES by assuming a pseudo-autocorrelation with high computational time and low accuracy. The proposed method improves the limitations by estimating the underlying Gaussian au-

tocorrelation without any approximation of evolutionary spectrum and matches the target non-Gaussian/non-stationary distribution.

Chapter 3 begins with explaining the limitation of the existing second-order based methodologies without satisfying higher-order orthogonalities of Cramèr representation. A new method by applying orthogonal increments with phase couplings fulfills the third-order condition and generates samples of stochastic processes matching the target power spectrum and bispectrum simultaneously. The author applies the proposed method on the generation of wind velocity histories of the large eddy simulations.

A new approach to characterize phase distributions of wave components is introduced for non-Gaussian spectral representation method in Chapter 4. The models and properties of circular probability distributions are examined and applied to represent phase coupling based on its difference distributions. Simultaneously, the orthogonal conditions of the Cramèr's spectral representation are satisfied with the trigonometric moments of the circular phase difference distribution. Examples with three and four waves stochastic processes with quadratic/cubic phase coupling are shown by matching a given power spectrum and bispectrum or trispectrum respectively.

As applications of the proposed methodologies, the simulation of material or geometrically nonlinear structural dynamics with the time histories generated by SRM, ITAM, and BSRM are compared in Chapter 5. At first, wind pressures from wind tunnel test data are characterized and represented by the ITAM and BSRM. The

performance of an elastic plastic hanging billboard structure is estimated. Secondly, time histories of wind velocity for aerodynamic simulation of a deck bridge are generated with the SRM, ITAM, and BSRM. The coupled self-excited and buffeting forces cause nonlinear excitations and displacements of the deck. The effects of the utilized methods are investigated, and differences in the maximum loading and higher-order spectral analysis are detected among SRM, BSRM and ITAM simulations.

There is immense future work in the simulation of non-Gaussian and non-stationary stochastic processes and fields. Recently, there are several developments to simulate realization of the realistic processes, but the author presented a new technique considering higher-order properties which is not done before. However, it remains to extend the methodology for multi-variate and multi-dimensional processes and fields. The cross-correlations between multi-variate and multi-dimension processes, for example, should be extended to the higher-order correlations and included during their generation.

Besides, there is a diverse potential for applications for the work including ocean surface waves. Specifically, the inner-shore waves include apparent phase coupling among their waves. The proposed methodology with quadratic phase coupling could improve the generation of the waves. The case of 2-dimensional simulation is required for the wave fields, too.

Finally, higher-order phase coupling ins necessary to represent the given trispectrum or fourth-order correlation of processes and beyond. The prescribed BSRM is

limited only up to the third-order correlation including skewed non-linearity. Therefore, it will be important to extend this methodology to include the symmetric non-linearity shown by trispectrum for accurate representation of stochastic processes. In this case, the method is expected to present more strongly non-Gaussian properties including kurtosis.

Appendix A

Newton-CG methodology for the nearest positive semidefinite matrix

Qi and Sun [58] dualized the linear constraints the nearest correlation matrix problem (5.22) with the convex optimization problem as:

$$\min_{y\in\mathbb{R}^n} \theta(y) := \frac{1}{2}\|(A + \mathrm{diag}(y))_+\|^2_{\mathrm{Fb}} - e^T y \tag{A.1}$$

where diag(y) represents the diagonal matrix with vector $y \in \mathbb{R}^n$ as elements, while Diag(B) is the vector of diagonal elements in matrix B.. The projection $(\cdot)_+$ maps symmetric matrix $B \in \mathbb{R}^{n\times n}$ onto the positive semidefinite matrix with spectral

decomposition $B = Q\Lambda Q^T$ where $Q^TQ = I$ and $\Lambda = \text{diag}(\lambda_i)$. The nearest positive semidefinite matrix to B in the Frobenius norm is $B_+ = Q\ \text{diag}(\max(\lambda_i, 0))\ Q^T$.

The following algorithm calculates the nearest matrix of A with given convergence tolerate tol based on Newton method. The methodology is quadratically convergent.

1. Initialize $y_0 \in \mathbb{R}^n$, $\eta \in (0, 1)$, $\rho, \sigma \in (0, 1/2]$, and $k = 0$.

2. Calculate gradient $\nabla\theta(y_k) = \text{Diag}((A + \text{diag}(y)_+) - e$. If $\|\theta(y_k)\|_2 \leq \text{tol}$, the nearest matrix is $(A + \text{diag}(y_k))_+$ and stop.

3. Calculate a spectral decomposition of $A+\text{diag}(y_k)$ and generate the matrix W_{y_k} as:

$$W_{y_k} = \begin{bmatrix} E_{\alpha\alpha} & E_{\alpha\beta} & \mathcal{T} \\ E_{\beta\alpha} & 0 & 0 \\ \mathcal{T} & 0 & 0 \end{bmatrix}, \mathcal{T} = \left(\frac{\lambda_i(y_k)}{\lambda_i(y_k) - \lambda_j(y_k)}\right)_{i\in\alpha, j\in\gamma}, \tag{A.2}$$

where the batchs $\alpha = i : \lambda_i(y_k) > 0$, $\beta = i : \lambda_i(y_k) = 0$, $\gamma = i : \lambda_i(y_k) < 0$, and $E_{\alpha\beta}$ indicates the matrix of ones of dimension $|\alpha| \times |\beta|$.

4. Determine the direction d_k by applicating an iterative method to

$$V_k d_k = \text{Diag}(P_{y_k}(W_{y_k} \circ (P_{y_k}^T D_k P_{y_k}))P_{y_k}^T) = -\nabla\theta(y_k) \tag{A.3}$$

where $d \in \mathbb{R}^n$, $D_k = \text{diag}(d_k)$, P_{y_k} is matrix which its columns are eigenvectors

of $A + \mathrm{diag}(y_k)$, and the operator $\circ$ is the Hadamard product($X \circ Y = (x_{ij}y_{ij})$) until satisfying the conditions:

$$\|\nabla\theta(y_k) + V_k d_k\|_2 \leq \eta_k \|\nabla\theta(y_k)\|_2 \tag{A.4}$$

$$-\frac{\nabla\theta(y_k)^T}{\|d_k\|_2} \cdot \frac{d_k}{\|d_k\|_2} \geq \eta_k \tag{A.5}$$

where $\eta_k = \min \eta, \|\nabla\theta(y_k)\|_2$. If not satisfying either one of conditions, generate the new direction as

$$d_k = -B_k^{-1}\nabla\theta(y_k) \tag{A.6}$$

where B_k is any symmetric positive definite matrix with uniformly bounded $\{\|B_k\|_2\}$ and $\{\|B_k^{-1}\|_2\}$. In this step, the CG method is employed as the solver for the linear system, Eq.(A.3).

5. Find an appropriate step length a_k by utilizing Armijo backtracking that calculate the smallest non-negative integer m_k satisfying the following condition:

$$\theta(y_k + \rho^{m_k} d_k) \leq \theta(y_k) + \sigma\rho^{m_k}\nabla\theta(y_k)^T d_k \tag{A.7}$$

6. Update $\alpha_k = \rho^{m_k}$, $y_{k+1} = y_k + \alpha_k d_k$, and $k = k + 1$. Return to step 2.

Appendix B

Orthogonality of proposed orthogonal increments

The following provides a proof that the proposed orthogonal increments in Eqs. (3.5) - (3.7) satisfy all orthogonality conditions of the Cramér spectral representation up to third-order.

1. The first-order conditions state that $E[du(\omega_k)] = E[dv(\omega_k)] = 0$. That the proposed orthogonal increments satisfy this condition can be proven as follows.

$$\begin{aligned}
&E[du(\omega_k)] = E[du_P(\omega_k) + du_I(\omega_k)] \\
&= E\Bigg[\sqrt{2 \cdot 2S(\omega_k)\Delta\omega_k}\Bigg\{\sqrt{1 - \sum_{i+j=k}^{i\geq j\geq 0} b^2(\omega_i, \omega_j)}\cos\phi_k \\
&+ \sum_{i+j=k}^{i\geq j\geq 0} |b(\omega_i, \omega_j)|\cos\left[\phi_i + \phi_j + \beta(\omega_i, \omega_j)\right]\Bigg\}\Bigg] \\
&= \sqrt{2 \cdot 2S(\omega_k)\Delta\omega_k}\Bigg\{\sqrt{1 - \sum_{i+j=k}^{i\geq j\geq 0} b^2(\omega_i, \omega_j)}E[\cos\phi_k] \\
&+ \sum_{i+j=k}^{i\geq j\geq 0} |b(\omega_i, \omega_j)|E\big[\cos\left[\phi_i + \phi_j + \beta(\omega_i, \omega_j)\right]\big]\Bigg\}
\end{aligned} \tag{B.1}$$

Recalling that ϕ are i.i.d. random phases $\sim U[0, 2\pi]$, it is clear that $E[\cos\phi_k] = 0$ and

$$\begin{aligned}
&E\{\cos\left[\phi_i + \phi_j + \beta(\omega_i, \omega_j)\right]\} \\
&= E\{\cos\left(\phi_i\right)\cos\left[\phi_j + \beta(\omega_i, \omega_j)\right]\} - E\{\sin\left(\phi_i\right)\sin\left[\phi_j + \beta(\omega_i, \omega_j)\right]\} \\
&= E\{\cos\left(\phi_i\right)\}E\{\cos\left[\phi_j + \beta(\omega_i, \omega_j)\right]\} - E\{\sin\left(\phi_i\right)\}E\{\sin\left[\phi_j + \beta(\omega_i, \omega_j)\right]\} \\
&= 0
\end{aligned} \tag{B.2}$$

Consequently, $E[du(\omega_k)] = 0$. Proof that $E[dv(\omega_k)] = 0$ follows in exactly the same way.

2. Second-order conditions:

The condition with identical orthogonal increments described as

$$E[du(\omega_k)du(\omega_l)] = E\{[du_P(\omega_k) + du_I(\omega_k)][du_P(\omega_l) + du_I(\omega_l)]\} \tag{B.3}$$

When $\omega_k = \omega_l$, Eq. (B.3) becomes as

$$\begin{aligned}
&E\{[du_P(\omega_k) + du_I(\omega_k)]^2\} = \\
&= 4|S(\omega_k)\Delta\omega_k|\Big\{\big(1 - \sum_{i+j=k}^{i\geq j\geq 0} b^2(\omega_i,\omega_j)\big)E(\cos^2\phi_k) \\
&+ 2\sum_{i+j=k}^{i\geq j\geq 0}|b(\omega_i,\omega_j)|\sqrt{1 - \sum_{i+j=k}^{i\geq j\geq 0} b^2(\omega_i,\omega_j)}E\{\cos\phi_k\cos\left[\phi_i + \phi_j + \beta(\omega_i,\omega_j)\right]\} \\
&+ \sum_{i+j=k}^{i\geq j\geq 0} b^2(\omega_i,\omega_j)E\{\cos^2\left[\phi_i + \phi_j + \beta(\omega_i,\omega_j)\right]\}\Big\}
\end{aligned} \tag{B.4}$$

The first expectation in Eq. (B.4) can be shown as

$$\begin{aligned}
E\{\cos^2\phi_k\} &= \int_0^{2\pi}\cos^2(\phi_k)\frac{1}{2\pi}d\phi_k \\
&= \int_0^{2\pi}\frac{1+\cos(2\phi_k)}{2}\frac{1}{2\pi}d\phi_k = \frac{1}{2}
\end{aligned} \tag{B.5}$$

and the second one can be shown with independent random phase ϕ,

$$\begin{aligned} E\{\cos\phi_k \cos\left[\phi_i + \phi_j + \beta(\omega_i, \omega_j)\right]\} &= E\{\cos\phi_k\} E\{\cos\left[\phi_i + \phi_j + \beta(\omega_i, \omega_j)\right]\} \\ &= 0 \end{aligned} \tag{B.6}$$

Lastly, the third expectation becomes similar to Eq. (B.5),

$$\begin{aligned} E\big\{\cos^2\left[\phi_i + \phi_j + \beta(\omega_i, \omega_j)\right]\big\} &= E\left\{\frac{1 + 2\cos\left[\phi_i + \phi_j + \beta(\omega_i, \omega_j)\right]}{2}\right\} \\ &= \frac{1 + 2E\{\cos\left[\phi_i + \phi_j + \beta(\omega_i, \omega_j)\right]\}}{2} = \frac{1}{2} \end{aligned} \tag{B.7}$$

Therefore, Eq. (B.4) is written with Eqs. (B.5), (B.6), and (B.7) as

$$\begin{aligned} &E[du^2(\omega_k)] \\ &= 4|S(\omega)\Delta\omega_k| \left[\frac{1 - \sum\limits_{i+j=k}^{i\geq j\geq 0} b^2(\omega_i, \omega_j) + \sum\limits_{i+j=k}^{i\geq j\geq 0} b^2(\omega_i, \omega_j)}{2}\right] \\ &= 2S(\omega_k)\Delta\omega_k \end{aligned} \tag{B.8}$$

Additionally, it can be shown that $E[dv^2(\phi_k)] = 2S(\omega_k)\Delta\omega_k$ in the exactly same way.

The second condition, Eq. (B.3), with different frequencies $\omega_k \neq \omega_l$ becomes zero because the expectation values of cosine terms with random phase becomes zero.

Finally, the expectation of mismatched orthogonal increments with identical

$\omega_k = \omega_l$ can be shown as

$$
\begin{aligned}
&E[du(\omega_k)dv(\omega_k)] \\
&= 4|S(\omega_k)\Delta\omega_k|\Big\{\big[1 - \sum_{i+j=k}^{i\geq j\geq 0} b^2(\omega_i,\omega_j)\big]E(\cos\phi_k \sin\phi_k) \\
&+ \sum_{i+j=k}^{i\geq j\geq 0} |b(\omega_i,\omega_j)|\sqrt{1 - \sum_{i+j=k}^{i\geq j\geq 0} b^2(\omega_i,\omega_j)}E\{\cos\phi_k \sin\big[\phi_i + \phi_j + \beta(\omega_i,\omega_j)\big]\} \\
&+ \sum_{i+j=k}^{i\geq j\geq 0} |b(\omega_i,\omega_j)|\sqrt{1 - \sum_{i+j=k}^{i\geq j\geq 0} b^2(\omega_i,\omega_j)}E\{\sin\phi_k \cos\big[\phi_i + \phi_j + \beta(\omega_i,\omega_j)\big]\} \\
&+ \sum_{i+j=k}^{i\geq j\geq 0} b^2(\omega_i,\omega_j)E\{\cos\big[\phi_i + \phi_j + \beta(\omega_i,\omega_j)\big]\sin\big[\phi_i + \phi_j + \beta(\omega_i,\omega_j)\big]\}\Big\}
\end{aligned}
\tag{B.9}
$$

The expected value in the first term becomes

$$
E\{\cos\phi_k \sin\phi_k\} = \int_0^{2\pi} \frac{\sin 2\phi_k}{2}\frac{1}{2\pi}d\phi_k = 0 \tag{B.10}
$$

Similar to Eq. (B.10), the remaining expectations in Eq. (B.9) with different trigonometric functions become zero, and the final result is written as

$$
E[du(\omega_k)dv(\omega_k)] = 0 \tag{B.11}
$$

With different frequencies $\omega_k \neq \omega_l$, the expected value of different orthogonal increments becomes zero and it can be shown in the synonymous way.

3. Third-order conditions:

When $\omega_k+\omega_l=\omega_m$, the term with $du_P(\omega_k)$, $du_P(\omega_l)$, and $du_I(\omega_m)$ only remains in expectation to have trigonometric functions without any random phase angle. All expression of terms in expected values can be checked in the supplementary data.

$$\begin{aligned}
&E[du(\omega_k)du(\omega_l)du(\omega_m)] \\
&= 8\sqrt{S(\omega_k)S(\omega_l)S(\omega_m)\Delta\omega_k\Delta\omega_l\Delta\omega_m}\sqrt{1-\sum_{i+j=k}^{i\geq j\geq 0} b^2(\omega_i,\omega_j)}\sqrt{1-\sum_{i+j=l}^{i\geq j\geq 0} b_p^2(\omega_i,\omega_j)} \\
&E\Big\{\sum_{i+j=m}^{i\geq j\geq 0} |b(\omega_i,\omega_j)|\cos\phi_k\cos\phi_l\cos\left[\phi_i+\phi_j+\beta(\omega_i,\omega_j)\right]\Big\}
\end{aligned} \tag{B.12}$$

By the definition of pure power spectrum, Eq. (5.22), power spectra at ω_k and ω_l becomes pure power spectra.

$$\begin{aligned}
&E[du(\omega_k)du(\omega_l)du(\omega_m)] \\
&= 8\sqrt{S_p(\omega_k)S_p(\omega_l)S(\omega_m)\Delta\omega_k\Delta\omega_l\Delta\omega_m} \\
&E\Big\{\sum_{i+j=m}^{i\geq j\geq 0} |b_p(\omega_i,\omega_j)|\cos\phi_k\cos\phi_l\cos\left[\phi_i+\phi_j+\beta(\omega_i,\omega_j)\right]\Big\}
\end{aligned} \tag{B.13}$$

In the summation part in Eq. (B.13), the cosine term with ϕ_k, ϕ_l and $\phi_k+\phi_l+\beta(\omega_k,\omega_j)$ only maintains itself in expectation among the pairs of ϕ_i and ϕ_j

satisfying $i + j = m$.

$$\begin{aligned} & E[du(\omega_k)du(\omega_l)du(\omega_m)] \\ & = 8\sqrt{S_p(\omega_k)S_p(\omega_l)S(\omega_m)\Delta\omega_k\Delta\omega_l\Delta\omega_m} \\ & |b_p(\omega_k,\omega_l)|E\Big\{\cos\phi_k\cos\phi_l\cos\big[\phi_k+\phi_l+\beta(\omega_k,\omega_l)\big]\Big\} \end{aligned} \tag{B.14}$$

The expectation of cosine terms is expressed as

$$\begin{aligned} & E\Big\{\cos\phi_k\cos\phi_l\cos\big[\phi_k+\phi_l+\beta(\omega_k,\omega_l)\big]\Big\} \\ & = E\Big\{\frac{\cos[\beta(\omega_k,\omega_l)]+\cos[2\phi_k+\beta(\omega_k,\omega_l)]+\cos[2\phi_l+\beta(\omega_k,\omega_l)]}{4} \\ & \quad + \frac{\cos(2\phi_k+2\phi_l+\beta(\omega_k,\omega_l))}{4}\Big\} \\ & = \frac{\cos[\beta(\omega_k,\omega_l)]}{4} \end{aligned} \tag{B.15}$$

Substituting Eq. (B.15) into (B.14), the result is written as

$$\begin{aligned} & E[du(\omega_k)du(\omega_l)du(\omega_m)] \\ & = 2\sqrt{S_p(\omega_k)S_p(\omega_l)S(\omega_m)\Delta\omega_k\Delta\omega_l\Delta\omega_m}|b_p(\omega_k,\omega_l)|\cos[\beta(\omega_k,\omega_l)] \end{aligned} \tag{B.16}$$

The discretized definition of partial bicoherence, Eq. (3.4), is applied in Eq.

(B.16) as

$$\begin{aligned}
&E[du(\omega_k)du(\omega_l)du(\omega_m)] \\
&= 2\sqrt{S_p(\omega_k)S_p(\omega_l)S(\omega_m)\Delta\omega_k\Delta\omega_l\Delta\omega_m} \\
&\sqrt{\frac{B^2(\omega_i,\omega_j)\Delta\omega_i^2\Delta\omega_j^2}{S_p(\omega_i)\Delta\omega_i S_p(\omega_j)\Delta\omega_j S(\omega_i+\omega_j)\Delta(\omega_i+\omega_j)}}\cos[\beta(\omega_k,\omega_l)] \\
&= 2|B(\omega_k,\omega_l)|\cos\beta(\omega_k,\omega_l)\Delta\omega_k\Delta\omega_l
\end{aligned} \tag{B.17}$$

With the relationship between biphase and bispectrum, Eq. (1.43), finally, the following result satisfy the condition as

$$E[du(\omega_k)du(\omega_l)du(\omega_m) = 2\Re B(\omega_k,\omega_l)\Delta\omega_k\Delta\omega_l \tag{B.18}$$

Finally, in same way it can be shown that

$$\begin{aligned}
E[dv(\omega_k)dv(\omega_l)dv(\omega_m)] &= -2\Im B(\omega_k,\omega_l)\Delta\omega_k\Delta\omega_l \\
E[du(\omega_k)du(\omega_l)dv(\omega_m)] &= 2\Im B(\omega_k,\omega_l)\Delta\omega_k\Delta\omega_l \\
E[du(\omega_k)dv(\omega_l)dv(\omega_m)] &= 2\Re B(\omega_k,\omega_l)\Delta\omega_k\Delta\omega_l
\end{aligned} \tag{B.19}$$

With different frequencies $\omega_k + \omega_l \neq \omega_m$, the expected value of triple pairs with orthogonal increments becomes zero and it can be shown in the synonymous way.

Bibliography

[1] M. Shinozuka, "Monte carlo solution of structural dynamics," *Computers & Structures*, vol. 2, no. 5, pp. 855–874, 1972.

[2] M. Shinozuka and C.-M. Jan, "Digital simulation of random processes and its applications," *Journal of sound and vibration*, vol. 25, no. 1, pp. 111–128, 1972.

[3] M. Shinozuka and G. Deodatis, "Simulation of stochastic processes by spectral representation," *Applied Mechanics Reviews*, vol. 44, no. 4, pp. 191–204, 1991.

[4] R. G. Ghanem and P. D. Spanos, *Stochastic finite elements: a spectral approach*. Courier Corporation, 2003.

[5] S. Huang, S. Quek, and K. Phoon, "Convergence study of the truncated Karhunen–Loève expansion for simulation of stochastic processes," *International journal for numerical methods in engineering*, vol. 52, no. 9, pp. 1029–1043, 2001.

[6] M. Schetzen, "The volterra and wiener theories of nonlinear systems," 1980.

[7] P. Spanos and M. Donley, "Equivalent statistical quadratization for nonlinear systems," *Journal of engineering mechanics*, vol. 117, no. 6, pp. 1289–1310, 1991.

[8] M. Grigoriu and E. Harper, *Applied Non-Gaussian Processes: Examples, Theory, Simulation, Linear Random Vibration, and MATLAB Solutions*. PTR Prentice Hall Upper Saddle River, NJ, 1995.

[9] H. Kim and M. D. Shields, "Modeling strongly non-gaussian non-stationary stochastic processes using the iterative translation approximation method and Karhunen–Loève expansion," *Computers & Structures*, vol. 161, pp. 31–42, 2015.

[10] M. D. Shields and H. Kim, "Simulation of higher-order stochastic processes by spectral representation," *Probabilistic Engineering Mechanics*, vol. 47, pp. 1–15, 2017.

[11] H. Cramér and M. Leadbetter, *Stationary and Related Stochastic Processes: Sample Function Properties and Their Applications*. Wiley, 1967.

[12] M. Rosenblatt, *Stationary Sequences and Random Fields*. Boston: Birkhäuser, 1985.

[13] D. R. Brillinger, "Some history of the study of higher-order moments and spectra," *Statistica Sinica*, vol. 1, no. 465-476, p. 24J, 1991.

[14] C. Nikias and A. Petropulu, *Higher-order Spectra Analysis: A Nonlinear Signal*

Processing Framework, ser. Prentice Hall signal processing series. PTR Prentice Hall, 1993.

[15] M. Rosenblatt and J. W. Van Ness, "Estimation of the bispectrum," *The Annals of Mathematical Statistics*, pp. 1120–1136, 1965.

[16] S. O. Rice, "Mathematical analysis of random noise," *Bell System Technical Journal*, vol. 23, no. 3, pp. 282–332, 1944.

[17] M. Shinozuka and G. Deodatis, "Simulation of multi-dimensional gaussian stochastic fields by spectral representation," *Applied Mechanics Reviews*, vol. 49, no. 1, pp. 29–53, 1996.

[18] G. Deodatis, "Simulation of ergodic multivariate stochastic processes," *Journal of engineering mechanics*, vol. 122, no. 8, pp. 778–787, 1996.

[19] N. Wiener, "Generalized harmonic analysis," *Acta mathematica*, vol. 55, no. 1, pp. 117–258, 1930.

[20] D. C. Champeney, *A Handbook of Fourier Theorems*. Cambridge University Press, 1987.

[21] M. Grigoriu, "On the spectral representation method in simulation," *Probabilistic Engineering Mechanics*, vol. 8, no. 2, pp. 75–90, 1993.

[22] M. Shields, G. Deodatis, and P. Bocchini, "A simple and efficient methodology to approximate a general non-Gaussian stationary stochastic process by a trans-

lation process," *Probabilistic Engineering Mechanics*, vol. 26, no. 4, pp. 511–519, 2011.

[23] W. Betz, I. Papaioannou, and D. Straub, "Numerical methods for the discretization of random fields by means of the Karhunen–Loève expansion," *Computer Methods in Applied Mechanics and Engineering*, vol. 271, pp. 109–129, 2014.

[24] K. Phoon, S. Huang, and S. Quek, "Simulation of second-order processes using Karhunen–Loève expansion," *Computers & structures*, vol. 80, no. 12, pp. 1049–1060, 2002.

[25] K. Phoon, H. Huang, and S. Quek, "Simulation of strongly non-Gaussian processes using Karhunen–Loève expansion," *Probabilistic engineering mechanics*, vol. 20, no. 2, pp. 188–198, 2005.

[26] M. Grigoriu, "Probabilistic models for stochastic elliptic partial differential equations," *Journal of Computational Physics*, vol. 229, no. 22, pp. 8406–8429, 2010.

[27] F. Ferrante, S. Arwade, and L. Graham-Brady, "A translation model for non-stationary, non-Gaussian random processes," *Probabilistic engineering mechanics*, vol. 20, no. 3, pp. 215–228, 2005.

[28] L. F. Shampine, "Matlab program for quadrature in 2D," *Applied Mathematics and Computation*, vol. 202, no. 1, pp. 266–274, 2008.

[29] M. Shields and G. Deodatis, "Estimation of evolutionary spectra for simulation of

non-stationary and non-Gaussian stochastic processes," *Computers & Structures*, vol. 126, pp. 149–163, 2013.

[30] M. Gioffre, V. Gusella, and M. Grigoriu, "Simulation of non-gaussian field applied to wind pressure fluctuations," *Probabilistic Engineering Mechanics*, vol. 15, no. 4, pp. 339–345, 2000.

[31] C. L. Nikias and M. R. Raghuveer, "Bispectrum estimation: A digital signal processing framework," *Proceedings of the IEEE*, vol. 75, no. 7, pp. 869–891, 1987.

[32] C. L. Nikias and J. M. Mendel, "Signal processing with higher-order spectra," *IEEE Signal processing magazine*, vol. 10, no. 3, pp. 10–37, 1993.

[33] S. Torquato, *Random Heterogeneous Materials: Microstructure and Macroscopic Properties*. Springer Science & Business Media, 2013, vol. 16.

[34] C. Yeong and S. Torquato, "Reconstructing random media," *Physical Review E*, vol. 57, no. 1, pp. 495–506, 1998.

[35] L. Graham-Brady and X. F. Xu, "Stochastic morphological modeling of random multiphase materials," *Journal of Applied Mechanics*, vol. 75, no. 6, p. 061001, 2008.

[36] L. D. Lutes and D. C. Chen, "Trispectrum for the response of a non-linear

oscillator," *International journal of non-linear mechanics*, vol. 26, no. 6, pp. 893–909, 1991.

[37] J. M. Mendel, "Tutorial on higher-order statistics (spectra) in signal processing and system theory: theoretical results and some applications," *Proceedings of the IEEE*, vol. 79, no. 3, pp. 278–305, 1991.

[38] J. Nichols, P. Marzocca, and A. Milanese, "The trispectrum for gaussian driven, multiple degree-of-freedom, non-linear structures," *International Journal of Non-Linear Mechanics*, vol. 44, no. 4, pp. 404–416, 2009.

[39] C. McComas and M. Briscoe, "Bispectra of internal waves," *Journal of Fluid Mechanics*, vol. 97, no. 01, pp. 205–213, 1980.

[40] K. Lii, M. Rosenblatt, and C. Van Atta, "Bispectral measurements in turbulence," *Journal of Fluid Mechanics*, vol. 77, no. 01, pp. 45–62, 1976.

[41] P. A. Bogenschutz, A. Gettelman, H. Morrison, V. E. Larson, C. Craig, and D. P. Schanen, "Higher-order turbulence closure and its impact on climate simulations in the community atmosphere model," *Journal of Climate*, vol. 26, no. 23, pp. 9655–9676, 2013.

[42] S. Elgar and R. Guza, "Observations of bispectra of shoaling surface gravity waves," *Journal of Fluid Mechanics*, vol. 161, pp. 425–448, 1985.

[43] J. Doering and A. Bowen, "Shoaling surface gravity waves: A bispectral analysis," in *Proc. 20th Int. Conf. Coastal Engineering*, 1986, pp. 150–162.

[44] M. R. A. Van Gent, "Wave interaction with permeable coastal structures," in *International Journal of Rock Mechanics and Mining Sciences and Geomechanics Abstracts*, vol. 6, no. 33, 1996, p. 277A.

[45] T. J. Maccarone, "The biphase explained: understanding the asymmetries in coupled fourier components of astronomical time series," *Monthly Notices of the Royal Astronomical Society*, p. stt1546, 2013.

[46] Y. C. Kim and E. J. Powers, "Digital bispectral analysis and its applications to nonlinear wave interactions," *Plasma Science, IEEE Transactions on*, vol. 7, no. 2, pp. 120–131, 1979.

[47] D. R. Brillinger, "An introduction to polyspectra," *The Annals of mathematical statistics*, pp. 1351–1374, 1965.

[48] W. Collis, P. White, and J. Hammond, "Higher-order spectra: the bispectrum and trispectrum," *Mechanical systems and signal processing*, vol. 12, no. 3, pp. 375–394, 1998.

[49] J. Fackrell, P. White, J. Hammond, R. Pinnington, and A. Parsons, "The interpretation of the bispectra of vibration signals—: I. theory," *Mechanical Systems and Signal Processing*, vol. 9, no. 3, pp. 257–266, 1995.

[50] A. Masuda and Y.-Y. Kuo, "A note on the imaginary part of bispectra," *Deep Sea Research Part A. Oceanographic Research Papers*, vol. 28, no. 3, pp. 213–222, 1981.

[51] J. Molle and M. J. Hinich, "The trispectrum," in *Higher-Order Spectral Analysis, 1989. Workshop on.* IEEE, 1989, pp. 68–72.

[52] D. Hasselman, "Elastic energy at fracture and surface energy as design criteria for thermal shock," *Journal of the American Ceramic Society*, vol. 46, no. 11, pp. 535–540, 1963.

[53] J. A. Brillinger, *The Collected Works of John W. Tukey: Time.* CRC Press, 1984, vol. 1.

[54] M. Raghuveer and C. Nikias, "Bispectrum estimation: A parametric approach," *IEEE Transactions on Acoustics, Speech, and Signal Processing*, vol. 33, no. 5, pp. 1213–1230, 1985.

[55] M. B. Priestley, "Evolutionary spectra and non-stationary processes," *Journal of the Royal Statistical Society. Series B (Methodological)*, pp. 204–237, 1965.

[56] B. A. Benowitz, M. D. Shields, and G. Deodatis, "Determining evolutionary spectra from non-stationary autocorrelation functions," *Probabilistic Engineering Mechanics*, vol. 41, pp. 73–88, 2015.

[57] N. J. Higham, "Computing the nearest correlation matrix—a problem from finance," *IMA journal of Numerical Analysis*, vol. 22, no. 3, pp. 329–343, 2002.

[58] H. Qi and D. Sun, "A quadratically convergent newton method for computing the nearest correlation matrix," *SIAM journal on matrix analysis and applications*, vol. 28, no. 2, pp. 360–385, 2006.

[59] R. Borsdorf and N. J. Higham, "A preconditioned newton algorithm for the nearest correlation matrix," *IMA Journal of Numerical Analysis*, vol. 30, no. 1, pp. 94–107, 2010.

[60] M. J. Hinich and M. Wolinsky, "Normalizing bispectra," *Journal of statistical planning and inference*, vol. 130, no. 1, pp. 405–411, 2005.

[61] J. S. Bendat and A. G. Piersol, *Random data: analysis and measurement procedures*. John Wiley & Sons, 2011, vol. 729.

[62] L. Shi and D. Yeo, "OpenFOAM Large-Eddy Simulations of Atmospheric Boundary Layer Turbulence for Wind Engineering Applications," National Institute of Standars and Technology, Tech. Rep., 2015.

[63] A. Swami, J. M. Mendel, and C. L. M. Nikias, "Higher-order spectral analysis toolbox," LIGO Caltech, Tech. Rep., 1993. [Online]. Available: https://labcit.ligo.caltech.edu/~rana/mat/HOSA/HOSA.PDF

[64] N. I. Fisher, *Statistical Analysis of Circular Data*. Cambridge University Press, 1995.

[65] K. V. Mardia and P. E. Jupp, *Directional Statistics*. John Wiley & Sons, 2009, vol. 494.

[66] S. R. Jammalamadaka and A. Sengupta, *Topics in Circular Statistics*. World Scientific, 2001, vol. 5.

[67] R. von Mises, "Über die 'ganzzahligkeit' der Atomgewicht und verwandte Fragen," *Physikalische Zeitschrift*, vol. 19, pp. 490–500, 1918.

[68] E. Gumbel, J. A. Greenwood, and D. Durand, "The circular normal distribution: Theory and tables," *Journal of the American Statistical Association*, vol. 48, no. 261, pp. 131–152, 1953.

[69] P. F. Felzenszwalb and D. P. Huttenlocher, "Pictorial structures for object recognition," *International journal of computer vision*, vol. 61, no. 1, pp. 55–79, 2005.

[70] X. Wang, K. Tieu, and E. Grimson, "Learning semantic scene models by trajectory analysis," *Computer Vision–ECCV 2006*, pp. 110–123, 2006.

[71] D. R. Brillinger and M. Rosenblatt, "Asymptotic theory of estimates of kth-order spectra," *Proceedings of the National Academy of Sciences*, vol. 57, no. 2, pp. 206–210, 1967.

[72] R. A. Haubrich, "Earth noise, 5 to 500 millicycles per second: 1. spectral stationarity, normality, and nonlinearity," *Journal of Geophysical Research*, vol. 70, no. 6, pp. 1415–1427, 1965.

[73] Tokyo Polytechnic University. TPU wind pressure database. [Online]. Available: http://wind.arch.t-kougei.ac.jp/system/eng/contents/code/tpu

[74] X. Chen, M. Matsumoto, and A. Kareem, "Time domain flutter and buffeting response analysis of bridges," *Journal of Engineering Mechanics*, vol. 126, no. 1, pp. 7–16, 2000.

[75] M. Matsumoto, X. Chen, and N. Shiraishi, "Buffeting analysis of long-span bridge with aerodynamic coupling," in *Proc., 13th National Symposium on Wind Engineering*, 1994, pp. 227–232.

[76] H. Xiang, C. Liu, and M. Gu, "Time domain analysis for coupled buffeting response of long-span bridges," in *Proceedings of the 9th International Conference on Wind Engineering, New Delhi, India*, 1995, pp. 881–892.

[77] G. Diana, S. Bruni, A. Collina, and A. Zasso, "Aerodynamic challenges in super long span bridges design," in *Proceedings of the International Symposium on Advances in Bridge Aerodynamics*, 1998, pp. 10–13.

[78] R. Scanlan, "The action of flexible bridges under wind, 2: Buffeting theory," *Journal of Sound and Vibration*, vol. 60, no. 2, pp. 201–211, 1978.

[79] P. P. Sarkar, N. P. Jones, and R. H. Scanlan, "Identification of aeroelastic parameters of flexible bridges," *Journal of Engineering Mechanics*, vol. 120, no. 8, pp. 1718–1742, 1994.

[80] Y. Lin and J. Yang, "Multimode bridge response to wind excitations," *Journal of Engineering Mechanics*, vol. 109, no. 2, pp. 586–603, 1983.

[81] C. G. Bucher and Y. K. Lin, "Stochastic stability of bridges considering coupled modes," *Journal of Engineering Mechanics*, vol. 114, no. 12, pp. 2055–2071, 1988.

[82] K. L. Roger, "Airplane math modeling methods for active control design," *AGARD-CP-228*, pp. 4–1–4–11, 1977.

[83] R. H. Scanlan, "Problematics in formulation of wind-force models for bridge decks," *Journal of engineering mechanics*, vol. 119, no. 7, pp. 1353–1375, 1993.

[84] A. G. Davenport, "Buffeting of a suspension bridge by storm winds," *Journal of the Structural Division*, vol. 88, no. 3, pp. 233–270, 1962.

[85] X. Chen, M. Matsumoto, and A. Kareem, "Aerodynamic coupling effects on flutter and buffeting of bridges," *Journal of Engineering Mechanics*, vol. 126, no. 1, pp. 17–26, 2000.

[86] X. Chen and A. Kareem, "Advances in modeling of aerodynamic forces on bridge decks," *Journal of Engineering Mechanics*, vol. 128, no. 11, pp. 1193–1205, 2002.

BIBLIOGRAPHY

[87] T. Theodorsen, "General theory of aerodynamic instability and the mechanism of flutter," 1949.

[88] W. Jones, "The generalized theodorsen function," *Journal of the Aeronautical Sciences*, vol. 19, no. 3, pp. 213–213, 1952.

[89] W. R. Sears, "Some aspects of non-stationary airfoil theory and its practical application," *Journal of the Aeronautical Sciences*, vol. 8, no. 3, pp. 104–108, 1941.

[90] I. Kavrakov and G. Morgenthal, "A comparative assessment of aerodynamic models for buffeting and flutter of long-span bridges," *Engineering*, 2017.

Vita

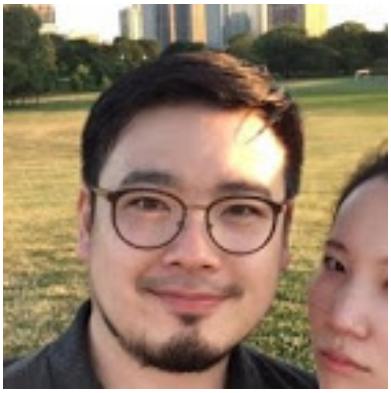

Hwanpyo Kim was born in Seoul, Republic of Korea (South Korea) on the 30th of July 1985. He received his B.S. and M.S. degrees in Civil Engineering from The University of Seoul in 2011 and 2013 respectively. He was inducted as Student President in the Student Club Association in 2010, and awarded Scholarship for Excellent Achievement in 2011 and 2012 in The University of Seoul. He also graduated on the Dean's list.

He enrolled in the Ph.D. program at the department of Civil Engineering at Johns Hopkins University with Civil Engineering Research Fellowship in 2013. He was supported by National Science Foundation in 2017. His research is focused on uncertainty modeling of structural excitations including wind fluctuations and earthquake accelerations. Hwanpyo's papers have been published in *Computers & Structures* and *Probabilistic Engineering Mechanics*.